118

Karlsruher Schriftenreihe
Fahrzeugsystemtechnik

Alexander Jackstadt

Constrained-layer damping in hybrid fibre metal elastomer laminates and its tolerance to damage

KIT Scientific Publishing

Alexander Jackstadt

Constrained-layer damping in hybrid fibre metal elastomer laminates and its tolerance to damage

Karlsruher Schriftenreihe Fahrzeugsystemtechnik
Band 118

Herausgeber
FAST Institut für Fahrzeugsystemtechnik
Prof. Dr.-Ing. Martin Cichon
Prof. Dr. rer. nat. Frank Gauterin
Prof. Dr.-Ing. Marcus Geimer
Prof. Dr.-Ing. Frank Henning
Prof. Dr.-Ing. Luise Kärger

Das Institut für Fahrzeugsystemtechnik besteht aus den Institutsteilen Bahnsystemtechnik, Fahrzeugtechnik, Leichtbau und Mobile Arbeitsmaschinen.

Eine Übersicht aller bisher in dieser Schriftenreihe erschienenen Bände finden Sie am Ende des Buchs.

Constrained-layer damping in hybrid fibre metal elastomer laminates and its tolerance to damage

by
Alexander Jackstadt

KIT Scientific Publishing

Karlsruher Institut für Technologie
Institut für Fahrzeugsystemtechnik

Constrained-layer damping in hybrid fibre metal elastomer laminates and its tolerance to damage

Zur Erlangung des akademischen Grades eines Doktors der Ingenieurwissenschaften von der KIT-Fakultät für Maschinenbau des Karlsruher Instituts für Technologie (KIT) genehmigte Dissertation

von Alexander Jackstadt, M.Sc.

Tag der mündlichen Prüfung: 12. April 2024
Hauptreferentin: Prof. Dr.-Ing. Luise Kärger
Korreferent: Prof. Dr.-Ing. Kay Weidenmann

Impressum

KIT Scientific Publishing

Karlsruher Institut für Technologie (KIT)
KIT Scientific Publishing
Straße am Forum 2
D-76131 Karlsruhe

www.bibliothek.kit.edu/ksp.php | E-Mail: info@ksp.kit.edu | Shop: www.ksp.kit.edu

Print on Demand 2025 – Gedruckt auf FSC-zertifiziertem Papier

ISSN 1869-6058
ISBN 978-3-7315-1376-6
DOI 10.5445/KSP/1000172235

Kurzfassung

Faserverstärkte Kunststoffe werden aufgrund ihrer herausragenden gewichtsspezifischen mechanischen Eigenschaften wie Steifigkeit und Festigkeit häufig als Leichtbaumaterial verwendet. In Kombination mit zusätzlichen Metallschichten, allgemein als Faser-Metall-Laminate (FML) bezeichnet, bieten solche Hybride zusätzlich eine hohe Widerstandsfähigkeit und Toleranz gegenüber Schädigung. Wie bei den meisten Leichtbaumaterialien gehen diese Vorteile jedoch mit Nachteilen einher. Insbesondere die hohe Steifigkeit und die niedrige Massendichte solcher Materialien oder Materialsysteme machen die entsprechenden Strukturen anfällig für Schwingungen, da herkömmliche Leichtbaumaterialien in der Regel nur eine vernachlässigbare Materialdämpfung bieten. Die Zugabe nachgiebiger Schichten aus viskoelastischen Elastomeren innerhalb des ansonsten steifen Laminats kann die erreichbare Dämpfung signifikant erhöhen. Dieses Prinzip ist als *constrained-layer damping* (CLD) bekannt. Eine solche Hybridisierung ermöglicht stark gedämpfte und leichte Laminatstrukturen, die auf spezifische Dämpfungseigenschaften abgestimmt werden können. Insbesondere untersucht diese Arbeit hybride Faser-Metall-Elastomer-Laminate (FMEL), bestehend aus kohlenstofffaserverstärktem Kunststoff (CFK), Aluminium und verschiedenen Elastomeren in unterschiedlichen Laminatkonfigurationen.

Diese hybriden FMEL bieten eine enorme Gestaltungsfreiheit hinsichtlich Materialauswahl, Schichtdicken und allgemeinem Laminataufbau. Da Herstellung und Charakterisierung neuer Laminate aufwendig sind, sind Vorhersagemodelle nötig, um optimale Designs im Voraus zu finden. Die Entwicklung

eines solchen Modells steht im Mittelpunkt dieser Arbeit. Hierzu wird ein analytisches Modell auf Basis einer Plattentheorie zur schnellen und präzisen Vorhersage des statischen Verformungsverhaltens, der modalen Eigenschaften und der Antwort auf erzwungene Schwingung der Laminate präsentiert. Anschließende Studien, die dieses Modell anwenden, untersuchen verschiedene FMEL hinsichtlich ihres Dämpfungsverhaltens, um allgemeine Zusammenhänge zwischen Laminatparametern und der erreichbaren Dämpfung aufzudecken.

Darüber hinaus ist bekannt, dass Elastomermaterialien bei mäßigen oder hohen Verformungen eine progressive zyklische Erweichung, den sogenannten Mullins-Effekt, aufweisen. Der aktuelle Stand der Forschung liefert keine Aussagen zum Einfluss des Mullins-Effekts in CLD-Laminaten, weshalb diese Arbeit experimentelle und numerische Methoden anwendet, um einen Einfluss auf das Dämpfungsverhalten hybrider CLD-Laminate aufzudecken.

FML und insbesondere FMEL wird eine hohe Toleranz gegenüber Schädigungen zugesprochen. Die Toleranz des intrinsischen CLD-Mechanismus gegenüber verschiedenen Arten von Schädigungen ist bisher jedoch gänzlich unbekannt. Die vorliegende Arbeit schließt diese Forschungslücke, indem experimentell das Auftreten von Schlagschäden in verschiedenen FMEL charakterisiert wird. Anschließend werden numerische Modelle dieser geschädigten Laminate verwendet, um den Einfluss der auftretenden Schädigungsarten auf die Dämpfungseigenschaften der FMEL zu identifizieren.

Insgesamt verdeutlicht diese Arbeit die Komplexität und zahlreichen Abhängigkeiten des CLD-Mechanismus innerhalb von FMEL. Sie präsentiert experimentelle, analytische und numerische Methoden zur Vorhersage der Dämpfungseigenschaften solcher Laminate, vornehmlich um deren Toleranz gegenüber Schäden zu bewerten.

Abstract

Fibre-reinforced polymers (FRPs) are widely used as a lightweight material of choice due to their outstanding weight-specific mechanical properties such as stiffness and strength. The combination with sheets of metal, commonly referred to as fibre metal laminates (FMLs), additionally provides a high resistance and tolerance to damage. As with most lightweight materials, these advantages come at a cost. In particular, the high stiffness and low mass density of such materials or material systems make the resulting structures prone to vibrations as conventional lightweight materials usually offer only negligible material damping. The addition of highly compliant layers consisting of viscoelastic elastomer materials within the otherwise stiff laminate can significantly increases the achievable damping, following the principle of constrained-layer damping (CLD). Such a hybridisation then allows for highly damped lightweight laminates, which can be tailored to achieve specific damping capabilities. In particular, this work considers hybrid fibre metal elastomer laminates (FMELs), consisting of carbon fibre-reinforced polymer (CFRP), aluminium and different elastomer compounds in various laminate configurations.

These hybrid FMELs offer a tremendous design freedom with regard to material selection, layer thicknesses and general laminate lay-up. Since manufacturing and testing of new laminates can be cumbersome, predictive models are desirable in order to find optimal designs beforehand. The development of such a model based is subject of this work. In particular, an analytical model based on a unified plate theory for the rapid and precise prediction of the laminates' static deformation behaviour, modal characteristics and steady-state response is presented. Subsequent studies

applying this model investigate different FMELs with regard to their damping behaviour in order to uncover general correlations between laminate parameters and the achievable damping.

Furthermore, elastomer materials are known to exhibit progressive cyclic softening, called Mullins effect, when subjected to moderate or high strains. As there is no previous research on the role of the Mullins effect in CLD laminates, this work employs experimental and numerical methods in order to uncover an influence on the damping behaviour of hybrid CLD laminates.

FMLs and FMELs in particular are known for their tolerance to damage. The tolerance of the intrinsic CLD mechanism with regard to different types of damage, however, is so far entirely unexplored. The present work addresses this research gap by employing experimental methods for the determination of low-velocity impact damage in different FMELs. Subsequently, numerical models of those damaged laminates are used in order to identify the influence of the occurring types of damage on the damping capabilities of FMELs.

Overall, this work highlights the complexity and numerous dependencies of the CLD mechanism within FMELs. It presents experimental, analytical and numerical methods for predicting the damping capabilities of such laminates, in particular in order to optimise and assess its tolerance to damage.

Danksagung

Die hier vorliegende Arbeit entstand während meiner Tätigkeit als akademischer Mitarbeiter am Karlsruher Institut für Technologie (KIT). Eine Vielzahl von Personen hat mich in dieser Zeit tatkräftig unterstützt und somit auf unterschiedlichste Art und Weise einen Beitrag zu dieser Arbeit geleistet. Ihnen allen gilt mein herzlichster Dank. Insbesondere möchte ich mich bei meiner Referentin Frau Prof. Dr.-Ing. Luise Kärger für die intensive und vertrauensvolle Betreuung der letzten Jahre bedanken. Immer ansprechbar, hat sie mich mit Hingabe und Fachwissen fachlich stets weitergebracht. Ebenso gilt mein Dank dem Korreferenten dieser Arbeit, Herrn Prof. Dr.-Ing. Kay Weidenmann, dessen hilfreiche Anregungen maßgeblich zu den experimentellen Anteilen dieser Arbeit beigetragen haben.

Außerdem möchte ich mich bei allen Arbeitskollegen und -kolleginnen bedanken, die mich über die Jahre begleitet haben. Sowohl am Institutsteil Leichtbau (LB) des Instituts für Fahrzeugsystemtechnik (FAST) als auch in der Gruppe Hybride Werkstoffe und Leichtbau (HWL) des Instituts für Angewandte Materialien – Werkstoffkunde (IAM-WK) schätzte ich den offenen, kooperativen und freundschaftlichen Umgang. Besonders hervorheben möchte ich hier die Kollegen Nils Meyer, Florian Wittemann, Siegfried Galkin und Constantin Krauß am FAST, auf deren Rat ich mich stets verlassen konnte. Ebenso gilt mein Dank Sarah Müller und Kevin Daiß, die durch ihren unermüdlichen Einsatz ein Forschen überhaupt erst möglich machen. Am IAM-WK möchte ich Wilfried Liebig, Vincent Sessner, Henrik Werner, Markus Muth und Benedikt

Scheuring meinen herzlichsten Dank für die tatkräftige Unterstützung bei diversen Experimenten und der Diskussion dieser aussprechen. Auch die Unterstützung von Christoph Schelleis am Fraunhofer Institut für Chemische Technologie (ICT) bei der Probenfertigung möchte ich besonders hervorheben.

Außerdem möchte ich mich bei allen von mir betreuten Studierenden für die schöne Zusammenarbeit bedanken. Insbesondere freue ich mich darüber, mit Felix Frölich und Sarah Dietrich einen sehr geschätzten Kollegen bzw. eine sehr geschätzte Kollegin gewonnen zu haben.

Für die Finanzierung der von mir bearbeiteten Projekte, deren Ergebnisse maßgeblich zu dieser Arbeit beigetragen haben, möchte ich mich bei der Deutschen Forschungsgemeinschaft (DFG) und der Vector Stiftung bedanken.

Auch in Zeiten von Verzweiflung und Verdruss in Anbetracht des eigenen wissenschaftlichen Fortschritts war es mein Freundeskreis, der mich stets aufzuheitern vermochte. Ein herzliches Dankeschön hierfür.

Besonderer Dank gilt meinen Eltern für die Unterstützung, nicht nur während der letzten sechs, sondern vielmehr der letzten 30 Jahre. Schließlich bedanke ich mich bei meiner Freundin Stephi für den liebevollen Rückhalt, die fortwährende Unterstützung und Geduld.

Karlsruhe, April 2024 *Alexander Jackstadt*

Contents

Acronyms and symbols

Acronyms

AEM	ethylene acrylic elastomer
ASTM	American Society for Testing and Materials
CFRP	carbon fibre-reinforced polymer
CLD	constrained-layer damping
CLT	Classical Lamination Theory
CUF	Carrera Unified Formulation
DFG	Deutsche Forschungsgemeinschaft
DIC	digital image correlation
DMA	dynamic mechanical analysis
DOF	degree of freedom
EPDM	ethylene propylene diene monomer
ESL	equivalent single layer
FE	finite element
FEM	Finite Element Method
FLD	free-layer damping
FMEL	fibre metal elastomer laminate
FML	fibre metal laminate
FRF	frequency response function
FRP	fibre-reinforced polymer
FSDT	First-Order Shear Deformation Theory
GFRP	glass fibre-reinforced polymer

GMM	Generalized Maxwell Model
GUF	Generalized Unified Formulation
HNBR	hydrated nitrile butadiene rubber
HyCEML	hybrid CFRP elastomer metal laminate
IAM-WK	Institute for Applied Materials - Materials Science and Engineering
KIT	Karlsruhe Institute of Technology
LW	layerwise
MEL	metal elastomer laminate
MFHL	mixed form of Hooke's law
MZZF	Murakami's zig-zag function
prepreg	preimpregnated
PVD	Principle of Virtual Displacements
RMVT	Reissner's Mixed Variational Theorem
RKU	Ross-Kerwin-Ungar
SBR	styrene butadiene rubber
TTS	time-temperature superposition
UD	unidirectionally reinforced
WLF	Williams-Landel-Ferry
ZZ	zig-zag

Constants

g	Gravity of Earth: $g = 9.81\,\mathrm{m\,s^{-2}}$
i	Imaginary unit: $\mathrm{i}^2 = -1$
R	Gas constant: $R = 8.31446\,\mathrm{J\,K^{-1}\,mol^{-1}}$
π	Archimedes constant: $\pi = 3.141\,59$

Scalars

a_{T}	Horizontal shift factor
b_{T}	Vertical shift factor
d_{f}	Fibre damage parameter
d_{m}	Matrix damage parameter
d_{s}	Interface damage parameter
E	Young's modulus
E^*	Complex modulus
E'	Storage modulus
E''	Loss modulus
f	Frequency
f_n	Natural frequency of the n^{th} vibration mode
G	Shear modulus
I_i	i^{th} Cauchy-Green invariant
J	Volume change
p	Pressure
Q	Load coefficient
U	Volumetric part of strain energy density
W	Deviatoric part of strain energy density
z	Thickness coordinate
β_a	Stress coefficients

γ_{ab}	Elasticity coefficients
δ	Loss angle
$\tan(\delta)$	Loss factor
ζ	Normalized thickness coordinate
η_1	Softening parameter
η_2	Permanent set
κ	Bulk modulus
λ	Stretch
λ_i	i^{th} principal stretch
μ	Lamé's second parameter
ν	Poisson's ratio
ξ_n	Modal damping ratio of the n^{th} vibration mode
ρ	Mass density
Ψ	Strain energy density function
ω	Circular frequency

Tensors (1st order)

$\boldsymbol{u}$	Displacement vector
$\boldsymbol{x}$	Location vector

Tensors (2nd order)

$\boldsymbol{F}$	Deformation gradient
$\boldsymbol{C}$	Left Cauchy-Green deformation tensor
$\boldsymbol{B}$	Right Cauchy-Green deformation tensor
$\boldsymbol{U}$	Stretch tensor
$\boldsymbol{V}$	Stretch tensor
$\boldsymbol{\sigma}$	Cauchy stress tensor
$\mathbf{1}$	Identity tensor
$\boldsymbol{\varepsilon}$	Logarithmic strain tensor
$\boldsymbol{e}$	Nominal strain tensor

Tensors (4th order)

$\mathbb{C}$	Stiffness tensor
$\mathbb{J}$	Compliance tensor

Vectors and matrices

$\mathbf{K}$	Stiffness matrix
$\mathbf{M}$	Mass matrix
$\mathbf{R}$	Right-hand side load vector
$\mathbf{U}$	Generalized displacement vector
$\mathbf{S}$	Generalized out-of-plane stress vector

Operators and math symbols

$\Re()$	Real part
$\Im()$	Imaginary part
$\otimes$	Dyadic product
$\hat{(\cdot)}$	Amplitude
$(\cdot)^*$	Complex valued quantity
$(\cdot)_\mathrm{p}$	In-plane quantity
$(\cdot)_\mathrm{n}$	Out-of-plane quantity
$(\cdot)^\mathrm{dev}$	Deviatoric quantity

1 Introduction

1.1 Motivation

Lightweight engineering within its technical, economical, environmental and social constraints is considered an important contribution towards reducing the energy and resources necessary for functioning technical systems. Reducing a component's weight by employing lightweight materials, which offer equal or better mechanical properties at a lower mass density, is one prominent option towards a successful lightweight design. Consequently, a lasting trend of developing new structural lightweight materials is observed in areas characterised by high energy consumption such as the transportation sector. The automotive and aerospace sectors in particular benefit from a reduced system mass and have increasingly employed modern lightweight material systems such as fibre-reinforced polymers (FRPs) or fibre metal laminates (FMLs). While such materials offer a substantial lightweight potential, they usually do not contribute to the smooth and calm operation of the system as their low mass and high stiffness make them, or any other lightweight structure, susceptible to increased vibrations due to either internal or external excitation. Vibrations are undesired in most technical systems for a number of reasons. First, they can limit the comfort, for example in the form of increased noise in automotives and aeroplanes. Furthermore, vibrations can lead to increased wear and even premature failure or need of maintenance. Some technical systems may even require vibrations to not exceed certain limits in order to be fully functional. Within the context of lightweight design, this can prove to be a conflict of interest as lightweight materials and structures for the most part offer almost no intrinsic damping and thus rely

on external damping measures, which in turn contribute additional weight. Therefore, an efficient and robust damping of structures is of paramount economical and ecological interest.

Within the Deutsche Forschungsgemeinschaft (DFG) (English: German Research Foundation) priority program SPP 1897 "Calm, Smooth and Smart - Novel Approaches for Influencing Vibrations by Means of Deliberately Introduced Dissipation ", a variety of approaches to tackle the outlined challenges have been developed and thoroughly investigated. One of those is the hybridisation of traditional lightweight FMLs in order to increase their intrinsic material damping by incorporating additional elastomer layers in order to invoke a mechanism commonly referred to as constrained-layer damping (CLD). Previous works have shown the effectiveness and potential of such laminates using experimental methods. These preceding studies also highlight the complexity of the CLD mechanism within hybrid laminates with regard to a vast variety of parameters, which influence the resulting damping behaviour. The present thesis aims at a closer investigation of some, and by no means all, of these influential factors using experimental, analytical and numerical methods. In particular, it considers the influence of material selection, various types of damage and non-linear material behaviour.

1.2 Thesis outline

In order to properly address these aims, this thesis is structured in the following way. Chapter 2 introduces selected fundamentals, which will be referenced throughout the remainder of this work, and outlines the current state of related research regarding the subjects addressed by this contribution. Following the identification of research gaps, the scientific objectives of this work are introduced in Chapter 3. The hybrid material system, which serves as a carrier for the numerous effects studied here, is introduced in Chapter 4. Specifically, the different configurations, the manufacturing process and mechanical properties are presented. Chapter 5 introduces

the reader to an analytical modelling approach, which has been specifically developed for predicting the static and vibrational behaviour of hybrid laminates. Furthermore, the influence of material and laminate parameters are investigated with a focus on the achievable damping characteristics. Chapter 6 is based on the hypothesis, that an accurate analysis of CLD also requires the consideration of large-strain phenomena such as the Mullins effect commonly observed in elastomer materials. Experimental methods are applied as well as numerical ones involving the development of suitable material models. In Chapter 7, experimental and numerical methods are employed in order to determine the influence of various types of damage resulting from low-velocity impact loading on the vibration characteristics of the studied laminates. While each chapter presents its own results followed by the discussion of the same, Chapter 8 provides a summary of the main contributions of this thesis to the state of research on CLD in hybrid laminates.

2 Fundamentals and related research

This chapter introduces selected theories, notations and correlations to the reader, which will be referenced in subsequent chapters. The aspects presented here are not part of the scientific contribution of this thesis. They merely serve the goal of introducing the reader to certain concepts, which will be taken up when the methodology of the scientific work is outlined. Furthermore, this chapter introduces the research related to this work, which forms the current state of the art at time of writing. From this, the research goals formulated in Chapter 3 are deducted.

2.1 Mechanical behaviour of elastomers

2.1.1 Hyperelasticity

Elastomer materials are commonly known to deform elastically to very large strains before onset of failure or plasticity effects. In addition, these deformations are often non-linear. Consequently, the theory of linear elasticity does not suffice for the modelling of such materials, if the whole range of their elasticity is to be taken into account. Hyperelasticity is a generalization of linear elasticity to incorporate the mentioned large strains and material non-linearity [1].

2.1.1.1 Kinematics

If a continuum body deforms due to applied loads or kinematic constraints from an undeformed reference configuration, occupying a region Ω_0, to its current configuration, it then occupies a region Ω. A material point in the reference configuration addressed by the vector $\boldsymbol{X} \in \Omega_0$ is consequently displaced by a function χ to the current configuration

$$\boldsymbol{x} = \chi(\boldsymbol{X}, t) \quad \boldsymbol{x} \in \Omega. \tag{2.1}$$

The displacement field of this material point

$$\boldsymbol{u}(\boldsymbol{X}, t) = \chi(\boldsymbol{X}, t) - \boldsymbol{X} = \boldsymbol{x} - \boldsymbol{X} \tag{2.2}$$

can be calculated accordingly. While Equation 2.2 fully defines the displacement of the body, it does not differentiate between rigid body motions and actual deformations. To remove pure translations, the deformation gradient is defined as

$$\boldsymbol{F} = \operatorname{grad}\left(\chi(\boldsymbol{X}, t)\right) = \frac{\partial \boldsymbol{x}}{\partial \boldsymbol{X}}. \tag{2.3}$$

The change of volume evoked by the deformation is calculated from its determinant

$$J = \det(\boldsymbol{F}). \tag{2.4}$$

Polar decomposition of the deformation gradient

$$\boldsymbol{F} = \boldsymbol{R}\boldsymbol{U} = \boldsymbol{V}\boldsymbol{R} \tag{2.5}$$

produces the pure stretch tensors $\boldsymbol{U}$ and $\boldsymbol{V}$ as well as the pure rotation tensor $\boldsymbol{R}$. Furthermore, the right and left Cauchy-Green deformation tensors $\boldsymbol{C}$ and $\boldsymbol{B}$ can be defined as

$$\boldsymbol{C} = \boldsymbol{F}^{\top}\boldsymbol{F} = \boldsymbol{U}^2 \tag{2.6}$$

and

$$\boldsymbol{B} = \boldsymbol{F}\boldsymbol{F}^{\top} = \boldsymbol{V}^2. \tag{2.7}$$

These symmetric tensors can also be expressed by their real-valued eigenvalues λ_α^2 and mutually orthogonal eigenvectors $\boldsymbol{n_\alpha}$ and $\boldsymbol{m_\alpha}$. Equation (2.6) and Equation (2.7) can then be rewritten as

$$\boldsymbol{C} = \sum_{\alpha=1}^{3} \lambda_\alpha^2 \left(\boldsymbol{n}_\alpha \otimes \boldsymbol{n}_\alpha\right) \tag{2.8}$$

and

$$\boldsymbol{B} = \sum_{\alpha=1}^{3} \lambda_\alpha^2 \left(\boldsymbol{m}_\alpha \otimes \boldsymbol{m}_\alpha\right). \tag{2.9}$$

In Equations (2.8) and (2.9), $\boldsymbol{m}_\alpha$ and $\boldsymbol{n}_\alpha$ are the principal directions in the material and spacial configurations. The eigenvalues λ_α^2 of both, right and left, Cauchy-Green tensors are the squared principal stretches of the deformation. Three invariants of both, the right and the left Cauchy-Green tensor, can consequently be defined as

$$\begin{aligned} I_1 &= \mathrm{tr}\left(\boldsymbol{C}\right) = \mathrm{tr}\left(\boldsymbol{B}\right) = \lambda_1^2 + \lambda_2^2 + \lambda_3^2 \\ I_2 &= \frac{1}{2}\left[\left(\mathrm{tr}\left(\boldsymbol{C}\right)\right)^2 + \mathrm{tr}\left(\boldsymbol{C}^2\right)\right] = \frac{1}{2}\left[\left(\mathrm{tr}\left(\boldsymbol{B}\right)\right)^2 + \mathrm{tr}\left(\boldsymbol{B}^2\right)\right] = \lambda_1^2\lambda_2^2 + \lambda_1^2\lambda_3^2 + \lambda_2^2\lambda_3^2 \\ I_3 &= \det\left(\boldsymbol{C}\right) = \det\left(\boldsymbol{B}\right) = \lambda_1^2\lambda_2^2\lambda_3^2 = J^2. \end{aligned} \tag{2.10}$$

A decomposition of the deformation gradient into deviatoric and volumetric contributions can often be required when implementing material models for use in finite element (FE) codes [1] or when used for modelling almost incompressible materials such as elastomers [2]. This multiplicative split is then defined as

$$\boldsymbol{F} = \left(J^{\frac{1}{3}}\mathbf{1}\right)\boldsymbol{F}^{\mathrm{dev}}, \tag{2.11}$$

where $J^{\frac{1}{3}}\mathbf{1}$ is the volumetric deformation, expressed as a ratio of the original volume. The unit tensor of second order is denoted by $\mathbf{1}$. Consequently, the following deviatoric quantities

$$\begin{aligned} \boldsymbol{C}^{\mathrm{dev}} &= J^{-\frac{2}{3}}\boldsymbol{C}, \\ \boldsymbol{B}^{\mathrm{dev}} &= J^{-\frac{2}{3}}\boldsymbol{B}, \\ \lambda_{\alpha}^{\mathrm{dev}} &= J^{-\frac{1}{3}}\lambda_{\alpha} \end{aligned} \tag{2.12}$$

are defined. The invariants with regard to the isochoric parts of the right and left Cauchy-Green tensors are defined by inserting Equation (2.12) into Equation (2.10). It is to be noted, that a fully incompressible material ($J = 1$) implies $I_1^{\mathrm{dev}} = I_1$, $I_2^{\mathrm{dev}} = I_2$ and $I_3^{\mathrm{dev}} = I_3 = 1$.

Besides the Cauchy-Green deformation tensors $\boldsymbol{C}$ and $\boldsymbol{B}$, see Equation (2.6) and Equation (2.7), some strain tensors are defined used for measuring the stretch of a material. The engineering or nominal strain is defined as

$$\boldsymbol{e} = \boldsymbol{V} - \mathbf{1}. \tag{2.13}$$

In addition, the true or logarithmic strain is defined as

$$\boldsymbol{\varepsilon} = \ln(\boldsymbol{V}). \tag{2.14}$$

Notably, both strains are defined with regard to the current configuration and take the value of $\mathbf{0}$ if no deformation is applied to the material.

2.1.1.2 Constitutive modelling

For a hyperelastic material, it is assumed, that the Helmholtz strain energy function Ψ, defined per unit volume, exists. Under the preposition of isothermal and isotropic behaviour, the strain energy function $\Psi = \Psi(\boldsymbol{F})$ is only dependent on the current state of deformation expressed by the deformation gradient. Consequently, the energy function can also be

expressed by the previously introduced invariants, see Equation (2.10), such as

$$\Psi = \Psi(I_1, I_2, J) \tag{2.15}$$

or by the principal stretches λ_α, so that

$$\Psi = \Psi(\lambda_\alpha, J). \tag{2.16}$$

The Cauchy stress tensor $\boldsymbol{\sigma}$ is calculated from the strain energy function as

$$\boldsymbol{\sigma} = \boldsymbol{F}\frac{\partial \Psi}{\partial \boldsymbol{F}} - p\mathbf{1} \tag{2.17}$$

with p denoting the hydrostatic pressure. Alternatively, Equation (2.17) can be expressed by the partial derivative with regard to right Cauchy-Green tensor $\boldsymbol{C}$, see Equation (2.6), as

$$\boldsymbol{\sigma} = \frac{2}{J}\boldsymbol{F}\frac{\partial \Psi}{\partial \boldsymbol{C}} - p\mathbf{1}. \tag{2.18}$$

The definition of isotropic hyperelastic material models is often facilitated, when the strain energy function is expressed in terms of invariants of $\boldsymbol{C}$ as defined in Equation (2.10) instead of actual $\boldsymbol{C}$. The expression for calculating the Cauchy stress tensor is then given as

$$\boldsymbol{\sigma} = \frac{2}{J}\left(\frac{\partial \Psi}{\partial I_1} + I_1\frac{\partial \Psi}{\partial I_2}\right)\boldsymbol{B} - \frac{2}{J}\frac{\partial \Psi}{\partial I_2}\boldsymbol{B}^2 + \frac{\partial \Psi}{\partial J}\mathbf{1}. \tag{2.19}$$

A comprehensive derivation of Equation(2.19) is omitted for brevity but is outlined in [1, 3]. An equivalent representation of the strain energy density function expressed in terms of the principal stretches λ_α leads to the Cauchy stress tensor expressed by

$$\boldsymbol{\sigma} = \sum_{\alpha=1}^{3}\frac{\lambda_\alpha}{J}\frac{\partial \Psi}{\partial \lambda_\alpha}(\boldsymbol{n}_\alpha \otimes \boldsymbol{n}_\alpha) \tag{2.20}$$

or when using the isochoric stretches $\lambda_\alpha^{\mathrm{dev}}$

$$\boldsymbol{\sigma} = \sum_{\alpha=1}^{3} \frac{\lambda_\alpha^{\mathrm{dev}}}{J} \frac{\partial \Psi}{\partial \lambda_\alpha^{\mathrm{dev}}} (\boldsymbol{n}_\alpha \otimes \boldsymbol{n}_\alpha) + \frac{\partial \Psi}{\partial J} \mathbf{1}. \tag{2.21}$$

The strain energy function can in this case also be split into a deviatoric and a volumetric contribution by introducing the isochoric strain energy W and the volumetric component U, which in sum give the strain energy function

$$\Psi = W\left(\lambda_\alpha^{\mathrm{dev}}\right) + U(J). \tag{2.22}$$

Equation (2.22) clearly allows for a separate modelling of deviatoric and volumetric material behaviour. In summary, in finite elasticity, a strain energy function Ψ is used to compute the stress and stiffness of a hyperelastic material. These quantities are fully defined by a second-order stress tensor and a fourth-order elasticity tensor. These tensors might be expressed in reference or current configurations, but the strain energy function remains identical.

Invariant-based constitutive models One commonly chosen approach for modelling the hyperelastic behaviour of elastomers is found in expressing the strain energy density function in terms of the isochoric Cauchy-Green invariants I_1^{dev} and I_2^{dev}. A summary of commonly used invariant-based models is given in Table 2.1. This summary is by no means complete, but gives an overview over the most commonly used models, especially in Finite Element Method (FEM) applications. A more comprehensive review of existing invariant-based hyperelastic models is given by Steinmann et al. [4] or the review paper by Melly et al. [5].

The contributions of $W\left(I_1^{\mathrm{dev}}, I_2^{\mathrm{dev}}\right)$ and $U(J)$ to the strain energy density function Ψ in Table 2.1 are, where possible, expressed in terms of the elastic shear modulus μ and the bulk modulus κ. Notably, some models feature a dependence on both invariants I_1^{dev} and I_2^{dev}, where others only depend on the first invariant I_1^{dev}.

Table 2.1: Overview of common invariant-based hyperelastic models. The strain energy density function Ψ is split into a deviatoric contribution $W\left(I_1^{\mathrm{dev}}, I_2^{\mathrm{dev}}\right)$ and a volumetric contribution $U(J)$.

Model	$W\left(I_1^{\mathrm{dev}}, I_2^{\mathrm{dev}}\right)$	$U(J)$	Reference
Neo-Hooke	$\frac{\mu}{2}\left(I_1^{\mathrm{dev}}-3\right)$	$\frac{\kappa}{2}(J-1)^2$	[6]
Mooney-Rivlin	$C_{10}\left(I_1^{\mathrm{dev}}-3\right)+C_{01}\left(I_2^{\mathrm{dev}}-3\right)$	$\frac{\kappa}{2}(J-1)^2$	[7, 8]
Yeoh	$C_{10}\left(I_1^{\mathrm{dev}}-3\right)+C_{20}\left(I_1^{\mathrm{dev}}-3\right)^2+C_{30}\left(I_1^{\mathrm{dev}}-3\right)^3$	$\frac{\kappa}{2}(J-1)^2$	[9]
Polynomial	$\sum_{i,j=0}^{N} C_{ij}\left(I_1^{\mathrm{dev}}-3\right)^i\left(I_2^{\mathrm{dev}}-3\right)^j$	$\sum_{i=1}^{N}\frac{1}{D_1}(J-1)^{2i}$	[10]

The latter ones can be experimentally calibrated with only one load case such as uniaxial tension. The determined material parameters are then likely to represent the material behaviour well for similar loading conditions but might lead to unstable behaviour under different load cases or multiaxial loading. This can be omitted by resorting to models with an additional I_2^{dev} dependence. In this case, however, at least two different load cases have to be tested experimentally for the determination of material parameters.

Principal stretch-based constitutive models Alternatively, a hyperelastic material model can be formulated by an expression of Ψ in terms of the three deviatoric principal stretches $\lambda_\alpha^{\mathrm{dev}}$ in order to fulfil Equation (2.21) following an initial hypothesis by Valanis and Landel [11]. Representative of this class of models is the one proposed by Ogden [12, 13]. The Ogden model assumes a deviatoric contribution

$$W\left(\lambda_1^{\mathrm{dev}}, \lambda_2^{\mathrm{dev}}, \lambda_3^{\mathrm{dev}}\right) = \sum_{k=1}^{3} \frac{2\mu_k}{\alpha_k^2}\left(\lambda_1^{\mathrm{dev}\,\alpha_k} + \lambda_2^{\mathrm{dev}\,\alpha_k} + \lambda_3^{\mathrm{dev}\,\alpha_k} - 3\right) \tag{2.23}$$

to the strain energy density function Ψ. The volumetric contribution is modelled as

$$U(J) = \sum_{k=1}^{N} \frac{1}{D_k}(J-1)^{2k}. \tag{2.24}$$

Notably, the Ogden-model features a number of parameters, which need to be determined for an accurate prediction of the material behaviour. By specific choices of N, α_k and μ_k, a number of invariant-based models in Table 2.1 can be obtained.

Further constitutive models Alternative approaches for formulating hyperelastic models are found in network models, which aim to mimic the physical molecular phenomena of elastomer hyperelasticity. A simplified unit cell of the elastomer material serves to approximate the material behaviour. Models falling into this category include the Three-Chain model by Wang and Guth [14] or the Eight-Chain model by Arruda and Boyce [15]. Furthermore, data-driven approaches model the deformation behaviour on the experimentally determined strain energy alone by interpolation based on the first invariant, such as the Marlow model [16]. Sussman and Bathe [17] pursue a similar approach, but use interpolation based on principal logarithmic strains.

In summary, the current state of the art in constitutive modelling of soft materials, such as elastomers, deformed to large strains offers a large number of different constitutive models, many of which are available in commercial FEM programs such as Abaqus [18]. The necessary amount of experimental characterisation needed for determining an optimal set of parameters for a given material depends on the model at hand [4]. For the context of this work, it can be concluded, that the current state of the art offers a large variety of hyperelastic models, which can be calibrated to reproduce experimental test data, when the large-strain response of the given elastomer materials is to be investigated. Furthermore, the introduced constitutive models are of key importance for the description of further mechanical effects observed in elastomer materials, such as the Mullins effect, which is addressed in Section 2.1.4 and Chapter 6, respectively.

2.1.2 Viscoelasticity

While the theory of elasticity accounts for materials which have a capacity to store mechanical energy with no dissipation of the same, a Newtonian viscous fluid in a non-hydrostatic stress state exhibits the capability for dissipating energy, but none for storing it. Elastomer materials and polymers in general, however, are outside the scope of these two material classes as they possess the capacity to both store and dissipate mechanical energy. The theory of viscoelasticity consequently describes the combination of both theories in a single solid or fluid. [19]

2.1.2.1 Theory of linear viscoelasticity

Within the limit of infinitesimal deformation, viscoelastic behaviour can be described by linear differential equations with constant coefficients. Most materials show linear time-dependent behaviour even in finite deformation as long as the strain remains below a certain limit, the linear viscoelastic limit [20]. This assumption is adopted for the present elastomer materials and the introduced fundamentals thus restricted to the theory of linear viscoelasticity.

Time domain viscoelasticity For viscoelastic materials in the time domain, two processes can be used to describe the material's time-dependent mechanical behaviour: creep and relaxation. The creep compliance $J_C(t)$ is used to describe the material's strain response $\varepsilon(t)$ to an applied constant load step σ_0 and is defined as

$$J_C(t) = \frac{\varepsilon(t)}{\sigma_0} \tag{2.25}$$

for the one-dimensional case. When applying a constant strain step ε_0, the relaxation modulus

$$E_R(t) = \frac{\sigma(t)}{\varepsilon_0} \tag{2.26}$$

is used to describe the observed decrease in the stress $\sigma(t)$. While Equation (2.25) and Equation (2.26) can be used for the identification of $J_C(t)$, respectively $E_R(t)$ by subjecting the material to a specific step in stress or strain and measuring the other quantity, they lack the capability of predicting the response to an arbitrary load. Instead, the convolution integrals

$$\sigma(t) = \int_{-\infty}^{t} E_R(t-\tau)\frac{d\varepsilon(\tau)}{d\tau}d\tau \tag{2.27}$$

and

$$\varepsilon(t) = \int_{-\infty}^{t} J_C(t-\tau)\frac{d\sigma(\tau)}{d\tau}d\tau \tag{2.28}$$

are used to fully describe the constitutive relation for a linear viscoelastic material based on the Boltzmann superposition [20]. Above Equations (2.27) and (2.28) are formulated in only one dimension under tension and for arbitrary strain and stress measures, but can be adapted to for example shear loading by replacing the relaxation modulus $E_R(t)$ with the corresponding relaxation shear modulus $G_R(t)$. A three dimensional generalization of the constitutive equations

$$\boldsymbol{\sigma}(t) = \int_{-\infty}^{t} \mathbb{C}(t-\tau)\frac{d\boldsymbol{\varepsilon}(\tau)}{d\tau}d\tau \tag{2.29}$$

$$\boldsymbol{\varepsilon}(t) = \int_{-\infty}^{t} \mathbb{J}(t-\tau)\frac{d\boldsymbol{\sigma}(\tau)}{d\tau}d\tau \tag{2.30}$$

is obtained by introducing the fourth-order time-dependent creep compliance and relaxation stiffness tensors $\mathbb{J}(t)$ and $\mathbb{C}(t)$.

Frequency domain viscoelasticity An equivalent representation of linear viscoelasticity can be formulated regarding the circular excitation frequency ω of a steady-state harmonic loading. The concept is introduced in the following using a simplified one-dimensional case. A generalized harmonic strain [20] excitation with an amplitude of $\hat{\varepsilon}(\omega)$ and a circular

frequency ω superimposes a static deformation ε_0, which is independent of time

$$\begin{aligned}\varepsilon(t) = \varepsilon_{\text{stat}} + \varepsilon_{\text{dyn}}(t) &= \varepsilon_0 + \hat{\varepsilon}(\omega)\left[\cos(\omega t) + \mathrm{i}\sin(\omega t)\right] \\ &= \varepsilon_0 + \hat{\varepsilon}(\omega)\, e^{\mathrm{i}\omega t},\end{aligned} \tag{2.31}$$

as visualized in Figure 2.1a. The letter i denotes the imaginary unit. Accordingly, the material's stress response is also decomposed into a static σ_{stat} and a dynamic σ_{dyn} contribution

$$\sigma(t) = \sigma_{\text{stat}} + \sigma_{\text{dyn}}(t). \tag{2.32}$$

Considering the complex valued strain excitation in Equation (2.31) and introducing a complex modulus E^* yields the oscillating contribution of the stress response as

$$\sigma_{\text{dyn}}(t) = E^*(\omega)\,\varepsilon_{\text{dyn}}(t) = E^*(\omega)\,\hat{\varepsilon}(\omega)\left[\cos(\omega t) + \mathrm{i}\sin(\omega t)\right]. \tag{2.33}$$

The frequency-dependent complex modulus E^* can further be decomposed into its real and imaginary components

$$\begin{aligned}E' &= \Re(E^*) \\ E'' &= \Im(E^*)\end{aligned} \tag{2.34}$$

so that

$$E^*(\omega) = E'(\omega) + \mathrm{i}E''(\omega) \tag{2.35}$$

as illustrated in Figure 2.1b. The real part E' is commonly referred to as the storage modulus and describes the purely elastic energy storage of the viscoelastic material behaviour. Analogously, the imaginary part E'' encompasses the purely viscous dissipation. The ratio of loss and storage modulus

$$\tan(\delta) = \frac{E''}{E'} \tag{2.36}$$

is often referred to as loss factor as it yields the share of viscously dissipated energy under harmonic loading. It is therefore commonly used as a measure

for a material's intrinsic damping capabilities. For weakly damped systems, $\tan(\delta) \ll 1$, this quantity is approximately equal to the modal damping ratio, see Equation (5.23), often determined in some experiments [21]. The angle δ, as shown in Figure 2.1a, also represents the phase lag between excitation and the material's response. Consequently, the complex modulus $E^*(\omega)$ can alternatively be expressed by its polar components of magnitude $|E^*(\omega)|$ and angle δ as

$$E^*(\omega) = \left|E^*(\omega)\right| e^{\mathrm{i}\delta(\omega)}. \tag{2.37}$$

The magnitude is calculated as $|E^*(\omega)| = \sqrt{E'(\omega)^2 + E''(\omega)^2}$. An illustration is given in Figure 2.1b. Inserting Equation (2.37) into the dynamic part of the resulting stress in Equation (2.33) yields

$$\begin{aligned} \sigma_{\mathrm{dyn}}(t) &= \left|E^*(\omega)\right| \hat{\varepsilon}(\omega)\, e^{\mathrm{i}(\omega t + \delta(\omega))} \\ &= \left|E^*(\omega)\right| \hat{\varepsilon}(\omega) \left[\cos(\omega t + \delta(\omega)) + \mathrm{i}\sin(\omega t + \delta(\omega))\right]. \end{aligned} \tag{2.38}$$

From above equation, it becomes apparent that the material's stress response is also harmonic, yet it lags behind the strain excitation by the phase angle $\delta(\omega)$. The amplitude of the stress response to the generalized harmonic strain excitation becomes apparent as

$$\hat{\sigma}(\omega) = \left|E^*(\omega)\right| \hat{\varepsilon}(\omega). \tag{2.39}$$

The magnitude of the complex modulus is thus the ratio of the resulting stress amplitude $\hat{\sigma}$ and the excitation strain amplitude $\hat{\varepsilon}$. An exemplary graphical representation of the superposition of static and harmonic loading and the resulting phase lag is given in Figure 2.1a.

The amount of energy lost during a full cycle due to the viscous behaviour is given by

$$W = \int_0^{2\pi/\omega} \sigma_{\mathrm{dyn}}(t)\, \dot{\varepsilon}_{\mathrm{dyn}}(t)\, \mathrm{d}t = \hat{\varepsilon}^2 \omega \pi E''(\omega) \tag{2.40}$$

and is dependent only on the imaginary part of the complex modulus. This amount of energy dissipates due to internal friction inside the polymeric

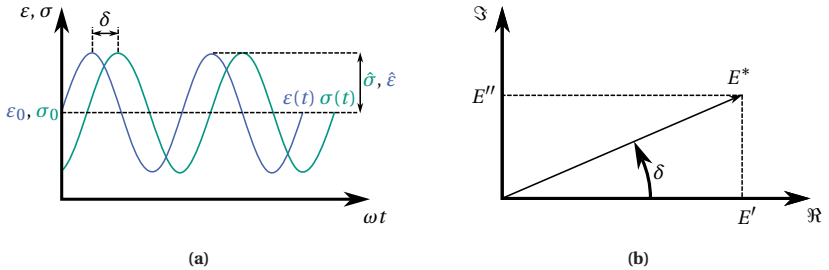

Figure 2.1: Visualization of frequency domain viscoelasticity. **(a)**: A viscoelastic material's stress response $\sigma(t)$ to a sinusoidal strain excitation $\varepsilon(t)$. The phase shift between excitation and response is given by the angle δ. **(b)**: Geometric representation of the complex modulus E^* in the complex plane

material. For a full cycle, no energy is stored in the material as it is fully unloaded. [22]

A generalization of preceding concept to an arbitrary three dimensional case is given by introducing the complex stiffness tensor $\mathbb{C}^*$ representing the, possibly anisotropic, viscoelastic behaviour. The constitutive relation then reads

$$\sigma_{\mathrm{dyn}}(t) = \mathbb{C}^*(\omega)\,\varepsilon_{\mathrm{dyn}}(t) = \left(\mathbb{C}'(\omega) + \mathrm{i}\mathbb{C}''(\omega)\right)\varepsilon_{\mathrm{dyn}}(t) \tag{2.41}$$

for a harmonic strain excitation $\varepsilon_{\mathrm{dyn}}$. A complex compliance tensor $\mathbb{J}^*$ for harmonic stress excitation could be defined accordingly.

2.1.2.2 Dynamic mechanical analysis

In order to experimentally determine the thermoviscoelastic behaviour of materials, a dynamic mechanical analysis (DMA) can be performed. The elastic and viscous properties and their dependence on temperature and time are investigated. For this purpose, a specimen is loaded with a static strain ε_0

and then harmonically excited around this base state so that the applied strain can for example be expressed as

$$\varepsilon(t) = \varepsilon_0 + \hat{\varepsilon} \sin(\omega t). \tag{2.42}$$

This corresponds to Equation (2.31), where only the real part is considered. Using a load cell, the real part of material's stress response

$$\sigma(t) = \sigma_0 + \hat{\sigma} \sin(\omega t + \delta) \tag{2.43}$$

is recorded, from which the magnitude of the complex modulus $|E^*(\omega)|$ is calculated based on amplitudes of strain and stress according to Equation (2.39). The phase angle δ can be calculated by various methods [23]. Consequently, the material's complex modulus $E^*(\omega)$ is determined as a function of the excitation frequency ω. Typically, frequency sweeps are conducted in order to determine E^* over a range of frequencies. In addition, the aforementioned frequency sweeps can be repeated at a number of temperatures yielding the complex modulus at the same frequencies for different discrete temperatures.

2.1.2.3 Time-temperature superposition

As the excitation frequencies in the experiment are strongly limited and might not cover the oscillatory loads in real-world applications exceeding these frequencies, the mechanical behaviour beyond those limits must often be determined by other means. This is achieved by the application of the time-temperature superposition (TTS) principle exploiting the correlation between temperature and time or frequency inherent to polymers. Accordingly, an increase in temperature has a similar effect as loading the material for a longer period of time or with a reduced frequency [24, 25]. Once the frequency-dependent curves of the complex modulus have been determined experimentally at several temperatures as outlined in Section 2.1.2.2, translation factors a_T are calculated, which horizontally shift an individual curve to a new

range of frequencies. For a given reference temperature T_{ref}, a so-called master curve can be created by horizontally shifting all other isotherms along the frequency axis. The complex modulus E^*, see Equation (2.35), measured at temperature T is hence shifted to temperature T_{ref} by

$$\begin{aligned} E'(\omega, T) &= E'(a_{\mathrm{T}}\omega, T_{\mathrm{ref}}) \\ E''(\omega, T) &= E''(a_{\mathrm{T}}\omega, T_{\mathrm{ref}}) \\ \tan(\delta(\omega, T)) &= \tan(\delta(a_{\mathrm{T}}\omega, T_{\mathrm{ref}})) \end{aligned} \tag{2.44}$$

with the constraints

$$\begin{aligned} a_{\mathrm{T}} &> 1 \quad \text{if } T < T_{\mathrm{ref}} \\ a_{\mathrm{T}} &= 1 \quad \text{if } T = T_{\mathrm{ref}} \\ a_{\mathrm{T}} &< 1 \quad \text{if } T > T_{\mathrm{ref}}. \end{aligned} \tag{2.45}$$

This principle of shifting is visualized in Figure 2.2 for two sweeps at different temperatures, which represent an arbitrary, typically the storage modulus, quantity Y. The higher temperature is taken as reference temperature T_{ref} and horizontal and vertical shifts are conducted in order to obtain a smooth curve at T_{ref}. The displayed vertical shift is addressed later in this section.

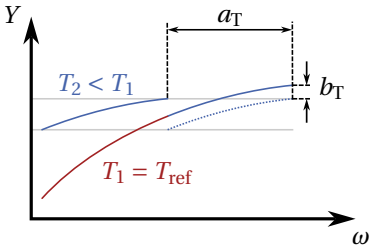

Figure 2.2: Schematic visualization of master curve generation. Two sweeps of an arbitrary viscoelastic quantity Y at different temperatures, T_1 and T_2, are shown. Temperature T_1 is taken as reference temperature and the curve of T_2 is shifted accordingly so that a smooth curve is obtained. The resulting curve is called master curve at temperature $T_{\mathrm{ref}} = T_1$. A horizontal (a_{T}) as well as a vertical (b_{T}) shift is shown.

It should be noted that the shift factors a_T do not only depend on the temperature of the initial frequency sweep, but also on the reference temperature T_{ref} at which the master curve is created. In practice, the temperature dependence of a_T is often modelled by using the well established Williams-Landel-Ferry (WLF) relation

$$\log a_T = \frac{-C_1 (T - T_{ref})}{C_2 + (T - T_{ref})} \tag{2.46}$$

by Williams et al. [26], which is usually applicable above the glass transition temperature T_G. Parameters C_1 and C_2 in Equation (2.46) are material specific and depend on the reference temperature T_{ref}. Below the glass transition temperature T_G, the Arrhenius law

$$\log a_T = -\frac{E_a}{2.303R}\left(\frac{1}{T} - \frac{1}{T_{ref}}\right) \tag{2.47}$$

is applied, where $R = 8.314\,\mathrm{J\,mol^{-1}\,K^{-1}}$ is the universal gas constant and E_a denotes the activation energy, which needs to be determined from experimental data [22].

Traditionally, this shift is conducted horizontally along the logarithmic frequency axis and is valid for thermo-rheologically simple materials. A thermo-rheologically simple material must fulfil the condition, that its mechanical behaviour at a reference temperature T_{ref} and at any other temperature T differ solely with regard to their relaxation times [19, 27]. Accordingly, the relaxation mechanisms present in the polymer are required to feature the same temperature dependence. From this condition, restrictions regarding the applicability of the TTS arise for inhomogeneous polymeric materials, such as blends, or generally in the vicinity of the glass transition area where entropy and energy induced relaxations occur [28]. A common procedure to identify whether TTS in terms of horizontal shifting is applicable to a material is the use of modified Cole-Cole plots [29], sometimes referred to as wicket plots [23, 30], or van Gurp-Palmen plots [28, 31]. A modified Cole-Cole plot features the logarithmic loss modulus E'' plotted over the logarithmic

storage modulus E' for each measurement point of the frequency sweeps at various temperatures. The measurement points should form a continuous curve without a noticeable temperature dependence as this would indicate an additional relaxation mechanism [30]. The curve should feature the shape of a wicket, hence the name wicket plot.

In case the Cole-Cole plot does indeed show some temperature dependence, additional vertical shifting of the frequency sweeps can become necessary in order for TTS to be applicable [32], which can also compensate for density changes of the material when a wide range of temperatures is investigated [23]. A vertical shift by a shift factor b_T then takes the form

$$\begin{aligned} E'(\omega, T) &= b_\mathrm{T} E'(\omega, T_\mathrm{ref}) \\ E''(\omega, T) &= b_\mathrm{T} E''(\omega, T_\mathrm{ref}) . \end{aligned} \tag{2.48}$$

Notably, the loss factor $\tan(\delta)$ remains unaffected by a vertical shift. An exemplary vertical shift is illustrated in Figure 2.2. Usually, sweeps are first shifted horizontally before being shifted vertically. A common procedure is determining the horizontal shift factors a_T by shifting the curves of the loss factor $\tan(\delta)$. The vertical shifts b_T are then determined based on the storage or loss modulus curves as the loss factor remains untouched by vertical shifting [22, 33].

In summary, Section 2.1.2 introduces the concept of viscoelasticity and the corresponding experimental characterisation procedures in the frequency-domain. These will be employed in Section 4.1.3 in order to determine the linear viscoelastic behaviour of the elastomer materials studied within this work with a focus on their damping capabilities.

2.1.3 The Payne effect

One effect commonly observed in elastomers related to its vibrational behaviour is the Payne effect. First reported by Fletcher and Gent [34] and

studied in more detail by its namesake [35, 36, 37], the Payne effect describes the amplitude dependence of a material's storage modulus under cyclic loading. As the amplitude of applied strain increases, a decrease in the storage modulus is observed. Phenomenologically, the Payne effect is characterised by a constant storage modulus up to a certain strain amplitude from which it decreases with larger amplitudes before converging to a minimum. This behaviour is attributed to stiffening filler-filler interactions within the material at very low strain amplitudes. With increasing amplitudes, the weak physical bonds between individual filler particles break and are reformed at lower amplitudes or fully unloading the material [38]. Consequently, the Payne effect is reversible even at room temperature and does usually not lead to any permanent alterations of the material [39]. Being a phenomenon occurring under cyclic loading at small strain amplitudes, the Payne effect is not to be confused with the large-strain phenomenon which is the Mullins effect introduced in Section 2.1.4.

2.1.4 The Mullins effect

2.1.4.1 Phenomenology

The phenomenon known as the Mullins effect [40] is a softening mechanism and characterises the distinctive material response exhibited by numerous elastomers subjected to cyclic loading. These materials demonstrate an altered hysteresis curve up to the previously applied maximum strain under cyclic deformation. An idealized illustration of this behaviour is shown in Figure 2.3 for a total of two load cycles with the second loading exceeding the first one. Notably, the loading curve of the second load cycles does not coincide with the first one up to Point II. Loading curves follow the material's virgin hyperelastic stress curve whenever the previous maximum stretch is exceeded. Unloading and subsequent reloading curves coincide up to the previous maximum stretch. While this effect has at first been observed in filled natural rubber only [41, 42], Harwood et al. [43, 44] soon

reproduce the effect in unfilled natural rubber as well. The results presented by Harwood and Payne [42] suggest, that the effect is rather a stress-softening than a strain-softening. The Mullins effect is reported for a number of other materials than natural rubber compounds such as ethylene propylene diene monomer (EPDM) [45, 46], styrene butadiene rubber (SBR) [45], hydrated nitrile butadiene rubber (HNBR) [45], thermoplastic elastomers [47] to only name a few. The amount of softening is furthermore shown to increase with the volume fraction of fillers, such as carbon black [45, 48, 49].

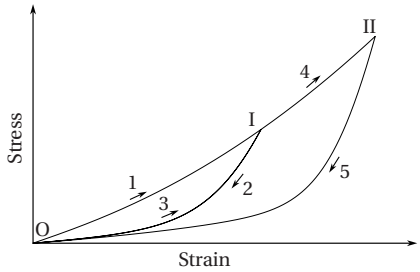

Figure 2.3: Illustration of the idealized Mullins effect. The material is loaded from its undeformed state O to point I and is then unloaded back to point O. In the next cycle, the material is loaded from O to II and unloaded to O. Notably, the first loading O to I is not equal to the second loading O to I. Arabic numbers indicate the loading and unloading path segments in chronological order.

Further works investigate the influence of crystallisation on the softening behaviour of various rubbers [50, 51]. Up to now, however, the Mullins softening has been demonstrated on pure unfilled elastomers only, which undergo crystallisation [52]. Consequently, the presence of either fillers or crystallisation is assumed a prerequisite for the occurrence of Mullins softening.

In addition to investigating the initiation of softening, the reversibility of the Mullins effect has also been examined. Mullins [40] has already observed a temperature dependence in recovery, with an acceleration of recovery achieved through an increase in temperature. Similar findings have been demonstrated in various studies involving different elastomers, indicating

complete recovery at an elevated temperature and accelerated recovery at higher temperatures [52, 53]. However, at room temperature, the recovery time significantly extends, and the elastomer typically exhibits an irreversible behaviour of strain softening [54, 52].

Another observation made in the context of Mullins softening is the residual extension remaining after a material sample is stretched and unloaded. This is commonly referred to as permanent set and is already reported in the early works on stress softening in filled natural rubbers [55, 56]. Mullins [56] notes that rubbers showing limited softening also exhibit less permanent set, linking the two phenomena. Other authors also discover that the amount of permanent set is proportional to the amount of fillers used in the material [57, 58, 59, 45]. A certain amount of the observed permanent set is shown to be reversible after annealing or long recovery periods [60]. Just as the softening, permanent set is observed under various load cases [61].

The reported Mullins softening is also known to induce an anisotropy into the otherwise isotropic material [62]. While softening is observed in subsequent load cycles in the same direction, the material behaves virgin in other directions [53, 63, 64]. This is not only reported under uniaxial tension, but also shear, planar tension as well as biaxial states of stress [61, 65].

2.1.4.2 Physical explanations

The underlying physical mechanism responsible for the Mullins effect is not yet agreed upon within the scientific community. Nevertheless, numerous explanations for its occurrence have been proposed, which for the most part are limited to filled rubbers. Ruptures of the chemical bonds between the vulcanized polymer network and agglomerations of filler particles or between filler particles are proposed as the leading cause for the softening after straining the material by Blanchard and Parkinson [66] and Bueche [67]. Breakage and subsequent reforming of bonds due to slippage of molecules along the elongated polymer chains is another theory, which also explains the

reversibility of the Mullins effect after prolonged periods of time. This theory is for example represented in the works of Aleksandrov and Lazurkin [68] and Houwink [69]. The disintegration of pure filler particle agglomerates is seen a a cause of Mullins softening by Kraus et al. [70]. Yet another theory proposed by Hanson et al. [63] suggests that the softening after initial loading results from the disentanglement of previously entangled polymer chain, which would also explain the anisotropy reported by other researchers. Consequently, the exact origins of the Mullins effect remain disputed. The variety of theories regarding its origins is thus reflected in the corresponding material models for its prediction outlined in the subsequent section.

2.1.4.3 Constitutive modelling

Since the Mullins effect is generally considered irreversible under normal conditions and limited time scales, predictive models treat this softening phenomenon as an occurrence of damage. Most models are consequently of a phenomenological nature and mimic a portion of the above experimental observations. Models based on macromolecular models taking into account physical considerations are also briefly introduced.

Phenomenological models Although phenomenological models fail to capture the micromechanical processes behind the Mullins effect, they are commonly used not only due to their simplicity, but also due to the ongoing disagreement in the scientific community regarding the underlying physical origins of said effect. One approach is the continuum damage approach with the definition of a scalar damage variable which is used to compute the effective stress on the damaged material. This approach is first introduced by Gurtin and Francis [71] and later picked up in the models by Simo [72], Miehe and Keck [73] and Chagnon et al. [74] to name only a few. Thermodynamic consistency can easily be achieved for such models by an appropriate definition of an evolution law for the damage variable [75]. For complex

evolution laws such as the one used by Kaliske et al. [76], however, parameter identification can be challenging [77].

A further approach in developing phenomenological models for predicting the Mullins effect is given by the initial theory of Mullins and Tobin [78] of a two-phase material, in which a soft and hard phase coexist. With increasing stretch, the hard phase is continuously transformed into the softer phase. Just like the models based on the continuum damage approach introduced in the previous paragraph, these models are not able to depict the observed residual strain after unloading [52]. Previous works are generalized by Beatty and Krishnaswamy [79]. A prominent model building on the two-phase concept is the model by Qi and Boyce [80].

The third class of phenomenological models builds on the concept of pseudo-elasticity. First introduced by the work of Ogden and Roxburgh [81], this concept describes the material's softening based on a hyperelastic undamaged strain energy function, which is scaled by a softening parameter. The form of the strain energy function is thus modified during the deformation history and represents an altered hyperelastic material behaviour [82]. The softening parameter is determined by a softening function, which depends on the previous maximum strain energy and is only active during unloading. Consequently, models of this type cannot respect the physical phenomenon of network changes during loading [74]. The model by Ogden and Roxburgh [81] assumes a softening function on the basis of the Gauss error function. For additional numerical stability, Mars [83] introduced a further parameter for better control of the unloading curve with regard to FEM implementations. Possible issues with thermodynamic consistency of pseudo-elastic models are addressed by Naumann and Ihlemann [75], although Ogden and Roxburgh [81] attest the concept conformity with the second law of thermodynamics. Diercks et al. [84], to the author's knowledge at the time of writing, publish the only model, which describes the Mullins effect in the frequency-domain. They use the Ogden-Roxburgh model [81] to model the softening within a viscoelastic Generalized Maxwell Model (GMM) and can thus predict the effect of preconditioning on the complex

modulus of an elastomer. An alternative exponential softening function is proposed by Elías-Zúñiga and Beatty [85]. One major advantage of pseudo-elastic models is the ease of fitting them to experimental data as shown in [77, 86]. An extension of the initial model proposed by Ogden and Roxburgh [81] is published by Dorfmann and Ogden [58] and is capable of additionally predicting permanent set via an added damage function. Successful applications of the model by Dorfmann and Ogden [58] are for example published in [87, 88]. Fazekas and Goda [89] complement said model by incorporating viscoelasticity as well as temperature dependence. Dorfmann and Pancheri [90] further generalize the model to incorporate the deformation-induced anisotropy. Similar models building on the concept of pseudo-elasticity have recently been published by Anssari-Benam et al. [91] and Wollner et al. [92].

The above summary on phenomenological constitutive models for predicting the Mullins effect is by no means complete due to the vast number and large variety of models developed in this context. A more comprehensive overview over existing models is given in the review paper by Diani et al. [52].

Micromechanical models Micromechanically inspired models have also been developed to model the softening behaviour of elastomer materials. One such model, introduced by Govindjee and Simo [93, 94], involves the decomposition of the rubber network into distinct components, namely a purely elastic polymer segment and a polymer-filler network. This framework, which incorporates the softening effect, adheres to the early assumption made by Büche [67]. Building upon this concept, Dargazany and Itskov [95, 96] extended the network decomposition to account for the deformation and rupture of filler aggregates. Another perspective is offered by the dynamic flocculation model proposed by Klüppel et al. [97]. This model considers the disintegration and subsequent reformation of filler clusters, and its applicability to finite element computations has been demonstrated by Freund et al. [98]. Numerous expansions of this model have been suggested, for example by works such as those by Lorenz and Klüppel [99] and Juhre et

al. [100]. The theory of link breakage outlined above serves as a foundational basis for the models introduced by Marckmann et al. [101], Chagnon et al. [102] and Diani et al. [60].

A more detailed review of micromechanical models is given in [52]. While the micromechanical models introduced above all model the softening of elastomers and diverse additional properties, they do not necessarily have an advantage over purely phenomenological models due to the fact, that the physics driving the Mullins effect is not yet agreed upon [75].

Section 2.1.4 introduces the Mullins effect as a loading-induced alteration of the hyperelastic behaviour of elastomer materials, which has been shown to also occur in EPDM compounds. Therefore, its occurrence in the elastomer materials studied in this work is expected, as two of those are also EPDM-based. No research on the Mullins effect in these particular materials, however, exists in literature, which demands a thorough investigation of those with regards to the Mullins effect. Furthermore, the current state of the art also lacks any evidence of the Mullins effect in ethylene acrylic elastomer (AEM)-based elastomers, which are also employed within this work. The occurrence of the Mullins effect within laminated structures has so far not been documented either. An accurate analysis of hybrid laminates containing such elastomer materials therefore requires an appropriate constitutive modelling, taking into account Mullins softening and related effects, if their presence can be experimentally proven.

2.2 Modelling of laminated structures

Composite materials such as FRPs are often made in the form of thin layers, called *laminae*. By stacking and bonding multiple *laminae*, a laminate is created [103]. Advances in the accurate and efficient modelling of laminated structures have led to a vast amount of techniques for predicting the structural response of composite and sandwich laminates in the form of beam, plate

and shell theories [103]. A full review of all theories developed for the modelling of laminated and sandwich structures is beyond the scope of this work, but comprehensive reviews are given by Carrera [104, 105], Hu et al. [106] and Caliri et al. [107]. Generally, modelling approaches can be classified into equivalent single layer (ESL), layerwise (LW) and zig-zag (ZZ) formulations [104]. A graphic representation of the three approaches is given in Figure 2.4 for linear approaches. Higher-order theories are feasible and have been used in all three categories [108]. An ESL approach assumes one homogenized distribution of the modelled field quantity over the whole thickness of the laminate with the approximating functions featuring C^1-continuity. Commonly used first-order theories, such as the Classical Lamination Theory (CLT) or the First-Order Shear Deformation Theory (FSDT), also called Reissner-Mindlin theory [109, 110], fall into this category. Notable theories of a higher order and thus increased accuracy are presented by Reddy [111], Pai and Palazotto [112] and Matsunaga [113] to only name a few. Since the CLD mechanism, see Section 2.3.2, requires layers that differ significantly in stiffness and feature a substantial thickness, their mechanical behaviour can rather be compared to sandwich structures than monolithic composite laminates. The significantly different transverse shear stresses occurring in such laminates lead to pronounced kinks of the displacement components at layer interfaces, which cannot be reproduced by ESL approaches [114]. This issue is visualized in Figure 2.4 for an arbitrary field quantity. Therefore, ESL approaches are not deemed suitable for an accurate strain and stress analysis of such sandwich-type laminates [115, 116]. In particular, the error in the response predicted by ESL models increases with laminate thickness and the mismatch of the adjacent materials' mechanical properties [117]. Consequently, ESL theories are not focused upon further in this review of related research.

One possible way of depicting these zig-zag effects is the use of so-called ZZ approaches based on Murakami's zig-zag function (MZZF) [118]. Building on the Reissner's Mixed Variational Theorem (RMVT) [119], see Section 5.1.2 for details, MZZFs prescribe a layerwise linear distribution of the displacement

components with alternating signs at each interface [120] as shown in Figure 2.4. Its amplitude is dependent on the layer thickness. This approach leads to only a minor increase in degrees of freedom (DOFs) compared to ESL theories, but the typical zig-zag effects can be reproduced. However, the relation between transverse shear strains of adjacent layers is prescribed *a priori*. Resulting from this, deformations of unsymmetrical laminates with unequal layer thicknesses cannot be depicted correctly [115]. As this permits the use of ZZ approaches for the modelling of the laminates considered herein, these theories lie beyond the scope of this work. A comprehensive review, however, is given by Carrera [121].

In a fully LW approach, the modelled field quantities are described by a set of layerwise-continuous functions, where continuity in the interfaces is usually enforced by separate continuity conditions. Furthermore, the functions used to model the displacement components over the thickness have to exhibit C^0-continuity only. This allows for the depiction of aforementioned zig-zag effects, see Figure 2.4, without the restrictions accompanying ZZ theories. In addition, the derivatives of the displacement components may become discontinuous and thus allowing in principal for continuous transverse stresses in layer interfaces within models based on the RMVT. The cost of LW theories, however, is a number of DOFs dependent on the number of layers in the laminate, which can increase computational cost significantly [103]. Notable LW theories are published by Kao and Ross [122], Reddy [123, 103], Valisetty and Rehfield [124], Cho et al. [125], and Ferreira [126].

Within the last two decades, variable kinematics models in the form of unified formulations have seen a steadily increasing interest. A unified formulation describes the plate or shell kinematics in a way, that is independent of the specific plate or shell at hand. In particular, unified formulations are not restricted to ESL, ZZ or LW approaches of a fixed order such as the theories introduced above. Foremost, the Carrera Unified Formulation (CUF) [105] allows to implement an infinite number of hierarchical, variable kinematics models within a single program by using a limited number of model-invariant 3×3 fundamental nuclei either based on the Principle of Virtual

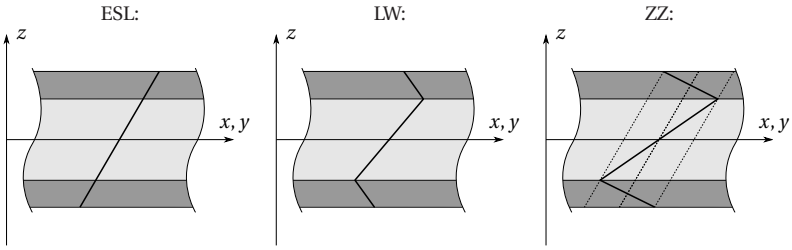

Figure 2.4: Illustration of different linear through-thickness approaches in plates and shells. Figure shows an Equivalent single layer (ESL), Layerwise (LW) and Zig-zag (ZZ) approach for an arbitrary field quantity in thickness-direction for a three-layered laminate. Adapted from Kärger [127].

Displacements (PVD) or RMVT. The axiomatically modelled field quantities are expanded in thickness direction using polynomials of order N, which is a free parameter of the analysis and can be chosen via a convergence analysis [128]. To be noted, all field quantities then feature the same order. The CUF can be used to formulate theories using ESL, LW and ZZ approaches [129]. With an appropriate choice of expansion order, common theories such as the CLT and FSDT can be reproduced using the CUF notation [117]. Numerous applications and refinements of the CUF have been published in recent years, either featuring analytical closed-form solutions [130] or FEM implementations [131]. Applications also include problems, which are thermoelastic [132] or piezo-electric [133] to only name a few. Regardless, however, of the solution procedure or the modelled field, within the CUF framework, all quantities are modelled using the same order of expansion, which naturally limits the number of possible theories. This limitation is lifted by an evolution of the CUF published by Demasi [134, 135], referred to as the Generalized Unified Formulation (GUF). Within a general framework [136], an infinite number of LW theories [137], higher-order ESL [138] and ZZ theories [139] are deducted based on the RMVT. Notably, the GUF is not restricted to the RMVT, but can also be developed based on the PVD as shown in [134, 135]. The previously mentioned model-invariant 3×3 fundamental nuclei of the CUF are replaced by so called 1×1 kernels in the GUF. Displacements and, in case of an RMVT based approach, out-of-plane stresses are axiomatically

modelled using polynomials of arbitrary order, thus lifting the limitations imposed by the CUF. A comparison of different theories is given in [140]. A further refinement of the GUF is proposed by D'Ottavio [141, 142], where multiple plies can be treated as an independent sublaminate in an otherwise LW description, allowing for different models to be used within the same laminate. As concluded by D'Ottavio [141], the proposed sublaminate GUF allows for a significant reduction of DOFs without loss of accuracy, thus increasing the computational efficiency of unified formulations.

In summary, a vast number of theories exist for the modelling of laminated structures. Unified formulations, especially the GUF, are of particular interest within the context of this work, as their variable-kinematics nature does not restrict them to specific laminate layups or choices of material. In particular, the possibility of axiomatically modelling the out-of-plane stress components, if such an approach is based on the RMVT, promises a more accurate analysis of highly heterogeneous laminates with regard to individual layer stiffness. Such laminates are considered within this work, where highly compliant plies of elastomer materials are adjacent to stiff structural materials such as aluminium or carbon fibre-reinforced polymer (CFRP).

2.3 Hybrid laminates

2.3.1 General definitions

A composite material is defined as a macroscopically quasi-homogeneous material, which consists of two or more components [143]. Such combinations of two or more materials are assembled in such a way as to have attributes not offered by either one alone [144]. A hybrid material, however, in this work is defined as a combination of two or more materials, which features a heterogeneous composition at the macro-scale. The aim is again to achieve a property profile, which monolithic materials cannot provide on their own. Consequently, the design space offered by conventional engineering materials can

thus be expanded to previously unattainable regions. A hybrid laminate is consequently defined as a laminate containing layers of two or more macroscopically different materials which might include composite layers.

2.3.2 Constrained-layer damping

The above introduced dissipative capabilities of polymer materials, elastomers in particular, can also be exploited in multi-material systems, such as hybrid laminates. If a viscoelastic material is present in such a laminate, special damping mechanisms can be invoked. A compliant and viscoelastic material can be applied on top of conventional structural materials such as metals or FRPs so that when the structure deforms, this damping material is deformed mainly in tension and compression [145, 146], allowing for the dissipation of part of the deformation energy in the viscoelastic damping material proportional to its loss modulus. Since the damping material is allowed to deform freely on the outside of the laminate, this damping mechanism is called free-layer damping (FLD) and was first proposed in 1952 by Oberst [147]. A further, more efficient with regard to weight [148], laminate damping mechanism and subject of this work is the so-called constrained-layer damping, where the highly compliant viscoelastic damping layer is constrained between two much stiffer constraining layers. Under bending deformation, which is the primary mode of deformation in most vibrations, the highly compliant constrained damping layer undergoes high transverse shear deformations and can thus dissipate a substantial amount of the vibration energy. A schematic illustration of this damping mechanism for an arbitrary bending deformation is given in Figure 2.5. A first mention of CLD in scientific literature is given by the work of Kerwin [149] in 1959 subsequent to the successful applications in aerospace engineering.

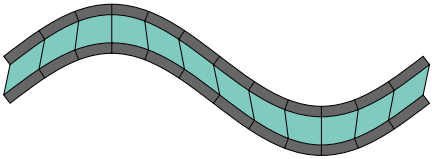

Figure 2.5: Schematic visualization of CLD showing the high transverse shear deformation of the constrained damping layer enabling dissipation of vibration energy through the viscoelastic material.

2.3.2.1 Predictive models for CLD[1]

The previously cited work by Kerwin [149] proposes a simple model for the prediction of damping factors of three-layered simply supported laminate beams. Kerwin [149] identifies the wavelength of bending waves, the layer thicknesses and the layers' stiffnesses as the influencing factors on the amount of damping. A generalization of the proposed model to incorporate an arbitrary number of damping layers is given by the Ross-Kerwin-Ungar (RKU) model [151] and modifications by Nashif et al. [152]. The successful application of the RKU-model to different boundary conditions is, among others, shown by Rao [153]. DiTaranto [154] and Mead and Markus [155] analytically derive governing equations for CLD beams for a variety of boundary conditions and state, that the vibration and damping behaviour of such structures is mostly independent of the boundary conditions. Instead, the amount of damping can be correlated to the wavelength of the CLD system. Further analytical models for the prediction of damping in CLD laminates exist and a comprehensive review of the earlier works is given by Kosmatka and Liguore [156]. Many of the earlier models, such as [155], however, yield significant errors for very thin damping layers. These limitation are overcome by newer analytical models such as the one presented by Huang et al. [157]. Further analytical models based on plate theories have also

[1] Section 2.3.2.1 is reproduced from Jackstadt et al. [150] with minor linguistic changes and additions.

been employed to analyse the damping capabilities of viscoelastic laminates. Saravanos and Pereira [158] determine the frequency response and modal damping parameters of simply supported composite plates with interlaminar damping layers using a discrete-layer laminate theory. An optimization procedure to increase the damping loss factor of plates under general edge conditions is presented by Li and Narita [159]. Alaimo et al. [160] determine the free vibration and forced vibration response of plates with the help of the fractional derivatives approach for the representation of the viscoelastic layers in frequency domain. The work of Valvano et al. [161] focuses on the sound transmission of shells including viscoelastic damping layers. Different types of loading are considered. Wang et al. [162] use an analytical model to predict the natural frequencies and modal loss factors of co-cured composite plates incorporating damping membranes using a first-order zig-zag theory. Li et al. [163] study the non linear vibration behaviour of cylindrical shells with partial CLD treatment with the help of an analytical model and find the achievable damping ratios to be dependent on the excitation amplitudes. Li et al. [164] also study the adaptive vibrational behaviour of plates with magnetorheological elastomer damping layers. The sublaminate-based GUF [141] is employed by D'Ottavio et al. [165] to identify frequency response, modal loss factors and damped natural frequencies of a variety of laminates incorporating viscoelastic damping layers. Many authors also employ numerical methods such as the FEM for the prediction of damping in plates with constrained viscoelastic layers. Early publications include Johnson and Kienholz [166] and Rikards et al. [167]. More recent works applying layerwise finite elements for predicting the dynamic response of CLD laminates include, but are not limited to, Moreira et al. [168], Plagianakos and Saravanos [169], Bilasse et al. [170], Akoussan et al. [171] and Ren et al. [172]. Zarraga et al. [173] develop a homogenized laminate formulation for the prediction of the dynamic response of FLD and CLD laminates. Ferreira et al. [174] and Liu et al. [175] employ a CUF-based finite element for the analysis of a viscoelastic sandwich plate in frequency domain. The CUF has also been used to calculate the dynamic response of CLD laminates by Filippi et al. [108] and Ribeiro et al. [176]. The review paper by Zhou et al. [177] summarizes

further models for predicting the vibrational response of laminates containing viscoelastic damping layers.

Notably, a number of predictive models and theories exist and have been applied to a variety of different hybrid laminates. A great share of those focus solely on modal parameters following a homogenized view of the laminates. While these models have been shown to yield accurate results, they do not allow for a closer investigation of the underlying deformation mechanisms within the laminate. Approaches based on a laminate theory, solved analytically or numerically, on the other hand, also offer the possibility of this close-up investigations of the laminate. As the focus of this work lies in the analysis of multiple different laminates and materials, such a deeper insight into the deformation behaviour, instead of focussing on modal parameters alone, is essential and will be addressed in Chapter 5.

2.3.2.2 Material and laminate influences on CLD

In general, CLD of a structure can be achieved in two ways. Traditionally, a vibrating structure is damped by the addition of CLD tapes, which are adhered to the structure. This method allows for the application of commercially available materials without the necessity of adapting the underlying structure in the design process. Another method is the design of intrinsic CLD laminates, in which the damping layers are an integral part of the laminate. This complicates the manufacturing and design process, but offers high customization and application-specific CLD treatments. Consequently, the damping of structures by CLD is complex and dependent on a large number of parameters. In particular, the choices of materials and their arrangement in laminated structures offer tremendous design freedom and have thus been investigated regarding their effectiveness in achieving high damping in numerous scientific contributions.

General laminate parameters, which influence CLD, are for example investigated by Saravanos and Pereira [158], who study different aspect ratios and

damping layer thicknesses within a CFRP plate embedding a damping film. By using finite elements, Zhang and Chen [178] determine optimal placements of damping layers in a composite laminate containing two damping layers. Sher and Moreira [179] conduct a parametric study based on finite element simulations on isotropic dimensionless CLD beams. They find, that a mode-dependent optimal damping layer thickness exists. Further findings include a dependence of optimal thickness ratios on the boundary conditions of the beam. Such thickness ratios for optimally damped beams are also determined by Teng and Hu [180]. A similar study for plates is published by Li and Narita [159]. In a sensitivity analysis, Akoussan et al. [181] also investigate the influence of damping layer thickness on the CLD in damped composite structures including different boundary conditions. They note, that an increase in modal damping does not necessarily come with a loss in static bending stiffness and stress the importance of a thorough analysis and optimization of possible CLD designs. The influence of layer thickness not only of the damping layers but also of the constraining composite layers is investigated by Wang et al. [162]. A further study based on finite elements is conducted by Wang et al. [182], who additionally recommend symmetric CLD structures for an increase in modal damping without significant loss in stiffness or decreasing natural frequencies.

A number of scientific publications also deal with the influence of material properties on the CLD mechanism. The previously introduced work by Saravanos and Pereira [158] for example investigate different fiber volume ratios of the constraining CFRP layers in a CLD laminate. They discover increased modal damping as well as static bending stiffness for higher fibre volume ratios and thus stiffer constraining layers. Öborn et al. [183] experimentally investigate different thermoplastic elastomer compounds modified with resin in isotropic CLD laminates featuring constraining layers made of steel. Further elastomeric damping materials are analysed by Hujare and Sahasrabudhe [184]. Several publications analyse how the degree of anisotropy of constraining layers influences modal damping, namely the fiber orientation found in constraining layers made up of FRPs [159, 178]. Wang

et al. [162] using the FEM generically investigate how the shear modulus and complex modulus of the constrained damping layers influence modal damping and are able to show, that an optimal stiffness exists for achieving maximum modal damping. Mateu Pastor et al. [185] take a different approach in preserving the high static bending stiffness of CFRP plates while incorporating viscoelastic damping layers. The constrained damping layer features a pattern of holes through which the resin can flow. They present an extensive study on the optimum location and size of the holes for maximum damping and stiffness.

The CLD mechanism in conditions such as elevated temperatures is for example investigated by Teng and Hu [180]. They illustrate how temperature influences the damping but also static stiffness of CLD laminates. Further work on the temperature dependence of CLD is conducted by Gröhlich et al. [186], who observe mode switches and a significant change in modal damping resulting from elevated temperatures. Depending on the vibration mode of the beam, different optimal damping layer thicknesses and widths are determined to compensate for changes in temperature. Li et al. [187] investigate the influence of geometric and material non-linearities on the CLD in damped FRPs and FMLs. They conclude, that there is a coupling phenomenon between the two types of non-linearities for high excitation amplitudes.

Taking into account the numerous influencing factors of CLD designs, a number of authors have published corresponding optimization strategies. Constrained optimization is for example conducted by Araújo et al. [188]. Madeira et al. [189] show a multiobjective optimization of a CLD laminate regarding damping, mass and cost. Noise reduction of a vibrating multilayered plate is achieved by CLD in an optimized design by Valvano et al. [190] using swarm optimization. Single-objective optimization for maximum damping is also shown by Wang et al. [182]. An optimization procedure for CLD taking into account different ambient temperatures is developed by Gröhlich et al. [191].

2.3.2.3 Applications and further developments of CLD

Some industrial applications of CLD are summarized by Rao [192], in particular in the automotive and commercial aeroplane sector. Automotive applications include passively damped door panels, roofs segments, floor panels as well as various covers related to the power train by means of superficially applied damping tapes. In aerospace applications, so-called stand-off layers provide a greater separation between the neutral axis of the base structure and the CLD treatment. The spacer thus acts as a kinematic amplifier to increase the shear deformation in the constrained layer. This allows for significant damping of aeroplane fuselages. Furthermore, more conventional damping tapes are also employed on planar components subjected to vibrations such as stringers and frames. Further applications within the automotive sector in terms of passively damped car doors are illustrated by Fasana et al. [193]. Ghiringhelli et al. [194] propose a CLD laminate for use in aircraft structures. Variations of CLD have also been proposed in literature. Partial CLD treatment involves constrained and constraining layers which do not encompass the whole component's surface, but are restricted to particular areas, which offer maximum damping such as vibration nodes. An optimization procedure is introduced by Zheng et al. [195], who determine optimal placement and coverage of partial CLD patches on vibrating beams. Similar results for sandwich plates are presented by Khalfi and Ross [196]. A further variation of conventional CLD, where the amount of shear deformation of the constrained layer is increased by actively deforming one constraining layer, is commonly referred to as active CLD. The constraining layer is usually deformed by a piezoelectric patch responding to a change in the applied electric current. A comprehensive review of such developments and possible applications is given by Stanway et al. [197]. Usually, the amount of damping achieved this way exceeds that given by conventional passive CLD [198]. An exemplary application featuring a car door is presented by Liu et al. [199]. As presented in the previous section, a number of publications have determined the strong influence of constrained layer thickness on the CLD mechanism. Compressible CLD exploits this

correlation by actively changing the thickness of the constrained layer in order to tune the damping behaviour. Ehrig et al. [200, 201] propose such a structure featuring a constrained layer made of compressible foam, which is compressed by an applied pressure. The actuation pressure is for example provided by vacuum, compressed air or hydraulic fluids. They achieve significant changes in the structures' mobility and sound transmission, thus proving the viability of this concept.

2.3.3 Fibre metal elastomer laminates

The combination of sheets of metal and sheets of FRP in one hybrid laminate is commonly referred to as FMLs [202]. The mechanical behaviour of FMLs, such as glass fibre-reinforced aluminium, has over the last decades attracted great interest from both, academia and industry, for use in lightweight load-bearing structures [203, 204]. For example, their superior fatigue and impact resistance [205, 206] allowed for a wide range of structural applications, especially in the aerospace sector [207]. However, the choice of materials used as constituents in FMLs can be limited. For example, a substantial mismatch in thermal expansion coefficients of aluminium and CFRP can lead to residual interface stresses, which can favour delaminations [208], especially under cyclic loading [209]. Furthermore, galvanic corrosion between carbon fibres and aluminium can also prevent the usage of those in FMLs [203]. The extent of such problems can be reduced by surface treatment of the constituents [210, 211] or by replacing the aluminium by other materials such as bulk metallic glass [212]. These options, however, increase the complexity of the manufacturing process and can thus again prevent the usage of such material combinations in FMLs [213]. The use of interlayers made of an elastomer material between polymer and metal layers can mitigate these problems altogether [213]. These types of hybrid laminates, namely those containing plies of metal, elastomer and FRP, are hence referred to as fibre metal elastomer laminates (FMELs) hereafter. The elastomer adhesively bonds, often with the help of additives, to the FRP and metal plies, thus replacing any other adhesives.

Academic research on the mechanical behaviour of FMELs begins with Sarlin et al. [214], who investigate hybrid laminates containing steel, two different EPDM based elastomers and sheets of glass fibre-reinforced polymer (GFRP). The authors give the first report on the vibration behaviour of FMELs. DMA experiments and vibration testing on a free-hanging plate are used to determine the loss factors of the constituents and various hybrid laminates. The authors highlight the strong frequency dependence of the loss factor of the hybrid structures and attribute it to the strong frequency dependence of the viscoelastic GFRP sheets. Furthermore, an increased damping is shown for laminates containing thicker elastomer plies. The use of a rule of mixture to determine loss factors of these FMELs is encouraged. Furthermore, Sarlin et al. [215, 216] investigate the high-velocity impact response of hybrid steel elastomer GFRP laminates and find a strong decrease in damage for these laminates compared to conventional FMLs. Although the total amount of energy absorbed does not differ, the elastomer layers absorb most of it, thus preventing damage of the other constituents. The results in [217] highlight the good adhesion properties of the elastomers used. The interface strengths within the hybrid laminates exceed those of the constituents, even without any pre-cleaning or other surface treatments is conducted prior to manufacturing. Further work includes an investigation of the ageing resistance of hybrid steel elastomer GFRP laminates by Sarlin et al. [218]. Temperature and moisture are found to have no effect on the interface strength in these laminates. FMELs containing layers of GFRP, aluminium and a natural rubber compound are investigated experimentally as well as numerically by Taherzadeh-Fard et al. [219] regarding their response to high-velocity impact. They find, that positioning the elastomer layer close to the impacted face increases the impact resistance of the laminate. A different material system, namely FMELs containing aluminium, CFRP and an EPDM based elastomer, is investigated by Stoll et al. [220] regarding the presence of galvanic corrosion after exposure to a salty environment. They find, that no decrease of mechanical properties for laminates occurs, where aluminium and CFRP are isolated by an elastomer layer. Laminates without elastomer layers, however, show galvanic corrosion in the interfaces and a strong loss

of stiffness and strength. The same type of hybrid laminates, also referred to as hybrid CFRP elastomer metal laminates (HyCEMLs), is investigated by Sessner et al. [221] regarding the damping properties under forced vibration. The authors investigate different laminate layups and elastomer materials. They show an increased damping, when a softer elastomer material is used instead of a stiffer one. These findings are confirmed by Sessner et al. [222] in DMA experiments and subsequent TTS. Furthermore, they propose a first numerical model for the simulation of these FMELs under free vibration in the time domain. Further numerical studies in the frequency domain are published by Liebig et al. [223]. In their work, the authors highlight the strong viscoelastic effects in FMELs as well as the influence of changes in the laminate layup. Stoll et al. [224] propose a new process to achieve different elastomer layer thicknesses from the same base EPDM sheets by using a solvent to obtain very thin pre-cured elastomer sheets. The authors show, that this additional process step does not decrease flexural and interface properties of the laminates, but offers the possibility of manufacturing FMELs with arbitrary lower thicknesses than those of the supplied base material. Further work on process development for manufacturing FMELs is conducted by Roth et al. [225], who propose a new process route for highly formed hybrid FMELs. Sessner and Weidenmann [226] use digital image correlation (DIC) to experimentally investigate the temperature dependence of the bending deformation behaviour of FMELs. In particular, the transverse shear strain within the elastomer layers responsible for the effectiveness of CLD is analysed. In Sessner et al. [227], the authors investigate multiple FMELs in a bending DMA setup and are able to reproduce the results numerically with FEM simulations taking into account the frequency-dependent material properties of the elastomers and the CFRP. Furthermore, they highlight the difficulties of applying the TTS to predict the viscoelastic behaviour over a wider frequency range. However, a simple rule of mixture is shown to provide acceptable results in predicting laminate loss factors based on the elastomer content, but neglects the frequency dependence of material properties. Sessner et al. [228], for the first time, experimentally investigate the modal damping behaviour of a curved FMEL structure. It is concluded,

that the geometry has a negligible influence on the general trends observed in multiple laminate configurations. Consequently, the conclusions obtained in earlier publications by the authors for plate geometries, can be transferred to 3D structures. Further experimental characterisation studies are published by Sessner et al. [229], where the authors compare different test methods to determine the damping properties of FMELs over a wider frequency and temperature range. A comprehensive summary on the experimental manufacturing and characterisation of FMELs is also given in the dissertation of Sessner [230]. This work also outlines the limitations of the RKU model when predicting modal damping of FMELs containing very thick or very thin constrained layers. A similar FMEL is investigated by Povolo et al. [231, 232], who analyse the failure behaviour and residual stresses of optimized hybrid CFRP aluminium tubes with an elastomer interlayer separating the two materials.

2.4 Hybrid laminates under impact loading[1]

Numerous publications deal with the impact behaviour of conventional FMLs, in which experimental, analytical and numerical methods are applied. Since the mechanical response of such laminates under low-velocity impact loading is well understood, a thorough review of the relating literature is omitted for brevity. Instead, the reader is referred to comprehensive review papers by Sinmazçelik et al. [205], Sadighi et al. [206] and He et al. [234] regarding this subject. The state of the art in impact behaviour of FMEL, however, is summarized in greater detail, beginning with Sarlin et al. [215, 216], who describe the effect of impact energy and rubber thickness on the high velocity impact properties of hybrid laminates containing steel, elastomer and glass fibre reinforced epoxy. The authors show that the addition of elastomer significantly reduces the interfacial and internal damage in the structure.

[1] Section 2.4 is reproduced from Jackstadt et al. [233] with minor linguistic changes and additions.

The total amount of energy absorbed, however, does not change. The area of damage is found to be linearly dependent on the impact energy. The main damage mechanisms are identified to be delamination in interfaces with rubber, as well as fibre matrix debonding. Düring et al. [235] investigate a similar material system consisting of CFRP and GFRP as well as steel plies and an EPDM based elastomer. The elastomer, however, is not situated in the interface between the FRP and steel but between FRP plies. The authors conduct low-velocity impact tests in order to determine the influence of different steel ply thicknesses and the addition of a rubber ply on internal and external damage, the absorbed energy, force evolution, and deformation. They conclude that the addition of a rubber ply increases the impact force threshold, below which the structure's response to impact is dominated by global elastic deformation and decreased damage. In another publication, Düring et al. [236] complement their previous studies by investigating the impact response and damage resistance of additional laminates containing two elastomer plies instead of one. They found that the additional ply leads to a significantly smaller delamination area, as well as minimizing the internal damage resulting from low-velocity impact loading. Li et al. [237] numerically investigate the low-velocity impact behaviour of different FMELs identical to those considered in the present study. They determine how the introduction of an elastomeric interlayer influences the damage evolution during impact events compared to conventional FMLs without elastomer plies. Similar conclusions to [236] are reached, namely a significant reduction of damaged areas after the introduction of elastomeric interlayers. FMELs containing GFRP, aluminium and natural rubber are investigated regarding low-velocity impact by Zarezadeh-Mehrizi et al. [238], who give insight into the optimal position of rubber plies within the laminate for minimal damage. Mahesh [239], similar to [237], finds that the introduction of elastomer plies in thermoplastic FMELs alter the load distribution during low-velocity impact events, thus causing a wider participation of material in the load bearing process.

Investigations on the vibrational response of damaged laminates, for example due to impact, have been explored in various studies. Notably, research is mostly conducted on delaminations within FRP structures to understand their impact on vibration characteristics. Early modelling efforts are presented by Ramkumar et al. [240], Wang et al. [241], and Mujumdar and Suryanarayan [242]. Grady and Meyn [243] experimentally and numerically investigate the vibration behaviour of impacted CFRP specimens. In their corresponding FEM model, they only consider delaminations and find that those lower the natural frequencies of the specimen, but report a significant increase in modal damping ratios. Shen and Grady [244] improve the alignment of analytical models with experimental results by analysing the free vibration of delaminated beams using a sublaminate model based on Timoshenko beams. This approach addresses the neglect of shear deformations in earlier models and accommodates both open and constrained delaminations, depending on whether the crack is allowed to open freely or is kinematically coupled with the adjacent sublaminate. Subsequent publications on the free vibration of delaminated beams expand on the concept of open and constrained delaminations. Examples include works by Della et al. [245], Ramtekkar et al. [246], Zhang et al. [247], Liu et al. [248], and Li et al. [249]. Luo and Hanagud [250] introduce considerations of non-linear effects in delaminated beams, while Jafari-Talookolaei et al. [251] address the behaviour of curved beams with delaminations. Additional research on the free vibration of delaminated composite beams, summarized comprehensively by Della and Shu [252], further contributes to the understanding of this complex phenomenon. Regarding delaminated plates, Yin and Jane [253] find that open delaminations modelled with an unconstrained approach lead to additional vibration modes, which is confirmed by Chen [254]. Further works apply the FEM [255, 256] or perturbation methods [257] to determine the vibration characteristics of delaminated plates and shells.

Other types of damage besides delaminations are for example investigated by Nguyen-Thoi et al. [258], who model the free vibration of plates featuring

various cracks. Viglietti et al. [259] apply the CUF for the analysis of localized damage in freely vibrating composite plies. They predict the natural frequencies and altered mode shapes of damaged components.

Most of the research on vibration of damaged laminates is limited to conventional composite materials. To the authors' knowledge, only Li et al. [260] have investigated the influence of low-velocity impact damage on the vibrational characteristics of FMEL. They present an analytical model and assume a stiffness degradation summarizing all types of occurring damage in a circular area around the point of impact. However, a change in damping is not addressed specifically. With regard to CLD in the FMELs previously investigated in [220, 227, 223] and within the present work, no related research is known, which explores the influence of impact damage. The occurrence of multiple types of damage under low-velocity impact loading, however is shown by Li et al. [237].

3 Objectives

Chapter 2 revisits the current state of research on FMELs. While there is quite comprehensive research on FMELs regarding their experimental characterisation under quasi-static, vibration and impact loading, a lack of predictive models for the vibration and damping behaviour is present. Simple models, such as the RKU model have been shown to produce satisfactory results for laminates not containing very thin or thick damping layers. Furthermore, existing models fail to capture the frequency-dependence of material properties. In addition, only a limited number of FMEL configurations has been investigated experimentally, but those studies show complex dependencies and non-trivial tendencies with regard to laminate lay-ups and materials selection. Given the often cumbersome manufacturing and testing procedures, a time- and resource-efficient model would greatly simplify the analysis and design of new FMELs and give a deeper insight into the deformation behaviour. While FEM models have been used in the analysis of the here considered hybrid FMELs, they usually are quite expensive computationally. Furthermore, the previously introduced research on CLD under different boundary conditions has shown that general trends and dependencies are not influenced by those. Therefore a computationally efficient analytical model with a strongly limited number of DOFs for simple plate geometries and boundary conditions is deemed sufficient for closing the outlined research gap, namely the fast analysis and design of new FMELs. Consequently, the following research objectives are defined:

- Objective 1-1: Development and verification of an analytical model for the efficient analysis of the static, modal and steady-state behaviour of hybrid FMELs
- Objective 1-2: Application of the developed model for the analysis of different configurations of hybrid FMELs with a strong focus on CLD and its dependence on laminate parameters
- Objective 1-3: Formulation of general design recommendations for CLD structures offering high damping capabilities and structural stiffness

Furthermore, Section 2.1.4 introduces the Mullins effect as a large-strain phenomenon occurring in filled and crystallising elastomers. An occurrence of the Mullins effect in EPDM compounds has also been reported by a number of researchers. Consequently, it is expected that at least some of the elastomer materials studied in this work also exhibit the Mullins effect. Although the CLD mechanism, which is the focus of this thesis, is studied in the context of low-strain vibrations, the underlying mechanism dictates that the compliant damping layers undergo a certain amount of shear deformation. This is also shown in Section 5.3. Furthermore, a CLD laminate or component might be subjected not only to vibrations, but also certain static, quasi-static or even dynamic loads which deform the laminate more than an excitation due to vibration. At the time of writing, the author is not aware of any previous investigations into the role of the Mullins effect within CLD laminates, let alone FMELs. In response to this research gap, this work attempts to provide some first findings. Consequently, the following

Hypothesis 1 *Non-linear phenomena known to occur at large strains in elastomer materials, under certain conditions, have to be considered in low-amplitude vibrations of FMELs.*

is postulated. In particular, proofing Hypothesis 1 is attempted by fulfilling the following objectives:

- Objective 2-1: Experimental characterisation and exploration of the Mullins effect in the elastomer compounds used throughout this work.
- Objective 2-2: Development and implementation of a constitutive model which allows for an explorative study of Mullins softening in frequency-domain FEM simulations.
- Objective 2-3: Validation of the developed model and subsequent analysis of Mullins softening in CLD laminates using experiments and simulations.

The literature review presented in Chapter 2 also introduces a limited number of publications, which deal with the impact behaviour of FMELs. Experimental methods are employed for determining the damage pattern under low- and high-velocity impacts on a number of laminate systems, but no results are published on FMELs featuring CLD with constraining layers consisting of CFRP as well as aluminium. Furthermore, current research attests FMELs a high damage resistance and tolerance regarding low-velocity impact. These laminates have been shown, not only within this work, to provide good damping capabilities by means of CLD while maintaining high structural stiffness. The tolerance of CLD regarding the occurrence of damage within the laminate is entirely unexplored. In particular, the influence of barely visible damages known to occur in conventional FMLs is of interest. This thesis therefore aims at fulfilling the following research objectives:

- Objective 3-1: Experimental investigation of the low-velocity impact behaviour of hybrid FMELs and the resulting damage pattern.
- Objective 3-2: Development of numerical methods for considering the observed types of damage in frequency-domain simulations.
- Objective 3-3: Identification of critical configurations of occurring damages with regard to their impact on the CLD capabilities.

4 Materials and manufacturing

This chapter introduces the different materials and laminates studied in this work. First, the individual constituents making up the fibre metal elastomer laminates are presented and their basic mechanical properties are summarized. Subsequently, the different lamination schemes, their corresponding nomenclature and their manufacturing process are described.

4.1 Constituents

The following three types of constituents are used in different configurations of FMELs within this work, whereby not all laminates comprise of all three constituents. The basic mechanical behaviour and corresponding properties of all the FMEL constituents are determined in a number of experiments. The following sections give a summary of the relevant findings which will be referenced in the remainder of this work.

4.1.1 Aluminium

The metal plies in the FMELs under investigations are comprised of aluminium wrought alloy EN AW-2024 T3 ALCLAD AMS-QQA-250/5 supplied as sheet metal by Kaiser Aluminium. The sheets have an initial thickness of 0.3 mm and are assumed to retain this thickness after manufacturing of the laminates.

4.1.1.1 Mechanical properties

The elastic properties of the present aluminium alloy are summarized in Table 4.1. The values are adopted from [223].

Table 4.1: Elastic properties of aluminium wrought alloy EN AW-2024 T3 ALCLAD AMS-QQA-250/5. Values adopted from [223].

Property	Unit	Value
Mass density	$\mathrm{kg\,m^{-3}}$	2780
Young's modulus E	GPa	73.1
Poisson's ratio ν	-	0.3

Although aluminium alloys are known to exhibit some intrinsic material damping, their dynamic behaviour is not subject of this work. Iriondo et al. [261] experimentally determined the loss factor $\tan(\delta)$ of EN AW-2024 T3 aluminium alloy to be approximately 1×10^{-3}. As this is magnitudes lower than the loss factors observed in the utilized elastomer materials, the dynamic properties of aluminium will be neglected throughout this study.

4.1.2 Carbon fibre-reinforced polymer

The majority of laminates studied in this work contain multiple plies of CFRP. Specifically, the preimpregnated (prepreg) unidirectionally reinforced (UD) epoxy HexPly-M77/38/UD150/CHS-12K-70 by Hexcel is used. The specifications of the supplied prepreg material are listed in Table 4.2. The fibre volume content has been experimentally determined by Sessner [230] using microscopy of prepared cross sections.

Table 4.2: Properties of the CFRP prepreg material HexPly-M77/38/UD150/CHS-12K-70 according to manufacturer's data sheet [262] and Sessner [230].

Property	Unit	Value	Reference
Fibre type	-	12K high strength carbon fibre	[230]
Matrix type	-	epoxy resin M77	[262]
Fibre mass density	$\mathrm{kg\,m^{-3}}$	1800	[262]
Matrix mass density	$\mathrm{kg\,m^{-3}}$	1150	[262]
Fabric weight	$\mathrm{g\,m^{-2}}$	150	[262]
Cured ply thickness	mm	0.15	[230]
Fibre volume content	%	50.5	[230]

4.1.2.1 Mechanical properties

The quasi-static elastic mechanical properties of the UD CFRP plies are assumed to be transversely isotropic. They are listed in Table 4.3 in the form of engineering constants, where the index $()_1$ indicates properties along the fibre direction.

Table 4.3: Linear elastic material parameters of CFRP under the assumption of transverse isotropy. Values marked with $()^*$ are not determined experimentally but calculated based on assumptions.

E_1 in GPa	E_2 in GPa	ν_{12}	G_{12} in GPa	G_{23} in GPa
103.10	7.7	0.34	3.76	2.75^*

The Young's moduli E_1 and E_2 as well as the in-plane shear modulus are determined in uniaxial tensile tests on specimens cut from laminates of eight stacked UD plies in 0°, 90° and ±45° orientation according to DIN EN ISO 527-5:2021 [263] and DIN EN 6031:2016-02 [264] respectively. The tests were carried out by the Karlsruhe Institute of Technology (KIT) Institute for Applied Materials - Materials Science and Engineering (IAM-WK). Under the

assumption of the out-of-plane Poisson's ratio being $\nu_{23} = 0.4$, the out-of-plane shear modulus G_{23} is calculated as

$$G_{23} = \frac{E_1}{2\,(1+\nu_{23})} \tag{4.1}$$

according to Schürmann [265]. Being a polymer, the epoxy matrix of the CFRP material employed within this work, also shows viscoelastic behaviour. A thorough investigation and modelling approach is given by Liebig et al. [266] for the given material system. These viscoelastic properties, however, are neglected in the present work as the loss factor $\tan(\delta)$ of the CFRP is magnitudes lower than that of the elastomer materials at room temperature [230].

4.1.3 Elastomers

All elastomers used in this work belong to the KRAIBON® range of products by Gummiwerk KRAIBURG GmbH & Co. KG and are supplied as unvulcanized calendered sheets. A summary of the three compounds is given in Table 4.4.

Table 4.4: Properties of the three KRAIBON® compounds SAA9579/52, HAA9275/45 and HVV9632/59 studied in this work according to data sheets supplied by the manufacturer [267, 268, 269].

	SAA9579/52	HAA9275/45	HVV9632/59
Base polymer	EPDM	EPDM	AEM
Mass density	$1180\,\mathrm{kg\,m^{-3}}$	$1250\,\mathrm{kg\,m^{-3}}$	$1350\,\mathrm{kg\,m^{-3}}$
Hardness	88 Shore A	98 Shore A	95 Shore A

Two of the three mixtures, namely SAA9579/52 and HAA9275/45, are based on EPDM, while the third compound HVV9632/59 is comprised of AEM. The materials' mass densities exhibit similar values, which is also true for the Shore A hardness also shown in Table 4.4.

4.1.3.1 Mechanical properties

Quasi-static behaviour The quasi-static mechanical properties of the three elastomer compounds are identified by tensile tests on the neat materials. In order to ensure a sufficient set of data for the parametrization of constitutive models, see Chapter 6, two load cases are tested, namely uniaxial tension and pure shear.

The uniaxial tensile tests are conducted in compliance with American Society for Testing and Materials (ASTM) standard D412-16 [270] and the specimen geometry corresponds to standard dumbbell specimen of type D. Tests are conducted with a constant strain rate of $10^{-3}\,\mathrm{s}^{-1}$ up to failure of the specimen. The temperature is held constant at approximately 21 °C. The force is measured using a load cell with a nominal capacity of 2.5 kN. Strains are calculated based on the crosshead displacement of the testing machine. No additional strain gauges are used due to the high applied strains, low strain rate and low material stiffness. The results for all three elastomer materials are shown in Figure 4.1.

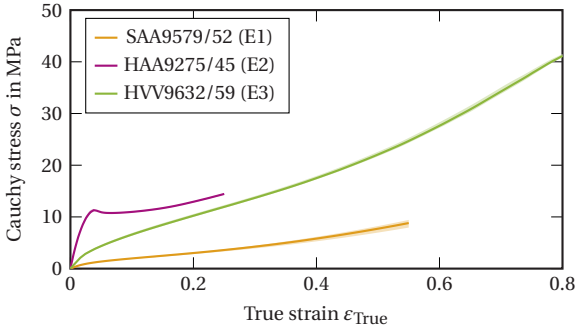

Figure 4.1: Mean stress-strain curves determined in uniaxial tension with a strain rate of $\dot{\varepsilon} = 10^{-3}\,\mathrm{s}^{-1}$. The shaded area illustrates the maximum range of values of all specimens tested. Three specimens are tested per material.

Since multiple specimens were tested, the curves shown represent the mean curves. The shaded areas indicate the maximum and minimum values of all curves. Generally, the elastomer SAA9579/52 shows the highest amount of scatter. This is attributed to the fact, that for this material specimens originate from multiple plates. Owing to limited availability, specimens from the other two materials originate from only one plate of neat material, indicating certain deviations in the manufacturing process.

The curves in Figure 4.1 clearly show the strongly different mechanical behaviour of the three elastomers. Compound SAA9579/52 exhibits a typical hyperelastic loading path as would be expected from an elastomer material with failure occurring at true strains exceeding 50 %. Also noteworthy is the pronounced decrease in stiffness at low strains. Material HAA9275/45 behaves entirely different as failure occurs at lower true strains from 25 %. Furthermore, a distinct linear elastic region up to approximately 5 % is observable until necking occurs. After necking, an increasing slope in the stress curve is visible. This behaviour is rather unusual for typical elastomer materials and resembles the kind of behaviour usually seen in thermoplastic polymers [271]. The third compound, HVV9632/59, on the other hand again exhibits typical hyperelastic behaviour. Failure, however, occurs at higher true strains than it does for material SAA9579/52, namely at true strains exceeding 80 %. Material HVV9632/59 also undergoes far higher stresses at similar strains than material SAA9579/52 indicating an overall stiffer behaviour.

Dynamic behaviour As the focus of this work is on the vibration damping capabilities of laminates containing the elastomers listed above, their dynamic behaviour under oscillating loads is paramount. DMA is used to characterise the viscoelastic behaviour at different frequencies and temperatures. The tests are performed on an Instron® E3000 ElectroPuls® electrodynamic testing machine by llinois Tool Works Inc. with a nominal force of 3 kN. A load cell with a capacity of 5 kN is used to measure the nominal dynamic force. The test temperature is varied using a climate chamber by Instron capable of heating and cooling. For cooling, nitrogen is used as a cryogenic gas.

The DMA is performed in tension mode as frequency sweeps from 0.1 Hz to 10 Hz. Specimens undergo strain-controlled harmonic tensile loading with an medium applied strain of $\varepsilon_m = 1\,\%$ and a strain amplitude of $\hat{\varepsilon} = 0.1\,\%$. These sweeps are repeated at different discrete temperatures with an increment of 5 °C starting from −80 °C and ending at 80 °C. After the initial cooling, a dwell time of 30 min is waited in order to ensure a constant temperature of all test components and the specimen. An additional dwell time of 10 min is adhered to after each temperature step. As occurrence of the Mullins effect, see Section 2.1.4, is expected, five preconditioning cycles to higher strains are conducted in order to eliminate any influence on the obtained dynamic behaviour.

Figure 4.2 shows the DMA results for the three materials in terms of their storage modulus E' and their loss factor $\tan\delta$ over the temperature for nine frequencies. All three elastomers show a characteristic drop in storage modulus and peak in loss factor in their glass transition region. This is most pronounced for compound SAA9579/52 while HAA9275/45 shows the lowest decrease in stiffness. It can likewise be noted, that the materials' stiffness above their glass transition temperature differ significantly. Compound HAA9275/45 is a magnitude stiffer than compound SAA9579/52 with HVV9632/59 lying in between the two. The materials' viscoelastic damping capability can be derived from its loss factor $\tan(\delta)$. The most compliant compound SAA9579/52 therefore offers the highest amount of damping, especially in the vicinity of its glass transition area with a loss factor as high as 0.5. The lowest loss factor is observed for the stiffest compound HAA9275/45. The loss factor ascertained for HVV9632/59 is slightly lower than the one for SAA9579/52. All three materials exhibit loss factors lower than 0.2 for temperatures in the vicinity of room temperature. The peaks of the loss factor curves at a frequency of 1 Hz are used to determine the materials' glass transition temperature T_G. The values are listed in Table 4.5 together with the maximum loss factors.

The temperature sweeps shown in Figure 4.2 give a good indication of the materials' behaviour over a wide range of temperatures, but, due to

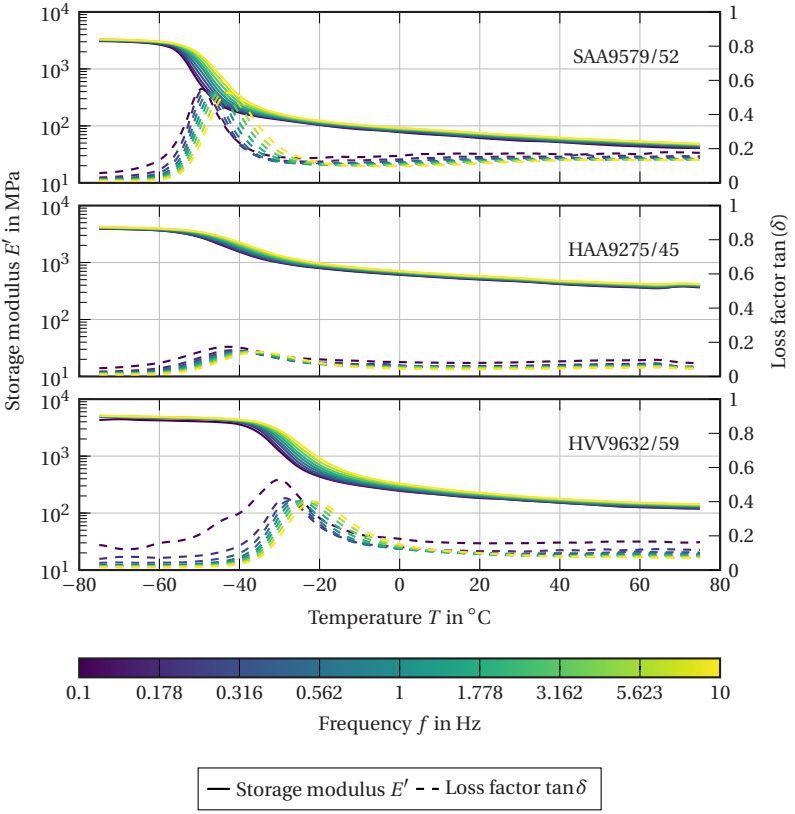

Figure 4.2: Temperature and frequency dependence of the three KRAIBON® compounds determined in DMA experiments. The stiffness (storage modulus) and damping (loss factor) over the temperature for the tested frequencies in the range of 0.1 Hz to 10 Hz is shown.

experimental restrictions, only cover a strongly limited frequency range. The TTS, as introduced in Section 2.1.2, is applied in order to determine the material behaviour beyond those limits. Prior, however, the applicability and limits of TTS are assessed with the help of van Gurp-Palmen plots introduced in Section 2.1.2.3. For all three elastomers, these plots are shown in Figure 4.3.

Table 4.5: Glass transition temperatures T_G determined from DMA by finding the maximum loss factor at a frequency of 1 Hz.

	SAA9579/52	HAA9275/45	HVV9632/59
T_G	−46.1 °C	−39.0 °C	−25.4 °C
$\max(\tan(\delta)(1\,\text{Hz}))$	0.52	0.14	0.40

In case of elastomer SAA9579/52, a clear wicket is distinguishable for the lower end of the temperature range up to approximately 20 °C. Upwards, diverging sweeps are observed. Consequently, TTS is applied only to a temperature range of −60 °C to 25 °C as sweeps below and above this range tend to fan out. As the same is observed for the other two elastomers, the same temperature range is chosen. Omitting the higher temperature from the creation of master curves is acceptable since the viscoelastic behaviour in this region undergoes only minor changes as seen in Figure 4.2. Elastomers HAA9275/45 and HVV9632/59 in addition show that for most sweeps, the lower frequencies of 0.1 Hz and 0.178 Hz diverge from the wicket. It is assumed, that for these low frequencies creep effect superimpose the harmonic oscillation in the DMA experiment. For subsequent TTS, these low frequencies are omitted as a consequence.

For all three elastomers, the master curves are created at a reference temperature equalling their glass transition temperature T_G using horizontal and vertical shifting. The optimal shift, horizontal as well vertical, for each sweep is determined using the normalized arc length minimization procedure as outlined by Kehrer et al. [33] based on Cho et al. [272] and Bae et al. [273], respectively. Subsequently, the generated master curves are shifted from the chosen reference temperature $T_{ref} = T_G$ to room temperature $T_R = 20\,°C$ using the WLF relation in Equation (2.46). The determined horizontal shift factors at T_G are listed in A.1.1 together with the parameters for the Arrhenius and WLF relations and the vertical shifts b_T. The resulting master curves at room temperature are shown in Figure 4.4 for a wide frequency range.

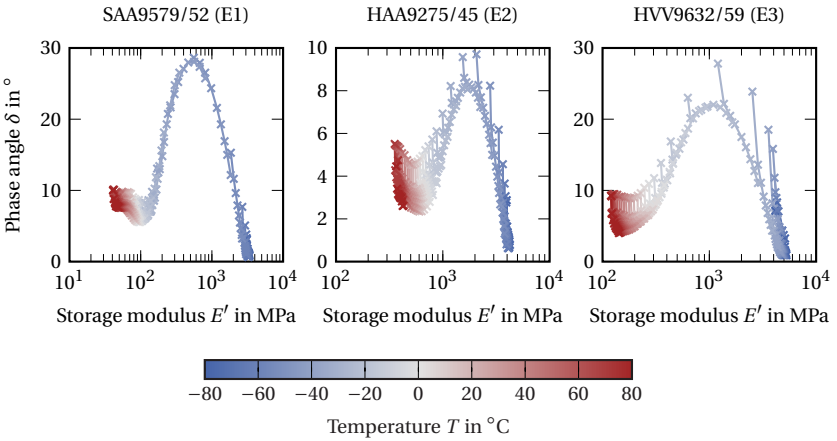

Figure 4.3: Van Gurp-Palmen plots of the three elastomer compounds. DMA tests conducted at frequencies of 0.1 Hz to 10 Hz.

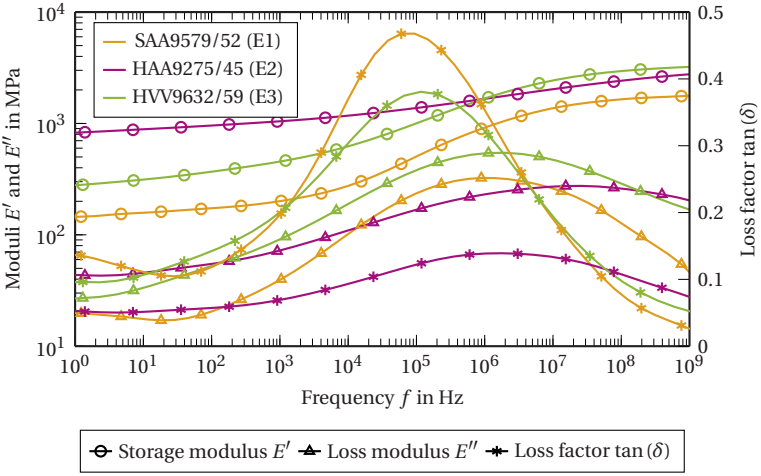

Figure 4.4: Master curves of the three elastomer materials at room temperature $T_R = 20\,°C$ generated from temperature and frequency sweeps in tension mode using TTS.

4.2 Fibre metal elastomer laminates

4.2.1 Laminate configurations

Six different FMELs and metal elastomer laminates (MELs) configurations are investigated and listed in Table 4.6. For the sake of brevity, all laminates are given a shortened notation, in which aluminium layers are denoted by A, CFRP layers by C and elastomer layers by the letter E. This notation is an adaption of the convention used by Sessner [227, 230] with the addition of a third elastomer compound. In order to differentiate the three elastomer compounds introduced in Section 4.1.3, the short title E1 is given to compound SAA9579/52, E2 stands for HAA9275/45 and E3 for HVV9632/59.

It should be noted that laminates of type A-E-C-E-A are non-symmetrical with regard to material orientation of the transversely isotropic CFRP plies. This serves the motive of retaining the same total thickness as the laminates of type C-E-A-E-C in order to facilitate a comparison of bending stiffness and other thickness-dependent properties. The three laminates A-E1-A, A-E2-A and A-E3-A merely serve the purpose of allowing for investigations of isolated viscoelastic effects in the elastomer layers without interference from the also viscoelastic CFRP layers. Laminates C-E3-A-E3-C and A-E3-C-E3-A are not manufactured and thus considered only in the simulation parts of this work.

4.2.2 Laminate manufacturing and specimen preparation

All laminates introduced above are manufactured as plates of dimensions 400 mm × 400 mm in a hot-mould process at the Fraunhofer Institute for Chemical Technology ICT. The constituents are manually cut to dimensions and stacked in a heated plate tool. Prior, the tool is treated with the release agent ATOL-PLUS by Technotrenn GmbH. As the aluminium sheets are delivered slightly oiled, they are cleaned prior to stacking using acetone.

Depending on the thickness of the elastomer layers, several sheets are stacked in order to achieve the desired overall thickness. It should be noted that no additional adhesive is used as the elastomer compounds vulcanize directly onto the adjacent materials. The mould is heated to 150 °C and a pressure of 40 bar is reached upon closing, which is then retained for 300 s allowing for consolidation of all constituents.

The same process is used for the manufacturing of neat elastomer plates. Although the material could be vulcanized using lower temperatures and pressure according to the manufacturer's data sheets, the same process parameters are maintained in order to ensure that the neat elastomer specimens depict the same material behaviour as the elastomer plies within the hybrid laminates.

Specimens for experimental tests and characterisation are then cut from the manufactured plates. In the case of laminates containing either aluminium or CFRP, this is done using a iCUTwater SMART waterjet cutting machine by imes-icore GmbH. Neat elastomer specimens are punched out of the plates using a standardized die in order to minimize any deformation of the material during preparation.

Table 4.6: MEL and FMEL configurations and naming convention. The notation is adopted from Sessner [230]. Lower indices state the layer's thickness in mm and upper indices, if applicable, state the material orientation with respect to the x-direction. The index $()_S$ indicates symmetric stacks of CFRP plies. The nominal thickness is the expected overall thickness and does not include any measurements of the actual thickness of the laminates.

Laminate	Abbreviation	Nominal thickness
$\left[A_{0.3}/E1_{0.5}/\left(C^{0°}_{0.15}/C^{90°}_{0.15}\right)_3/E1_{0.5}/A_{0.3}\right]$	A-E1-C-E1-A	2.5 mm
$\left[A_{0.3}/E2_{0.5}/\left(C^{0°}_{0.15}/C^{90°}_{0.15}\right)_3/E2_{0.5}/A_{0.3}\right]$	A-E2-C-E2-A	2.5 mm
$\left[A_{0.3}/E3_{0.5}/\left(C^{0°}_{0.15}/C^{90°}_{0.15}\right)_3/E3_{0.5}/A_{0.3}\right]$	A-E3-C-E3-A	2.5 mm
$\left[\left(C^{0°}_{0.15}/C^{90°}_{0.15}\right)_S/E1_{0.5}/A_{0.3}/E1_{0.5}/\left(C^{0°}_{0.15}/C^{90°}_{0.15}\right)_S\right]$	C-E1-A-E1-C	2.5 mm
$\left[\left(C^{0°}_{0.15}/C^{90°}_{0.15}\right)_S/E2_{0.5}/A_{0.3}/E2_{0.5}/\left(C^{0°}_{0.15}/C^{90°}_{0.15}\right)_S\right]$	C-E2-A-E2-C	2.5 mm
$\left[\left(C^{0°}_{0.15}/C^{90°}_{0.15}\right)_S/E3_{0.5}/A_{0.3}/E3_{0.5}/\left(C^{0°}_{0.15}/C^{90°}_{0.15}\right)_S\right]$	C-E3-A-E3-C	2.5 mm
$[A_{0.3}/E1_{2.0}/A_{0.3}]$	A-E1-A	2.6 mm
$[A_{0.3}/E2_{2.0}/A_{0.3}]$	A-E2-A	2.6 mm
$[A_{0.3}/E3_{2.0}/A_{0.3}]$	A-E3-A	2.6 mm

5 Analytical modelling of constrained-layer damping laminates

5.1 Modelling approach[1]

The following sections introduce the variable kinematics modelling approach based on the GUF framework used for modelling the hybrid laminates in this work. The corresponding analytical solution procedures for different types of loading are outlined subsequently. Both have previously been published by the author in [274, 275, 150].

5.1.1 Laminate coordinate system

The geometric description in thickness direction of a laminated plate is illustrated in Figure 5.1. A global thickness coordinate is denoted by z. The plate consists of an arbitrary number of material plies with individual thicknesses h_k, which are assumed to have ideal adhesion. For each material layer k the dimensionless coordinate

$$\zeta^k = \frac{2}{z^k_{\text{top}} - z^k_{\text{bot}}} z - \frac{z^k_{\text{top}} + z^k_{\text{bot}}}{z^k_{\text{top}} - z^k_{\text{bot}}} \tag{5.1}$$

[1] Section 5.1 is reproduced from Jackstadt et al. [274, 275, 150] with minor linguistic changes and additions.

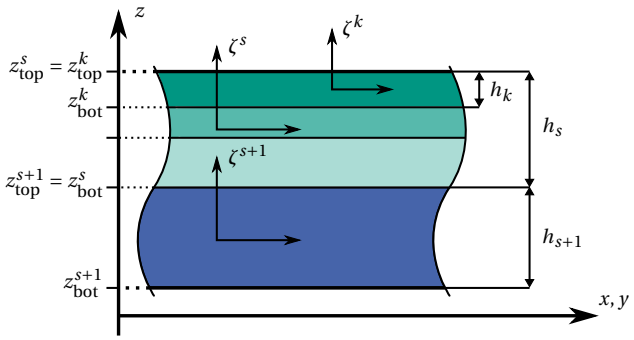

Figure 5.1: Laminate coordinate system showing two sublaminates s (green) and $s+1$ (blue). Layer s consists of multiple material layers. For the topmost layer in s, namely k, the local material coordinate ζ_k is shown as an example. Reproduced from Jackstadt et al. [150].

is defined so that $\zeta^k(z^k_{\text{top}}) = 1$ and $\zeta^k(z^k_{\text{bot}}) = -1$, where z^k_{top} and z^k_{bot} are the upper and lower interfaces of ply k in the global coordinate z. Each material ply k is thus described by its coordinates $(z^k_{\text{top}}, z^k_{\text{bot}})$ and its own constitutive law. Furthermore, the laminated plate is partitioned into sublaminates. Each sublaminate s consists of one or more material layers k. Again, a dimensionless coordinate ζ^s is introduced as

$$\zeta^s = \frac{2}{z^s_{\text{top}} - z^s_{\text{bot}}} z - \frac{z^s_{\text{top}} + z^s_{\text{bot}}}{z^s_{\text{top}} - z^s_{\text{bot}}} \tag{5.2}$$

for each sublaminate s with z^s_{top} and z^s_{bot} being its upper and lower interface in global coordinates. Figure 5.1 exemplarily depicts two sublaminates, sublaminate s in green and sublaminate $s+1$ in blue. Sublaminate s consists of three individual material plies, whereas sublaminate $s+1$ incorporates only one material ply.

5.1.2 Variational principle

As this work aims at the understanding of the CLD mechanism, which is driven by transverse shear stresses, see illustration in Figure 2.5, a suitable modelling approach must depict those sufficiently well. Furthermore, the elastomer layers in the present laminates are comparably thick. For this reason, the RMVT [119]

$$\int_\Omega \left(\delta \boldsymbol{\varepsilon}_{\mathrm{pG}}^\top \boldsymbol{\sigma}_{\mathrm{pH}} + \delta \boldsymbol{\varepsilon}_{\mathrm{nG}}^\top \boldsymbol{\sigma}_{\mathrm{nM}} + \delta \boldsymbol{\sigma}_{\mathrm{nM}}^\top (\boldsymbol{\varepsilon}_{\mathrm{nG}} - \boldsymbol{\varepsilon}_{\mathrm{nH}}) \right) \mathrm{d}V = \delta L_{\mathrm{ext}} - \int_\Omega \rho \delta \boldsymbol{u}^\top \ddot{\boldsymbol{u}} \mathrm{d}V \tag{5.3}$$

instead of the PVD is used as basis for the modelling approach, following recommendations [276, 277, 278] for similar laminates.

In Equation (5.3), index p denotes in-plane quantities, whereas out-of-plane quantities are indexed with n. In the modified Voigt notation used here, the two vectors containing the infinitesimal strains are $\boldsymbol{\varepsilon}_{\mathrm{p}} = \begin{pmatrix} \varepsilon_{xx} & \varepsilon_{yy} & \gamma_{xy} \end{pmatrix}^\top$ and $\boldsymbol{\varepsilon}_{\mathrm{n}} = \begin{pmatrix} \gamma_{xz} & \gamma_{yz} & \varepsilon_{zz} \end{pmatrix}^\top$. Stress vectors $\boldsymbol{\sigma}_{\mathrm{p}} = \begin{pmatrix} \sigma_{xx} & \sigma_{yy} & \sigma_{xy} \end{pmatrix}^\top$ and $\boldsymbol{\sigma}_{\mathrm{n}} = \begin{pmatrix} \sigma_{xz} & \sigma_{yz} & \sigma_{zz} \end{pmatrix}^\top$ are introduced accordingly. Stress quantities which are modelled by an explicit modelling approach are identified by index M. Strain components featuring index G are directly derived from the displacement field $\boldsymbol{u}$ by the known geometric relations. Index H indicates, that the quantity is calculated from the mixed form of Hooke's law introduced below in Section 5.1.3. The right-hand side of Equation (5.3) summarizes the virtual variation of work δL_{ext} performed by external loads as well as the inertia term containing the acceleration $\ddot{\boldsymbol{u}}$.

5.1.3 Constitutive relations

Following the mixed nature of the variational principle used in this model, a mixed constitutive law which takes into account the out-of-plane stresses $\boldsymbol{\sigma}_\mathrm{n}$ is needed. Starting from the orthotropic linear elastic classic form of Hooke's law

$$\begin{Bmatrix} \boldsymbol{\sigma}_\mathrm{p} \\ \boldsymbol{\sigma}_\mathrm{n} \end{Bmatrix} = \begin{Bmatrix} \tilde{\boldsymbol{C}}_\mathrm{pp} & \tilde{\boldsymbol{C}}_\mathrm{pn} \\ \tilde{\boldsymbol{C}}_\mathrm{np} & \tilde{\boldsymbol{C}}_\mathrm{nn} \end{Bmatrix} \begin{Bmatrix} \boldsymbol{\varepsilon}_\mathrm{p} \\ \boldsymbol{\varepsilon}_\mathrm{n} \end{Bmatrix} \tag{5.4}$$

with the classical Hooke's stiffness matrix $\tilde{\boldsymbol{C}}$ in a modified Voigt notation

$$\begin{bmatrix} \sigma_{11} \\ \sigma_{22} \\ \sigma_{12} \\ \sigma_{13} \\ \sigma_{23} \\ \sigma_{33} \end{bmatrix} = \begin{bmatrix} \tilde{C}_{11} & \tilde{C}_{12} & \tilde{C}_{14} & 0 & 0 & \tilde{C}_{13} \\ \tilde{C}_{12} & \tilde{C}_{22} & \tilde{C}_{24} & 0 & 0 & \tilde{C}_{23} \\ \tilde{C}_{14} & \tilde{C}_{24} & \tilde{C}_{44} & 0 & 0 & \tilde{C}_{34} \\ 0 & 0 & 0 & \tilde{C}_{55} & \tilde{C}_{56} & 0 \\ 0 & 0 & 0 & \tilde{C}_{56} & \tilde{C}_{66} & 0 \\ \tilde{C}_{13} & \tilde{C}_{23} & \tilde{C}_{34} & 0 & 0 & \tilde{C}_{33} \end{bmatrix} \begin{bmatrix} \varepsilon_{11} \\ \varepsilon_{22} \\ \gamma_{12} \\ \gamma_{13} \\ \gamma_{23} \\ \varepsilon_{33} \end{bmatrix} \tag{5.5}$$

with $\boldsymbol{\sigma}_\mathrm{p} = [\sigma_{11}\ \sigma_{22}\ \sigma_{12}]^\top$, $\boldsymbol{\sigma}_\mathrm{n} = [\sigma_{13}\ \sigma_{23}\ \sigma_{33}]^\top$ and strain vectors $\boldsymbol{\varepsilon}_\mathrm{p}$ and $\boldsymbol{\varepsilon}_\mathrm{n}$ being defined accordingly, the components of the mixed stiffness matrix $\boldsymbol{C}$ are calculated by

$$\begin{aligned} \boldsymbol{C}_\mathrm{pp} &= \tilde{\boldsymbol{C}}_\mathrm{pp} - \tilde{\boldsymbol{C}}_\mathrm{pn}\tilde{\boldsymbol{C}}_\mathrm{nn}^{-1}\tilde{\boldsymbol{C}}_\mathrm{np} \\ \boldsymbol{C}_\mathrm{pn} &= \tilde{\boldsymbol{C}}_\mathrm{pn}\tilde{\boldsymbol{C}}_\mathrm{nn}^{-1} \\ \boldsymbol{C}_\mathrm{np} &= -\tilde{\boldsymbol{C}}_\mathrm{nn}^{-1}\tilde{\boldsymbol{C}}_\mathrm{np} \\ \boldsymbol{C}_\mathrm{nn} &= \tilde{\boldsymbol{C}}_\mathrm{nn}^{-1} \end{aligned} \tag{5.6}$$

according to [279, 136]. It should be noted, that in the remainder of Chapter 5, a tilde $\tilde{(\cdot)}$ denotes stiffness components from the classical form of Hooke's law (5.4), whereas for reasons of readability, components from the mixed

form of Hooke's law (MFHL) are not marked specifically. Following the transformations in Equation (5.6) the MFHL is given by

$$\begin{bmatrix} \sigma_{11} \\ \sigma_{22} \\ \sigma_{12} \\ \gamma_{13} \\ \gamma_{23} \\ \varepsilon_{33} \end{bmatrix} = \begin{bmatrix} C_{11} & C_{12} & C_{14} & 0 & 0 & C_{13} \\ C_{12} & C_{22} & C_{24} & 0 & 0 & C_{23} \\ C_{14} & C_{24} & C_{44} & 0 & 0 & C_{34} \\ 0 & 0 & 0 & C_{55} & C_{56} & 0 \\ 0 & 0 & 0 & C_{56} & C_{66} & 0 \\ -C_{13} & -C_{23} & -C_{34} & 0 & 0 & C_{33} \end{bmatrix} \begin{bmatrix} \varepsilon_{11} \\ \varepsilon_{22} \\ \gamma_{12} \\ \sigma_{13} \\ \sigma_{23} \\ \sigma_{33} \end{bmatrix} \tag{5.7}$$

and

$$\begin{Bmatrix} \boldsymbol{\sigma}_{\mathrm{p}} \\ \boldsymbol{\varepsilon}_{\mathrm{n}} \end{Bmatrix} = \begin{Bmatrix} \boldsymbol{C}_{\mathrm{pp}} & \boldsymbol{C}_{\mathrm{pn}} \\ \boldsymbol{C}_{\mathrm{np}} & \boldsymbol{C}_{\mathrm{nn}} \end{Bmatrix} \begin{Bmatrix} \boldsymbol{\varepsilon}_{\mathrm{p}} \\ \boldsymbol{\sigma}_{\mathrm{n}} \end{Bmatrix}, \tag{5.8}$$

respectively. Equation (5.8) is used in the following to describe the materials' linear elastic and linear viscoelastic mechanical behaviour. In frequency domain linear viscoelasticity including damping, a complex valued stiffness matrix $\tilde{\boldsymbol{C}}^*$ is needed. Equation (5.8) therefore becomes complex valued as well and is expressed by the material's Poisson ratio ν and the complex shear modulus $G^*(\omega)$. The two complex valued Lamé constants

$$\begin{aligned} \mu^* &= G^* \\ \lambda^* &= \frac{2G^*\nu}{1-2\nu} \end{aligned} \tag{5.9}$$

are then used to calculate the complex components of the isotropic stiffness tensor $\tilde{C}^*_{ijkl} = \lambda^* \delta_{ij}\delta_{kl} + \mu^* \left(\delta_{ik}\delta_{jl} + \delta_{il}\delta_{jk}\right)$, which, in turn, is transformed into the mixed form in Equation (5.8) according to the relations in Equation (5.6).

5.1.4 Laminate kinematics

This section introduces the axiomatic modelling approach based on the GUF used to formulate the present plate model. A layerwise description is used for the three displacement and three out-of-plane stress components, where for each material layer k according to Figure 5.1 the distributions

$$\begin{aligned}
u_x^k(x,y,z) &= U^k_{x,\alpha_{u_x}} F_{\alpha_{u_x}}(z)\Phi_{u_x}(x,y)\\
u_y^k(x,y,z) &= U^k_{y,\alpha_{u_y}} F_{\alpha_{u_y}}(z)\Phi_{u_y}(x,y)\\
u_z^k(x,y,z) &= U^k_{z,\alpha_{u_z}} F_{\alpha_{u_z}}(z)\Phi_{u_z}(x,y)\\
\sigma_{xz}^k(x,y,z) &= S^k_{xz,\alpha_{\sigma_{xz}}} F_{\alpha_{\sigma_{xz}}}(z)\Phi_{\sigma_{xz}}(x,y)\\
\sigma_{yz}^k(x,y,z) &= S^k_{yz,\alpha_{\sigma_{yz}}} F_{\alpha_{\sigma_{yz}}}(z)\Phi_{\sigma_{yz}}(x,y)\\
\sigma_{zz}^k(x,y,z) &= S^k_{zz,\alpha_{\sigma_{zz}}} F_{\alpha_{\sigma_{zz}}}(z)\Phi_{\sigma_{zz}}(x,y)
\end{aligned} \tag{5.10}$$

are prescribed. In Equation (5.10), indices α are summation indices according to Einstein's summation convention. For each displacement or out-of-plane stress component, an ansatz of arbitrary order is chosen. The corresponding indices α_{u_i} and $\alpha_{\sigma_{iz}}$ then run from 1 to $N_{u_i}+1$ and $N_{\sigma_{iz}}+1$, respectively, indicating that a specific layer displacement or out-of-plane stress component is expressed by $N+1$ variables $U^k_{i,\alpha_{u_i}}$ and $S^k_{iz,\alpha_{\sigma_{iz}}}$, which are unknown so far. While this ansatz allows for the description of displacements and out-of-plane stresses in the thickness direction z, the in-plane dependencies are summarized as functions $\Phi(x,y)$ in Equation (5.10) and will be addressed in Section 5.1.5. The functions used to expand displacement and out-of-plane stress components $F_{\alpha_{u_i}}(z)$ and $F_{\alpha_{\sigma_{iz}}}(z)$ in the thickness direction are combinations of Legendre polynomials and defined as

$$\begin{aligned}
F_1 &= \frac{P_0+P_1}{2}\\
F_m &= P_m - P_{m-2} \quad m \in [2,N]_{\mathbb{N}}\\
F_{N+1} &= \frac{P_0-P_1}{2},
\end{aligned} \tag{5.11}$$

with $P_n(\zeta_k)$ being the Legendre polynomials of orders $n \in [0, N]_{\mathbb{N}}$. A graphical representation of the Legendre polynomials P_n and the Legendre functions F_n used for the expansion in thickness direction up to an order of $N = 5$ is given in Figure 5.2. In this example, it can be noted that all functions F_n are zero on the domain's borders respectively at the top and bottom surface of layer k, with the exception of F_1 and $F_{N+1} = F_6$. Consequently, according to Equation (5.10), the first and last entry of $\mathbf{U}_i^k$ and $\mathbf{S}_{iz}^k$ equal the displacement or out-of-plane stress respectively at the top or bottom of layer k.

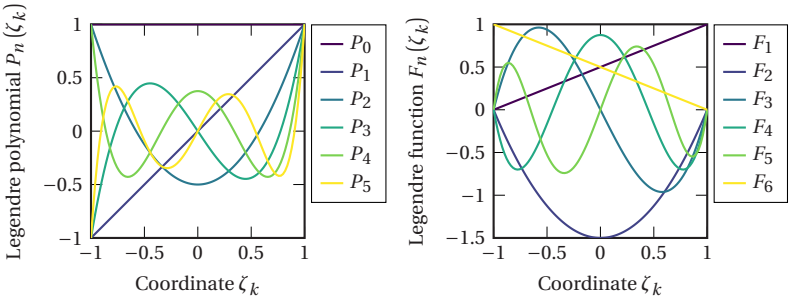

Figure 5.2: Legendre polynomials (left) and Legendre functions (right) for an order of expansion of $N = 5$.

5.1.5 Governing equations and analytic solutions for a simply supported plate

The vibration and damping behaviour of hybrid laminates is assessed on the example of a simply supported plate. The plate's coordinate system and some points of interest for subsequent evaluation of field variables are shown in Figure 5.3. The plate has the in-plane dimensions a and b in x- and y-direction. Coordinates of points A to E are listed in Table 5.1.

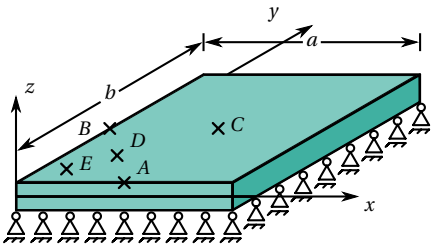

Figure 5.3: Simply supported plate of dimensions a and b with global coordinate system and points of interest. Reproduced from Jackstadt et al. [150].

Table 5.1: Evaluation points on the simply supported plate in Figure 5.3

	A	B	C	D	E
x	$0.5a$	0.0	$0.5a$	$0.25a$	$0.125a$
y	0.0	$0.5b$	$0.5b$	$0.25b$	$0.125b$

An exact Navier-type solution [103] satisfying the simply supported boundary condition shown in Figure 5.3 can be obtained, when the three trigonometric distributions for displacements and out-of-plane stresses

$$\begin{aligned}
\Phi_x &:= \Phi_{u_x}(x,y) = \Phi_{\sigma_{xz}}(x,y) = \cos\left(\frac{m\pi x}{a}\right)\sin\left(\frac{n\pi y}{b}\right)\\
\Phi_y &:= \Phi_{u_y}(x,y) = \Phi_{\sigma_{yz}}(x,y) = \sin\left(\frac{m\pi x}{a}\right)\cos\left(\frac{n\pi y}{b}\right)\\
\Phi_z &:= \Phi_{u_z}(x,y) = \Phi_{\sigma_{zz}}(x,y) = \sin\left(\frac{m\pi x}{a}\right)\sin\left(\frac{n\pi y}{b}\right)
\end{aligned} \tag{5.12}$$

are assumed. The parameters m and n in Equation (5.12) correspond to the number of half waves in x- and y-direction across the plate. These distributions are also used to describe loads in x-, y- and z-direction accordingly. In the following, the loads are restricted to those acting perpendicular to the x,y-plane on the top or bottom surface of a layer k and are expressed by

$$q_z^{k,\mathrm{top}}(x,y) = \Phi_z Q_z^{k,\mathrm{top}} \tag{5.13}$$

and

$$q_z^{k,\mathrm{bot}}(x,y) = \Phi_z Q_z^{k,\mathrm{bot}} \tag{5.14}$$

with $Q_z^{k,\text{top}}$ and $Q_z^{k,\text{bot}}$ being generic pressure load coefficients, which will be specified later depending on the loading type. Notably, the assumed load in Equation (5.14) corresponds to a sinusoidally distributed pressure across the plate's surface. In-plane loads are not considered here, but can be treated accordingly as shown in Appendix A.2.2.

For the deduction of governing equations for each layer k, the approximations for displacements u_i^k and out-of-plane stresses σ_{iz}^k as stated in Equation (5.10) are inserted into the RMVT in Equation (5.3). By imposing the virtual variations of layerwise displacement and out-of-plane stress components, $\delta u_{i_{\alpha_i}}$ and $\delta\sigma_{iz_{\alpha_{iz}}}$, the governing equations listed in Appendix A.2.1 are obtained. Following the GUF framework, 13 stiffness kernel matrices can be obtained for each layer k from the governing equations. Additionally, the inertia terms are expressed by three mass kernel matrices $\mathbf{M}_{U_iU_i}^k$. External loads are contained in the three right-hand side resultant load kernels $\mathbf{R}_i^k$. For the sake of brevity, these matrices are not shown here, but are listed in Appendix A.2.2. Following the expansion of the kernel matrices in each material layer k, the sublaminates s, as introduced in Section. 5.1.1 and Figure 5.1, are assembled. This is done according to the ESL assembly procedure outlined in [138]. Thus, the displacement DOFs of one sublaminate follow an ESL description while out-of-plane stress DOFs preserve their layerwise nature and the equilibrium at the interfaces within the sublaminate is imposed. Matrices containing all the kernels of present sublaminates are then assembled in a LW manner. This procedure, as well as the distinction between LW and ESL assembly, is shown in Figure 5.4 for two sublaminates $s+1$ (green) and s (blue) and two materials layers $k+1$ and k, respectively. The right-hand side vector and mass matrices are assembled accordingly, for details see Appendix A.2.2.

LW assembly:

$$\mathbf{K}_{U_iS_j} = \begin{bmatrix} K^s_{U_iS_j,11} & K^s_{U_iS_j,12} & K^s_{U_iS_j,13} & K^s_{U_iS_j,14} & 0 & 0 & 0 \\ K^s_{U_iS_j,21} & K^s_{U_iS_j,22} & K^s_{U_iS_j,23} & K^s_{U_iS_j,24} + K^{s+1}_{U_iS_j,11} & K^{s+1}_{U_iS_j,12} & K^{s+1}_{U_iS_j,13} & K^{s+1}_{U_iS_j,14} \\ 0 & 0 & 0 & K^{s+1}_{U_iS_j,21} & K^{s+1}_{U_iS_j,22} & K^{s+1}_{U_iS_j,23} & K^{s+1}_{U_iS_j,24} \end{bmatrix}$$

ESL assembly:

$$\mathbf{K}_{U_iU_j} = \begin{bmatrix} K^k_{U_iU_j,11} + K^{k+1}_{U_iU_j,11} & K^k_{U_iU_j,12} + K^{k+1}_{U_iU_j,12} & K^k_{U_iU_j,13} + K^{k+1}_{U_iU_j,13} & K^k_{U_iU_j,14} + K^{k+1}_{U_iU_j,14} \\ K^k_{U_iU_j,21} + K^{k+1}_{U_iU_j,21} & K^k_{U_iU_j,22} + K^{k+1}_{U_iU_j,22} & K^k_{U_iU_j,23} + K^{k+1}_{U_iU_j,23} & K^k_{U_iU_j,24} + K^{k+1}_{U_iU_j,24} \end{bmatrix}$$

$$\mathbf{K}_{U_iS_j} = \begin{bmatrix} K^k_{U_iS_j,11} & K^k_{U_iS_j,12} & K^k_{U_iS_j,13} & K^k_{U_iS_j,14} + K^{k+1}_{U_iS_j,11} & K^{k+1}_{U_iS_j,12} & K^{k+1}_{U_iS_j,13} & K^{k+1}_{U_iS_j,14} \\ K^k_{U_iS_j,21} & K^k_{U_iS_j,22} & K^k_{U_iS_j,23} & K^k_{U_iS_j,24} + K^{k+1}_{U_iS_j,21} & K^{k+1}_{U_iS_j,22} & K^{k+1}_{U_iS_j,23} & K^{k+1}_{U_iS_j,24} \end{bmatrix}$$

Figure 5.4: LW (top) and ESL (bottom) assembly procedure for different types of stiffness matrices with arbitrary expansion orders $N_i = 1$ and $N_j = 3$. For LW theories, all matrices are assembled as shown. For ESL theories three types are differentiated: $\mathbf{K}_{U_iU_j}$, $\mathbf{K}_{U_iS_j}$ and $\mathbf{K}_{S_iS_j}$. While type $\mathbf{K}_{S_iS_j}$ is assembled in a LW manner, types $\mathbf{K}_{U_iU_j}$ and $\mathbf{K}_{U_iS_j}$ are assembled as shown below in order to enforce an equilibrium and compatibility. For matrices $\mathbf{K}_{S_iU_j}$, the transpose of $\mathbf{K}_{U_iS_j}$ is assembled.

With the aid of these assembled matrices, the global system of equations

$$\begin{aligned}
&\mathbf{K}_{U_xU_x}\mathbf{U}_x + \mathbf{K}_{U_xU_y}\mathbf{U}_y + \mathbf{K}_{U_xS_x}\mathbf{S}_x + \mathbf{K}_{U_xS_z}\mathbf{S}_z + \mathbf{M}_{U_xU_x}\ddot{\mathbf{U}}_x = \mathbf{R}_x \\
&\mathbf{K}_{U_yU_x}\mathbf{U}_x + \mathbf{K}_{U_yU_y}\mathbf{U}_y + \mathbf{K}_{U_yS_y}\mathbf{S}_y + \mathbf{K}_{U_yS_z}\mathbf{S}_z + \mathbf{M}_{U_yU_y}\ddot{\mathbf{U}}_y = \mathbf{R}_y \\
&\mathbf{K}_{U_zS_x}\mathbf{S}_x + \mathbf{K}_{U_zS_y}\mathbf{S}_y + \mathbf{K}_{U_zS_z}\mathbf{S}_z + \mathbf{M}_{U_zU_z}\ddot{\mathbf{U}}_z = \mathbf{R}_z \\
&\mathbf{K}_{S_xU_x}\mathbf{U}_x + \mathbf{K}_{S_xU_z}\mathbf{U}_z + \mathbf{K}_{S_xS_x}\mathbf{S}_x = \mathbf{0} \\
&\mathbf{K}_{S_yU_y}\mathbf{U}_x + \mathbf{K}_{S_yU_z}\mathbf{U}_z + \mathbf{K}_{S_yS_y}\mathbf{S}_y = \mathbf{0} \\
&\mathbf{K}_{S_zU_x}\mathbf{U}_x + \mathbf{K}_{S_zU_y}\mathbf{U}_y + \mathbf{K}_{S_zU_z}\mathbf{U}_z + \mathbf{K}_{S_zS_z}\mathbf{S}_z = \mathbf{0}
\end{aligned} \tag{5.15}$$

is formulated. The vector containing all displacement and out-of-plane DOFs will in the following be denoted by $\mathbf{U} = \begin{pmatrix}\mathbf{U}_x & \mathbf{U}_y & \mathbf{U}_z & \mathbf{S}_x & \mathbf{S}_y & \mathbf{S}_z\end{pmatrix}^\top$ so that the global system of equations in Equation (5.15) can be written as

$$\mathbf{K}\mathbf{U} = \mathbf{R} - \mathbf{M}\ddot{\mathbf{U}} \tag{5.16}$$

and solved accordingly. The solution procedure is outlined in the following sections.

5.1.5.1 Static loading

When modelling the static behaviour of hybrid laminates, sinusoidally distributed pressure loads are considered in correspondence to the exact Navier type boundary conditions outlined in the previous section and Equation (5.12). This work restricts those to ones applied on the top surface $k = 1$ of the plate only. The load coefficient in Equation (5.13) then equals the maximum pressure $p_{\max}$ in the plate's centre. Consequently, the load distribution is given by

$$q_z^{1,\mathrm{top}}(x,y) = \Phi_z Q_z^{1,\mathrm{top}} = \sin\left(\frac{m\pi x}{a}\right)\sin\left(\frac{n\pi y}{b}\right)p_{\max}. \tag{5.17}$$

As inertia terms are absent under static loading, the system of equations becomes

$$\mathbf{KU} = \mathbf{R} \tag{5.18}$$

and will be solved in closed form for the generalized displacement vector $\mathbf{U}$ containing all DOFs. Following the axiomatic approach outlined in Equation (5.10) and the constitutive relation in Equation (5.8), the resulting through-thickness displacement and stress fields are calculated at desired coordinates x and y. By recommendation of Park [280], out-of-plane stress quantities are recalculated *a posteriori* by integration of the indefinite three-dimensional equilibrium equations in z-direction

$$\begin{aligned}
\frac{\partial \sigma_{xz}}{\partial z} &= -\left(\frac{\partial \sigma_{xx}}{\partial x} + \frac{\partial \sigma_{xy}}{\partial y} \right) \\
\frac{\partial \sigma_{yz}}{\partial z} &= -\left(\frac{\partial \sigma_{xy}}{\partial x} + \frac{\partial \sigma_{yy}}{\partial y} \right) \\
\frac{\partial \sigma_{zz}}{\partial z} &= -\left(\frac{\partial \sigma_{xz}}{\partial x} + \frac{\partial \sigma_{yz}}{\partial y} \right).
\end{aligned} \tag{5.19}$$

This serves as a measure to compensate for possible oscillations in the solution, especially for theories of lower order. The effectiveness of this procedure for the given material systems is outlined in Jackstadt et al. [274].

5.1.5.2 Free vibration

Free vibration in absence of any external loads is considered with the goal of determining the plate's natural frequencies, corresponding mode shapes and modal damping ratios. A generalized harmonic displacement field

$$\boldsymbol{u}\left(x, y, z, t\right) = \mathrm{e}^{\mathrm{i}\omega t}\, \hat{\boldsymbol{u}}(x, y, z) = \mathrm{e}^{\mathrm{i}\omega t} \hat{\mathbf{U}}(z) \Phi(x, y) \tag{5.20}$$

is assumed, so that the system of equations reads

$$\left(\mathbf{K}^*_{mn} - \lambda^*_{mn} \mathbf{M}_{mn} \right) \hat{\mathbf{U}}^*_{mn} = \mathbf{0} \tag{5.21}$$

and is solved for its complex eigenvalues λ^*_{mn} for each mode shape (m,n). Indices m and n indicate the present mode's number of half-waves across the plate in x- and y-directions. In the following, quantities representing an amplitude of a harmonic oscillation with regard to time t are marked by $\hat{()}$. Due to the assumptions made in Equation (5.12), the stiffness and mass matrices vary with m and n as the corresponding kernels in A.2.2 are dependent on the functions Φ_x, Φ_y and Φ_z. The damped angular natural frequency is calculated as

$$\omega_{mn} = \sqrt{\Re\left(\lambda^*_{mn}\right)}. \tag{5.22}$$

The modal damping capability of the plate is analysed on the basis of the modal damping ratio

$$\xi_{mn} = \frac{\Im\left(\lambda^*_{mn}\right)}{\Re\left(\lambda^*_{mn}\right)}. \tag{5.23}$$

The mode shapes corresponding to modes (m,n) considered hereafter are illustrated in terms of the normalized transverse displacement in Figure 5.5.

In order to consider the frequency-dependency of the viscoelastic material of the damping layers, an iterative algorithm, similar to the one presented in [165], is used to approximate the eigenvalues in Equation (5.21). The algorithm is outlined in Figure 5.6. Owing to reasons of readability, the undamped variant of Equation (5.21) is shown, but the procedure remains identical for the damped case with complex stiffness matrix.

5.1.5.3 Forced vibration

Complex valued frequency response functions (FRFs) of plates can be determined for an harmonic excitation of the structure. The method employed here and illustrated hereafter is published in Jackstadt and Kärger [275]. In this study, point loads are considered and as no exact solution exists for these loads and the chosen boundary conditions, the Navier method [103] is used, which superimposes a number of exact solutions of the Navier type, see Equation (5.10) and Equation (5.12), to approximate the solution for a point

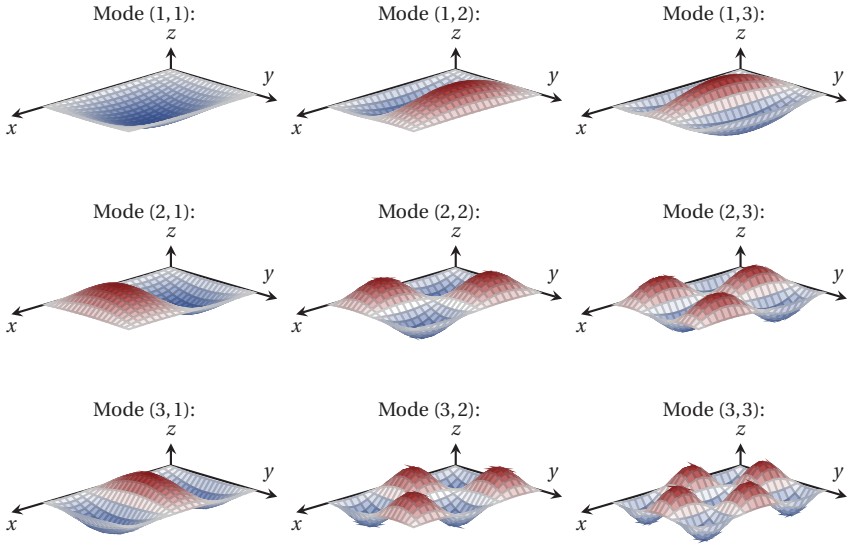

Figure 5.5: Schematic mode shapes of a simply supported plate. Red and blue colour indicate maxima and minima in the normalized transverse displacement. Reproduced from Jackstadt et al. [150].

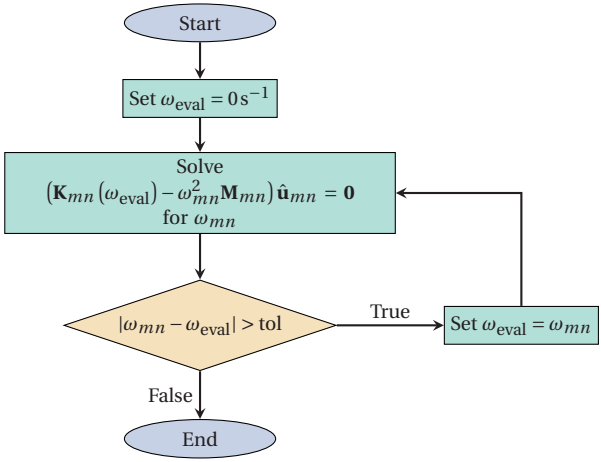

Figure 5.6: Flow chart of the iterative eigenvalue solver used for the calculation of natural frequencies [150].

load. The approximating surface load is expressed as a double trigonometric series

$$q_z^{1,\mathrm{top}}(x,y,t) = \sum_{m=1}^{\infty}\sum_{n=1}^{\infty} \hat{Q}_{mn} \mathrm{e}^{\mathrm{i}\omega t} \approx \sum_{m=1}^{M}\sum_{n=1}^{N} \hat{Q}_{mn} \mathrm{e}^{\mathrm{i}\omega t}, \tag{5.24}$$

where the load coefficient

$$\hat{Q}_{mn} = \frac{4\hat{F}_0}{ab} \Phi_z\left(x = x_0, y = y_0, m, n\right) \tag{5.25}$$

depends on m and n according to Equation (5.12). Coordinates, where the concentrated force $F_0 = \hat{F}_0 \mathrm{e}^{\mathrm{i}\omega t}$ is applied, are denoted with x_0 and y_0. Expanding the series in Equation (5.24) towards infinity will depict a concentrated force exactly. For reasons of practicality, however, a cut-off value M respectively N is defined for this model. Reasonable values for M and N have been investigated in [160] and [275]. For each value of m and n the system of equations

$$\left(\mathbf{K}^*_{mn} - \omega^2 \mathbf{M}_{mn}\right) \hat{\mathbf{U}}^*_{mn} = \hat{\mathbf{R}}_{mn} \tag{5.26}$$

is solved for the amplitude solution vector $\hat{\mathbf{U}}^*_{mn}$. The corresponding layerwise through-thickness distributions of displacement and stress fields are calculated by the superposition

$$\begin{aligned}
u_x^{*k}(x,y,z,t) &= \sum_{m=1}^{M}\sum_{n=1}^{N} \hat{U}^{*k,mn}_{x,\alpha_{u_z}} F_{\alpha_{u_z}}(z) \Phi_x(x,y,m,n) \mathrm{e}^{\mathrm{i}\omega t} \\
u_y^{*k}(x,y,z,t) &= \sum_{m=1}^{M}\sum_{n=1}^{N} \hat{U}^{*k,mn}_{y,\alpha_{u_y}} F_{\alpha_{u_y}}(z) \Phi_y(x,y,m,n) \mathrm{e}^{\mathrm{i}\omega t} \\
u_z^{*k}(x,y,z,t) &= \sum_{m=1}^{M}\sum_{n=1}^{N} \hat{U}^{*k,mn}_{z,\alpha_{u_z}} F_{\alpha_{u_z}}(z) \Phi_z(x,y,m,n) \mathrm{e}^{\mathrm{i}\omega t} \\
\sigma_{xz}^{*k}(x,y,z,t) &= \sum_{m=1}^{M}\sum_{n=1}^{N} \hat{S}^{*k,mn}_{xz,\alpha_{\sigma_{xz}}} F_{\alpha_{\sigma_{xz}}}(z) \Phi_x(x,y,m,n) \mathrm{e}^{\mathrm{i}\omega t} \\
\sigma_{yz}^{*k}(x,y,z,t) &= \sum_{m=1}^{M}\sum_{n=1}^{N} \hat{S}^{*k,mn}_{yz,\alpha_{\sigma_{yz}}} F_{\alpha_{\sigma_{yz}}}(z) \Phi_y(x,y,m,n) \mathrm{e}^{\mathrm{i}\omega t} \\
\sigma_{zz}^{*k}(x,y,z,t) &= \sum_{m=1}^{M}\sum_{n=1}^{N} \hat{S}^{*k,mn}_{zz,\alpha_{\sigma_{zz}}} F_{\alpha_{\sigma_{zz}}}(z) \Phi_z(x,y,m,n) \mathrm{e}^{\mathrm{i}\omega t}.
\end{aligned} \tag{5.27}$$

For the forced vibration analysis, the frequency range of interest is discretized, and the above solution is calculated on each frequency point. It should be noted that due to the assumed loss factor damping, the above quantities are complex valued and frequency-dependent.

5.2 Model verification and choice of theory

The analytical variable-kinematics modelling approach introduced above is verified against state-of-the-art refined 3D FEM models. In doing so, an optimal choice of expansion orders N_α is determined for the laminates considered in this work, which is to be used from here on. Furthermore, the possibility of a further reduction of DOFs by means of ESL and sublaminate approaches is explored.

As a test case, a simply supported square plate with dimensions $a = b = 100\,\text{mm}$ as shown in Figure 5.3 is considered representing a laminate C-E1-A-E1-C according to Table 4.6. The verification procedure includes comparisons of the static behaviour, the modal behaviour under free vibration as well as the steady-state behaviour under harmonic excitation or forced vibration, respectively.

5.2.1 Static loading

In the static case, a sinusoidally distributed pressure load with $m = n = 1$ according to Equation (5.17) with a maximum pressure of $\bar{p} = 0.1\,\text{MPa}$ is applied to the plate. Field quantities are evaluated in terms of through-thickness distributions at the points $A = (0.5a|0)$, $B = (0|0.5b)$, $C = (0.5a|0.5b)$ and $E = (0.125a|0.125b)$ as shown in Figure 5.3 and Table 5.1.

5.2.1.1 Investigation of higher order theories

As the GUF-based modelling approach used in this work allows for arbitrary orders of expansion of field quantities, this section is dedicated to the determination of a suitable theory for the subsequent investigations of CLD. Table 5.2 shows three fully layerwise theories up for comparison. On the one hand, theory LW^{111}_{111} offers the least amount of DOFs possible within this framework as it assumes a layerwise linear distribution of displacements and out-of-plane stresses. On the other hand, theory LW^{555}_{333} will be used a convergence limit, because no further gain in fidelity of the solution is expected for even higher orders of expansion. Theory LW^{223}_{112} is also investigated as the orders of expansion used here are more natural choices in terms of what is expected of the corresponding through-thickness distributions.

Table 5.2: Full layerwise theories with different orders of expansion for displacements u_i and out-of-plane stresses σ_{iz}.

Name	N_{u_x}	N_{u_y}	N_{u_z}	$N_{\sigma_{xz}}$	$N_{\sigma_{yz}}$	$N_{\sigma_{zz}}$
LW^{111}_{111}	1	1	1	1	1	1
LW^{223}_{112}	1	1	2	2	2	3
LW^{555}_{333}	3	3	3	5	5	5

Results generated by these theories are compared to those obtained from refined 3D FEM models solved with the commercial FE software package Abaqus/Standard 2023. For the three displacement components, these are shown in Figure 5.7. Excellent agreement with the FEM reference model is observed for the two in-plane displacement components u_x and u_y for all theories. The out-of-plane displacement in the centre of the plate, thus the deflection, however, is slightly underestimated by the analytical models. Furthermore, no differences between the theory with a linear approximation of u_z and the other two, featuring higher order approximations, can be seen.

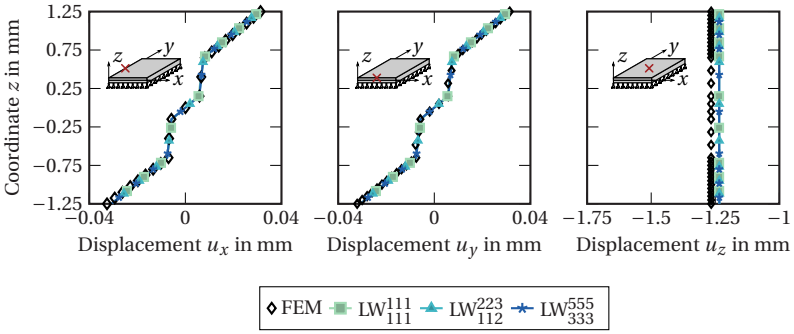

Figure 5.7: Through-thickness distributions of displacement components calculated numerically by FEM and three fully layerwise analytic models for a pressure load of $p(x,y) = -0.1\,\mathrm{MPa}\sin(\pi x/a)\sin(\pi y/b)$.

A comparison of the normal stresses is given in Figure 5.8. This serves as a verification of the constitutive relations used in the analytical model, namely the MFHL introduced in Equation (5.7). All analytical models match the FEM results exactly, thus verifying the constitutive relations.

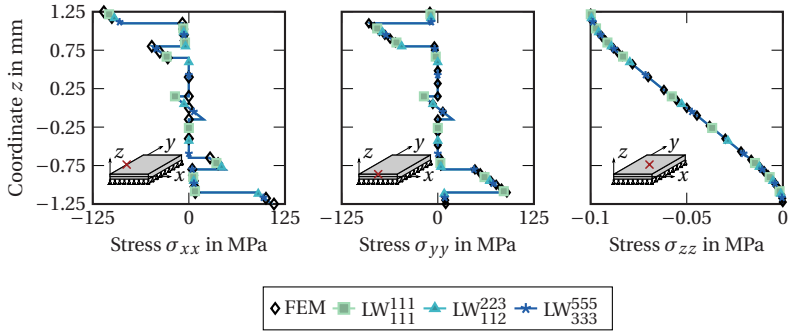

Figure 5.8: Through-thickness distributions of normal stress components calculated numerically by FEM and three fully layerwise analytic models for a pressure load of $p(x,y) = -0.1\,\mathrm{MPa}\sin(\pi x/a)\sin(\pi y/b)$.

Additionally, the transverse strain components are verified against the FEM solution in Figure 5.9, as these strains are key to analysing the CLD mechanism on a mesoscale. The two elastomer damping layers are clearly recognizable when considering the two transverse shear strains γ_{xz} and γ_{xz}, where all analytical solutions agree well with the numerical reference solution. Small differences, however, are observed for the fully linear theory LW^{111}_{111}, which overestimates the transverse shear strains of the aluminium layer in the plate's neutral plane as it assumes layerwise constant strains. This is also visible for the third out-of-plane strain component ε_{zz}.

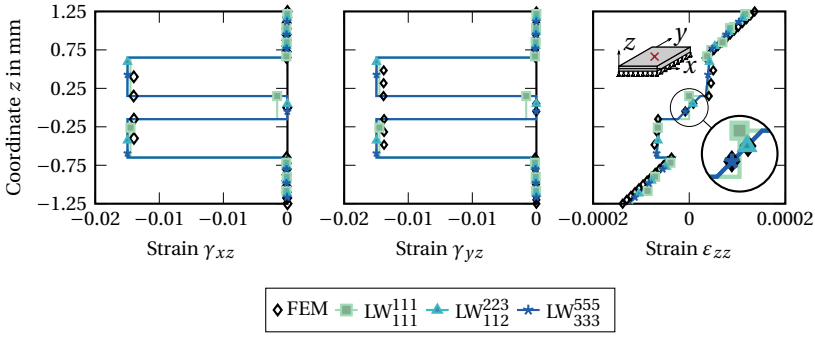

Figure 5.9: Through-thickness distributions of transverse strain components calculated numerically by FEM and three fully layerwise analytic models for a pressure load of $p(x,y) = -0.1\,\mathrm{MPa}\sin(\pi x/a)\sin(\pi y/b)$.

From this, it is concluded that theory LW^{223}_{112} is capable of resolving all field quantities in very good agreement with the reference solution generated by FEM. These orders of expansion result in a comparably low small number of DOFs, making this theory computationally efficient and thus, this theory will be used in the remainder of this work. Since through-thickness distributions of field quantities, especially the transverse deflection and out-of-plane shear strains, are depicted accurately, it is assumed that global quantities such as natural frequencies and modal damping ratios can also be calculated accurately.

5.2.1.2 Investigation of layerwise, equivalent single layer and sublaminate approaches

The feasibility of a further reduction of DOFs, and thus computational effort, by the use of ESL and sublaminate theories is assessed hereafter. Table 5.3 shows three theories, which are considered. The fully layerwise theory LW_{112}^{223} determined above as accurate, serves as a reference. Furthermore, an ESL theory ESL_{112}^{223} is considered, where only one sublaminate spans the whole laminate, meaning that each displacement component is modelled by one ansatz across all material layers k of the laminate. As stated before in Section 5.1.5, the out-of-plane stress components retain a layerwise approach. A compromise between those two theories is theory Sub_{112}^{223}, which features five sublaminates. Whereas the aluminium and elastomer plies are modelled layerwise with their own through-thickness approaches, the two stacks of CFRP plies are modelled with an ESL approach each. Notably, all theories feature the same orders of expansion N_{u_i} and $N_{\sigma_{iz}}$.

Table 5.3: Example layup with material layer index k from top to bottom, orientations θ_k, layer thicknesses t_k and sublaminate index s for layerwise (LW), sublaminate (Sub) and equivalent single layer (ESL) approaches.

Material	k	θ_k in °	t_k in mm	s_{LW}	s_{Sub}	s_{ESL}
CFRP	1	0	0.15	1	1	1
CFRP	2	90	0.15	2	1	1
CFRP	3	90	0.15	3	1	1
CFRP	4	0	0.15	4	1	1
Elastomer	5	0	0.5	5	2	1
Aluminium	6	0	0.3	6	3	1
Elastomer	7	0	0.5	7	4	1
CFRP	8	0	0.15	8	5	1
CFRP	9	90	0.15	9	5	1
CFRP	10	90	0.15	10	5	1
CFRP	11	0	0.15	11	5	1

The numbers of DOFs N_{DOF} of the three theories are listed in Table 5.4. It should be noted, that these values not only depend on the orders of expansion, but also on the laminate at hand. In this case, the eleven-layered laminate C-E1-A-E1-C is considered. The number of DOFs remaining for the sublaminate approach again depends on how different material layers are summarized in a sublaminate. In this case, eight material layers of CFRP are summarized in two sublaminates, leading to the number of DOFs listed in Table 5.4.

Table 5.4: Number of DOFs N_{DOF} for a laminate C-E1-A-E1-C for three different theories.

	LW_{112}^{223}	Sub_{112}^{223}	ESL_{112}^{223}
N_{DOF}	127	103	87

Figure 5.10 shows the through-thickness distributions of displacement components for the three theories. Theories LW_{112}^{223} and Sub_{112}^{223} yield identical results in all three cases. Theory ESL_{112}^{223}, however, fails to resolve different slopes in the individual layers, as is expected from an ESL approach. In addition, it strongly overestimates the plates overall bending stiffness as can be seen from the plate's maximum deflection in terms of displacement u_z. Owing to the homogenizing ESL approach, it fails to capture the strong mismatch in layer stiffnesses, especially of the elastomer material, leading to artificial stiffening of the structure.

The through-thickness distributions of the axiomatically modelled out-of-plain stress components determined by the three theories are shown in Figure 5.11. For all theories, the distributions are recalculated using the equilibrium relations in Equation (5.19). Again, theories LW_{112}^{223} and Sub_{112}^{223} yield identical results for all out-of-plane stress components. Notably, the ESL approach yields plausible results as well, deviating only slightly from the other two theories in case of the out-of-plane shear stresses. The transverse normal stress σ_{zz}, however, is represented accurately by the single cubic expansion across all layers.

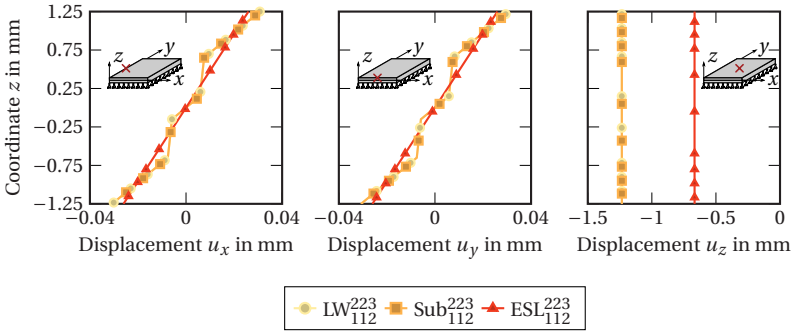

Figure 5.10: Through-thickness distributions of displacement components calculated by fully LW theory, a sublaminate based theory and an ESL theory for a pressure load of $p(x,y) = -0.1\,\text{MPa}\sin(\pi x/a)\sin(\pi y/b)$.

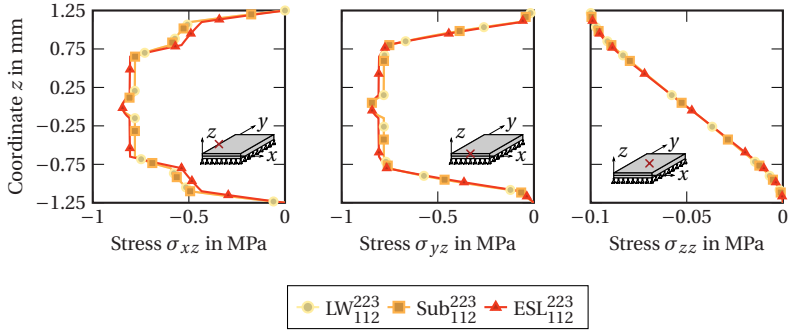

Figure 5.11: Through-thickness distributions of out-of-plane stress components calculated by fully LW theory, a sublaminate based theory and an ESL theory for a pressure load of $p(x,y) = -0.1\,\text{MPa}\sin(\pi x/a)\sin(\pi y/b)$.

Figure 5.12 shows the predictions of transverse strains for the three approaches, where the ESL theory ESL^{223}_{112} fails to capture the large transverse shear strains responsible for the CLD mechanism. The layerwise and sublaminate approaches, on the other hand, do capture those in identical ways. The transverse normal strain ε_{33} is predicted to be linear over the whole thickness by the ESL approach due to the quadratic expansion. While this suffices to predict the overall laminate compression quite well when compared to the other two approaches, it does not depict the inhomogeneous

distribution in the layers, especially the lower elastomer ply. This effect, though, is reproduced well by the other approaches. However, it should be noted that the overall out-of-plane normal strain is comparably diminutive.

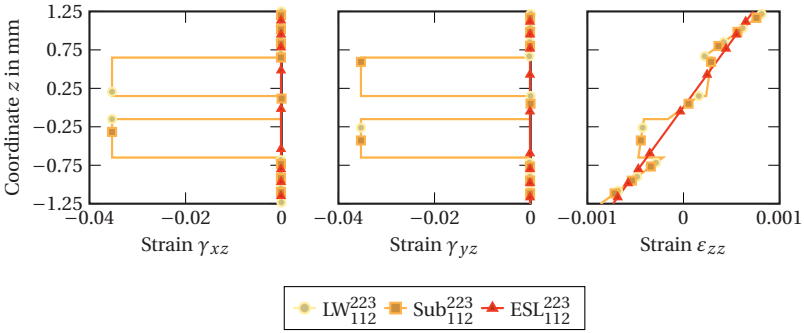

Figure 5.12: Through-thickness distributions of out-of-plane strain components calculated by fully LW theory, a sublaminate based theory and an ESL theory for a pressure load of $p(x,y) = -0.1\,\mathrm{MPa}\sin(\pi x/a)\sin(\pi y/b)$.

In conclusion, the example above shows, that a reduction of DOFs by means of a sublaminate approach is feasible, since the results obtained with a full LW approach are reproduced in an exact manner. An ESL approach, although delivering acceptable results for most field quantities, is not suitable for the analysis of FMELs with strong heterogeneity in layer stiffnesses as considered here. In particular, the overall laminate bending stiffness is shown to be greatly overestimated, so that an accurate depiction of global dynamic properties such as natural frequencies and frequency response functions is unlikely. As a consequence, only the sublaminate approach Sub^{223}_{112} is used for the remainder of this work as it requires significantly less DOFs than a full layerwise theory, but yields identical results.

5.2.2 Free vibration

Figure 5.13 shows the complex natural frequencies f and modal damping ratios ξ of the first nine vibration modes of the simply-supported plate. These are calculated using the FEM as well as analytically using theory Sub_{112}^{223} and the procedures outlined in Section 5.1.5. Quantities of $\bar{f}_{mn}$ and $\bar{\xi}_{mn}$ are calculated by only considering the materials long-term viscoelastic behaviour, whereas in case of f_{mn} and ξ_{mn}, the iterative eigensolver introduced in Section 5.1.5, see Figure 5.6, is used to capture the material's frequency-dependency. Natural frequencies and modal damping ratios are calculated non-iteratively by FEM using a constant property evaluation frequency of 0 Hz, which corresponds to the long-term viscoelastic behaviour.

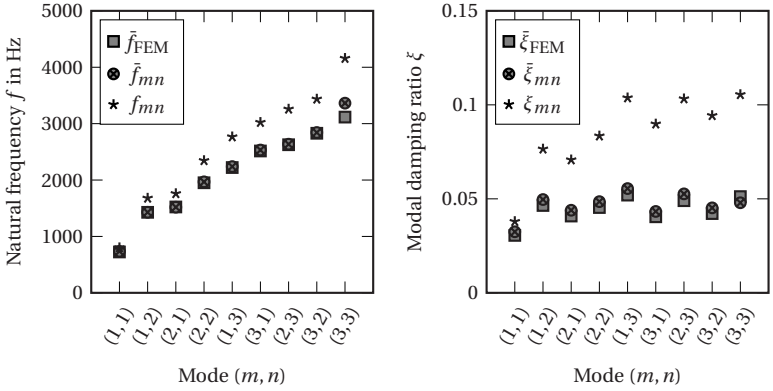

Figure 5.13: Complex natural frequencies and modal damping ratios calculated by FEM and analytically using theory Sub_{112}^{223}. For the analytical results, a comparison between using the iterative eigensolver and omitting the material's frequency-dependent properties is shown as well.

The left graph of Figure 5.13 shows, that the natural frequencies calculated non-iteratively by theory Sub_{112}^{223} match those obtained by FEM almost exactly, thus verifying the modal solution procedure. Symmetric modes such as Mode $(1,2)$ and Mode $(2,1)$ differ slightly in their natural frequencies due to the material anisotropy of the square plate. The natural frequencies f_{mn}

calculated iteratively, and thus taking into account the frequency-dependency of the material, are increasingly higher with higher modes. This is due to the increase of stiffness with frequency as seen from the storage modulus E' of the elastomer material's mastercurve in Figure 4.4. The corresponding modal damping ratios displayed in the right graph also show excellent agreement of the values calculated analytically by theory Sub_{112}^{223} and FEM. This verifies the calculation of modal damping ratios and the processing of the complex-valued constitutive relation. For the given verification example, the modal damping ratios calculated iteratively take values approximately twice as high, when the iterative eigensolver is used. The reason is again found in the elastomer's underlying mastercurve, where the loss factor $\tan(\delta)$ quantifying the material's intrinsic damping, shows a significant increase in the relevant frequency range.

To conclude, the analytical solutions procedure introduced in Section 5.1 yields natural frequencies and modal damping ratios identical to those obtained by state-of-the-art FEM simulations. Furthermore, a theory with a reduced number of DOFs due to the use of the sublaminate approach does not lead to a loss of accuracy when determining global quantities such as natural frequencies and modal damping ratios. The comparison between a conventional and an iterative procedure produces significant discrepancies, highlighting the importance of using such iterative algorithms when frequency-dependent material properties are present. This is especially true, when comparing materials with varying frequency-dependencies.

5.2.3 Forced vibration

Finally, the analytical model is verified under forced vibration. An oscillating point load with an amplitude of $\hat{F}_0 = 10\,\mathrm{N}$ according to Equation (5.25) acting on Point E (cf. 5.3) of the simply-supported plate is considered. Point E is chosen as the point of excitation, because it allows for the excitation of the majority of vibration modes as shown in [150]. The results in terms of transverse displacement amplitude and phase angle also obtained at Point

E are shown in Figure 5.14 for different cut-off values $M = N$ of the series expansion of the Navier approximation method introduced in Equation (5.24). An expansion up to order $M = N = 64$ is shown as higher orders of expansions yield identical results [275]. Results obtained by FEM are also shown for comparison.

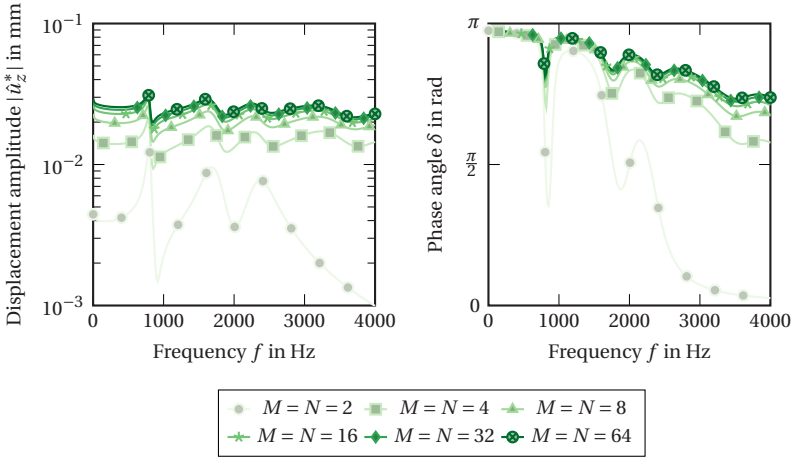

Figure 5.14: Simply-supported plate's steady-state response to harmonic excitation in Point E according to Figure 5.3. Results obtained numerically with FEM and analytically by use of the Navier method and theory Sub_{112}^{223}. Results shown for different pairs of M and N in Equation (5.25).

In the left graph, showing the transverse displacement magnitude $|\hat{u}_z^*|$, a clear convergence is visible with results obtained by $M = N = 32$ differing only marginally from those obtained by $M = N = 64$. The lowest order shown here, $M = N = 2$ does depict the lower resonance peaks, but fails to capture higher ones as higher values of M and N do. Furthermore, lower cut-off values underestimate the resulting deflection amplitude of the plate, whereas higher values of M and N lead to convergence in terms of displacement amplitude. When considering the phase angle in the right graph, differences between the higher cut-off values diminish. It is therefore concluded, that values of $M = N = 32$ suffice to capture the desired effects in FMELs in a relevant

frequency range. These values are consequently used in the subsequent studies involving forced vibration. It should be noted, that for an accurate resolution of higher frequencies and vibration modes, respectively, the Navier approximation might have to be expanded further, which does increase computational time significantly.

5.3 Analysing the damping behaviour of hybrid FMELs

5.3.1 Laminates

In the following, multiple simply supported FMEL plates are analysed with regard to their static, modal and steady-state behaviour. All analyses are conducted using the sublaminate based theory Sub_{112}^{223} and the solution procedures outlined earlier in this chapter. The plates have the dimensions $a = 150\,\mathrm{mm}$ and $b = 100\,\mathrm{mm}$ according to Figure 5.3 as these geometries will also be considered in Chapter 7. All FMELs introduced in Table 4.6 are investigated. Specifically, three different elastomer damping materials are considered in laminates of either type A-E-C-E-A or C-E-A-E-C. Furthermore, select laminate and material parameters are varied in order to give a more detailed insight into the numerous dependencies that affect the CLD mechanism.

5.3.2 Static behaviour

A sinusoidal pressure load with $m = n = 1$ according to Equation (5.17) with a maximum pressure of $p_{\mathrm{max}} = 0.1\,\mathrm{MPa}$ acting on multiple simply-supported FMELs is considered. The resulting through-thickness distributions for different laminates are shown in Figure 5.15.

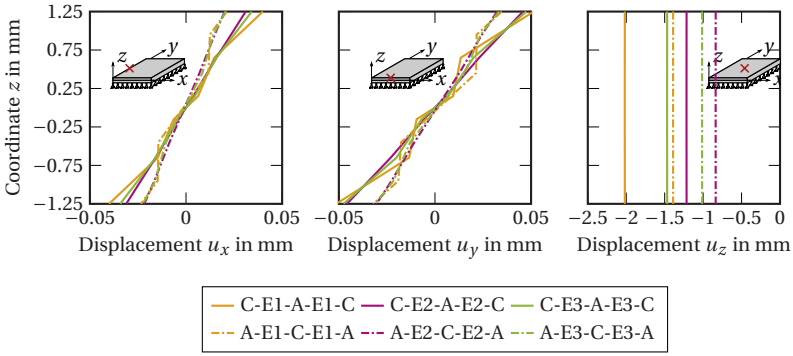

Figure 5.15: Through-thickness distributions of displacement components of six different types of FMELs calculated by theory Sub^{223}_{112}.

Upon consideration of the in-plane displacements u_x and u_y, two separate groups are distinguishable. On the one hand, laminates of type C-E-A-E-C show only marginally deviating curves and on the other hand, laminates of type A-E-C-E-A yield similar distributions. In general, laminates with the aluminium plies on the outside, show smaller displacements of the plate's edge towards the centre under the given loading as they feature the slimmer sublaminate beyond the elastomer plies. For all laminates, the choice of elastomer material influences the slope of in-plane displacement components across the thickness and is thus responsible for the distribution of the load to the other material plies. The resulting displacement u_z serves as and indicator of the plate's overall bending stiffness. Here, no clear distinction between the two laminate types A-E-C-E-A and C-E-A-E-C can be made, although when featuring the same elastomer compound, a laminate of type A-E-C-E-A is notably stiffer due to the more favourable distribution of layer thicknesses.

Figure 5.16 shows the corresponding out-of-plane stresses in the loaded plates. These are recalculated *a posteriori* from the in-plane stresses using the equilibrium equations (5.19).

Again, a clear distinction between the two types of laminates is observed. While the distributions of laminates of type C-E-A-E-C are symmetric with

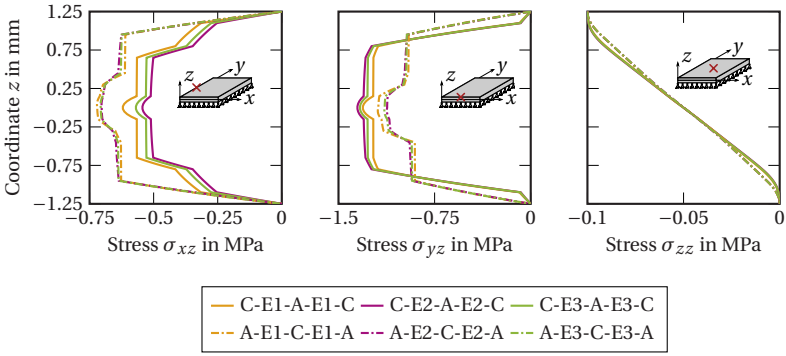

Figure 5.16: Through-thickness distributions of out-of-plane stress components of six different types of FMELs calculated by theory Sub_{112}^{223}.

regards to the plate's centre plane, those of laminates A-E-C-E-A are not, due to the nonsymmetric layup of these laminates according to Table 4.6. Furthermore, the anisotropic face sheets of laminates C-E-A-E-C lead to greater differences between transverse shear stresses σ_{xz} and σ_{yz} with regard to their overall level. The outermost layers have the predominant influence for a bending loadcase as considered here. Consequently, isotropic outer layers such as aluminium cause a more balanced distribution of the stresses. Although the choice of elastomer material has a smaller influence on the transverse stress distributions than the overall laminate layup of these FMELs, it does influence stress levels in different ways. While a stiffer elastomer, such as E2, slightly reduces both transverse shear stresses in the six CFRP plies around the centre plane of laminates A-E-C-E-A, a different behaviour is observed in laminates C-E-A-E-C, where σ_{xz} and σ_{yz} are influenced in opposing ways. In these laminates, a stiffer elastomer material reduces transverse shear stresses in the x-direction of the plate, but leads to higher transverse stresses perpendicular in y-direction, especially within the aluminium ply. With regard to the normal transverse stress σ_{zz}, no influence of the choice of elastomer material is observed. Merely the overall laminate layup has a small influence on the through-thickness distribution of the stress.

The through-thickness distributions of transverse strains are shown in Figure 5.17 for the six FMELs up for comparison. The two types of laminates are clearly distinguishable with regard to the out-of-plane shear strains by the location of the elastomer plies, which are recognized as sections with significant transverse shear strains. In all laminates, the transverse shear strains are neglectable in all other material plies than the elastomer layers. Moreover, stiffer elastomer materials such as E2 and E3 lead to significantly smaller shear strains, as is expected. Similar to what is observed for the transverse shear stresses in Figure 5.16, the shear strains in laminates C-E-A-E-C differ more in x- and y-directions than they do in laminates A-E-C-E-A due to the anisotropic nature of the outer CFRP sublaminates compared to the isotropic aluminium plies in case of laminates A-E-C-E-A. A strong dependence on laminate layup and elastomer material is also visible for the transverse normal strain ε_{zz}, although this strain component is generally small under the given load and for the materials used.

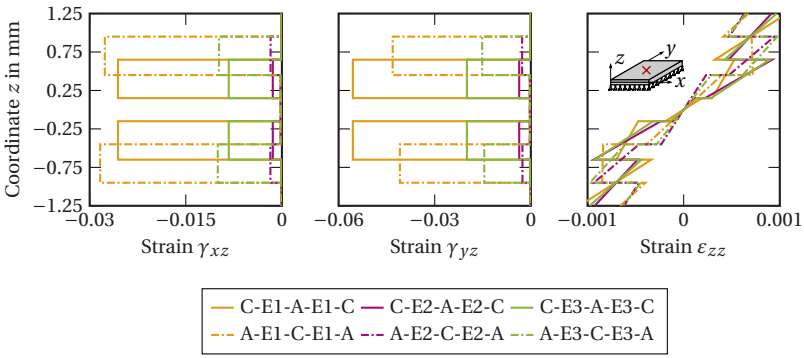

Figure 5.17: Through-thickness distributions of out-of-plane strain components of six different types of FMELs calculated by theory Sub_{112}^{223}.

The analysis of six different FMELs under static loading by means of the analytical model proposed in this work, shows that the general laminate layup has a predominant influence on the resulting stress distributions and deformation of the laminates as it dictates the transverse position of the

compliant elastomer layers within the laminate. Consequently, the choice of elastomer damping material is of secondary importance, but given the same overall layup, has a considerable influence. The two different laminate lay-ups considered here, namely C-E-A-E-C and A-E-C-E-A, however, are influenced in different ways by the choice of the elastomer material. This further highlights the complexity of the deformation behaviour of FMELs and motivates the use of fast analysis methods such as the one presented here.

5.3.3 Modal behaviour

Following the analysis of the deformation behaviour under static loading, the different FMELs are investigated regarding their modal behaviour hereafter. The simply-supported plates are allowed to vibrate freely and the corresponding natural frequencies and modal damping ratios are determined iteratively using the algorithm outlined in Figure 5.6. Thus, the frequency-dependencies of the three different elastomer compounds are taken into account. The resulting natural frequencies and modal damping ratios for the nine vibration modes (m,n) according to Figure 5.5 are graphically represented in Figure 5.18, where the modal damping ratio ξ_{mn} of a vibration mode (m,n) is plotted over the corresponding natural frequency f_{mn}. It should be noted, that the order of occurrence of these nine modes is identical for all six laminates and the given simply-supported boundary condition.

A clear distinction between laminates featuring different elastomer materials can be made. Specifically, laminates with the same elastomer material show a similar increase of modal damping ratios. The two laminates including the elastomer E1 exhibit the highest modal damping ratios and comparably low natural frequencies. The rather stiff elastomer E2 leads to the lowest modal damping ratios. The natural frequencies, however, of laminates including elastomers E2 and E3 are similar, although the inclusion of elastomer E3 leads to significantly higher modal damping ratios. These results are plausible when being compared with the elastomer materials' loss factors $\tan(\delta)$ determined by DMA in Figure 4.4, where elastomer E1 features the highest loss factor

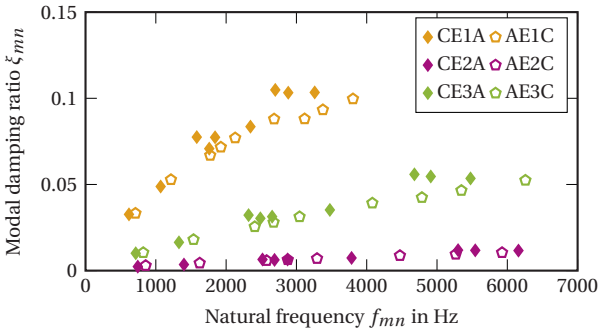

Figure 5.18: Modal damping ratio over corresponding natural frequency of six different types of FMELs calculated by theory Sub_{112}^{223} using the iterative eigensolver in Figure 5.6. Values used in this figure are listed in Table A.3.

in the frequency range under investigation, followed by elastomer E3 and elastomer E2. Regardless of the specific elastomer used in the given FMELs, laminates of type C-E-A-E-C exhibit slightly higher modal damping than their respective counterparts of type A-E-C-E-A at the cost of slightly lower natural frequencies.

As opposed to the static loading investigated above, the choice of elastomer material has the predominant influence on the modal behaviour of the FMELs considered here. While the general laminate lay-up does have an influence, it can be considered minuscule compared to the elastic properties of the elastomer damping layers.

5.3.4 Steady-state behaviour

In order to investigate the response to forced vibration, the different FMELs are excited by an harmonic force of amplitude $\hat{F}_0 = 10\,\mathrm{N}$ acting in Point E of the simply-supported plates. The structures' response is calculated as displacement amplitudes $|\hat{u}_z^*|$ and phase angles δ also in Point E and shown in Figure 5.19 for a frequency-range of 1 Hz to 2000 Hz.

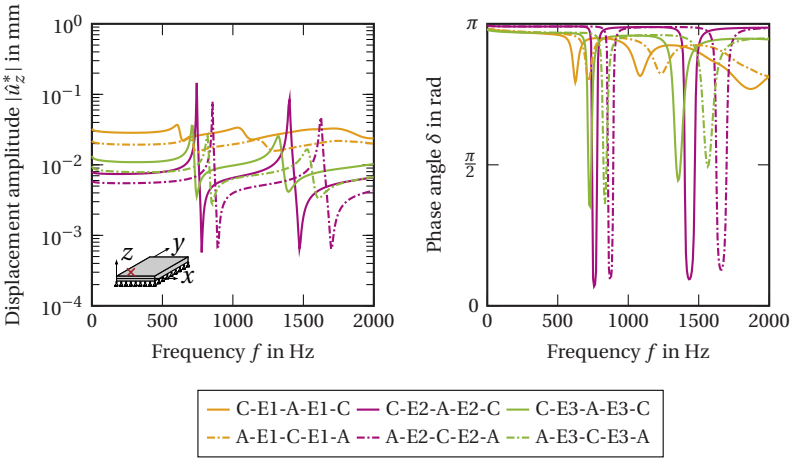

Figure 5.19: Frequency response to forced vibration of six different types of FMELs calculated by theory Sub_{112}^{223} in terms of transverse displacement amplitude and phase angle.

In the left graph of Figure 5.19, the resulting overall displacement amplitudes of the FMELs are shown. They are determined by the choice of elastomer material, in that the most compliant elastomer E1 yields the highest amplitudes. However, in the proximity of natural frequency peaks in the response curve, laminates featuring stiffer elastomers, such as E2, show the highest amplitudes. In addition, the peaks are narrower than those of laminates with more compliant damping layers, indicating smaller modal damping values. The phase angle between the applied oscillating force excitation and the recorded displacement is shown in the right graph. Excited vibration modes can be identified by a shift in the phase angle δ of π or less, depending on how strongly the mode is damped. Consequently, higher modal damping factors lead to a smaller shift in phase angle. For higher excitation frequencies, the distinct modes become harder to identify, especially for laminates featuring the very compliant elastomer E1. Generally, the considered plates are strongly damped in this example due to their relatively small in-plane dimensions compared to the laminate thickness.

The results presented for the forced vibration of the six FMELs are coherent with the findings obtained in the preceding modal analyses. They confirm, that the choice of elastomer material not only dictates the overall level of vibration damping, but also the structures' dynamic stiffness expressed by the resulting displacement amplitudes. In contrast to the findings obtained under static loading in Section 5.3.2, the overall laminate lay-up has comparably small influence.

5.3.5 Influence of damping layer properties

The results presented in the preceding sections show a paramount dependence of the vibration and damping behaviour seen in FMELs on the elastomer material used in the damping layers. However, these results only take into consideration the three commercially available elastomer compounds of the KRAIBON® range. Since elastomers offer not only an enormous variety of mechanical properties [271], often adjusted by the addition of fillers [281], but also vary strongly with temperature, the following section is dedicated to the closer investigation of the influence of the elastomer layers' properties on the CLD mechanism. In addition, the laminates' structures offer endless possibilities regarding stacking sequences and layer thicknesses, enlarging the parameter space available for the design of CLD applications in hybrid FMELs. Especially the thickness of elastomer layers is easily adaptable either by obtaining sheets calendered to the specified thickness from the manufacturer or stacking several sheets in-mould [230].

5.3.5.1 Influence of elastomer stiffness

In order to investigate the influence of the elastomer material's elastic stiffness on the CLD mechanism, the previously considered three elastomer compounds are scaled by a stiffness scaling factor. The scaling factor κ_{E^*} is applied to the complex Young's modulus of the elastomer materials,

$$\tilde{E}^*(\omega) = \kappa_{E^*} E^*(\omega) = \kappa_{E^*} \left(E'(\omega) + \mathrm{i} E''(\omega) \right), \tag{5.28}$$

so that the material damping expressed by the material's loss factor $\tan(\delta)$, see Equation (2.36), remains unchanged. This allows for an isolated investigation of stiffness variation without changing the dissipative capabilities of the damping material.

Figure 5.20 shows the influence of stiffness variation on laminate types C-E-A-E-C and A-E-C-E-A with the underlying mastercurve of elastomer E1, which is the most compliant one of the three compounds considered in this work. It also features a high material damping as seen from the loss factor curve in Figure 4.4. The upper two graphs compare the natural frequencies for nine vibration modes relative to the reference laminates C-E1-A-E1-C and A-E1-C-E1-A, respectively.

In general, the vibration characteristics of both types of laminates are influenced in a very similar way by the stiffness variation of elastomer E1. A stiffening of the damping plies in both cases leads to higher natural frequencies with higher modes experiencing larger shifts. Reducing the stiffness, however, decreases this mode dependency. Decreasing as well as increasing the stiffness of the damping layers only shows an effect in a certain range, with convergence towards a plateau visible in both directions. A different influence is seen when considering the modal damping ratios, which again behave similarly for both types of laminates. All of the nine modes considered here exhibit a distinct maximum in their modal damping ratio within the range of the scaling factor κ_{E^*}. The maximum modal damping of each mode is obtained at different values of κ_{E^*}. While the higher modes don't exceed the damping achieved in the reference configuration ($\kappa_{E^*} = 1$), a significant increase in modal damping can be reached for the first two vibration modes by using a more compliant elastomer. For the given plate dimensions and the elastomer E1, an optimum in modal damping seems to

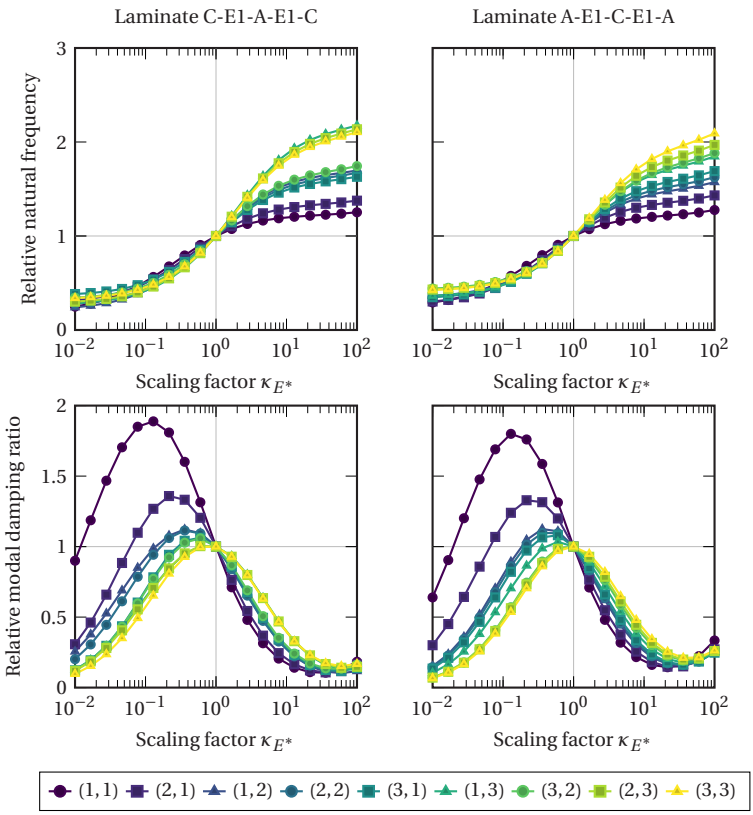

Figure 5.20: Relative natural frequencies and modal damping ratios for laminates C-E1-A-E1-C and A-E1-C-E1-A with varied complex stiffness in terms of κ_{E^*}. Results iteratively calculated by theory Sub_{112}^{223}.

The same study is again conducted for both types of laminates with the mastercurve of elastomer E2 being scaled. As previously shown and visible in Figure 4.4, this elastomer compound is the stiffest one in the relevant frequency range of 1 Hz to 10^4 Hz and features the lowest loss factor $\tan\delta$. The relative natural frequencies and modal damping ratios obtained for a stiffness variation of 10^{-2} to 10^2 are shown in Figure 5.21 for the two types of laminates.

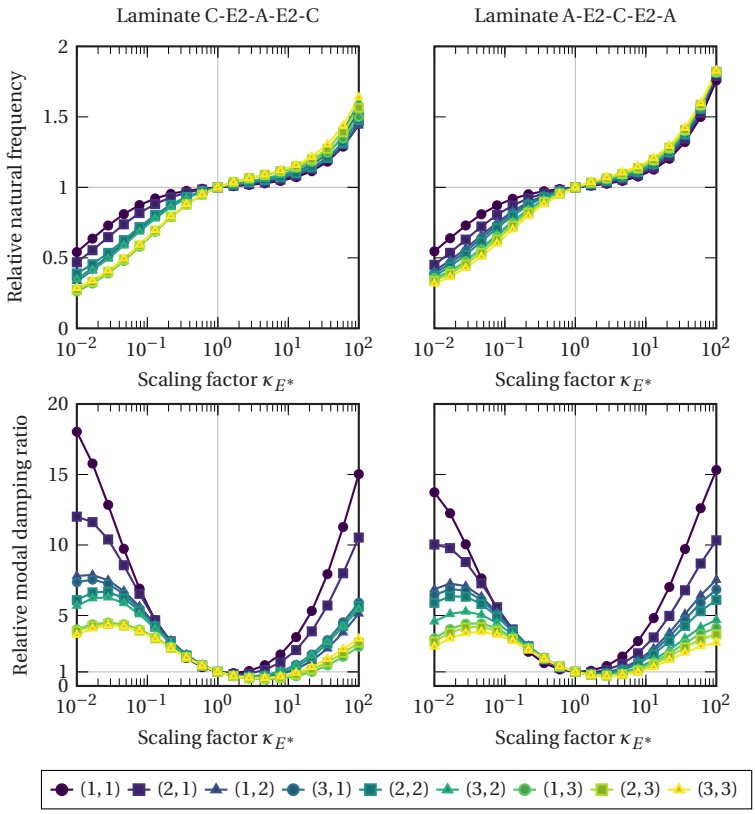

Figure 5.21: Relative natural frequencies and modal damping ratios for laminates C-E2-A-E2-C and A-E2-C-E2-A with varied complex stiffness in terms of κ_{E^*}. Results iteratively calculated by theory Sub_{112}^{223}.

A stiffening of the elastomer E2 leads to an increase of the natural frequencies in both laminates, which is slightly more pronounced in laminate type A-E2-C-E2-A. As opposed to the previous example, almost no mode dependency is observed for laminates with a stiffened elastomer E2. The decrease in natural frequencies caused by values of $\kappa_{E^*} < 1$, however, is slightly more pronounced for higher modes than it is for the lower modes. Another difference to the previous example involving a variation of the mastercurve of elastomer E1,

is the fact that neither very low nor very high values of κ_{E^*} lead to a plateau in the relative natural frequencies. On the contrary, an increase in slope is observable for increasing values of κ_{E^*} for both types of laminates. The relative modal damping ratios shown in the bottom graphs, again, show a strong dependency on the corresponding vibration mode and exhibit similar behaviour for both types of laminates. Modal damping ratios of the lower modes benefit the most from either an increase or a decrease in elastomer stiffness for the given case, in which a configuration close to the reference configurations with $\kappa_{E^*} \approx 1$ offer the lowest modal damping for almost all of the nine vibration modes. With exception of the first two vibration modes, a maximum in modal damping is reached for values of $\kappa_{E^*} \approx 0.03$.

A number of conclusions are obtained from the stiffness variation of the elastomer layers conducted above. First, the overall laminate layup is shown to be of neglectible influence on the modal damping ratios and natural frequencies when compared to the influence of the elastomer stiffness. This confirms previously obtained findings on the vibrational behaviour in Section 5.3.3. Second, a change in elastomer stiffness has a larger effect on the modal damping ratios than on the natural frequencies. While the natural frequencies change monotonously with the elastomer stiffness, in that they increase for a stiffer elastomer, the modal damping ratios show distinct maxima and minima. Notably, a more compliant elastomer does not necessarily lead to higher modal damping. The vibration modes investigated here all show the same tendencies in modal damping ratios over elastomer stiffness, but differ in the extent. Lower modes experience a stronger increase in modal damping ratios than higher ones do, when the elastomer stiffness is chosen accordingly. The fact, that two different elastomers and their respective mastercurves are varied in stiffness, and the minima and maxima in modal damping ratios are obtained by different values of the scaling factor κ_{E^*}, suggests that for the given simply-supported plate a correlation can be made.

As seen in Figure 4.4, the elastomers E1 and E2 differ in stiffness approximately by a factor of ten. When comparing the location of the minima in modal damping ratios for the laminates based on the two different elastomers in Figure 5.20 and Figure 5.21, these are also set apart by a factor of ten. This suggests that for the given laminates and plate dimensions, one or more optimum stiffnesses of the elastomer layer exist, with which the highest modal damping is achieved. As seen from the two figures, this can even be accompanied by an increase in natural frequency, thus a higher overall plate stiffness.

5.3.5.2 Influence of elastomer layer thickness

Subsequent to the influence of elastic stiffness of the elastomer, the influence of damping layer thickness is investigated in this section. In order to do so, the elastomer layer thickness t_{El} of laminates of type C-E-A-E-C and A-E-C-E-A with elastomers E1 and E2 are varied according to

$$\tilde{t}_{\mathrm{El}} = \kappa_t \, t_{\mathrm{El}} \tag{5.29}$$

with κ_t being the scaling factor ranging from 1×10^{-1} to 1×10^{1}. The initial elastomer thickness t_{El} is taken to be 0.5 mm in accordance with the previously analysed hybrid FMELs. The resulting relative natural frequencies and modal damping ratios relative to the reference laminates C-E1-A-E1-C and A-E1-C-E1-A are shown in Figure 5.22.

The upper two graphs compare the relative natural frequencies of the two laminate types featuring elastomer E1. Both have in common that an increase in the elastomer layer's thickness has a higher influence of the lower modes. Higher modes even experience a slight decrease in their natural frequencies for higher values of κ_t. Accordingly, such modes also see an increase in their natural frequency for thinner elastomer plies. The relative modal damping ratios shown in the lower two graphs of Figure 5.22 feature a more uniform trend, in that thicker elastomer plies always lead to higher modal damping

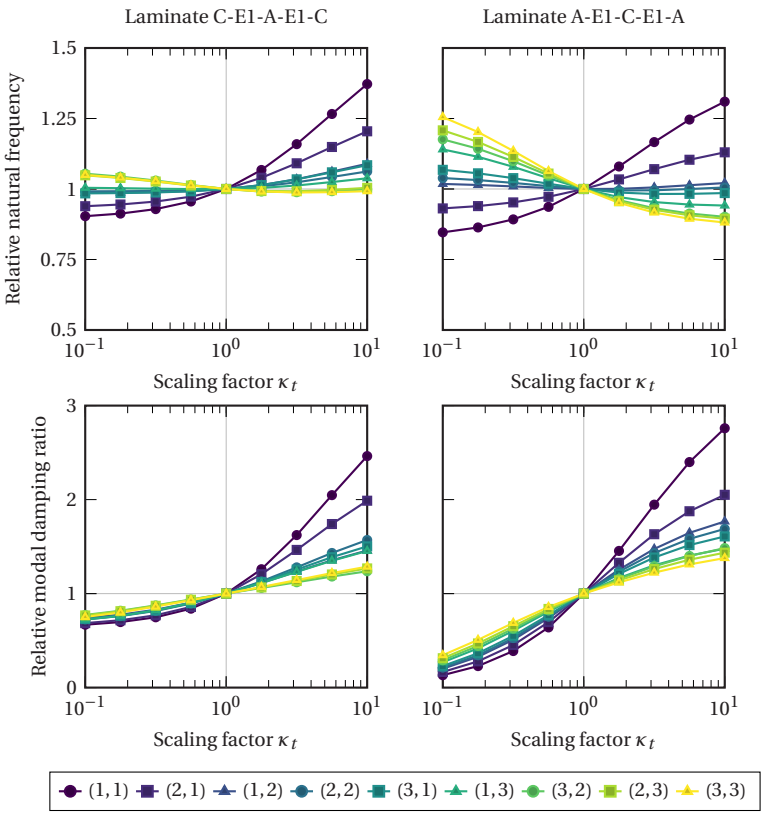

Figure 5.22: Relative natural frequencies and modal damping ratios for laminates C-E1-A-E1-C and A-E1-C-E1-A with varied elastomer thickness. Results iteratively calculated by theory Sub_{112}^{223}.

ratios. This is the case for both laminates, although laminate A-E1-C-E1-A, with the affected elastomer layer lying further outside, exhibits a stronger decline in modal damping than laminate C-E1-A-E1-C, which reaches a plateau for thin elastomer plies. As previously seen for a variation in elastomer stiffness, the variation of elastomer ply thickness influences the lower modes stronger than higher ones. This holds true for both, natural frequencies and modal damping ratios.

The corresponding results for laminates containing elastomer E2 as a reference are shown in Figure 5.23. The relative natural frequencies and modal damping ratios differ only marginally between laminate C-E2-A-E2-C and A-E2-C-E2-A, with the latter one exhibiting slightly higher changes. For elastomer ply thicknesses smaller than the reference, $\kappa_t = 1$, a plateau is reached, where natural frequencies and modal damping ratios remain at a minimum. By increasing the ply thickness, however, a substantial gain in modal damping is achieved. This is again more pronounced for the lower vibration modes than it is for the higher ones.

In conclusion to the results presented above, thicker elastomer plies always lead to higher modal damping for the laminates considered here with a decreasing effect for higher vibration modes. The achievable amount of increase in modal damping shows a higher dependency on the stiffness and thickness of the elastomer material than on the overall laminate layup as has been shown for the four laminates considered here.

5.3.6 Generalisation for arbitrary CLD laminates

The previous Sections 5.3.5.1 and 5.3.5.2 have shown that the properties of the damping layers within the FMELs have a tremendous influence on the modal damping capabilities. In particular, Section 5.3.5.1 highlights the fact, that the choice of elastomer stiffness is crucial for achieving maximum modal damping, which does not necessarily coincide with a more compliant material. Whereas only a neglectable dependence on the overall laminate layup was shown, Section 5.3.5.2 uncovers the influence on the elastomer ply thickness on the CLD. These parameter variations, however, only take into account the FMELs considered in this work, i.e., laminates which contain aluminium and CFRP plies in addition to the studied elastomers. Consequently, this section aims at the generalization of the results obtained above to the CLD mechanism in the wider sense. Specifically, stiffness and thickness of the damping ply is expressed relative to the constraining layers instead of being expressed as absolute values. As the results presented

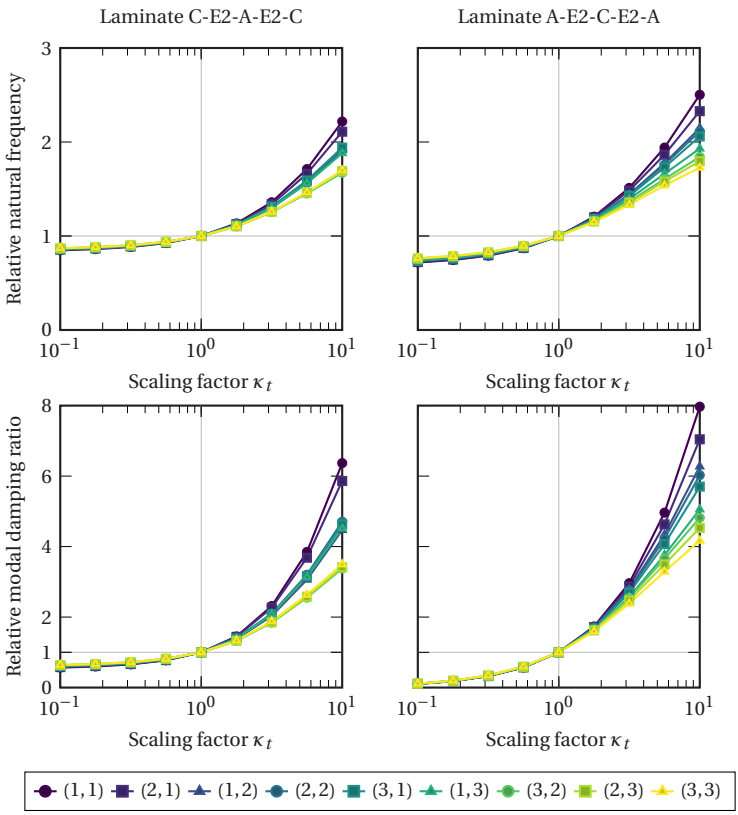

Figure 5.23: Relative natural frequencies and modal damping ratios for laminates C-E2-A-E2-C and A-E2-C-E2-A with varied elastomer thickness. Results iteratively calculated by theory Sub_{112}^{223}.

above indicate, that the overall laminate layup is of minor significance, this section considers a simplified CLD laminate consisting of only three layers, in particular two linear elastic isotropic constraining layers and one viscoelastic constrained damping layer with no frequency dependence. The constraining layers are assumed to have the linear elastic properties of aluminium as listed in Table 4.1 and a thickness of $t_{\text{constraining}} = 0.3\,\text{mm}$. The storage and loss moduli of the constrained layer are calculated relative to the constraining

layers and are assumed to have a constant, thus frequency-independent, loss factor $\tan(\delta) = 0.1$. The plate's dimensions are again taken as $a = 150\,\text{mm}$ and $b = 100\,\text{mm}$. It should be noted, that previous studies have shown no unexpected size effects regarding the plate's external dimensions.

Figure 5.24 shows the absolute natural frequencies and modal damping ratios of the introduced simplified CLD laminate. Specifically, the values for the first vibration mode, Mode $(1,1)$, are shown as this mode has shown the highest sensitivity to changes of the elastomer damping layer in the previous sections. The graphs show the stiffness of the constrained damping layer $\left|E^*_{\text{core}}\right|$ relative to the stiffness of constraining layers E_{face} on the horizontal axis and the thickness of the constrained damping layer t_{core} relative to the thickness of constraining layers t_{face} on the vertical axis, thus creating heat maps for the natural frequency and modal damping ratio of Mode $(1,1)$.

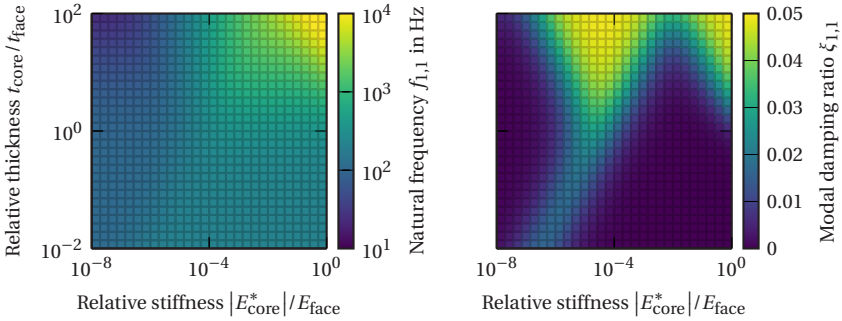

Figure 5.24: Natural frequencies and modal damping ratios of Mode $(1,1)$ for a generic three-layered CLD laminate with varying relative stiffness and layer thickness. Results calculated by theory LW^{223}_{112}. Note: Natural frequencies (left) are colour-coded logarithmically in order to clearly show minima and maxima.

The natural frequency shown in the left-hand side graph of Figure 5.24 exhibits a clear maximum in the top right corner corresponding to the thickest and stiffest elastomer layers. A minimum is seen in the top left corner for the most compliant but thickest elastomer plies. Furthermore, the influence of the

material's stiffness decreases with thinner constrained layers. Considering the natural frequency $f_{1,1}$ as an indicator for the plate's structural stiffness, these correlations are in line with expectations.

For the given case, values achieved for the modal damping ratio $\xi_{1,1}$ range from 0.0 to 0.05. Almost no modal damping is achieved for very thin damping layers or a damping material which is too compliant. In both cases, not enough deformation or stress is transmitted to the damping material, thus not much energy compared to the overall deformation energy can be dissipated. The highest modal damping is reached for damping plies significantly thicker than the constraining layers. The exact relative thickness, which is necessary to achieve the maximum in modal damping, depends on the choice of relative stiffness. For damping materials, which are three or four magnitudes less stiff than the constraining layers, thinner damping plies can be chosen. This is desirable in lightweight design as less damping material is required to achieve the same amount of modal damping. The top right of the heat map also shows high modal damping values, when constrained and constraining layers are equally stiff and the viscoelastic core layer is comparably thick. This, however, is not considered CLD, but is simply attributed to the intrinsic viscoelastic material damping of the damping material, which in this case makes up of the majority of the laminate.

From a simplified perspective, the damping capabilities of the FMELs of this work can be found in Figure 5.24. With an elastomer layer thickness of 0.5 mm and constraining layer thicknesses of 0.3 mm for the aluminium plies or between 0.6 mm and 0.9 mm for the CFRP sublaminates, a thickness ratio of $t_{\mathrm{core}}/t_{\mathrm{face}} \approx 1$ is given for the different types of FMELs. Laminates containing the highly compliant elastomer E1 as their constrained damping layer thus feature a stiffness ratio of $\left|E^*_{\mathrm{core}}\right|/E_{\mathrm{face}} \approx 1 \times 10^{-4}$ according to Table 4.1, Table 4.2 and Figure 4.4. FMELs based on the stiffer elastomer compound E2, however, feature a higher ratio of $\left|E^*_{\mathrm{core}}\right|/E_{\mathrm{face}} \approx 1 \times 10^{-3}$. From the heat map in Figure 5.24, a modal damping ratio for the FMELs containing elastomer E1 of approximately 0.03 can be read. Analogously, for FMELs featuring elastomer E2, this simplified model predicts a modal damping ratio between zero and

0.01. These values correspond very well with those obtained in Section 5.3.3 and shown in Figure 5.18, respectively.

In summary, this study on a simplified CLD laminate confirms the assumptions made above, that the ratios of constrained layer properties are crucial in achieving optimal modal damping. Furthermore, this can greatly simplify the design process of CLD structures as materials and ply thicknesses can be determined based on the ratios determined above. This also motivates the development of even simpler models for the prediction of modal damping based solely on ratios. In addition, the results highlight the importance of employing predictive models, such as the one proposed in this work, as the maximum modal damping is not always achieved by the most compliant materials and large ply thicknesses. Specifically, a lightweight CLD structure can profit from the fact, that optimal damping can be achieved by selecting materials with specific stiffness ratios at the lowest possible thickness ratio, thus ensuring a minimal use of damping material. In particular, configurations offering high modal damping do not necessarily coincide with the configurations offering the lowest structural stiffness.

5.4 Discussion and concluding remarks

In this chapter, an analytical model based on the GUF is proposed for the analysis of laminated plates. The model uses a layerwise description of displacement and out-of-plane stress components and is enhanced by a sublaminate approach which allows for an ESL description of adjacent and similarly stiff layers within the global LW model. The model accurately reproduces results obtained by 3D full-field FEM models for static loading as well as forced and free vibration. A slight discrepancy of the results with regard to the absolute deflection is attributed to the handling of an almost incompressible material within the FEM solution procedure, see [282]. A fulfilment of Objective 1-1 is therefore given. In a convergence study, the optimal orders of expansion for the six modelled field quantities

are determined. This further reduces the model's number of DOFs significantly when compared to similar variable-kinematics approaches such as the CUF [105] or GUF [137] introduced in Chapter 2 without any loss in accuracy for the given laminates. These findings are coherent with those published in [165] for a similar sublaminate based approach. ESL approaches, as pointed out in [114, 116], are shown not to accurately describe the behaviour, not even in terms of global quantities such as total bending deflection, of FMELs containing compliant damping layers. It should be noted at this point, that the assumption of geometric linearity might be exhausted when predicting the transverse strain field within the compliant elastomer plies. These can consequently be used for qualitative comparisons of different laminates as done in Section 5.3.2, see Figure 5.17, but quantitative statements should be carefully questioned. In order to take into account the experimentally determined frequency-dependent material properties of the elastomer materials, see Section 4.1.3, in modal analysis, an iterative eigensolver is proposed and implemented. This allows for more accurate comparisons of laminates containing different elastomer materials with varying frequency-dependencies. The proposed model in its current formulation is limited to the analysis of simply supported plates. An extension to different boundary conditions, such as clamped or free, is considered feasible. Instead of the exact Navier type solution used in this work, the approximating Ritz method [283] could be used. This method has previously been applied to variable kinematics plate problems [284] and sublaminate based theories [142].

In the light of Objective 1-2, the proposed model is used to analyse different FMELs regarding their static deformation behaviour, modal characteristics and response to forced vibration. A comparison of the different laminate types, namely those featuring either aluminium or stacked CFRP plies on the outside, and elastomer damping materials is conducted. The results presented show that, while the static behaviour in terms of total bending deflection is predominantly dictated by the general type of laminate lay-up, the modal damping is determined by the elastomer material used. This has

been observed in the previously introduced work by Sessner et al. [228] in experimental modal analysis on the same FMELs, although under different boundary conditions, and thus confirms the trends seen with the analytical model. While the different boundary conditions certainly do have an effect on the absolute modal damping values, general trends and comparisons are expected to remain untouched by this, which has previously been shown in literature [155, 228]. This effect offers the possibility of designing CLD laminates, which offer high bending stiffness under static loading while also being highly damped under vibration. Confirmation is given by the results from forced vibration, see Figure 5.19, where laminates of type A-E-C-E-A show smaller dynamic deflections than those of type C-E-A-E-C, but at the same time show comparable damping, when featuring the same elastomer. Nevertheless, the layup-type still has an influence on the laminates' damping behaviour, as shown in Figure 5.18 and Figure 5.19. Especially when taking into consideration higher modes, laminates of type C-E-A-E-C show slightly higher damping values. Again, the previous research by Sessner et al. [227] and Sessner [230] also shows this effect based on experimental work on the same laminates. Based on the experiment alone, one possible explanation could be given by the viscoelasticity of the CFRP, which is not only present in a higher volume ratio in laminates C-E-A-E-C, but also located further on the outside, thus undergoing higher strains. In this analytical work, however, the CFRP plies are modelled in absence of any viscous contributions. Instead, the origin of differences in damping values can be found in the ratio of constraining layer to constrained layer and location of the elastomer ply within the laminate. Zhang and Chen [178] proclaim in their work a face layer thickness slightly thinner than the central layer to be optimal in a similar laminate layup with two damping plies. Transferred to the laminates considered here, this ratio is rather given by laminate C-E-A-E-C than laminates A-E-C-E-A resulting in higher shear deformation of the constrained layers. In case of laminates A-E-C-E-A, the thinner face layers are constricted in their confining capability on the damping layers' shear deformation resulting in lower loss factors.

Further investigations on the influence of elastomer damping layer properties are carried out as parametric studies in order to address Objective 1-3 of this thesis. A variation of the elastomers' complex stiffness while maintaining a constant material damping shows the existence of an optimal elastomer stiffness for maximum damping, see Figure 5.20 and Figure 5.21. Similar curves are obtained by Wang et al.[162] for CLD treated CFRP laminates, who also report the mode-dependency of the optimal damping layer stiffness seen in the present work. To the author's knowledge outlined in Chapter 2, no other publications exist reporting similar findings. The maximum in modal damping for an optimal elastomer layer stiffness is attributed to the resulting ideal transverse shear strain pattern produced inside the dissipating damping layers by transferring just enough load to the underlying stiff centre sublaminate to create maximum shear. An increase of the elastomer layers' thickness in both laminate types results in increased modal damping as shown in Figure 5.22 and Figure 5.23. This is observed in the early work of Saravanos and Pereira [158], who also report this continuous increase for different laminates. The works of Sher and Moreira [179], Wang et al. [162] and Wang et al. [182], however, report the existence of an optimal damping layer thickness. Accordingly, a decrease in modal damping is shown for very thick damping layers. This effect is not reproduced for the laminates investigated here. An explanation is given by Sher and Moreira [179], who reveal, that the optimal damping layer thickness depends on the aspect ratio of the plate as well as on the thickness of constraining sublaminates and not always does an optimum exist. Indeed, for the plate and laminate dimensions analysed here, the presence of an optimum is not expected.

In conclusion, the proposed modelling approach reproduces the experimental findings on the studied FMELs provided by the works of Sessner et al. [222, 227, 228, 230]. The experimental characterisation techniques are therefore complemented and extended by an efficient modelling approach allowing for the analysis of further laminates and materials without the discussed cumbersome characterisation procedures addressed in [229]. The findings are coherent with those produced by other authors for a variety of different

material systems, boundary conditions and laminate lay-ups. Furthermore, the model, opposed to the commonly used RKU model, gives a more detailed insight into the deformation on a mesoscale while being able to not only depict modal behaviour but also static loading and forced vibration. The previously mentioned limitations of the RKU model regarding very thin and very thick layers are consequently lifted. The Objectives 1-1 to 1-3 of this thesis are considered fulfilled.

6 The Mullins effect in constrained-layer damping laminates

6.1 Experimental characterisation of the Mullins effect

6.1.1 Methods

This section addresses the experimental characterisation of the Mullins effect. On constituent level, Section 6.1.1.1 introduces the experimental procedures employed to characterise the Mullins effect on neat elastomer specimens. On a laminate level, Section 6.1.1.2 outlines the experimental test setup for investigating the Mullins effect in simplified CLD laminates.

6.1.1.1 Characterisation on constituent level

In above Figure 4.1 of Section 4.1.3, results of uniaxial tensile tests are presented for the three elastomer compounds subject to this work. These indicate large elastic strains resembling hyperelastic behaviour in the case of elastomers E1 and E3. Elastomer E2, however, also being the stiffest, fails at much lower strains and thus avoids the large strain regime entirely. The Mullins effect, generally considered a large-strain phenomenon, is consequently not expected to occur in elastomer E2. Therefore, this chapter

solely focuses on elastomers E1 and E3. Relevant dependencies and further aspects, which need to be accounted for in a numerical model are to be determined.

The basic characterisation of the Mullins effect is done in uniaxial tension. Dumbbell specimens of Type C according to ASTM D412-16 [270] are punched from consolidated neat elastomer plies, see details in Section 4.2, of thickness 2 mm using a die. The tests are then conducted on a universal testing machine zwickiLine by ZwickRoell GmbH & Co. KG equipped with a load cell featuring a maximum load capacity of 2.5 kN. The strain is determined from the machine's crosshead displacement and no additional strain gauges are employed.

At first, the two elastomers E1 and E3 are tested in cyclic uniaxial tensile tests. A constant strain rate of $\dot{\varepsilon} = 10^{-3}\,\mathrm{s}^{-1}$ is chosen in order to mitigate viscoelastic, thus rate-dependent, effects as much as possible. The specimens are uniaxially strained to a defined stretch

$$\lambda_1 = \frac{l}{l_0} \tag{6.1}$$

and then unloaded until the load cell measures zero force. The stretch $\lambda_1^{\max}$ to which the specimen is extended in each cycle is increased with each cycle, so that values of 1.1, 1.2, 1.4 up to 1.8 are reached. The characteristics of the Mullins effect are then compared between the two materials.

By the example of elastomer E1, the same experiment is repeated with an increased strain rate of $\dot{\varepsilon} = 10^{-2}\,\mathrm{s}^{-1}$, thus ten times as fast, in order to investigate a possible rate-dependency of the Mullins effect. In addition, a further study on elastomer E1 is conducted aiming at the investigation of a possible evolution of the Mullins effect at repeated cycles (cyclic softening as reported in [61, 48]) to constant strains. In this case, ten loading and unloading cycles to a maximum stretch of 1.2 are followed by another ten cycles to 1.4. This is conducted at a strain rate of $\dot{\varepsilon} = 10^{-2}\,\mathrm{s}^{-1}$ to accelerate the lengthy experiment. Owing to limited material availability, these studies are constrained to elastomer E1.

For the evaluation of the experiments outlined above, the following metric is proposed. First, a measure for the softening of the material is defined. Softening, in this study, is defined using a relative secant modulus upon reloading

$$\alpha_{\text{soft}} = \frac{E_{\text{s}}\left(\lambda_1^{\max}\right)}{E_{\text{s}}\left(\lambda_1 = 1\right)}. \tag{6.2}$$

with the secant modulus E_{s} being the ratio of engineering stress increment and engineering strain increment

$$E_{\text{s}} = \frac{\Delta\sigma}{\Delta\varepsilon} = \frac{\sigma\left(\varepsilon = 2\,\%\right) - \sigma\left(\varepsilon = 0.01\,\%\right)}{2\,\% - 0.01\,\%} \tag{6.3}$$

in the range of 0.01 % to 2 %. Notably, the stress increment in Equation (6.3) depends on the previously maximum stretch $\lambda_1^{\max}$ if a Mullins effect is present. Only loading and reloading paths are used for measuring the softening. Consequently, the softening parameter α_{soft} takes the value of 1 for a previously unloaded specimen and decreases in the presence of softening. Furthermore, permanent set, as introduced in Chapter 2, is quantified as the amount of engineering strain remaining as soon as the specimen is fully unloaded to the point of no stress acting on the specimen. Naturally, this evaluation is conducted only for unloading paths.

6.1.1.2 Characterisation on laminate level

In order to determine a possible influence of the Mullins effect in CLD applications, DMA experiments of predeformed laminates are conducted. Simplified CLD laminates are studied within this chapter to eliminate any other viscoelastic effect contributed by the CFRP layers. In particular, laminates A-E1-A and A-E2-A, cf. Table 4.6, are considered. As outlined in Chapter 4, these have been manufactured with a thicker, 2 mm instead of 0.5 mm, elastomer layer to increase their bending stiffness. The specimens have a length of a = 100 mm and a width of b = 15 mm at a total thickness of t = 2.6 mm. The DMA is conducted within a three-point bending setup

with a support distance of $l_{\mathrm{spt}} = 62\,\mathrm{mm}$ on an Instron® E3000 ElectroPuls® electrodynamic testing machine by llinois Tool Works Inc. A load cell with a capacity of 5 kN is used to measure the nominal dynamic force. The supports as well as the load fin have a radius of 10 mm. The specimen dimensions and experimental setup are illustrated in Figure 6.1.

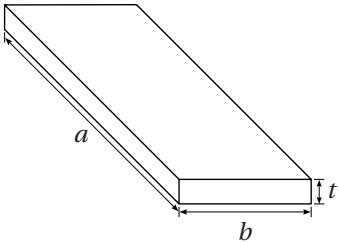

(a) Specimen dimensions

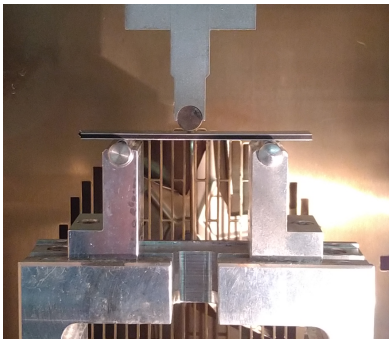

(b) Bending setup

Figure 6.1: Experimental setup for bending DMA. **(a)**: Specimen dimensions. **(b)**: Test setup with specimen, pressure fin and supports.

Isothermal frequency sweeps are conducted after each loading and unloading cycle of increased quasi-static deflection. In particular, each specimen is subjected to quasi-static deflections of 1 mm, 2 mm and 4 mm and subsequent unloading. After each unloading, a frequency sweep from 0.1 Hz to 10 Hz is conducted with a displacement amplitude of $\hat{u} = 0.075\,\mathrm{mm}$. In order to ensure permanent contact of the pressure fin with the specimen, a constant quasi-static deflection of 0.2 mm is applied. The experiments are carried out at room temperature and evaluated with regard to the resulting bending storage modulus, bending loss modulus and bending loss factor $\tan(\delta)$. The bending storage modulus is determined as

$$E'_{\mathrm{3pb}} = \frac{\hat{\sigma}}{\hat{\varepsilon}} \tag{6.4}$$

from the stress and strain amplitudes $\hat{\sigma}$ and $\hat{\varepsilon}$, which are calculated as

$$\begin{aligned} \hat{\sigma} &= 3\hat{F}\frac{l_{\mathrm{spt}}}{2bt^2}, \\ \hat{\varepsilon} &= 6t\frac{\hat{u}}{l_{\mathrm{spt}}^2} \end{aligned} \tag{6.5}$$

with $\hat{F}$ and $\hat{u}$ being the force and displacement amplitudes. The other quantities in Equation (6.5) are the specimen dimensions according to Figure 6.1a.

6.1.2 Results

6.1.2.1 Characterisation on constituent level

Comparison of two elastomers Figure 6.2 shows the Cauchy stress over the applied stretch in uniaxial tension for the two elastomers E1 and E3. For both materials, the occurrence of a Mullins effect is clearly visible.

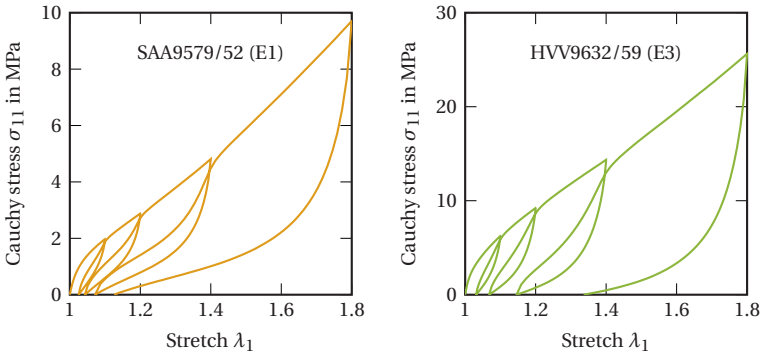

Figure 6.2: Mullins effect in elastomers E1 and E3 determined from a cyclic uniaxial tensile test with a constant strain rate of $\dot{\varepsilon} = 10^{-3}\,\mathrm{s}^{-1}$. The maximum stretches $\lambda_1^{\max}$ for consecutive cycles are 1.1, 1.2, 1.4 and 1.8.

In particular, three distinct phenomena can be observed. First, both materials exhibit an altered behaviour upon reloading up to the previous point of maximum extension. With increasing stretch beyond this point, the response follows the hyperelastic envelope. This behaviour is in line with typical Mullins softening as introduced in Chapter 2. Second, considerable permanent set is observed upon fully unloading the specimens to a stress-free state. The AEM based elastomer E3 shows more permanent set than the EPDM based elastomer E1. However, elastomer E3 is much stiffer and thus undergoes more stress during this deformation. Thirdly, both materials exhibit a mismatch in unloading and subsequent reloading curves. Under the occurrence of an ideal Mullins effect, these two curves would coincide up to the point of previous maximum stretch.

A more detailed comparison of the two elastomers regarding their softening and permanent set is shown in Figure 6.3. On the left hand, both materials are compared with regard to their relative secant modulus upon reloading serving as an indicator of softening. The secant modulus is determined for low strains of 0.01 % to 2 %. According to Figure 6.3, both elastomer materials soften after being extended to 40 % engineering strain to approximately half their initial stiffness at primary loading. Although the two materials differ significantly in their elastic stiffness, see Figure 4.1 and Figure 6.2, they show almost identical softening under uniaxial tension. With regard to permanent set, on the other hand, a significant difference is observed. Elastomer E3 accumulates far more permanent set than the other compound. The accumulation of permanent set, for both materials, is almost linear in the applied maximum stretch $\lambda_1^{\max}$ under the given loadcase and range of extension.

Rate dependency Figure 6.4 shows two cyclic experiments conducted on elastomer E1 at two different strain rates, namely $10^{-2}\,\mathrm{s}^{-1}$ and $10^{-3}\,\mathrm{s}^{-1}$. Clearly, both experiments show a Mullins effect. The curve determined at the higher strain rate of $10^{-2}\,\mathrm{s}^{-1}$ exhibits a steeper hyperelastic envelope, which is expected from a viscoelastic material. Interestingly, despite the two strain rates differing by a factor of ten, the unloading paths and, in particular, the

resulting permanent set mostly coincide. The reloading paths on the other hand differ slightly, with the higher strain rate leading to a higher slope.

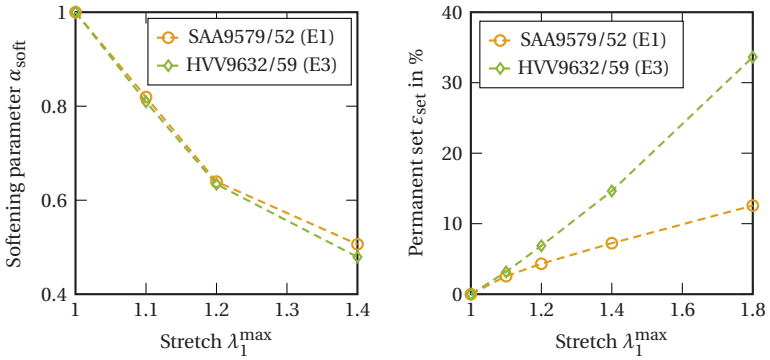

Figure 6.3: Comparisons of Mullins softening and permanent set in elastomers E1 and E3 determined from a cyclic uniaxial tensile test with a constant strain rate of $\dot{\varepsilon} = 10^{-3}\,1/s$. The maximum stretches λ_1^{max} for consecutive cycles are 1.1, 1.2, 1.4 and 1.8. Secant modulus is determined for loading/reloading paths in a strain range of 0.01 % to 2 %.

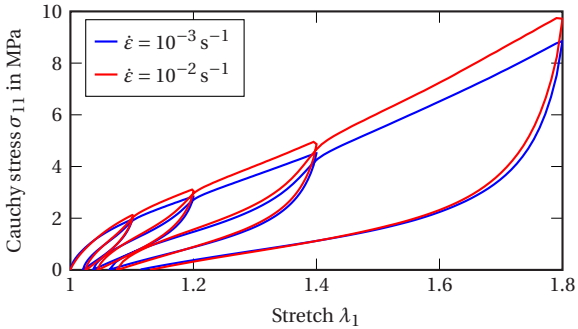

Figure 6.4: Rate-dependency of the Mullins effect shown on elastomer E1.

A more detailed evaluation of the two strain rates is given in Figure 6.5. In terms of the relative secant modulus, both strain rates lead to an identical decrease over the applied stretch. Regarding the resulting permanent set, only a minor difference between the two strain rates is visible. This small difference

can be attributed to more relaxation during unloading for the lower strain rate since the unloading in this case is ten times longer. Consequently, less residual stress is present in the material upon fully unloading to zero applied force, leading to less residual strain. To the keen eye, a slight discrepancy between the curves in Figure 6.5 and Figure 6.3 in terms of decrease of the secant modulus is perceptible, although the same material E1 is investigated. It should be noted at this point, that the curves comparing the two strain rates are determined on a different testing machine and, more importantly, on specimens, which in contrast to all others, are older and might have undergone some ageing.

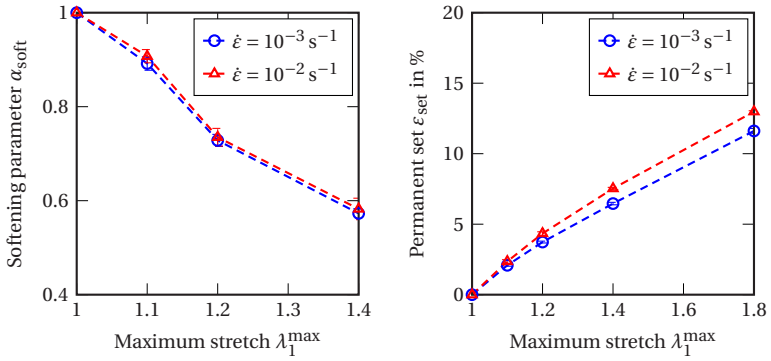

Figure 6.5: Rate-dependency of softening and permanent set shown on elastomer E1. Relative secant modulus upon loading/reloading. Reproduced from Jackstadt et al. [285, 286].

Regarding the strain rate-dependency of Mullins softening, Merckel et al. [48] obtain the same conclusion, in that the softening is unaffected by the material's inherent viscoelasticity. They also test strain rates differing by the factor ten, however, the investigated material is a filled SBR compound. Consequently, a strain rate-dependency of the Mullins effect is not addressed in the remainder of this work as experiments and simulations are carried out in the same strain-rate regime. Possible deviations, however, at extreme strain rates cannot be ruled out, but are not part of this study.

Evolution and saturation behavior The results of repeated cycles to a constant maximum stretch are shown in Figure 6.6 for the elastomer E1. The specimen in stretched to $\lambda = 1.2$ and fully unloaded for ten times before being stretched to $\lambda = 1.4$ and fully unloaded for another ten cycles. A strong cyclic softening and development of permanent set are observed for the first loading and unloading cycles to $\lambda = 1.2$ and $\lambda = 1.4$, respectively. Repeated cycles to the same stretch lead to an accumulation of loading and unloading curves with minor evolution of softening and permanent set.

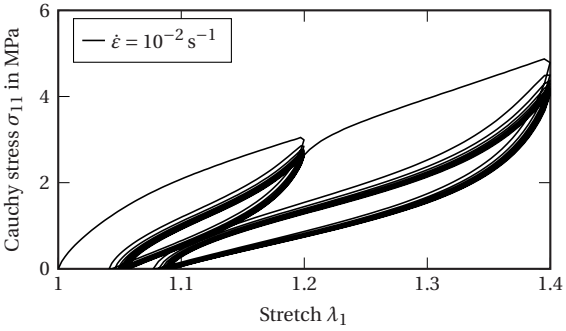

Figure 6.6: Evolution of the Mullins effect shown on elastomer E1. The specimen is subjected to ten load cycles to a maximum stretch of $\lambda_{\max} = 1.2$ followed by another ten load cycles to a maximum stretch of $\lambda_{\max} = 1.4$.

A more detailed view of this evolution is given in Figure 6.7 with regard to cyclic softening and permanent set. The relative secant modulus shows a severe drop after the first cycle to a new maximum stretch. Subsequent loadings do not differ as much with regard to the secant modulus, indicating a quick saturation of the Mullins softening. Similar behaviour, however slightly less pronounced, is seen for the evolution of permanent set at subsequent reloading to constant stretch. In this case, the permanent set does not go into full saturation within ten cycles. Nevertheless, the vast majority of residual strain is accumulated within the first loading and unloading cycle.

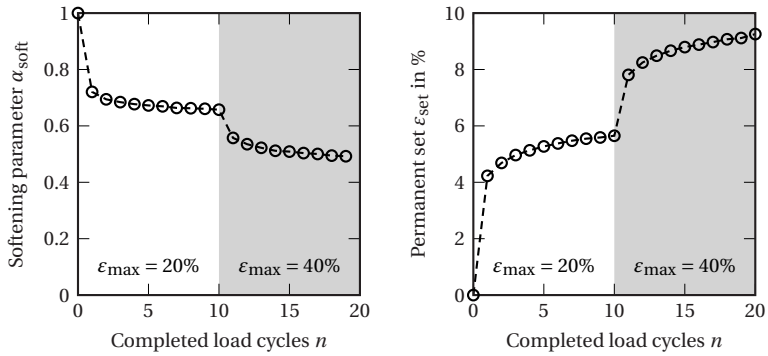

Figure 6.7: Evolution of softening and permanent set shown on elastomer E1. The specimen is subjected to ten load cycles to a strain of $\varepsilon_{max} = 20\,\%$ followed by another ten load cycles to a stain of $\varepsilon_{max} = 40\,\%$. Evolution of softening determined from the secant modulus upon loading/reloading. Reproduced from Jackstadt et al. [286].

To summarize, the investigations on cyclic softening and the evolution of permanent set shows a quick transition into a plateau with the majority of effects occurring upon primary loading to a new maximum stretch. Thus, for the subsequent exploratory investigations of the Mullins effect in terms of softening and permanent set in hybrid CLD laminates, this cyclic behaviour is not further considered.

6.1.2.2 Characterisation on laminate level

The results of three-point bending DMA on the two laminates A-E1-A and A-E3-A are shown in Figure 6.8 and Figure 6.9. The results are given in terms of a relative bending storage modulus and a relative loss factor, meaning that the results are normalized with regard to those obtained without any predeformation.

The storage modulus of laminate A-E1-A is seen to decrease after quasi-statically loading and unloading the specimen. A clear correlation between the loss in stiffness and the level of predeformation is present especially for the lower end of the considered frequency range. This correlation is less

pronounced for higher frequencies close to 10 Hz. With regard to loss factor $\tan(\delta)$, increased quasi-static predeformations lead to a significant increase. The frequency, however, does not have as much of an influence as it has on the storage modulus.

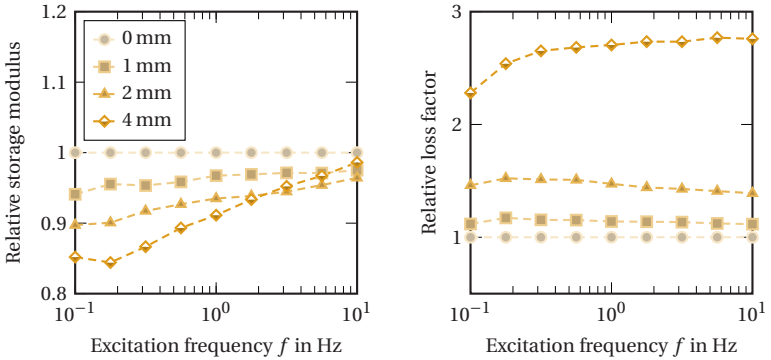

Figure 6.8: Results of isothermal bending DMA on laminate A-E1-A after different stages of predeformation.

Similar results are obtained for laminate A-E3-A, although the decrease in storage modulus is less pronounced than it is for the laminate featuring the softer elastomer E1. For frequencies close to 10 Hz, almost no difference is recorded between the virgin and preloaded material. In terms of the loss factor, higher predeformations also lead to an increase, which again turns out lower than in laminate A-E1-A. A strong frequency-dependency is observed for the loss factor measured after subjecting the specimen to a deflection of 4 mm.

Regardless of the laminate, it should be noted that the specimens are deformed plastically after a quasi-static deflection of 4 mm. The amount of residual deflection is the same in both laminates, indicating that the aluminium is plastically deformed. Consequently, the geometric stiffness of the specimens changes and the evaluation of the storage modulus and loss factor is not permissible for a quasi-static preload of 4 mm. Furthermore, due to the plastic deformation of the specimen, permanent contact between

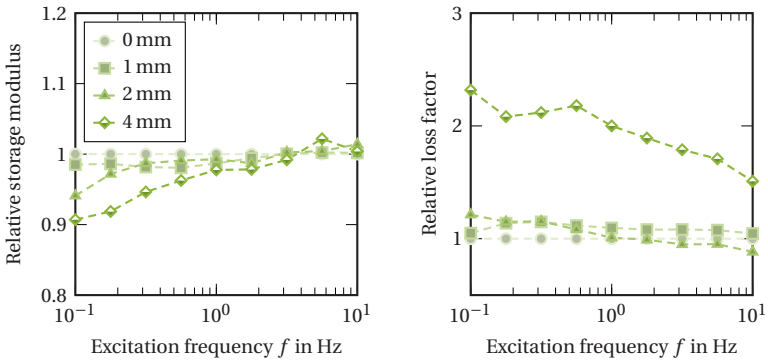

Figure 6.9: Results of isothermal bending DMA on laminate A-E3-A after different stages of predeformation.

the oscillating pressure fin and the specimen's surface cannot be guaranteed and friction could be present. This is a possible explanation for the disproportionally high loss factor obtained in both laminates for a quasi-static deflection of 4 mm.

Even when disregarding the curves of maximum deflection, laminate A-E1-A shows notably more softening due to predeformation than laminate A-E3-A although undergoing the same quasi-static predeformation. Laminate A-E3-A, however, is assumed to have a higher bending stiffness due to the stiffer elastomer as seen in Figure 4.1 or Figure 4.4. The analytical studies of different FMELs in Chapter 5 have also predicted higher bending stiffness for laminates containing elastomer E3 than for those featuring elastomer E1. At the same time, the elastomer layers experience much higher shear deformations in case of the softer elastomer as shown in Figure 5.17. Consequently, given the identical quasi-static deflections of both laminates, it is safe to assume, that in the bending experiment studied here, the elastomer E1 also undergoes more transverse shear deformation than elastomer E3. It is shown in Figure 6.3, that both elastomers experience almost identical softening behaviour with regard to stretch, which explains, why in the given experiment, the same level of quasi-static deflection leads to more softening in laminate A-E1-A than in

laminate A-E3-A. This serves a strong indicator, that the observed decrease in storage modulus is indeed caused by Mullins softening.

Another aspect worth noting, is the observation, that the initially decreased storage moduli show a slight increase over the course of the frequency sweep. This is attributed to viscoelastic relaxation processes occurring after unloading to zero force and during the actual DMA. Notably, the sweeps are conducted from low to high frequencies with numerous cycles per frequency. Consequently, the material is cycled at very low strain rates for a few minutes allowing for relaxation processes to occur, which then in turn lead to more force required to oscillate at a constant displacement amplitude. This then leads to the calculation of a slightly increased stiffness, thus storage modulus.

It should be noted, that the experiments conducted here also feature a certain amount of scatter and uncertainty due to the fact, that the experiments are performed using a load cell with a nominal capacity magnitudes higher than the forces required to oscillate the highly compliant laminates. However, multiple specimens of the same laminate type produce similar results, all featuring the same trends. Consequently, the results presented herein are considered to prove the occurrence of the Mullins effect in CLD laminates given moderate quasi-static preloading.

6.2 Numerical modelling of the Mullins effect

6.2.1 Methods[1]

6.2.1.1 Constitutive model development

The experimental investigations presented above show the occurrence of the Mullins effect in the elastomers E1 and E3. In particular, softening and permanent set are observed. Therefore, a material model for the subsequent analysis in CLD laminates needs to take these two aspects into account in order to quantify their influence. The aim of this study does not lie in the accurate stress analysis of the actual loading and unloading cycles of the material, but in the analysis of said effects, for example resulting from a quasi-static preload or other prior load cycles, under vibration depicted by linear frequency-domain simulations. Consequently, the highly non-linear large-strain deformation behaviour of the elastomer compounds needs to be depicted prior to the frequency-domain analysis to obtain an accurate material stiffness. The following requirements can thus be formulated for the constitutive model:

- Material softening due to high-strain preloading is considered.
- Ppermanent set and possible residual stresses within the laminate are considered.
- The exact stiffness tensor and corresponding tangent matrix after non-linear quasi-static loading in time domain is calculated prior to the transfer as the long-term or instantaneous stiffness into the frequency-domain.

[1] Section 6.2.1 is reproduced from Jackstadt et al. [287, 285, 286] with minor linguistic changes and additions.

- Frequency-dependent changes in stiffness and damping according to Figure 4.4 are considered.

Pseudo-elastic model Based on these requirements and the approaches for modeling the Mullins effect introduced in Section 2.1.4, the concept of pseudo-elasticity is pursued hereafter. On the one hand, such models can be calibrated on experimental cyclic tests alone, rendering additional material characterisation of physical properties redundant. In addition, pseudo-elasticity allows the equilibrium response of the undamaged material to be modeled by conventional hyperelastic material models. The disputed thermodynamic consistency under certain conditions as pointed out in [75], on the other hand, is not considered a limitation in this work due to the fact that the pseudo-elastic material model merely serves to provide the linearized material stiffness upon onset of vibration. Possible discrepancies in energy dissipation during loading and unloading cycles beforehand are therefore irrelevant.

The Dorfmann-Ogden model [58] is selected as a basis for the proposed material model. The undamaged hyperelastic material is described with an appropriate and yet to be determined strain energy density function according to Equation (2.22). In addition, two parameters η_1 and η_2 are introduced which describe the softening and permanent set, respectively. The material's of the strain energy function then reads

$$\Psi = W\left(\lambda_i^{\mathrm{dev}}, \eta_1, \eta_2\right) + U(J)\,. \tag{6.6}$$

Notably, this work considers any Mullins effect only for the deviatoric part in Equation (6.6) due to the almost incompressible nature of the studied materials. Both parameters, η_1 and η_2, are used to describe the Mullins effect, which inherently leads to a difference in loading and unloading paths. Consequently, the parameters η_1 and η_2 are required to be active during unloading and the subsequent loading up to the maximum deformation reached during the previous loading. As soon as the previous maximum

deformation is reached, both parameters are required to be inactive again in order for the material to further deform along the undamaged hyperelastic envelope. This of course is also the case upon primary loading, so that the constraint

$$W\left(\lambda_i^{\mathrm{dev}}, \eta_1 = 1, \eta_2 = 1\right) = W_0\left(\lambda_i^{\mathrm{dev}}\right) \tag{6.7}$$

presupposing that an inactive parameter η takes the value of 1. W_0 denotes the hyperelastic strain energy density of the undamaged hyperelastic material. Both parameters are also required to be continuous in order to avoid the need for jump conditions [288]. In equilibrium in absence of any external forces acting on the material, the conditions

$$\frac{\partial W\left(\lambda_i^{\mathrm{dev}}, \eta_1, \eta_2\right)}{\partial \eta_1} = 0, \quad \frac{\partial W\left(\lambda_i^{\mathrm{dev}}, \eta_1, \eta_2\right)}{\partial \eta_2} = 0 \tag{6.8}$$

are formulated. As proposed in the original model by Dorfmann and Ogden [58], the deviatoric part of the strain energy density function is then written as

$$W\left(\lambda_i^{\mathrm{dev}}, \eta_1, \eta_2\right) = \eta_1 W_0\left(\lambda_i^{\mathrm{dev}}\right) + \left(1 - \eta_2\right) N\left(\lambda_i^{\mathrm{dev}}\right) + \Phi\left(\eta_1, \eta_2\right). \tag{6.9}$$

In Equation 6.9, $N\left(\lambda_i^{\mathrm{dev}}\right)$ is an energy function characterising the residual strain and $\Phi\left(\eta_1, \eta_2\right)$ summarizes the dissipation resulting from differing loading and subsequent unloading curves including the permanent set. Inserting Equation (6.9) into Equation (6.8) gives

$$\frac{\partial \Phi\left(\eta_1, \eta_2\right)}{\partial \eta_1} = \Phi_1'\left(\eta_1\right) = -W_0\left(\lambda_i^{\mathrm{dev}}\right), \quad \frac{\partial \Phi\left(\eta_1, \eta_2\right)}{\partial \eta_2} = \Phi_2'\left(\eta_2\right) = N\left(\lambda_i^{\mathrm{dev}}\right) \tag{6.10}$$

which defines the variables implicitly in terms of principal stretches. Regarding the Mullins softening, one possible function for $\Phi_1'\left(\eta_1\right)$ leads to the softening parameter

$$\eta_1 = 1 - \frac{1}{r}\mathrm{erf}\left(\frac{W_{\max}^{\mathrm{dev}} - W_0^{\mathrm{dev}}}{m + \beta W_{\max}^{\mathrm{dev}}}\right), \tag{6.11}$$

depending on the previously reached maximum deviatoric strain energy $W_{\max}^{\mathrm{dev}}$ as well as material parameters $r \geq 1$, $m \geq 0$ and $\beta \geq 0$. The Gauss error function $\operatorname{erf}(x)$ is defined as

$$\operatorname{erf}(x) = \frac{2}{\sqrt{\pi}} \int_0^x e^{-t^2} \mathrm{d}t. \tag{6.12}$$

Equation (6.11) differs from the original models by Ogden and Roxburgh [81] as well as Dorfmann and Ogden [58] in the addition of the parameter β, which is often used in FEM implementations in order to soften the unloading curve for added stability [61]. The parameter describing the permanent set is given assumed as

$$\eta_2 = \tanh\left[\left(\frac{W_0^{\mathrm{dev}}\left(\lambda_i^{\mathrm{dev}}\right)}{W_{\max}^{\mathrm{dev}}}\right)^{\alpha\left(W_{\max}^{\mathrm{dev}}\right)}\right] / \tanh(1) \tag{6.13}$$

with $\alpha\left(W_{\max}^{\mathrm{dev}}\right) = b + \bar{c} W_{\max}^{\mathrm{dev}}$. Material parameters b and $\bar{c}$ are dimensionless. Following up on an initial suggestion by Dorfmann and Ogden [58], the residual strain contribution $N\left(\lambda_i^{\mathrm{dev}}\right)$ is modelled by a Neo-Hookean strain energy function as

$$N\left(\lambda_i^{\mathrm{dev}}\right) = \frac{1}{2}\left[\nu_1\left(\lambda_1^{\mathrm{dev}^2} - 1\right) + \nu_2\left(\lambda_2^{\mathrm{dev}^2} - 1\right) + \nu_3\left(\lambda_3^{\mathrm{dev}^2} - 1\right)\right] \tag{6.14}$$

with

$$\nu_i = \mu_0\left[\bar{q} - \bar{s}\tanh\left(\frac{\lambda_{i,\max}^{\mathrm{dev}} - 1}{h}\right)\right] \tag{6.15}$$

introducing the material parameters $\bar{q}$, $\bar{s}$ and $h \neq 0$. As the model is formulated in the isochoric stretches, the incompressibility, Equation (2.10), allows for the third deviatoric stretch to be expressed as $\lambda_3^{\mathrm{dev}} = \left(\lambda_1^{\mathrm{dev}}\lambda_2^{\mathrm{dev}}\right)^{-1}$. This simplifies Equation (6.14) to

$$N\left(\lambda_1^{\mathrm{dev}}, \lambda_2^{\mathrm{dev}}\right) = \frac{1}{2}\left[\nu_1\left(\lambda_1^{\mathrm{dev}^2} - 1\right) + \nu_2\left(\lambda_2^{\mathrm{dev}^2} - 1\right) + \nu_3\left(\frac{1}{\lambda_1^{\mathrm{dev}^2}\lambda_2^{\mathrm{dev}^2}} - 1\right)\right]. \tag{6.16}$$

Naturally, the same simplification can be made for W_0, so that $W\left(\lambda_i^{\mathrm{dev}}, \eta_1, \eta_2\right) = W\left(\lambda_1^{\mathrm{dev}}, \lambda_1^{\mathrm{dev}}, \eta_1, \eta_2\right)$. Notably, the model reduces to a special form of the original pseudo-elastic model by Ogden-Roxburgh [81], when the parameter η_2 is kept at one by, for example, setting $b = \bar{c} = 0$. The model will thus predict no permanent set.

Implementation in principal stretches The material model outlined in the previous section is fully, or partially, defined in principal stretches and not in terms of deformation tensor invariants. An implementation for use in an implicit FEM solver, such as Abaqus/Standard, usually requires the definition of a stress tensor and some form of a consistent tangent operator or elasticity tensor. While the former can be easily obtained from the strain energy function, for example by using Equation (2.20) in case of the Cauchy stress, the latter poses a challenge. For common hyperelastic material models, consistent elasticity tensors can be found in literature such as [4, 289]. For the given pseudo-elastic models, no such closed-form formulation is known to the author at the time of writing. Originally, an elasticity tensor for a material model formulated in principal stretches is derived from explicitly calculating the eigenvalues and corresponding eigenvectors as originally proposed by Chadwick and Ogden [290, 291]. As this procedure is computationally expensive, alternative methods by Simo and Taylor [292] are often used, which, however, can exhibit instabilities, especially in deformations featuring equal principal stretches [293, 294]. In this work, an alternative method based on the explicit calculation of the principal stretches and associated principal directions developed by Connolly et al. [295] for isotropic hyperelasticity is employed and extended to pseudo-elasticity.

The proposed framework by Connolly et al. [295] is utilized to implement the pseudo-elastic model by Dorfmann and Ogden [58] as a user defined material model UMAT in the FEM software Abaqus/Standard by Dassault Systèmes

Simulia Corp. The algorithm of obtaining exact elasticity tensors and the corresponding Jaumann rate of the Cauchy stress tensor

$$\mathbb{C}^{\mathrm{J}} = \frac{1}{J}\frac{\partial \Delta(J\boldsymbol{\sigma})}{\partial \Delta \varepsilon} \tag{6.17}$$

required as tangent modulus by the FE solver Abaqus/Standard [296, 18], is outlined in the following.

From the deformation gradient $\boldsymbol{F}$ passed to the material subroutine at each integration point of the FEM model, the corresponding eigenvalues λ_a^2 and eigenvectors $\boldsymbol{m}_a$ for the left Cauchy-Green tensor $\boldsymbol{B}$ are computed using an iterative Jacobi algorithm by Kopp [297]. The isochoric stress coefficients

$$\beta_a^{\mathrm{dev}} = \lambda_a^{\mathrm{dev}}\frac{\partial W}{\partial \lambda_a^{\mathrm{dev}}} - \frac{1}{3}\sum_{b=1}^{3}\lambda_b^{\mathrm{dev}2}\frac{\partial W}{\partial \lambda_b^{\mathrm{dev}}}. \tag{6.18}$$

then allow for the Cauchy stress tensor to be defined as

$$\begin{aligned}\boldsymbol{\sigma} &= \boldsymbol{\sigma}^{\mathrm{dev}} + \boldsymbol{\sigma}^{\mathrm{iso}} \\ &= \frac{1}{J}\sum_{a=1}^{3}\beta_a(\boldsymbol{m}_a \otimes \boldsymbol{m}_a) + \frac{\partial U}{\partial J}\mathbf{1}.\end{aligned} \tag{6.19}$$

The isochoric spatial elasticity tensor is derived by Connolly et al.[295] in the form

$$\begin{aligned}\mathbb{C}^{\mathrm{dev}} = &\sum_{a,b=1}^{3}\gamma_{ab}^{\mathrm{dev}} - 2\delta_{ab}\beta_a(\boldsymbol{m}_a \otimes \boldsymbol{m}_a \otimes \boldsymbol{m}_b \otimes \boldsymbol{m}_b) \\ + &\sum_{a,b=1;a\neq b}^{3}\frac{\beta_b{\lambda_a}^2 - \beta_a{\lambda_b}^2}{{\lambda_b}^2 - {\lambda_a}^2}\left[(\boldsymbol{m}_a \otimes \boldsymbol{m}_b) \otimes (\boldsymbol{m}_a \otimes \boldsymbol{m}_b \otimes \boldsymbol{m}_b \otimes \boldsymbol{m}_a)\right]\end{aligned} \tag{6.20}$$

with the isochoric elasticity coefficients defined as

$$\begin{aligned}\gamma_{ab}^{\mathrm{dev}} = &\left[\lambda_b^{\mathrm{dev}}\left(\lambda_a^{\mathrm{dev}}\frac{\partial W}{\partial \lambda_a^{\mathrm{dev}}}\right)\frac{\partial W}{\partial \lambda_b^{\mathrm{dev}}}\right] + \frac{1}{9}\sum_{c,d=1}^{3}\left[\lambda_d^{\mathrm{dev}}\left(\lambda_c^{\mathrm{dev}}\frac{\partial W}{\partial \lambda_c^{\mathrm{dev}}}\right)\frac{\partial W}{\partial \lambda_d^{\mathrm{dev}}}\right] \\ &-\frac{1}{3}\sum_{c=1}^{3}\left[\lambda_c^{\mathrm{dev}}\left(\lambda_a^{\mathrm{dev}}\frac{\partial W}{\partial \lambda_a^{\mathrm{dev}}}\right)\frac{\partial W}{\partial \lambda_d^{\mathrm{dev}}} + \lambda_b^{\mathrm{dev}}\left(\lambda_c^{\mathrm{dev}}\frac{\partial W}{\partial \lambda_c^{\mathrm{dev}}}\right)\frac{\partial W}{\partial \lambda_b^{\mathrm{dev}}}\right].\end{aligned} \tag{6.21}$$

For a detailed derivation of Equation (6.20) and Equation (6.21), the reader is referred to [291, 298]. Notably, the second term in Equation (6.20) includes a division by 0 for two or more unique principal stretches λ_a. Connolly et al. [295] apply L'Hôpital's rule to analytically derive the approximation

$$\lim_{\lambda_a\to\lambda_b}\frac{\beta_b\lambda_a^2-\beta_a\lambda_b^2}{\lambda_b^2-\lambda_a^2} = \lambda_a^4\lambda_b^{-2}\left(\frac{1}{2}\gamma_{bb}-\beta_b\right)-\frac{1}{2}\gamma_{ab} \tag{6.22}$$

for similar or identical eigenvalues λ_a^2. While for identical eigenvalues, above Equation (6.22) gives an exact solution, numerically similar eigenvalues can lead to instability due to floating-point precision limits of computers. A tolerance value is defined in order to determine, whether L'Hôpital's rule (6.22) is applied or whether the second term in Equation (6.20) is calculated directly. The algorithm, supplied as Fortran subroutines, is adopted from [299] and used in the implementation outlined here. More details on the implementation and validation of this algorithm are found in [298]. If compressibility is taken into account, the volumetric spatial elasticity tensor is calculated as

$$\mathbb{C}^{\mathrm{vol}} = J\left(\frac{\partial U}{\partial J}+\frac{\partial^2 U}{\partial J^2}J\right)(\mathbf{1}\odot\mathbf{1}) - 2\frac{\partial U}{\partial J}J(\mathbf{1}\odot\mathbf{1}) \tag{6.23}$$

from the hyperelastic strain energy function. Eventually, the Jaumann rate of the Cauchy stress tensor, which is required by Abaqus/Standard as a tangent stiffness within the UMAT interface, is given by

$$\mathbb{C}^{\mathrm{J}} = \frac{1}{J}\left(\mathbb{C}^{\mathrm{iso}}+\mathbb{C}^{\mathrm{vol}}\right) + (\boldsymbol{\sigma}\odot\mathbf{1}) + (\mathbf{1}\odot\boldsymbol{\sigma}). \tag{6.24}$$

The product $\boldsymbol{A} \odot \boldsymbol{B}$ used in Equation (6.23) and Equation (6.24) is defined as a symmetric fourth-order dyadic product, which is written as

$$(\boldsymbol{A} \odot \boldsymbol{B})_{ijkl} = \frac{1}{2}\left(A_{ik}B_{jl} + A_{il}B_{jk}\right) \tag{6.25}$$

in index notation. It should be noted, that for the implementation of above procedure in a construct of multiple Fortran subroutines, parts of the original implementation by Connolly et al. [295], which is published in [299], have been adopted and adapted.

Using Equation (6.23) and the isochoric elasticity coefficients in Equation (6.21), $\mathbb{C}^{\mathrm{J}}$ in Equation (6.24) can be calculated. Consequently, only the expressions

$$\begin{aligned}
\frac{\partial W}{\partial \lambda_i^{\mathrm{dev}}} &= \eta_1 \frac{\partial W_0}{\partial \lambda_i^{\mathrm{dev}}} + \left(1-\eta_2\right)\frac{\partial N}{\partial \lambda_i^{\mathrm{dev}}} \\
\frac{\partial^2 W}{\partial \lambda_i^{\mathrm{dev}} \partial \lambda_i^{\mathrm{dev}}} &= \eta_1 \frac{\partial^2 W_0}{\partial \lambda_i^{\mathrm{dev}} \partial \lambda_i^{\mathrm{dev}}} + \left(1-\eta_2\right)\frac{\partial^2 N}{\partial \lambda_i^{\mathrm{dev}} \partial \lambda_i^{\mathrm{dev}}} \\
\frac{\partial^2 W}{\partial \lambda_i^{\mathrm{dev}} \partial \lambda_j^{\mathrm{dev}}} &= \eta_1 \frac{\partial^2 W_0}{\partial \lambda_i^{\mathrm{dev}} \partial \lambda_j^{\mathrm{dev}}} + \left(1-\eta_2\right)\frac{\partial^2 N}{\partial \lambda_i^{\mathrm{dev}} \partial \lambda_j^{\mathrm{dev}}}
\end{aligned} \tag{6.26}$$

are needed for an implementation of the Dorfmann-Ogden model [58] in principal stretches in terms of a spatial elasticity tensor. The partial derivatives of the residual strain function $N\left(\lambda_i^{\mathrm{dev}}\right)$ are given by

$$\begin{aligned}
\frac{\partial N}{\partial \lambda_i^{\mathrm{dev}}} &= \nu_i \lambda_i \\
\frac{\partial^2 N}{\partial \lambda_i^{\mathrm{dev}^2}} &= \nu_i \\
\frac{\partial^2 N}{\partial \lambda_i^{\mathrm{dev}} \partial \lambda_j^{\mathrm{dev}}} &= 0.
\end{aligned} \tag{6.27}$$

When compressibility is to be considered, the quantities $\frac{\partial U}{\partial J}$ and $\frac{\partial^2 U}{\partial J^2}$ are furthermore required and are calculated from the undamaged hyperelastic strain energy function.

It should be noted, that the tangent stiffness obtained in Equation 6.24 is used by the Abaqus/Standard solver as the consistent Jacobian operator for the calculation of force residuals, which in turn are used to assess convergence and adapt the load increments in static and quasi-static loading [18]. The stress response, however, is calculated separately within the UMAT framework and is supplied directly as the Cauchy stress tensor, see Equation (6.19). Consequently, an exact tangent stiffness is not necessary in static and quasi-static analysis and approximations would suffice in order to achieve convergence. Within this work, however, quasi-static loading is only used as a preload for invoking the Mullins effect. Subsequently, complex modal analyses of steady-state dynamic procedures are executed. These procedures directly use the supplied tangent stiffness operator for the formulation of the linearized global stiffness matrix such as presented in Equation (7.4). In this case, an exact tangent matrix is mandatory in order to achieve correct results in the frequency-domain, such as natural frequencies, modal damping ratios or FRFs.

Frequency-domain viscoelasticity Subsequent to the formulation of the Dorfmann-Ogden model in principal stretches outlined above, the viscoelastic material behaviour is incorporated into the constitutive model. The scope of this work is to analyze CLD in the frequency-domain. Time-domain viscoelastic effects, such as the difference in unloading and subsequent loading curves outlined in Section 6.1.2 are not of interest as dissipation during loading is neglected and does not influence steady-state behaviour in the frequency-domain. Consequently, viscoelasticity is incorporated into the model solely within the frequency-domain. The consistent Jacobian operator expressed by the Jaumann rate of stress in Equation (6.24) describes the effective elasticity of the material in its predeformed state at any given

point on the loading or unloading curve. The transition into the frequency-domain freezes this state of the material, including any stresses present, at the onset of vibration. Consequently, the $\mathbb{C}^{\mathrm{J}}$ is taken as the absolute value of the complex-valued elasticity tensor $\mathbb{C}^{\mathrm{J}*}$, with its real and imaginary parts $\Re\left(\mathbb{C}^{\mathrm{J}}\right)$ and $\Im\left(\mathbb{C}^{\mathrm{J}}\right)$. Within this work, viscoelasticity is constrained to deviatoric contributions. Consequently, the frequency-dependent real and imaginary parts of the consistent Jacobian operator are given by

$$\begin{aligned}\Re\left(\mathbb{C}^{\mathrm{J}}\right) &= \frac{1}{J}\left(\left(1-\omega\Im\left(g^*\right)\right)\mathbb{C}^{\mathrm{iso}}|_\infty + \mathbb{C}^{\mathrm{vol}}|_\infty\right) + \left(\boldsymbol{\sigma}|_\infty \odot \mathbf{1}\right) + \left(\mathbf{1} \odot \boldsymbol{\sigma}|_\infty\right)\\ \Im\left(\mathbb{C}^{\mathrm{J}}\right) &= \frac{1}{J}\left(\omega\Re\left(g^*\right)\mathbb{C}^{\mathrm{iso}}|_\infty + \mathbb{C}^{\mathrm{vol}}|_\infty\right) + \left(\boldsymbol{\sigma}|_\infty \odot \mathbf{1}\right) + \left(\mathbf{1} \odot \boldsymbol{\sigma}|_\infty\right),\end{aligned} \tag{6.28}$$

where g^* is the Fourier transform of the material's relaxation function. The material's long-term, fully relaxed stiffness is denoted as $\mathbb{C}|_\infty$. The real and imaginary parts of g^* are given by

$$\begin{aligned}\omega\Re\left(g^*\right) &= \frac{G''}{G_\infty}\\ \omega\Im\left(g^*\right) &= 1-\frac{G'}{G_\infty}.\end{aligned} \tag{6.29}$$

In Equation (6.29), G' and G'' denote the frequency-dependent storage and loss shear moduli of the material, which can be calculated from the mastercurve of a complex Young's modulus E^* as displayed in Figure 4.4. This concludes the constitutive model used for modelling the elastomer plies in CLD laminates for quasi-static preloads and subsequent vibration under consideration of Mullins softening and permanent set.

6.2.1.2 Model calibration

The cyclic uniaxial tension data obtained at a strain rate of $\dot{\varepsilon} = 10^{-3}\,\mathrm{s}^{-1}$ is used to calibrate the long-term material response $\mathbb{C}^{\mathrm{iso}}|_\infty$ prior to vibration. For both elastomers E1 and E3, two sets of parameters are determined, namely

one considering permanent set according to Dorfmann and Ogden [58] and another one neglecting the same, giving the Ogden-Roxburgh model [81]. The Differential Evolution algorithm by Storn and Price [300] is relied upon to fit the three, respectively eight, parameters to the experimental data. According to Equation (2.21), for uniaxial tension with $\lambda_1 = \lambda$ and $\lambda_2 = \lambda_3 = \frac{1}{\sqrt{\lambda}}$ and full incompressibility, the Ogden-Roxburgh model yields the Cauchy stress

$$\sigma_{11} = \sigma = \eta_1 \sigma_0, \tag{6.30}$$

where σ_0 is the Cauchy stress predicted by the virgin hyperelastic material model. For the Dorfmann-Ogden model, the expression

$$\sigma_{11} = \sigma = \eta_1 \sigma_0 + \left(1 - \eta_2\right)\left(\nu_1 \lambda^2 - \frac{\nu_2 + \nu_3}{2}\frac{1}{\lambda}\right) \tag{6.31}$$

is obtained. Notably, for an incompressible material under uniaxial tension, it can be shown that $\nu_2 = \nu_3$ in Equation (6.31).

6.2.1.3 Model verification and validation

Verification As no mention of the implementation of a pseudo-elastic material model in principal stretches using the algorithm outlined above to obtain a consistent tangent stiffness exists in literature, a thorough model verification for quasi-static and modal behaviour is conducted hereafter. For this purpose, this implementation is compared with the built-in implementation of the Ogden-Roxburgh model in Abaqus/Standard. An incompressible Neo-Hookean hyperelastic model, cf. Table 2.1, with $\mu = 3.715\,\mathrm{MPa}$ is assumed, which represents the elastomer E1. Consequently, a mass density of $1180\,\mathrm{kg\,m^{-3}}$ as listed in Table 4.4 is specified. The model parameters r, m, β from Table 6.1 are used. Cyclic uniaxial tension is applied to a single hybrid continuum element with reduced integration C3D20RH in multiple large-strain loading and unloading steps. The thus softened

material is then subjected to modal analysis, determining the single element's eigenmodes and corresponding natural frequencies.

Validation In order to validate the developed constitutive models with regard to their ability of reproducing the effects seen in experiments in Section 6.1.2, a FEM simulation of the experimental three-point-bending DMA setup is created. The model is pictured in Figure 6.10. The aluminium plies are modelled as linear elastic according to the properties listed in Table 4.1. They are represented by three reduced integration quadratic continuum elements of type C3D20R across the thickness. In order to avoid numerical problems with the almost incompressible elastomer layers, see Poisson's ratios in Table 4.4, the hybrid element formulation C3D20RH is chosen, which treats pressure stress as an independently interpolated basic solution variable, that is coupled to the displacement solution through the constitutive law and a compatibility condition [18, 282]. Six elements are stacked along the thickness of the elastomer layers. The elastomers' E1 and E3 virgin hyperelastic responses are modelled as Neo-Hookean solids, cf. Table 2.1, with an initial shear modulus of 3.715 MPa and 9.001 MPa, respectively. The Mullins effect is modelled using the Ogden-Roxburgh model [81] with the previously determined material parameters listed in Table 6.1. Due to observed convergence issues with the Dorfmann-Ogden model for complex models at higher levels of deformation, this model is omitted in the validation procedure outlined here. The frequency-dependent viscoelastic behaviour of the elastomers in the frequency-domain is considered according to the DMA mastercurves shown in Figure 4.4. The two supports as well as the pressure fin are modelled as undeformable rigid bodies according with dimensions according to the bending DMA experiments introduced in Section 6.1.1.2. A frictionless contact between the specimen and the pressure fin and supports is assumed.

Following quasi-static predeformation induced by a transverse displacement of the pressure fin by 1 mm, 2 mm and 4 mm, a steady-state analysis is carried out in the range of 0.1 Hz to 10 Hz by oscillating the pressure fin

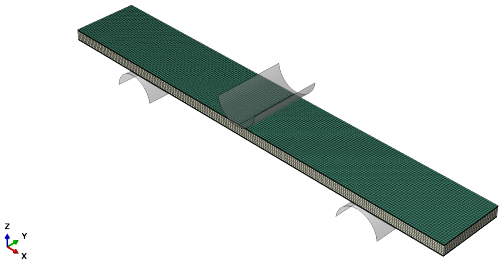

Figure 6.10: FEM model of three-point-bending DMA created in Abaqus/Standard. Different materials are distinguished by colour.

with an amplitude of $\hat{u} = 0.075\,\text{mm}$. The constant preload in form of a static transverse deflection of $u_0 = -0.2\,\text{mm}$ used in the experiments is also accounted for. The simulations are evaluated in terms of storage bending modulus and corresponding loss factor, which are calculated from the prescribed displacement amplitude and resulting reaction force on the pressure fin according to Equation (6.4).

6.2.2 Results

6.2.2.1 Model calibration

The material parameters optimized according to Section 6.2.1.2 for both elastomers are listed in Table 6.1 in case of the Ogden-Roxburgh model [81] and Table 6.2 for the Dorfmann-Ogden model [58].

Table 6.1: Model parameters for the modified Ogden-Roxburgh [81] model without permanent set for the two elastomer materials under investigation.

Elastomer	r	m in MPa	β
SAA9579/52 (E1)	1.356	8.488×10^{-2}	2.071×10^{-1}
HVV9632/59 (E3)	1.148	3.099×10^{-1}	1.670×10^{-1}

Table 6.2: Model parameters for the modified Dorfmann-Ogden [58] model with permanent set for the two elastomer materials under investigation.

Elastomer	r	m in MPa	β	b	$\bar{c}$	$\bar{q}$ in MPa	$\bar{s}$ in MPa	h
SAA9579/52 (E1)	2.358	0.319	0.193	5.282	11.01	−0.232	4202	4894
HVV9632/59 (E3)	1.608	0.510	0.254	5.233	5.138	−0.637	−4745	−1869

The model predictions using the optimized material parameters from Table 6.1 and Table 6.2 are plotted in Figure 6.11 for uniaxial tension. The Ogden-Roxburgh model yields acceptable predictions of the initial unloading curves, but diverges from the experimental curve when approaching the fully unloaded state as it does not capture the occurring permanent set. This discrepancy is more pronounced with elastomer E3, which shows significantly more permanent set, see Figure 6.3. In this case, the unloading curves become almost horizontal and thus underestimate the stiffness of the material in the fully unloaded state. The Ogden-Roxburgh model on the other hand captures the experimental data quite accurately, apart from the difference in unloading and reloading curves due to the neglected viscoelasticity. In particular, the permanent set is predicted well by the model as soon as the applied stress reaches zero. Figure 6.11 also shows the prediction for when the material is deformed back to its original length for which the model then naturally predicts residual stresses within the material. These again turn out larger for elastomer E3 than for elastomer E1.

6.2.2.2 Model verification and validation

Verification The results of this verification procedure is shown in Figure 6.12. Perfect agreement between the reference solution provided by the built-in Abaqus model and the user implementation in principal stretches is achieved for the three loading and unloading cycles. This verifies the correct calculation of the stress coefficients β_a^{dev} in Equation (6.18) as well as the eigenvectors and eigenvalues of the left Cauchy-Green tensor $\boldsymbol{B}$. As a correct

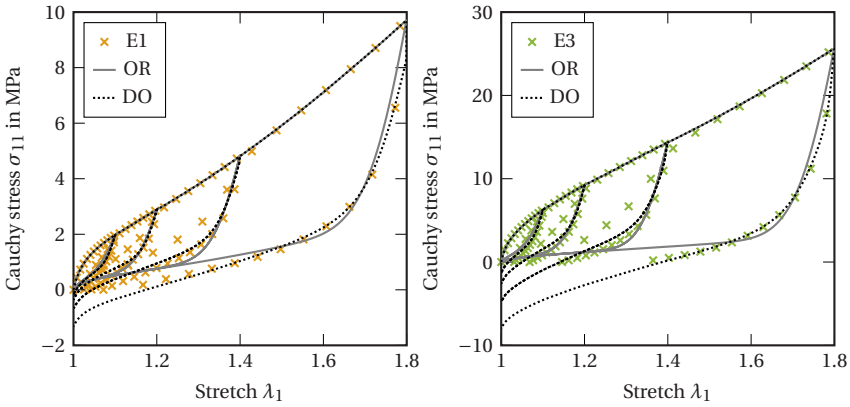

Figure 6.11: Calibration of the Ogden-Roxburgh (OR) and Dorfmann-Ogden (DO) model to experimental data obtained in uniaxial tension according to Equation (6.30) and Equation (6.31).

alteration of the strain energy density function is needed to depict the softening effect, the evolution of the softening parameter η_1 is therefore also verified. The right-hand side of Figure 6.12 shows the natural frequencies of the associated eigenmodes of the element, including six rigid body modes. Again, excellent agreement between the two implementations is given. As the eigenvalue problem is solved using the element's tangent stiffness to directly formulate the global system of equations, a verification of the implemented elasticity coefficients γ_{ab} is thereby given. Consequently, the implementation of a pseudo-elastic material model in principal stretches to be used within Abaqus/Standard is proven feasible and accurate

Validation The results of the model validation procedure under three-point bending outlined in Section 6.2.1.3 are presented in the following. In Table 6.3, the distribution of the softening parameter η_1 according to Equation (6.11) within elastomer plies of laminates A-E1-A and A-E3-A is shown after undergoing different levels of quasi-static preloading and subsequent unloading. The contour plots in Table 6.3 show the material in the

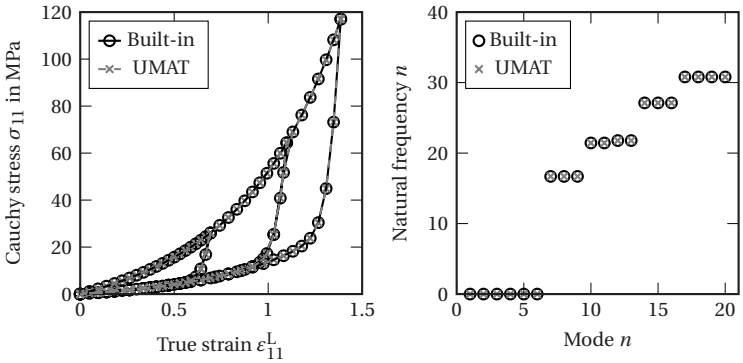

Figure 6.12: Single-element verification of the implementation of pseudo-elasticity in principal stretches using the example of the Ogden-Roxburgh (OR) model. Comparison between built-in material model (Built-in) and implemented user-defined material (UMAT).

fully unloaded state. A value of $\eta_1 = 1.0$ corresponds to an undamaged, virgin elastomer material. In all cases, a localization of the Mullins damage is evident in the area between the pressure fin and the supports with the remainder of the specimen remaining unaffected. For all three levels of preloading, laminate A-E1-A featuring the more compliant elastomer E1 shows lower values of η_1, thus more Mullins damage, than laminate A-E3-A.

Figure 6.13 shows the results obtained for laminate A-E1-A in terms of its relative storage bending modulus (left) and resulting relative loss factor (right) for the prescribed levels of quasi-static predeformation. Notably, the model predicts a strong decrease in the bending storage modulus due to the Mullins effect, which increases with the level of preloading. Preloads of 1 mm and 2 mm lead to a decrease of almost 50 %, whereas a preload of 4 mm yields an even lower storage modulus. The loss modulus is also predicted to decline following quasi-static preloading. Again, higher levels of preload lead to a more pronounced decline.

Figure 6.14 presents the results obtained for laminate A-E3-A. The predicted decrease in bending storage modulus is not as high as in laminate A-E1-A, yet

Table 6.3: Numerically determined distribution of softening parameter η_1 within the constrained elastomer layer of laminates A-E1-A and A-E3-A subjected to different levels of preceding bending deformation. Results are obtained using Abaqus/Standard and the Ogden-Roxburgh model [81] in the UMAT implementation outlined in Section 6.2.1.

Deflection	A-E1-A	A-E3-A	Legend
1 mm	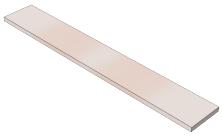	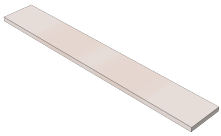	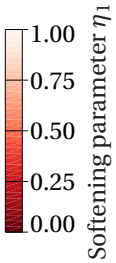
2 mm	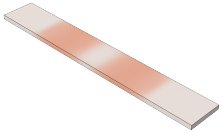	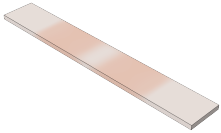	
4 mm	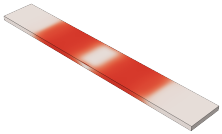	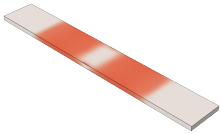	

still quite pronounced with higher levels of preloading yielding a lower relative modulus compared to the virgin material state. All levels of preloading also lead to a decrease in the bending loss factor. However, no clear correlation between increased preloading and reduction in loss factor is observable as the highest preloading with 4 mm yields a higher residual loss factor than the other two levels of preloading.

The numerical results presented here are in disagreement with the experimental ones presented in Figure 6.8 and Figure 6.9. The models overestimate the reduction of the storage bending modulus for both laminates. Qualitatively, however, the model does capture the fact, that laminate A-E1-A is

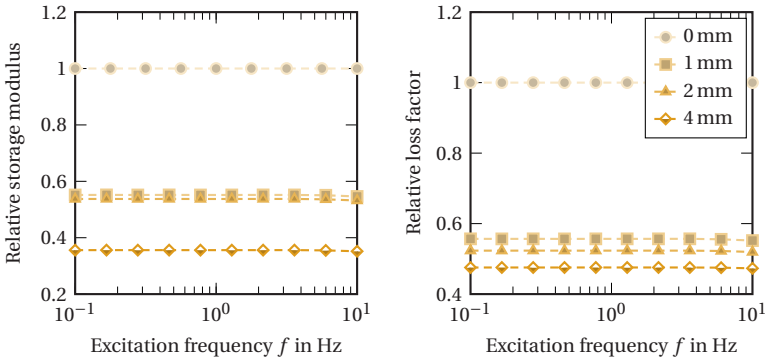

Figure 6.13: Results of numerical frequency-sweeps on laminate A-E1-A after different stages of bending predeformation. Results are obtained with the FEM model shown in Figure 6.10 and the Ogden-Roxburgh model [81].

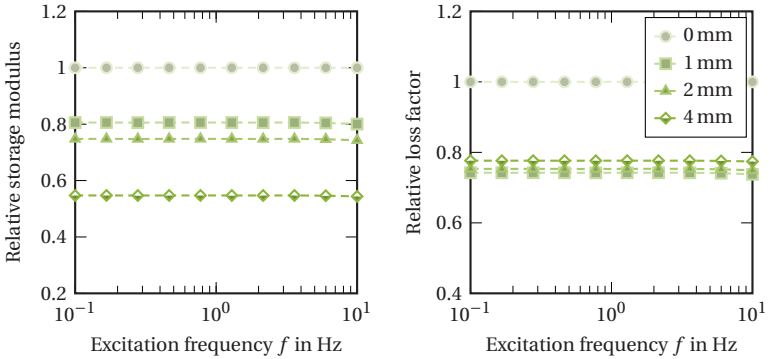

Figure 6.14: Results of numerical frequency-sweeps on laminate A-E3-A after different stages of bending predeformation. Results are obtained with the FEM model shown in Figure 6.10 and the Ogden-Roxburgh model [81].

affected more by Mullins softening than laminate A-E3-A as seen in the experiments in terms of the bending storage modulus. Contrary to the experimental results, the models predict a reduced loss factor, whereas the experiments show an increased loss factor after preloading the specimens. Similar to the experimental results, the curves obtained for laminate A-E3-A are in closer proximity to each other than those of laminate A-E1-A. Possible reasons and

implications of this mismatch between the experimental and numerical results are addressed in Section 6.3.

6.3 Discussion and concluding remarks

6.3.1 Experimental characterisation

Section 6.1 introduces the experimental methods used to characterise the Mullins effect in two of the elastomer materials used throughout this work and showcases the corresponding results. In particular, Section 6.1.2.1 presents the characterisation of the neat elastomer materials. In both materials, the occurrence of the Mullins effect is shown. As elastomer E1 belongs to the class of EPDM elastomers, the observation of the Mullins effect is coherent with previous reports in literature [45, 46]. In AEM rubbers, on the other hand, no mention of the Mullins effect occurring is known from literature, making this the first reference. Both elastomers are also shown to retain some permanent set after unloading, which is commonly associated with the Mullins effect, see Section 2.1.4. For EPDM elastomers, such as elastomer E1 of this work, permanent set has previously been shown in [52, 45]. It should be noted, that the permanent set determined in the experiments presented in Section 6.1.2.1 most likely include viscoelastic strains which were not allowed to recover. Waiting times between the individual loading and unloading cycles would mitigate those, but lead to difficulties fitting the proposed pseudo-elastic models to the data. Another aspect unveiled by the experiments on neat elastomer specimens in Section 6.1.2.1 is the discrepancy between unloading and subsequent reloading curves deviating from the idealized Mullins effect shown schematically in Figure 2.3. Fazekas and Goda [89] also report this phenomenon for a filled EPDM rubber compound and attribute this to a viscoelastic stress reduction, which, for example, is reproduced using a hyper-viscoelastic modelling approach in [89].

The cyclic softening in the context of the Mullins effect shown in Figure 6.7 is also documented in limited previous research. Merckel et al. [48] investigate this effect in filled SBR compounds and define a similar measure for softening upon reloading. In contrast to this work, their investigations are focused on high-cycle behaviour with up to 1000 cycles to the same maximum stretch. Nevertheless, their experiments show far less softening than observed here, while also taking several 100 cycles before reaching saturation. Merckel et al. [48] also investigate the influence on filler volume content on the cyclic behaviour and find, that higher contents of fillers, in their case carbon black, leads to more cyclic softening. Due to the fact that the elastomers used in this work are commercially available, no information on filler content is available at the time of writing. However, tensile tests conducted on this exact material E1 by Sessner [230] reveal comparably low strains upon failure for this material. Comparison with other EPDM based compounds in literature shows, that much higher failure strains are possible, indicating that the material E1 at hand are highly reinforced by fillers, such as carbon black. Furthermore, the investigated elastomers are developed for structural purposes, again indicating a desired high stiffness. Consequently, a high filler content in the materials E1 and E3 is deduced, which in turn explains the extensive cyclic softening observed in the experiments with regard to literature. Similar investigations on filled SBR by Brieu et al. [301] show a strong dependency of cyclic softening and the resulting permanent set on the amplitude of stretch. For lower stretch amplitudes, a saturation of softening is reached earlier. While in their experiment the lowest strain amplitude is 100 %, corresponding to a maximum stretch $\lambda_1^{\max}$ of 2, the maximum stretches in this work are even lower, which, according to [301], suggests an even quicker transition into a plateau. Yu et al. [302] investigate the evolution of permanent set for repeated stretching to the same stress and determine that the majority of residual strain accumulates after the first cycle with saturation being observed after approximately ten cycles. Although their work focuses on filled natural rubber, the behaviour is identical to the one observed here for the EPDM based elastomer E1.

Section 6.1.2.2 presents, for the first time in literature, results regarding the Mullins effect occurring within a laminate. The results presented here show a strong alteration of the laminates' loss factor under steady-state conditions due to Mullins softening. There is no indication in literature on a possible influence of the Mullins effect on the elastomers' viscous damping mechanism. Given that the theories aimed at an explanation of the Mullins effect on a physical basis, cf. Section 2.1.4, mostly suggest changes in the microstructure of the polymer network of the material, such an influence is undoubtedly imaginable. However, the findings by Diercks et al. [84] show that the Mullins effect influences storage and loss modulus in nearly identical fashion. This would in fact leave the loss factor $\tan(\delta)$ mostly unaltered, cf. Equation (2.36) by any Mullins softening. At the very least, it cannot explain the pronounced increase in loss factor observed here. Consequently, this increase in loss factor seen in Figures 6.8 and 6.9 is attributed to the loss of stiffness due to Mullins softening. As the results presented in Section 5.3.5.1 show, a decrease in elastomer layer stiffness often leads to a significant rise in damping.

Possible weak points of the experimental characterisation procedure on laminate level under three-point-bending can also be addressed. First, the plastic deformation occurring during preloading the specimen to a deflection of 4 mm addressed in Section 6.1.2.2 might have caused the pressure fin to loose contact with the specimen. Although no plastic deformation is visually detectable for predeformations of 1 mm or 2 mm, some plasticity might have occurred and thus modified the specimen's surface and shape on a small scale. Given the very low force amplitudes in the bending DMA, such small changes to the upper aluminium layer could have altered the contact between the pressure fin and the specimen, yielding results not entirely comparable to those obtained under a previous level of predeformation. Second, due to the specimen manufacturing process outlined in Section 4.2, the specimens cannot be guaranteed to be perfectly plane. Consequently, the induced deformation, in particular during the dynamic DMA part of the experiment, may not correspond to a pure bending deformation.

6.3.2 Numerical modelling

The implementation of pseudo-elastic models, such as the Ogden-Roxburgh model [81] as well as the Dorfmann-Ogden model [58] in principal stretches using the method proposed by Connolly et al. [295] has been verified in Section 6.2.2 for a fully incompressible material. The exact agreement of stresses and natural frequencies obtained with the Ogden-Roxburgh in this implementation with those obtained via a built-in model in Abaqus/Standard prove the applicability of this method. Furthermore, an identical number of increments is needed for convergence of the Ogden-Roxburgh model when compared with the built-in model. This confirms the findings in [295], where this has been shown for the hyperelastic Yeoh model, see Table 2.1. However, convergence of the Dorfmann-Ogden model in the implementation in principal stretches could not be achieved for models of increased size and more complex deformation as mentioned in Section 6.2.1.3. This issue is also reported in [303] and [304], although no details on the implementation in Abaqus and, in particular, on the calculation of the tangent matrix are shared. It should be noted at this point, however, that the calculation of the tangent matrix in terms of principal stretches as pursued in this work is assumed correct, also for the Dorfmann-Ogden model, since a simplification of the model yielding the Ogden-Roxburgh model leads to identical convergence as the built-in model.

While numerous constitutive models for predicting permanent set associated with the Mullins effect exist in literature, these are mostly restrained to analytical expressions for the sake of determining material parameters. To the author's knowledge only the recent works of Wollner et al. [92] and Terzano et al. [305], respectively, address the issue of implementing such models for the use in commercial FEM codes. They also follow the concept of pseudo-elasticity for depicting the Mullins effect and permanent set, but employ the perturbation method by Miehe [306] for the calculation of the consistent tangent matrix for their implementation as a user-defined material model in

Abaqus/Standard. Their material model is thus seen as a promising alternative for a continuation of this work.

Another possible reason for the mentioned convergence issues could be an unfavourable set of material parameters in Table 6.2 specifying the permanent set, although these represent the material behaviour well as shown in Figure 6.11. This issue has been foreshadowed in [303] and taken up by Anssari-Benam et al. [91], who propose a model for permanent set without the need of a separate strain energy function modelling the residual strain and thus requiring fewer material parameters. Another alternative is seen in the statistical model by Diani et al. [59].

Subsequent simulations of simplified CLD laminates featuring two different elastomer materials using the Ogden-Roxburgh model in Section 6.2.1.3 have revealed a substantial disagreement with the experimental results. On the one hand, the decrease in bending storage modulus due to Mullins softening is overestimated by the model. This is attributed to the neglect of the observed permanent set, which leads to a lower material stiffness upon fully unloading the material as seen in Figure 6.11. Consequently, the dynamic modulus is predicted lower by the Ogden-Roxburgh model than perceptible from the experiment. On the other hand, modelling the elastomer materials with the Ogden-Roxburgh model predicts a decrease in the bending loss factor, which is contrary to the experimental findings. While possible issues with the experimental setup have been discussed in Section 6.3.1, this mismatch could also originate from limitations of the material model. The aforementioned underestimation of the elastomers' stiffness subsequent to quasi-static preloading yields an altered ratio of core stiffness to face stiffness of the laminate, which under some circumstances can lead to a lower achievable damping as shown in Section 5.3.6. Consequently, depicting the permanent set accurately would yield a more realistic stiffness and could thus lead to an increase in loss factor after predeformation as seen in the experiments. The modelling approach pursued in this work assumes no actual change of the viscous properties of the elastomers due to the Mullins effect, but restricts the Mullins effect to a change of modulus alone. This is coherent

with the findings by Diercks et al. [84], although their work focusses on a filled natural rubber. The influence of the Mullins effect on the present materials' loss factor tan(δ) therefore remains to be investigated.

6.3.3 Conclusions

In conclusion, the research presented in this chapter experimentally proves the occurrence of the Mullins effect in two of the elastomers used throughout this work, fulfilling Objective 2-1 of this work. Both neat materials are tested under uniaxial tension to a maximum stretch and subsequently unloaded before being loaded again to an increased stretch. In addition to the softening of the materials in terms of its secant modulus, both materials retain a significant amount of residual strain after unloading, commonly referred to as permanent set. The experiments also show that a rate dependency of the softening due to the Mullins effect as well as the permanent set does not exist. Mullins softening and permanent set are shown to not only depend on the maximum stretch applied to the material, but also the number of load cycles to that maximum stretch. However, the majority of softening and set accumulates during the first cycle.

Isothermal bending DMA on simplified CLD laminates consisting of two plies of aluminium constraining a thicker elastomer layer are conducted. The resulting storage bending modulus and loss factor are shown to depend on the amount of quasi-static predeformation of the laminate, indicating the occurrence of the Mullins effect within the elastomer plies under bending. A decrease in storage modulus as well as an increase in the loss factor is observed for laminates containing both elastomers.

Two pseudo-elastic material models, namely the Ogden-Roxburgh model and the Dorfmann-Ogden model, are calibrated to reproduce the stress strain curves of both materials. While the former only depict the altered material stiffness, the latter additionally captures the observed permanent set. Very good agreement with the experimental uniaxial test data is achieved. Both

models are implemented as a user-defined material model for the commercial FEM code Abaqus/Standard. The employed numerical implementation in principal stretches for the pseudo-elastic material models is proven feasible and accurate. For larger models, however, convergence issues with the Dorfmann-Ogden model depicting permanent set are encountered in the implementation used featuring the determined material parameters, thus only partially fulfilling Objective 2-2 of this thesis.

A validation of the Ogden-Roxburgh model dictated by Objective 2-3 for the given laminates shows high discrepancies between the experiments and simulations with regard to the dynamic behaviour of predeformed laminates. This disagreement is attributed to the model's inability to capture the occurring permanent set. Furthermore, questions remain regarding the validity of the experiments themselves. Nevertheless, both, experiments and simulations, demonstrate within their own limitations an influence of the Mullins effect in CLD laminates and by doing so, prove this work's Hypothesis 1. Furthermore, the outlined differences between experiment and simulation further strengthens the need for an accurate constitutive model, which depicts the Mullins effect and accompanying permanent set in frequency-domain analysis.

7 Impact damage in constrained-layer damping laminates

7.1 Experimental characterisation of impact damage in hybrid FMELs[1]

7.1.1 Methods

The experimental investigations in this chapter involve the laminates A-E1-C-E1-A, A-E2-C-E2-A, C-E1-A-E1-C and C-E2-A-E2-A according to Table 4.6. Two instead of the three elastomer compounds are considered as these two represent the largest span in stiffness as well as viscous damping. Pre-damage in the FMELs is induced by means of low-velocity instrumented drop-weight impact tests. The experimental setup and execution are based on ASTM standard D7136 [307]. A testing machine Magnus 1300 by Coesfeld GmbH & Co. KG is used with a custom support fixture, see Figure 7.1a, adhering to the boundary conditions specified in [307]. The opening dimensions of the fixture are 125 mm and 75 mm, respectively. The four clamps with neoprene tips hold down the specimen during the impact event. The plate specimens of length 150 mm and width 100 mm are impacted by a semi-spherical steel impactor with a diameter of 20 mm shown in Figure 7.1b. The photograph also shows the integrated load cell used for acquiring the force history during

[1] Section 7.1 is reproduced from Jackstadt et al. [286, 233] with linguistic changes and additions.

the impact event. The impactor mass is set as $m = 5.25\,\mathrm{kg}$. Furthermore, every impact experiment is recorded by a high-speed camera in order to assess the impact event for possible rebounds or other undesired effects. Furthermore, this allows for a qualitative assessment of the specimens' shape immediately after the impact event.

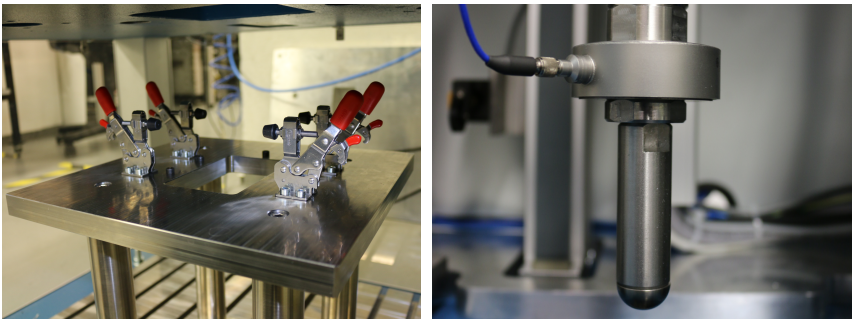

(a) Support fixture **(b)** Impactor with load cell

Figure 7.1: Experimental setup for low-velocity impact tests. **(a)**: support fixture with four retaining clamps in the open position. **(b)**: semi-spherical impactor and load cell.

Impact tests with different impact energies E_{imp} are executed by changing the height h_{imp} from which the impactor is released. The corresponding height is given by

$$h_{\mathrm{imp}} = \frac{E_{\mathrm{imp}}}{mg} \tag{7.1}$$

where $g = 9.81\,\mathrm{m\,s^{-2}}$ denotes the gravitational acceleration. Table 7.1 gives an overview of the three impact scenarios.

Table 7.1: Parameters for the drop-weight impact experiments. All tests are conducted with a constant mass.

E_{imp}	m_{imp}	h_{imp}
5 J	5.25 kg	97.08 mm
10 J	5.25 kg	194.17 mm
20 J	5.25 kg	388.33 mm

In order to assess the post-impact damage, microsections of select damaged specimens are prepared. Small samples are cut from the damaged plates with an Accutom wet cut-off machine from Struers GmbH at a very low feed of $0.1\,\mathrm{mm\,s^{-1}}$ at 2800 rpm to prevent any further damage progression. The samples are then sanded using grinding disks of grit sizes 600, 1000 and 2500. Finally, they are embedded in epoxy resin for subsequent light microscopy.

7.1.2 Results

The results of the drop-weight impact experiments on the four FMELs are presented in the following. Figure 7.2 shows two examples of an impact event with the maximum impact energy of $E_{\mathrm{imp}} = 20\,\mathrm{J}$. For both laminates shown, a significant transverse deflection as well as deformation is visible.

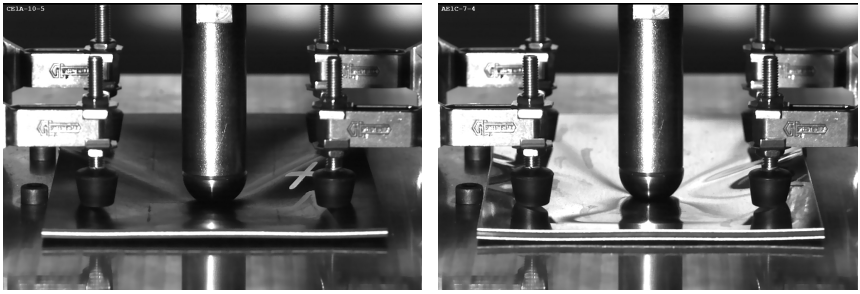

(a) Laminate C-E1-A-E1-C **(b)** Laminate A-E1-C-E1-A

Figure 7.2: High-speed photographs of two laminates during low-velocity impact with $E_{\mathrm{imp}} = 20\,\mathrm{J}$.

Figure 7.3 shows the recorded history of force F over time t during the impact events of different impact energies. In all four laminates, the strong strain rate dependency resulting from the viscoelastic, thus rate-dependent, elastomer plies is visible, as greater impact energies lead to higher impact velocities. Steeper slopes in the loading part of the curves are the result. Considering the curves with an impact energy of 5 J, where no damage onset in the form of oscillations is visible, almost no difference is visible between laminates

A-E1-C-E1-A and A-E2-C-E2-A. Laminates C-E1-A-E1-C and C-E2-A-E2-C on the other hand visibly differ in their loading curve. Consequently, the choice of elastomer material is more defining under impact loading in laminates of type C-E-A-E-C due to the thicker outer CFRP sublaminate. This is coherent with the above calculated static bending deflections in Section 5.3.2. When impacted with energies of 10 J, all laminates except C-E1-A-E1-C show oscillations indicating the onset of damage at forces exceeding approximately 3000 N. An impact energy of 20 J consequently leads to damage in all laminates. Laminates featuring the stiffer elastomer E2 exhibit oscillations of higher amplitudes, indicating reduced damping by the material due to its lower loss factor, see Figure 4.4. Furthermore, oscillations are assumed to be the result of progressive failure such as intra-ply damage within the CFRP plies or delaminations. Plastic deformation, mostly of the aluminium plies, is not known to cause strong oscillations but rather a decrease in slope of the loading curve. This explains the stronger oscillations in laminates of type C-E-A-E-C as here the CFRP plies are in direct contact with the impactor. Furthermore, whereas in laminates A-E-C-E-A only the aluminium ply is in contact as the remainder of the laminate is below the first elastomer ply, and thus protected from the impact, in case of laminates C-E-A-E-C, four plies of CFRP receive the largely undamped force of the impactor. Consequently, damage is assumed in all four plies of CFRP, superimposing each other and thus causing the more oscillations.

The force-displacement curves of the impact events in Figure 7.4 give an indication of the remaining deformation after the impact event. These curves, however, do not give an insight into the exact location of occurring plasticity and thus these are referred to as permanent deformations hereafter since not all layers in permanently deformed laminate necessarily deform plastically on a material level. Generally, laminates A-E1-C-E1-A and A-E2-C-E2-A exhibit higher permanent deformations than those laminates where the CFRP plies are located on the outside, which can be attributed to the higher amount of plastically deforming aluminium plies as well as their direct contact with the impactor.

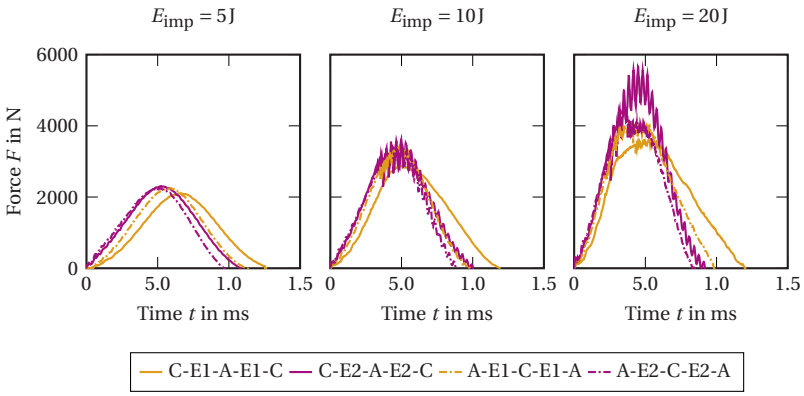

Figure 7.3: Results of low-velocity drop-weight experiments for three different impact energies and four different FMELs. Plots show impact force F over time t.

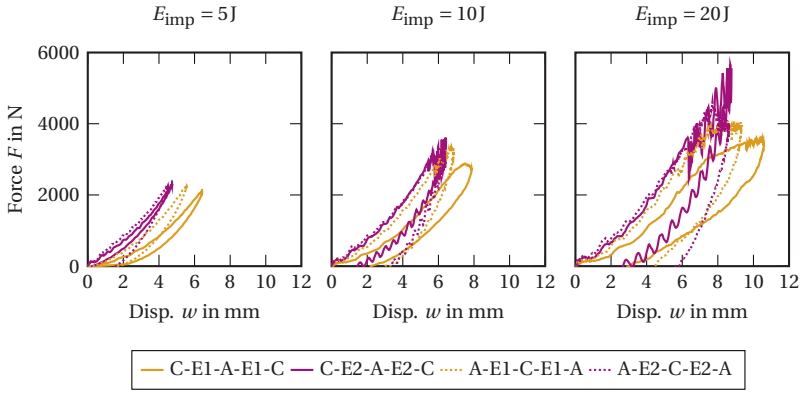

Figure 7.4: Results of low-velocity drop-weight experiments for three different impact energies and four different FMELs. Plots show impact force F over transverse displacement w.

Figure 7.5 shows the energy, calculated from the force-displacement curves by continuous integration, transferred to the specimens during impact. Notably, not all energy is transferred back to the impactor at the end of the impact event. This is due to a number of dissipative phenomena. First of all, some amount of energy is dissipated as heat during the deformation of the viscoelastic elastomers. This portion, however, is small as can be seen in

the 5 J curves of laminates C-E1-A-E1-C and C-E1-A-E1-C, where no damage is assumed. In consequence of the higher elastic deformation and higher loss factor of laminates containing the softer elastomer E1, more energy is dissipated in these laminates than in those containing the stiffer elastomer E2. Due to the aforementioned plastic deformation of the aluminium layers and the subsequent permanent deformation of the whole laminate, some more energy is dissipated in the other two laminates. This is confirmed by the curves from higher impact energies, which show significant amounts of permanent deformation according to Figure 7.4.

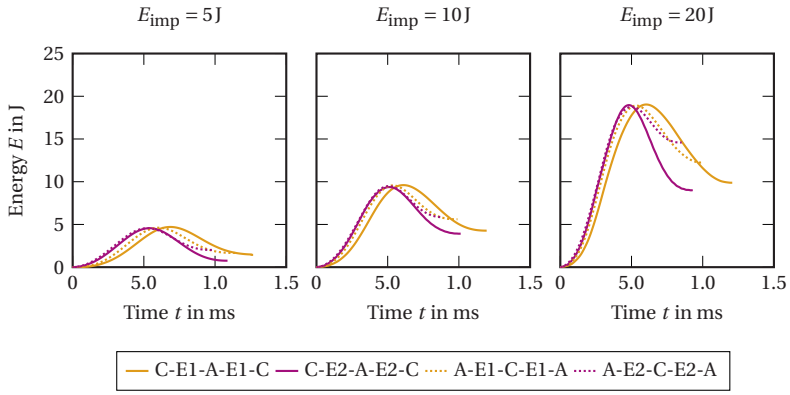

Figure 7.5: Results of low-velocity drop-weight experiments for three different impact energies and four different FMELs. Plots show impact energy E_{imp} over time t.

Microsections of damaged plates impacted with an energy of 10 J are shown in Figure 7.6. The strong permanent deformations of laminates of type A-E-C-E-A, compare Figure 7.4, are also visible here. Furthermore, observed damage types include intra-ply damage of the CFRP plies as well as delaminations between 0° and 90° layers within CFRP sublaminates. In the microsection of laminate C-E1-A-E1-C, there are no visible delaminations only a single localized crack in one of the CFRP layers. This indicates, that no damage has occurred with the given impact energy, which is confirmed by the absence of

oscillations or drops in the force-time curve in Figure 7.3. Solely laminate A-E1-C-E1-A shows a ruptured lower elastomer layer. This likely resulted from a delamination between the elastomer layer and the lowest of CFRP plies. The delamination is then open following the elastic spring-back of the central CFRP sublaminate after the impact when at the same time the plastically deformed lower aluminium ply is constraining the movement of the elastomer ply. As a consequence, the edges of the delaminated area become crack tips from which the elastomer ruptures at an angle until the crack reaches the next interface, in this case with the lower aluminium ply.

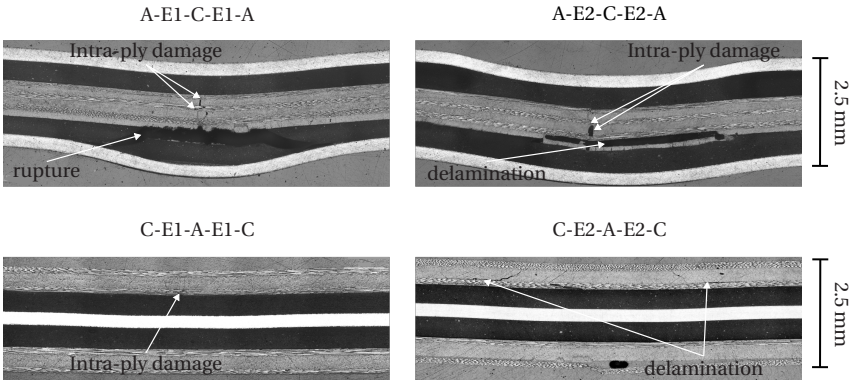

Figure 7.6: Microsections of four damaged laminates impacted with an impact energy of 10 J. Visible types of damage include intra-ply failure in CFRP plies, delaminations, permanent deformation and a ruptured elastomer layer.

To summarize, the experimental results outlined above indicate the presence of damage even at low impact energies. Laminates of type C-E-A-E-C offer a higher impact resistance in terms of occurring damage than laminates of type A-E-C-E-A, which, in turn, dissipate more impact energy due to more plastic deformation of the aluminium layers. The observed types of damage are intra-ply damage of CFRP plies, delaminations not restricted to specific interfaces and extensive permanent deformation caused mainly by the aluminium alloy's plasticity. Since the aforementioned rupture of the

elastomer layer is essentially a delamination, it will be treated as such in the following. Further microsections of different specimens at the same and varying impact energies do not reveal a different damage pattern and are thus omitted for brevity.

7.2 Numerical modelling of impact damage within CLD[1]

7.2.1 Methods

7.2.1.1 Finite element modelling of FMEL

The FEM is employed for creating and solving models of damaged FMELs in the frequency-domain. The commercial FE solver Abaqus/Standard 2023 is used for this purpose. The laminates are modelled as solid 3D deformable bodies. Each material layer is discretized by three elements over its thickness. CFRP layers are modelled using linear continuum shell elements SC8R with reduced integration. Quadratic continuum elements of type C3D20R with reduced integration are chosen for the aluminium plies. Analogously to Section 6.2.1.3, reduced integration hybrid elements C3D20RH are used to model the elastomer layers. The laminates' vibration and damping behaviour is determined through complex modal analysis representing free vibration, yielding the natural frequencies

$$f_n = \frac{|\Im(\lambda_n^*)|}{2\pi} \tag{7.2}$$

[1] Section 7.2 is reproduced from Jackstadt et al. [233] with minor linguistic changes and additions.

and effective modal damping ratios

$$\xi_n = -2\frac{\Re\left(\lambda_n^*\right)}{\left|\Im\left(\lambda_n^*\right)\right|}. \tag{7.3}$$

These are calculated from the complex eigenvalue λ_n^* of the n^{th} vibration mode of the complex eigenvalue problem

$$\left(\lambda_n^{*2}\mathbf{M} + \mathbf{K}^*\right)\Phi_n = \mathbf{0} \tag{7.4}$$

with the complex valued stiffness matrix $\mathbf{K}^*$, mass matrix $\mathbf{M}$ and the n^{th} eigenvector Φ_n of the FEM model.

7.2.1.2 Modelling of impact damage

In Section 7.1.2, the occurring types of damage in FMELs under low-velocity impact loading have been determined to be intra-ply damage of FRP layers, delaminations in arbitrary interfaces and permanent deformation of the whole laminate. The following paragraphs introduce the modelling approaches for depicting these three damage phenomena . The proposed modelling approaches do not aim at modelling damage initiation and evolution, but are meant to depict the effect of said types of damage in the vibration and damping behaviour of FMELs in the frequency-domain.

Intra-ply damage The observed intra-ply damage within the CFRP plies is modelled as an effective stiffness degradation based on the progressive damage model proposed by Lapcyk and Hurtado [308]. In a state of plane stress, as imposed by the continuum shell formulation, stresses are given as $\boldsymbol{\sigma} = (\sigma_{11} \quad \sigma_{22} \quad \sigma_{12})^\top$ and elastic strains as $\boldsymbol{\varepsilon} = \left(\varepsilon_{11} \quad \varepsilon_{22} \quad \gamma_{12}\right)^\top$. The constitutive relation is then given by

$$\boldsymbol{\sigma} = \boldsymbol{C}_{\text{d}}\boldsymbol{\varepsilon}_{\text{el}}. \tag{7.5}$$

The damaged elasticity matrix is defined to be

$$\boldsymbol{C}_{\mathrm{d}} = \frac{1}{d}\begin{bmatrix} (1-d_{\mathrm{f}})\,E_1 & (1-d_{\mathrm{f}})\,(1-d_{\mathrm{m}})\,\nu_{21}E_1 & 0 \\ (1-d_{\mathrm{f}})\,(1-d_{\mathrm{m}})\,\nu_{12}E_2 & (1-d_{\mathrm{m}})\,E_2 & 0 \\ 0 & 0 & (1-d_{\mathrm{s}})\,dG_{12} \end{bmatrix}. \quad (7.6)$$

In Equation (7.6), three parameters describe the current state of damage. First of all, parameter d_{f} quantifies the degree of fibre damage. Matrix damage is represented by parameter d_{m}. A distinction between tension and compression for fibre and matrix damage parameters d_{f} and d_{m} is omitted as opposed to the original model as this cannot be considered in modal analysis. Shear damage of the fibre-matrix interface is accounted for by the damage parameter

$$d_{\mathrm{s}} = 1-(1-d_{\mathrm{f}})^2\,(1-d_{\mathrm{m}})^2\,. \quad (7.7)$$

The combined damage parameter d is introduced as

$$d = 1-(1-d_{\mathrm{f}})\,(1-d_{\mathrm{m}})\,\nu_{12}\nu_{21}. \quad (7.8)$$

Notably, parameters d_{s} and d are not independent model parameters as they are calculated from parameters d_{f} and d_{m}. The above constitutive relation, Equation (7.5), is implemented in dependence on damage input parameters d_{f} and d_{m} as a user-defined material Fortran subroutine UMAT for Abaqus/Standard. Plane stress is enforced by the use of continuum shell elements for all CFRP plies.

Delaminations The occurrence of delaminations after impact in arbitrary plies is modelled based on an unconstrained approach as first proposed in [241]. This modelling approach is chosen as it represents the lower bound for the natural frequency of the delaminated structure [245, 251] and is thus assumed to also represent the lowest load transmission into the damping layers, making it the worst case for the CLD mechanism. The laminated plate is divided into separate domains at interfaces in which a delamination

is to be modelled. The delaminated area of arbitrary shape and size is thus described by one surface each on both domains. The surfaces making up the remainder of the interface, which is not delaminated, are permanently bonded using a kinematic tie constraint, preventing any relative motion. This tie constraint is resolved on the two surfaces making up the delamination. This modelling approach allows for an opening of delaminations during vibration, which has been reported to occur in experiments by Shen and Grady [244] and subsequent papers. Penetration of the two domains, however, is not prevented. Furthermore, this approach, as opposed to modelling the delamination with cohesive elements, does not introduce an additional thickness into the laminate, facilitating comparisons with undamaged models without any interface modelling.

Permanent deformation In this work, the permanent deformation of impacted laminates is modelled by a stress-free mesh deformation approach. First, a finite element model of the undeformed laminate is created. Subsequently, all nodes are translated in transverse direction based on an analytical function $w = f(x, y)$ describing the predeformed structure. As this corresponds to a simple shear deformation, this mesh transformation is isochoric, thus not changing volume or mass of the model. The function used throughout this work is given by

$$w\left(x, y\right) = -w_{\max} \exp\left(-\frac{\left(\frac{2x}{a} - 1\right)^2 + \left(\frac{2y}{b} - 1\right)^2}{4s} \right), \tag{7.9}$$

where $w_{\max}$ is the maximum permanent translation in z-direction. Parameters a and b correspond to the rectangular plate's in-plane dimensions in x- respectively y-direction. The origin of the coordinate system lies in the corner of the plate. Furthermore, the parameter s controls the localization of the permanent deformation towards the centre of the plate, respectively the location of impact. The influence of this parameter s is shown in Figure 7.7, where higher values of s signify a less localized deformation.

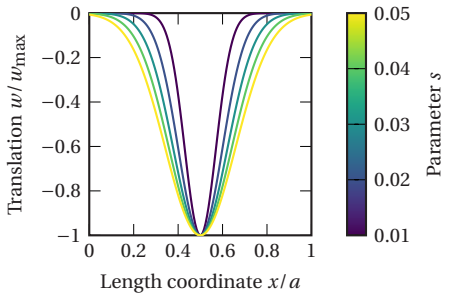

Figure 7.7: Normalized display of $w(x, y)$ in Equation (7.9) for $y = b/2$. The figure shows the deflection distribution for multiple values of s. Higher values of s lead to a more localized deformation.

7.2.1.3 Parametric study

The modelling approaches proposed above are utilized to numerically assess, how different states and types of damage influence the damping behaviour of FMELs. The three individual modes of damage, namely intra-ply damage, delamination and permanent deformation, are investigated individually and include, but are not limited to, those seen in the accompanying experiments. The corresponding numerical parametric studies are introduced in the following paragraphs. In each case, an impacted plate of dimensions $a = 150\,\text{mm}$ and $b = 100\,\text{mm}$ is considered. The same four configurations as experimentally investigated in Section 7.1 are considered. Figure 7.8 shows the naming convention for plies and interfaces used for the two laminate types, namely C-E-A-E-C (left) and A-E-C-E-A (right).

A free-free boundary condition is chosen to analyse the plates' first ten vibration modes under free vibration. For these studies, a property evaluation frequency in the complex modal analysis is set as $f_{\text{eval}} = 1500\,\text{Hz}$. This frequency is chosen, because it represents the centre of the interval, in which the natural frequencies of the first ten vibration modes lie.

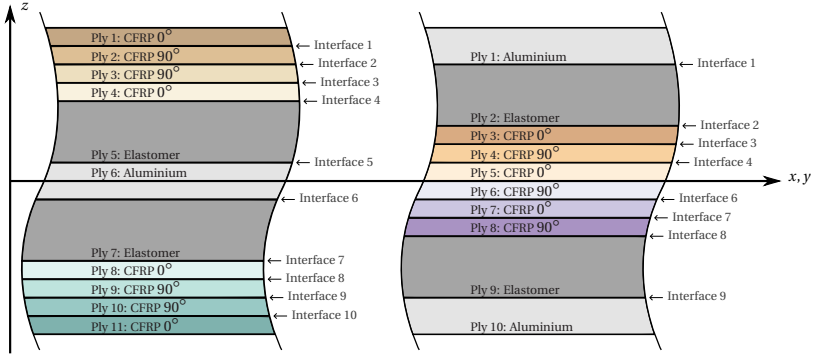

Figure 7.8: Schematic layup illustration of laminate types C-E-A-E-C (left) and A-E-C-E-A (right). Plies and interfaces are numbered accordingly. Both types have the same overall thickness and the same volume fraction of elastomer material. Dimensions not to scale. Reproduced from Jackstadt et al. [233].

Intra-ply damage The analysis of the influence of reduced load-bearing capabilities in the CFRP plies on the CLD mechanism within FMELs is undertaken herein. To achieve this, intra-ply damage is presumed to manifest independently in each CFRP ply, facilitating the identification of critical plies within the laminates. The maximum occurring value for the fibre damage parameter in Equation (7.6) is set at $d_{\mathrm{f,max}} = 0.9$. Simultaneously, the same value is assigned to the maximum matrix damage parameter as $d_{\mathrm{m,max}} = 0.9$, resulting in a peak shear damage parameter of $d_{\mathrm{s,max}} \approx 1$. This extent of intra-ply damage is illustrated in Figure 7.9a. Subsequently, for the plies identified as critical through this methodology, both damage parameters, $d_{\mathrm{f,max}}$ and $d_{\mathrm{m,max}}$, are systematically varied within the range of 0 to 1. This variation aims to explore the influence of both fibre and matrix damage on the CLD mechanism.

Delaminations In the context of this investigation, it is postulated that delaminations may theoretically manifest in all interfaces of the laminates under consideration. The primary objective of the initial phase of this study is to pinpoint critical interfaces, where potential delaminations exert

the most significant impact on vibration and damping characteristics. To achieve this, a systematic examination is conducted by introducing a hypothetical circular delamination with a defined radius $r = 25\,\text{mm}$ at the central point of the plate, corresponding to the point of impact. This hypothetical scenario is individually applied to each interface, encompassing instances where delaminations are experimentally observed. Figure 7.9b illustrates the visualization of such a delamination in one representative interface. Subsequently, an analysis is performed to scrutinize the influence of delamination size on selected interfaces.

Permanent deformation The examination of the influence of permanently deformed FMELs is undertaken through the utilization of multiple plates subjected to deformation as prescribed by Equation (7.9). The parameter w_{max}, denoting the maximum deformation, is systematically varied within the interval of 0 mm to 10 mm. This range encompasses the deformations observed in the impact experiments and is incremented by 1mm, employing a distribution parameter s set at 0.05. It is noteworthy that identical meshes are employed for each laminate prior to the initiation of mesh predeformation. Figure 7.9c visually represents a mesh permanently deformed with $w_{\text{max}} = 10\,\text{mm}$, serving as an illustrative example.

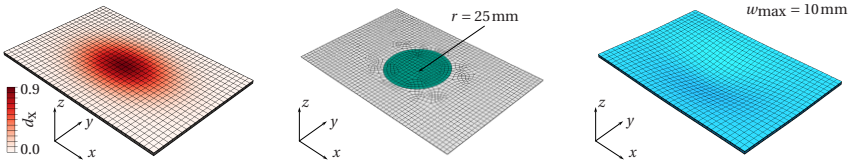

(a) Intra-ply damage **(b)** Delamination **(c)** Permanent deformation

Figure 7.9: FEM models or parts of those representing the three types of damage resulting from impact loading. **(a)**: Exemplary distribution of fibre or matrix parameters d_{f} and d_{m}. **(b)**: Circular delamination. **(c)**: Stress-free deformed mesh. Reproduced from Jackstadt et al. [233].

7.2.2 Results

7.2.2.1 Undamaged laminates

The first ten modes for a free-free boundary condition determined in numerical complex modal analysis on undamaged laminates are shown in Table 7.2 for the four different configurations of FMELs. Whereas the occurring mode shapes are mostly identical for lower modes, they differ for the higher modes. The values listed in Table 7.2 differ from those previously presented in Figure 5.18 and Table A.3 due to the difference in boundary conditions.

Table 7.2: First ten mode shapes of four undamaged FMELs determined numerically. Colours indicate the normalized deflection in transverse direction. The occurrence of specific modes is dependent on the laminate in some cases. Reproduced from Jackstadt et al. [233].

Laminate	1	2	3	4	5	6	7	8	9	10
C-E1-A-E1-C										
C-E2-A-E2-C										
A-E1-C-E1-A										
A-E2-C-E2-A										

The modes in terms of their natural frequencies f_n and corresponding modal damping ratios ξ_n are shown in Figure 7.10. These mode-based values will serve as objects of comparison for those determined on damaged laminates below. The results in Figure 7.10 show that the four laminates have similar stiffness as their natural frequencies differ only slightly. When considering the higher modes, laminates C-E2-A-E2-C and A-E2-C-E2-A appear to be stiffer than laminates C-E1-A-E1-C and A-E1-C-E1-A, indicating that the stiffness of the elastomer has a higher influence on the natural frequency than the general layup of the laminate. A comparison of the modal damping

ratios shows significantly higher damping of laminates C-E1-A-E1-C and A-E1-C-E1-A compared to the laminates containing the stiffer elastomer E2. These observations are in accordance with those determined analytically for simply-supported plates of identical dimensions, see Figure 5.18. The same arguments apply regarding elastomer E1's higher loss factor tan (δ).

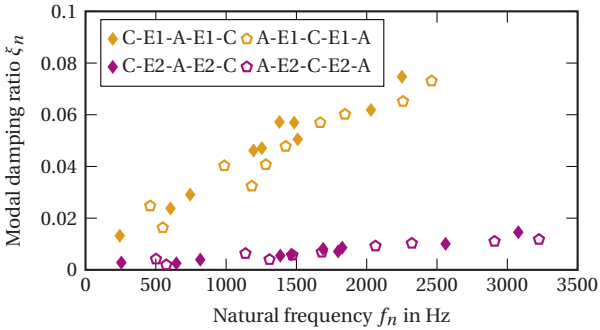

Figure 7.10: Natural frequencies and modal damping ratios of undamaged FMEL plates for their first ten vibration modes as listed in Table 7.2. Reproduced from Jackstadt et al. [233].

7.2.2.2 Influence of intra-ply damage

Influence of location For the ten vibration modes listed in Table 7.2, Figure 7.11 displays the relative changes in natural frequencies and modal damping ratios compared to an undamaged laminate of the same configuration for individual intra-ply damages in different CFRP plies.

In all scenarios examined, the introduction of intra-ply damage induces a noticeable decrease in natural frequencies, primarily attributable to an overall reduction in the laminates' bending stiffness. This reduction, however, exhibits a discernible dependence on the specific vibration mode n, accompanied by occasional shifts in mode shapes. Particularly noteworthy is the extent of this decrement, which can be substantial, reaching up to approximately 8 % for laminates C-E1-A-E1-C and C-E2-A-E2-C. In contrast,

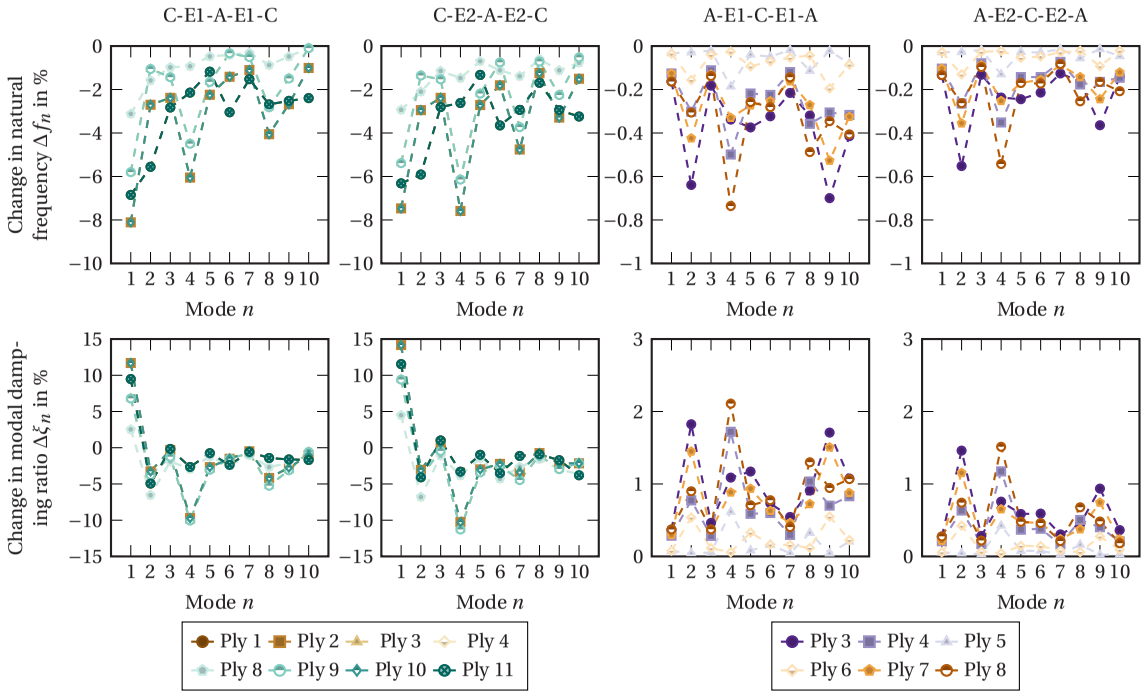

Figure 7.11: Relative change in natural frequencies and modal damping ratios of the vibration modes listed in Table 7.2 compared to an undamaged plate (Figure 7.10). Results are displayed for four different FMELs and different individual CFRP plies affected by intra-ply damage. Reproduced from Jackstadt et al. [233].

laminates A-E1-C-E1-A and A-E2-C-E2-A experience a considerably smaller decrease, staying below 1 %. This disparity is attributed to the fact, that the damaged CFRP plies in laminates of type C-E-A-E-C are further on the outside than in laminates of type A-E-C-E-A. Therefore, a change in stiffness due to damage has a comparably higher influence. Another difference between the two types of laminates is attributed to the balanced nature of laminates of type C-E-A-E-C, as depicted in Figure 7.8, where opposing plies (e.g., Ply 1 and Ply 11 or Ply 3 and Ply 9) yield identical outcomes. On the other hand, laminates A-E1-C-E-A and A-E2-C-E2-A, classified as unbalanced laminates, exhibit asymmetrical responses. Turning attention to the analysis of relative changes in modal damping ratios, laminates C-E1-A-E1-C and C-E2-A-E2-C demonstrate a nuanced pattern with both positive and negative variations. For instance, Mode 1 exhibits an increased damping ratio when subjected to damage in all plies, while Mode 4 shows a damping minimum for damage in Ply 2 and Ply 10. In the case of laminates A-E1-C-E1-A and A-E2-C-E2-A, the influence on modal damping ratios due to intra-ply damage is generally smaller, and the changes consistently manifest a positive trend. It is noticeable that Mode 4, characterised by an identical shape across all laminates, experiences the most pronounced impact in terms of altered damping ratios.

In order to identify pivotal plies, in which intra-ply damage has the strongest influence on CLD, the median relative change in natural frequencies and modal damping ratios of the first ten vibration modes is considered for damage in each ply. These results are shown as box plots in Figure 7.12 for the four FMELs.

When examining the median change in natural frequencies in Figure 7.12, the pronounced influence of intra-ply damage in the outermost CFRP plies becomes evident, resulting in a reduction of natural frequencies. Notably, laminates A-E1-C-E1-A and A-E2-C-E2-A, with CFRP plies positioned further outward,as illustrated in Figure 7.8, exhibit median changes in natural frequencies that are less pronounced by an order of magnitude compared to laminates C-E1-A-E1-C and C-E2-A-E2-C. It is noteworthy that laminates

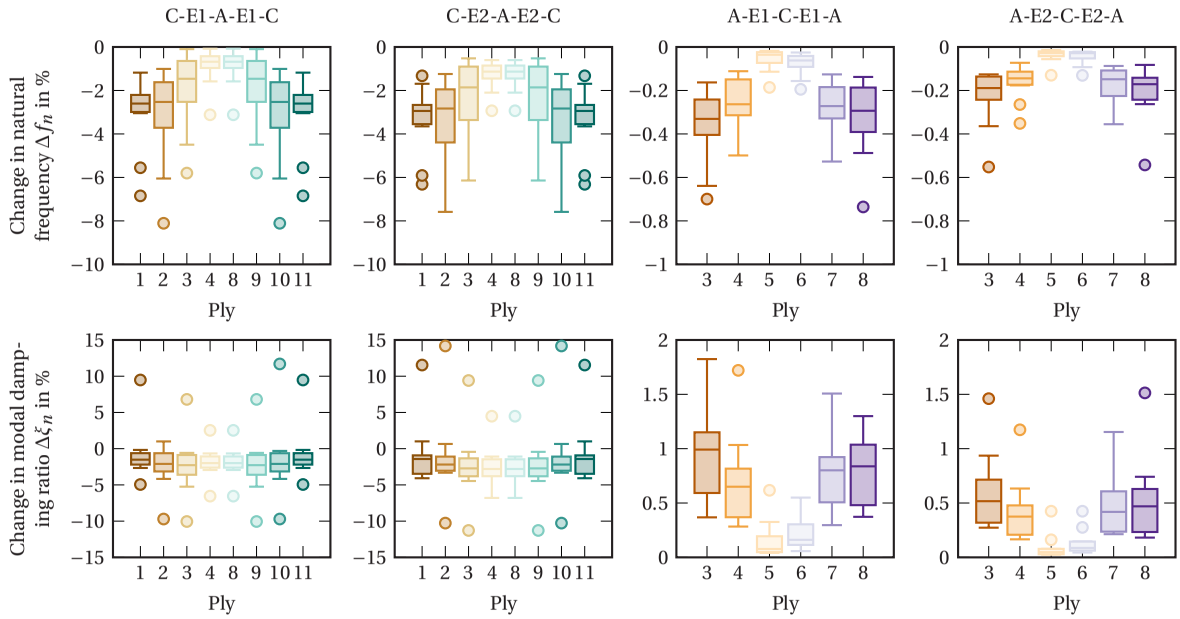

Figure 7.12: Box plots showing the change of natural frequency and modal damping ratio of the first ten vibration modes caused by intra-ply damage in the individual CFRP plies corresponding to Figure 7.8. Plots show the median values, the lower and upper quartiles as boxes, the smallest and largest change values within one and a half times the interquartile range as whiskers and outliers as points. Adapted from Jackstadt et al. [233].

A-E1-C-E1-A and A-E2-C-E2-A display unsymmetrical median changes in natural frequencies relative to their unsymmetrical stacking sequence. Upon assessing median changes in modal damping ratios, laminates C-E1-A-E1-C and C-E2-A-E2-C display lower modal damping ratios in response to intra-ply damage. Conversely, laminates A-E1-C-E1-A and A-E2-C-E2-A demonstrate an increase in modal damping due to intra-ply damage. Notably, intra-ply damage in Ply 3 and Ply 8 in laminates A-E1-C-E1-A and A-E2-C-E2-A results in a comparably high median change in modal damping, given their adjacency to the elastomer damping layers. A similar observation is made for laminate C-E2-A-E2-C, where damage in Ply 4 and Ply 8 exerts the strongest influence on the modal damping ratio. In contrast, laminate C-E1-A-E1-C sees the highest median change as a consequence of intra-ply damage in its two 90° plies. Additionally, insights drawn from Figure 7.12 highlight the role of elastomer selection in FMELs. The utilization of the softer elastomer E1 enhances damage tolerance in laminate C-E1-A-E1-C compared to laminate C-E2-A-E2-C, both in terms of stiffness reduction and modal damping ratios. Conversely, this observation is reversed when comparing laminates A-E1-C-E1-A and A-E2-C-E2-A, where the stiffer elastomer E2 contributes to a higher tolerance to the specified states of intra-ply damage.

To summarize, the results presented above show, that intra-ply damage within the CFRP affects the vibration characteristics of FMELs to different extents. The natural frequencies of a structure are predominantly influenced by damaged CFRP layers the furthest away from the neutral plane, as these usually bear the majority of the load. A different conclusions is reached for the modal damping ratios. Here, plies closest or adjacent to the elastomer damping layers are deemed critical as damage, and thus stiffness reduction, impedes their ability in fulfilling their role as a constraining layer within the CLD setup.

Influence of damage extent Figure 7.13 shows the influence of damage parameters $d_{\mathrm{f,max}}$ and $d_{\mathrm{m,max}}$ for an intra-ply damage in Ply 4 of laminate C-E1-A-E1-C, which is adjacent to the elastomer damping layer and, according

to Figure 7.12, has the highest median influence on modal damping. Depicted are the natural frequencies and modal damping ratios of the first four vibration modes according to Table 7.2 relative to the undamaged state. The contour lines represent states of equal damage regarding a change in natural frequency or modal damping ratio, respectively. While for Mode 1, fibre as well as matrix damage seem to have an equal influence on both, natural frequency and modal damping ratio, Mode 2 is dominated by fibre damage alone. Modes 3 and 4 show a significantly lower dependence on intra-ply damage, see Figure 7.11.

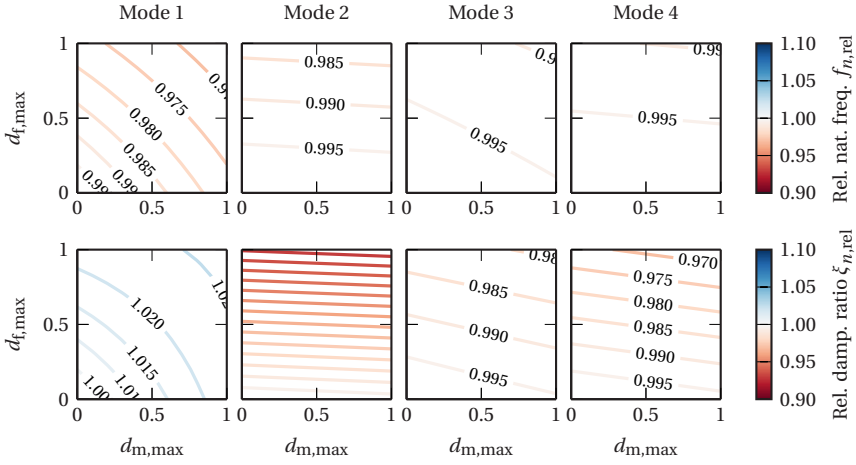

Figure 7.13: Relative natural frequencies (top) and relative modal damping ratios (bottom) of laminate C-E1-A-E1-C for different values of maximum fibre damage $d_{\mathrm{f,max}}$ and maximum matrix damage $d_{\mathrm{m,max}}$ in Ply 4 (see Figure 7.8) for the first four vibration modes. Contour lines represent an equal extent of damage-induced change in natural frequency or modal damping ratio. Contour line labels are omitted for Mode 2 for the sake of readability. Reproduced from Jackstadt et al. [233].

Analogously, Figure 7.14 shows the influence of fibre and matrix damage on the first four vibration modes of laminate A-E1-C-E1-A with a damaged Ply 3, again adjacent to the elastomer damping layer. Here, Mode 2 is influenced

significantly stronger than the other modes, although matrix damage has almost no influence. The contour lines follow the same trajectories as for laminate C-E1-A-E1-C, suggesting a similar dependence on fibre and matrix damage. Modal damping ratios of laminate C-E1-A-E1-C, however, are influenced much stronger than the natural frequencies, as indicated by the proximity of contour lines.

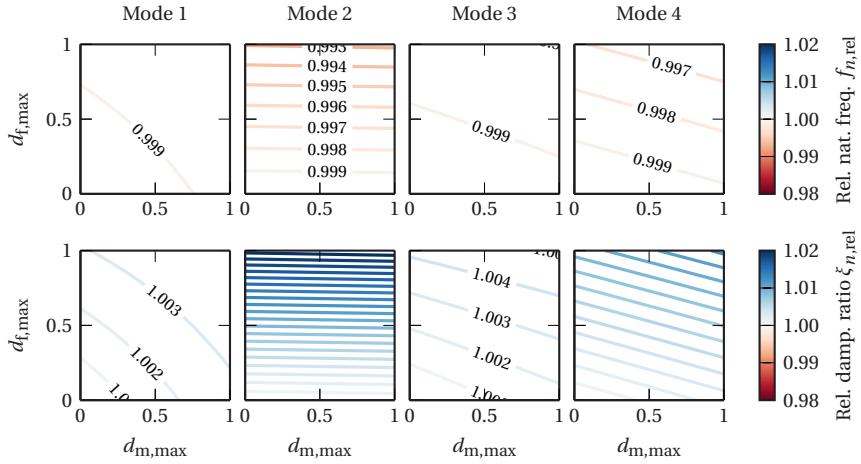

Figure 7.14: Relative natural frequencies (top) and relative modal damping ratios (bottom) of laminate A-E1-C-E1-A for different values of maximum fibre damage $d_{f,max}$ and maximum matrix damage $d_{m,max}$ in Ply 3 (see Figure 7.8) for the first four vibration modes. Contour lines represent damage an equal extent of damage-induced change in natural frequency or modal damping ratio. Contour line labels are omitted for Modes 2 and 4 for the sake of readability. Reproduced from Jackstadt et al. [233].

7.2.2.3 Influence of delaminations

Influence of location The comparative analysis of relative changes in natural frequencies and modal damping ratios of delaminated plates, in relation to the undamaged ones of the same laminate type, is presented

in Figure 7.15. Focused on individual delaminations with a fixed radius of $r = 25\,\text{mm}$ occurring in distinct interfaces, defined according to Figure 7.8, it is essential to note that only the modes specified in Table 7.2 are considered in the subsequent presentation. However, due to the unconstrained modelling approach, additional opening modes of the delaminated areas emerge. These additional modes are also evident in forced vibration of a simply supported plate, as depicted in Figure 7.16 for laminate A-E2-C-E2-A.

Furthermore, an increased incidence of mode shifts, surpassing those observed for intra-ply damage, is noted. This means that the mode shapes shown in Table 7.2 occur in a different order. Laminates C-E1-A-E1-C and C-E2-A-E2-C exhibit symmetric outcomes concerning their neutral plane, consistent with their symmetric layup. In contrast, the other two laminates do not show this symmetry. Generally, the presence of a delamination tends to result in a decrease in natural frequencies, with certain exceptions, such as observed in delaminated Interfaces 3 and 8 in laminates C-E1-A-E1-C and C-E2-A-E2-C according to Figure 7.8 for some modes. In these instances, the vibration mode of the damaged laminate is a superposition of the global mode, as pictured in Table 7.2, and an opening mode, denoted as a local mode, specific to the delaminated sublaminate. Across all laminates, a pronounced mode dependency is discerned, both in terms of natural frequencies and modal damping ratios, with changes in modal damping reaching up to 40 %. Laminates C-E1-A-E1-C and C-E2-A-E2-C exhibit the most substantial alterations in natural frequency and modal damping ratios for delaminations in interfaces between CFRP layers with 0° and 90° fibre orientation for certain modes. These delaminations align with those observed experimentally and visible in Figure 7.6. Additionally, laminate C-E2-A-E2-C experiences significant stiffness loss when Interface 5 and Interface 7, connecting to the elastomer layer, undergo delamination, highlighting the load-bearing role of the stiffer elastomer E2 compared to the softer elastomer E1 in laminate C-E1-A-E1-C. The most notable changes in natural frequency and modal damping ratio in laminates A-E1-C-E1-A and A-E2-C-E2-A are observed when interfaces connecting the elastomer layers are damaged. Notably, the choice

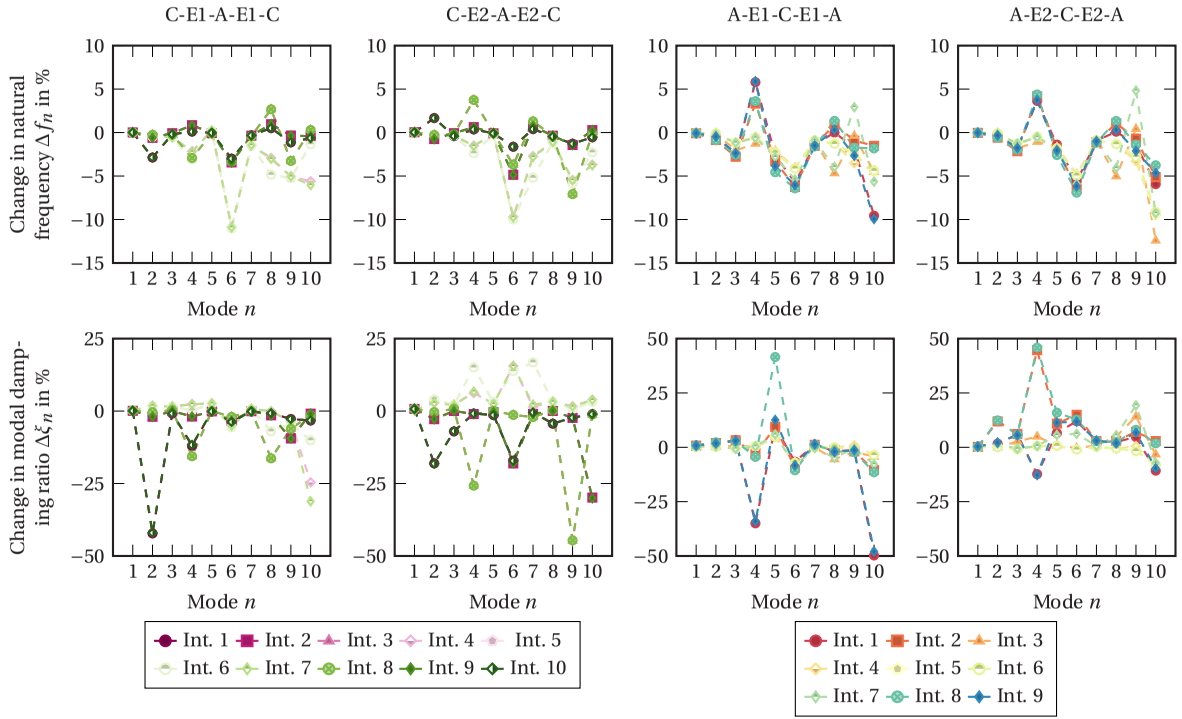

Figure 7.15: Relative change in natural frequencies and modal damping ratios of the vibration modes listed in Table 7.2 compared to an undamaged plate (Figure 7.10). Results are displayed for delaminations in different interfaces. Reproduced from Jackstadt et al. [233].

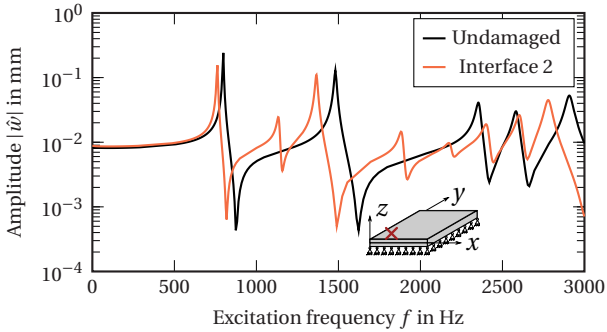

Figure 7.16: Numerically determined frequency response of simply supported laminates A-E2-C-E2-A to forced vibration. Comparison of an undamaged laminate and one with a delamination in Interface 2 (see Figure 7.8). Response recorded at $x = 0.2a$ and $y = 0.2b$. Reproduced from Jackstadt et al. [233].

of elastomer has a comparatively smaller impact on the vibrational behaviour of delaminated laminates of type A-E-C-E-A than on laminate type C-E-A-E-C.

The box plots in Figure 7.17 present the median alteration in natural frequencies and modal damping ratios, specifically focusing on the initial ten vibration modes induced by delaminations in distinct interfaces. Across all laminates, a consistent observation is a negative median change in natural frequency. Notably, laminates A-E1-C-E1-A and A-E2-C-E2-A exhibit heightened sensitivity to delaminations within the median of ten vibration modes compared to the other laminates. While the median influence on natural frequencies due to delaminations is similar for A-E1-C-E1-A and A-E2-C-E2-A, a notable difference is observed in C-E1-A-E1-C and C-E2-A-E2-C. In these laminates, the innermost interfaces, particularly those adjacent to the elastomer layers, exert a significantly more pronounced influence than interfaces situated between CFRP plies. Remarkably, Laminate A-E1-C-E1-A exhibits minimal median change in modal damping ratios, a characteristic attributed to the oscillation of the relative change values around zero in Figure 7.15 serving as the foundation for the median values shown here. Conversely, delaminations adjacent to the stiff elastomer layers in laminate

A-E2-C-E2-A result in exceptionally high median changes in modal damping ratios.

In conclusion, the results presented above serve to identify critical interfaces within the FMELs, which can impede the CLD mechanism. The natural frequencies as well as the modal damping ratios are altered the most by damaged interfaces adjacent to the elastomer damping layers. However, it depends on the laminate at hand as well as on the specific vibration mode to determine whether an increase or a decrease in modal damping occurs.

Influence of size Figure 7.18 illustrates the impact of varying delamination sizes on modal parameters, specifically exemplified for the second vibration mode, as detailed in Table 7.2. The analysis focuses on a single circular delamination, varying in radius, situated in the interface between CFRP and elastomer plies. For laminates of type C-E-A-E-C, this delamination is located in Interface 4, while for type A-E-C-E-A, it is positioned in Interface 2. For all four laminates, minimal changes in natural frequency are observed for delaminations smaller than 10 % of the overall interface area. Beyond this threshold, a linear decline in natural frequency is apparent, particularly pronounced in laminates A-E1-C-E1-A and A-E2-C-E2-A. Laminates C-E1-A-E1-C and C-E2-A-E2-C exhibit a more gradual decrease in the second natural frequency. Notably, laminates incorporating the stiffer elastomer E2 demonstrate a slightly lower susceptibility to increasing delamination size in the considered interfaces. The modal damping ratios for the second vibration mode generally experience an increment with larger delaminations. This effect is most conspicuous in laminate A-E2-C-E2-A. Interestingly, laminate A-E1-C-E1-A demonstrates a decrease in modal damping for delaminations exceeding 20 %. This phenomenon, attributed to superimposed opening modes of delaminated areas in laminate A-E1-C-E1-A, is unique among the configurations studied here. The decrease in modal damping ratios is explained by the deformation of elastomer Ply 2 in the superimposed opening mode. Driven by the significantly stiffer aluminium Ply 1, this mode induces high shear deformations in the bonded elastomer layer, creating an

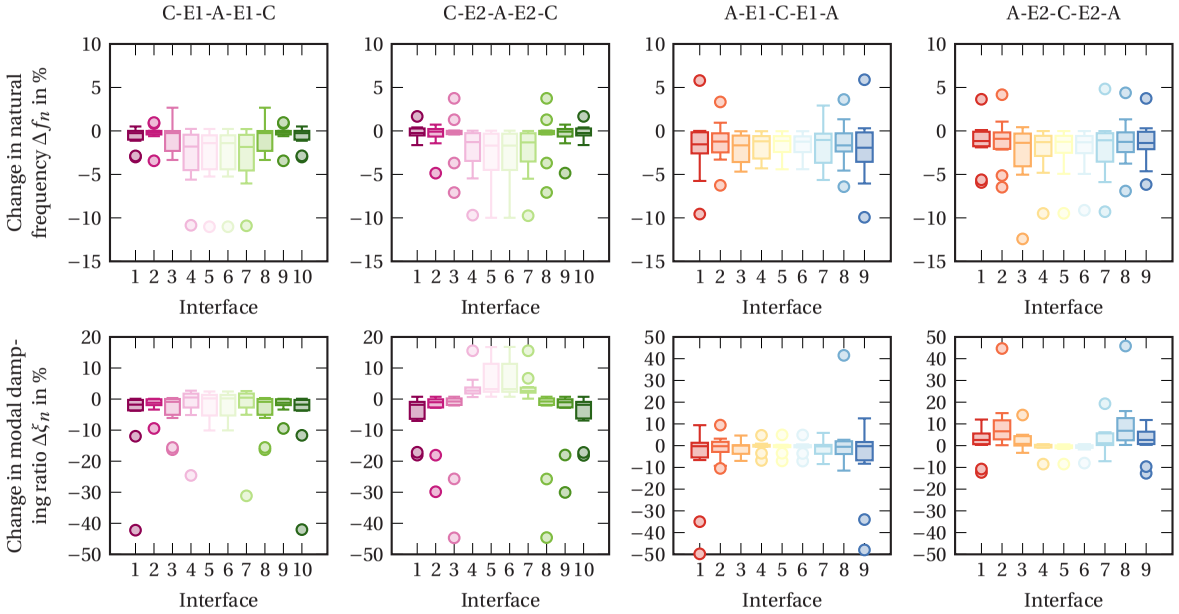

Figure 7.17: Box plots showing the change of natural frequency and modal damping ratio of the first ten vibration modes caused by delaminations in individual interfaces, according to Figure 7.8. Plots show the median values, the smallest and largest change values within one and a half times the interquartile range as whiskers and outliers as points. Adapted from Jackstadt et al. [233].

FLD effect. This effect is less effective for the more compliant elastomer E1, resulting in lower modal strain energies and, consequently, only one of the two elastomer layers actively participating in the dissipation of vibration energy. The CLD mechanism is far more effective, particularly for softer materials. However, for stiffer materials, FLD becomes dominant, leading to a significant increase in modal damping, as observed in laminate A-E2-C-E2-A. In contrast, laminates C-E1-A-E1-C and C-E2-A-E2-C, in this specific example of the second vibration mode, do not exhibit opening modes of delaminated areas. These correlations are outlined in the context of the second vibration mode only, emphasizing the robust mode dependency of CLD in damaged laminates. It is crucial to note that these relationships may differ for other vibration modes, underscoring the strong mode-dependency of CLD in the context of damaged laminates.

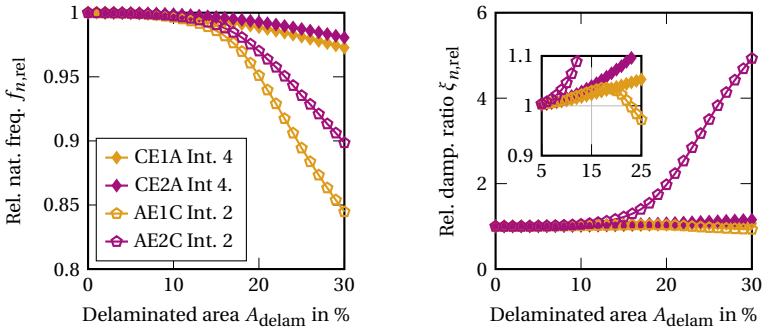

Figure 7.18: Influence of delamination size on the second vibration mode according to Table 7.2 for delaminations in critical interfaces. Reproduced from Jackstadt et al. [233].

7.2.2.4 Influence of permanent deformation

The results of varying stages of predeformation in FMEL plates due to impact are shown in Figure 7.19 in terms of change in natural frequencies and modal damping ratios. Different levels of permanent deformation are defined by variation of the parameter $w_{\max}$ in Equation (7.9).

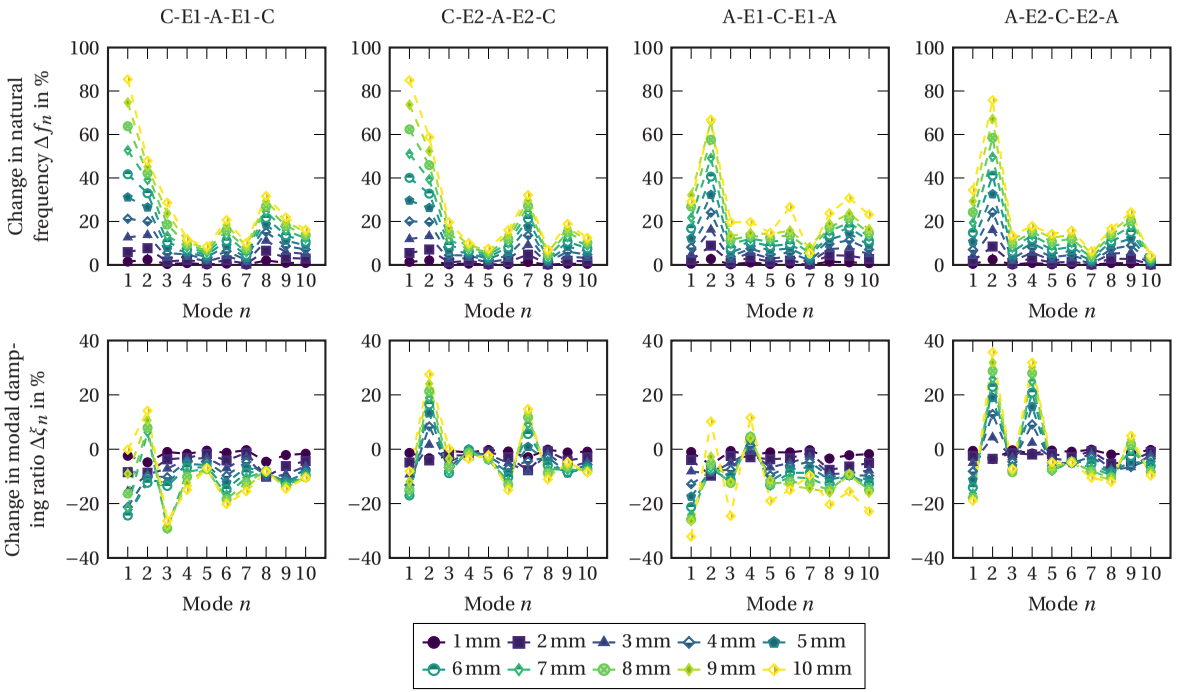

Figure 7.19: Relative change in natural frequencies and modal damping ratios of the vibration modes listed in Table 7.2 compared to an undamaged plate (Figure 7.10). Results are displayed for four different FMELs and ten different values of maximum predeformation depth $w_{\max}$ in Equation (7.9). Reproduced from Jackstadt et al. [233].

The imposition of permanent deformation across all examined FMELs consistently results in an increase of natural frequencies across the entire spectrum of considered vibration modes. Generally, more pronounced levels of permanent deformation act akin to reinforcements, contributing to heightened plate stiffness. However, the extent to which individual natural frequencies shift exhibits a strong dependency on the specific vibration mode. In the case of laminates C-E1-A-E1-C and C-E2-A-E2-C, the first vibration mode displays the most substantial shifts, particularly notable for higher values of parameter $w_{\max}$. Additionally, Mode 8 in C-E1-A-E1-C and Mode 7 in C-E2-A-E2-C exhibit noteworthy shifts compared to other modes. Remarkably, these modes, as documented in Table 7.2, are identical in both laminates, suggesting a similar mode of stiffening induced by the permanent deformation. Laminates A-E1-C-E1-A and A-E2-C-E2-A exhibit the most significant shifts in natural frequencies for Mode 2 and Mode 9, coinciding with the first and third one-dimensional longitudinal bending modes as illustrated in Table 7.2. Moreover, the second one-dimensional bending mode, Mode 6, also manifests a comparatively substantial shift in natural frequencies, especially in laminate A-E1-C-E1-A. Conversely, the trends in relative changes in modal damping ratios do not exhibit the uniformity observed in alterations of natural frequencies. While most states of permanent deformation result in reduced modal damping across the majority of modes, exceptions are evident. In the case of laminates C-E1-A-E1-C and C-E2-A-E2-C, for example, Mode 2 demonstrates significantly higher modal damping for higher values of $w_{\max}$. Notably, elevated values of $w_{\max}$ do not consistently correlate with a greater change in modal damping ratio, as observed for Mode 1 in laminates C-E1-A-E1-C and C-E2-A-E2-C. Further noteworthy observations pertain to laminate C-E2-A-E2-C, where Mode 7 shows a decrease in modal damping for lower levels of predeformation, while increased modal damping ratios are observed for values of $w_{\max}$ exceeding 5 mm. In Modes 2 and 4 of laminate A-E1-C-E1-A, elevated values of $w_{\max}$ lead to an increase in modal damping, whereas lower values yield a decrease. Similarly, in the case of laminate A-E2-C-E2-A, both Mode 2 and Mode 4 exhibit an increase in modal damping, even for lower levels of predeformation.

Figure 7.20 illustrates the median alterations in natural frequencies and modal damping ratios for the FMELs plates subject to permanent deformation defined by variations in w_{max} with the help of box plots. The median changes in natural frequencies exhibit an approximately linear correlation with the parameter w_{max}. Merely a deformation of $w_{max} = 10\,mm$ in laminate A-E1-C-E1-A results in a disproportionately higher median change in natural frequencies, attributed to the characteristics of the median employed. Notably, Modes 6 and 9 display an over-proportional shift for $w_{max} = 10\,mm$, see Figure 7.19, contributing to an elevated median change. In contrast, a clear linear trend is not evident in the median change of modal damping ratios, despite a consistent negative trend that intensifies with higher levels of pre-deformation in most cases. A comparison of median changes in modal damping ratios highlights a similarity between laminates featuring the same elastomer material. Laminates C-E1-A-E1-C and A-E1-C-E1-A, incorporating the softer elastomer material, exhibit a higher median decrease in modal damping ratios at equivalent levels of permanent deformation. Conversely, laminates C-E2-A-E2-C and A-E2-C-E2-A appear to be less affected in their modal damping capabilities by pre-deformation. Moreover, values of w_{max} exceeding 8 mm seem to mitigate the median decrease in modal damping ratios. The choice of elastomeric damping material, in this context, appears to exert a more substantial influence on the damage tolerance of the CLD mechanism than the general laminate layup. Importantly, the median changes in natural frequencies and modal damping ratios induced by permanent deformation surpass those caused by the other two types of damage.

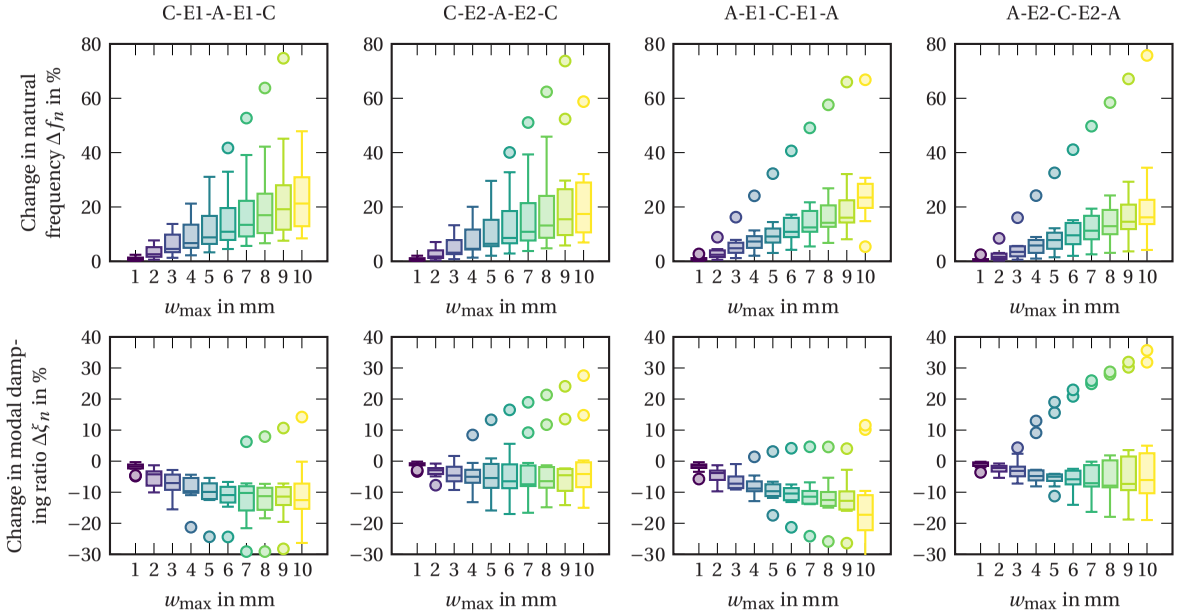

Figure 7.20: Box plots showing the change of natural frequency and modal damping ratio of the first ten vibration modes caused by ten different levels of predeformation expressed by the maximum deformation depth w_{max} in Equation (7.9). Plots show the median values, the lower and upper quartiles as boxes, the smallest and largest change values within one and a half times the interquartile range as whiskers and outliers as points. Adapted from Jackstadt et al. [233].

7.3 Discussion and concluding remarks

7.3.1 Experimental characterisation

The results from experimental drop-weight low-velocity impact experiments presented in Section 7.1.2 revealed intra-ply damage, delaminations and permanent deformation as the occurring types of damage under the given loading. Those are also observed by Sarlin et al. [215, 216] for FMELs containing layers of steel instead of aluminium. In their work, however, the permanent deformation is limited to an indent on the impacted side, whereas in this work, deformation occurs through the whole thickness. This difference is explained by the more compliant aluminium layers used in the present FMELs as well as the fact, that the steel layers are almost twice as thick. Furthermore, the experiments show, that laminates containing more aluminium, e.g. type A-E-C-E-A, deform more and dissipate more energy in the process. In the work by Li et al. [237], who numerically investigate laminate A-E1-C-E1-A under impact loading, the authors reproduce this effect using damage models and also come to the conclusion that plastic deformation is the pivotal source of dissipation under low-velocity impact loading for the given laminate. An investigation under high-velocity impact, however, might lead to different results due to strain-hardening effects in the aluminium plies, but is beyond the scope of this work.

7.3.2 Numerical modelling

Section 7.2.2 outlines the results obtained from a parametric study on the vibration of damaged FMELs. The numerically determined impact of intra-ply damage on CLD in FMELs exhibits a significant dependence on the specific vibration mode under consideration, generally consistent with findings reported by Gröhlich et al. [186] in the context of thermal impact on CLD beams. In addition, the damage tolerance of the CLD mechanism in the investigated FMELs is influenced by both lamination scheme and the choice

of elastomeric damping material. Laminates of type A-E-C-E-A demonstrate enhanced tolerance to intra-ply damage within the CFRP plies due to their positioning closer to the neutral plane of the laminate, mitigating the impact of the incurred damages. Furthermore, the vibrational behaviour is shown to be more significantly influenced by fibre damage compared to matrix damage. These findings specifically align with the observations reported in [257].

The numerical analysis of delaminations in vibrating FMELs shows the occurrence of additional opening modes compared to undamaged laminates. This phenomenon is observed in prior studies [253, 254, 251], both numerically employing similar modelling techniques and experimentally. Furthermore, pronounced mode shifts are observed in the numerical results. A sensitivity of the order of occurrence of vibration modes in CLD laminates is also reported by Gröhlich et al. [186] in the context of varying thermal conditions, which also alter the stiffness distribution within the laminate, similar to the effect of damage. Mode shifts for a generic occurrence of localized damage is also reported by Viglietti et al. [259] for composite panels.

The permanent deformation of the laminates due to impact is found to be the primary contributor of changes to the vibration behaviour of FMEL. To the author's knowledge, no similar investigations have been published. However, Sessner et al. [228] and Sessner [230] experimentally investigate plates as well as 3D curved structures made from the same FMELs materials as analysed in this work. As previously stated in Chapter 2, both types of specimen follow the same trends with regard to natural frequencies and modal damping ratios, regardless of the geometry. The actual absolute values, on the other hand, differ drastically. This works towards the plausibility of results presented here, since the permanent deformation produces large alterations in natural frequencies and modal damping ratios, but hardly shows any mode-dependency. Consequently, permanent deformation due to impact stiffens the laminate and reduces its modal damping capabilities, but does not change the general vibration characteristics.

While the numerical results presented herein are deemed plausible due to the arguments put forward above, the chosen modelling approaches do have limitations which are discussed in the following. The chosen unconstrained modelling approach for delaminations has been discussed in numerous publications as outlined in Chapter 2. While most authors favour this approach over a constrained or contact modelling strategy, other have achieved better agreement with experimental results using a different approach. However, as highlighted above, the fully unconstrained approach represents a worst-case with regards to residual load-bearing capabilities of the laminate [251] and is thus deemed suitable for the analysis of damage in CLD. What all approaches, including contact formulations, lack when being applied in the frequency domain, however, is the ability to include possible friction effects. It is assumed that a delamination under vibration generates friction between adjacent plies, which is an additional source of dissipation. In linear frequency-domain procedures as applied in this study, such non-linear effects cannot be represented. Consequently, the predicted modal damping ratios of delaminated plates might be underestimated. On the other hand, the chosen unconstrained modelling approach assumes zero residual stiffness or transmission of force in the delaminated region, thus underestimating the overall laminate stiffness and possibly overestimating the amount of damping. These discussed limitations primarily address the calculation of exact absolute values. This study, however, is focused on the comparison of different materials and laminates, which are unaffected by such limitations.

The proposed stress-free mesh deformation for depicting the geometrical changes due to permanent deformation yields altered plates, which closely resemble those after experimental impact. What this modelling approach, however, does not take into account are possible residual stresses within the laminate. While the aluminium plies are assumed to deform plastically and are thus stress-free, the CFRP and especially the elastomer layers might be kept in deformation, thus developing residual stresses. Residual stresses might act as a further stiffening or softening of the structure, altering natural

frequencies and modal damping ratios. Increased natural frequencies due to thermal residual stresses in monolithic CFRP laminates are observed by Almeida and Hansen [309] and and Capote Rodríguez et al. [310]. The Mullins effect investigated in Chapter 6 could also lead to an alteration of the elastomer layers in the event of an impact, if the laminate is predominantly deformed elastically, allowing for sufficient unloading to trigger this effect.

7.3.3 Conclusions

This chapter investigates the impact behaviour of FMELs and explores the influence of resulting damages on their vibration and damping behaviour. In fulfilment of Objective 3-1, experimental low-velocity impact tests are carried out on four different hybrid FMELs featuring two different elastomer materials. In all laminates, regardless of layup and elastomer material, intra-ply damage, delaminations and a permanent deformation are identified as the occurring types of damage. The choice of a softer elastomer material is shown to delay the onset of most types of damage, increasing the impact resistance of the laminate. Laminates containing more aluminium plies and in particular those which expose the aluminium to the location of impact are observed to experience increased permanent deformation of the whole laminate.

Using FEM models, the observed types of damage are modelled for representation in the frequency-domain as demanded by Objective 3-2. In a parametric study, the individual influence of each type of damage on the natural frequencies and modal damping ratios is investigated. The effects of intra-ply damage and delaminations demonstrate a strong dependency on the considered vibration mode. Nevertheless, with regard to Objective 3-3, it can be concluded, that critical locations regarding the modal damping capabilities for the occurrence of both types of damage are layers, or interfaces respectively, closest to the elastomer damping layers. Noteworthy is also an increase in modal damping for some modes in delaminated laminates. Both types of damage, however, exert a limited influence on the vibration characteristics when compared to different levels of permanent deformation.

Deformed laminates generally act stiffer than virgin ones, increasing natural frequencies but decreasing modal damping. Overall, the FMELs under investigation in this work are shown to be damage-tolerant regarding their CLD capabilities. This is particularly the case, when permanent deformation due to the plasticity of aluminium plies can be limited, for example by a lamination scheme, which prevents direct contact of the aluminium with the impactor.

8 Final remarks

8.1 Summary

Following a review of related literature on the topic of fibre metal elastomer laminates (FMELs) and constrained-layer damping (CLD) in Chapter 2 and the deduction of this work's research objectives in Chapter 3, Chapter 4 introduces the FMELs and its constituents subject to the investigations of this work. A brief summary of the manufacturing process and the basic mechanical properties is presented.

Chapter 5 introduces an analytical model based on a sublaminate unified formulation for plates. The model takes into account viscoelasticity in the frequency-domain as well as the accompanying frequency-dependence of the material parameters. The implemented model is verified against state-of-the-art full-field finite element models and excellent agreement with only a fraction of required degrees of freedom (DOFs) is shown. The developed model is then applied to different FMELs to investigate their static, modal and steady-state behaviour. Subsequently, the influence of elastomer layer properties such as stiffness and thickness on the damping behaviour of the laminates is investigated. Design recommendations with regard to maximizing modal damping for arbitrary CLD laminates are given subsequently. The research Objectives 1-1 to 1-3 are considered to be fulfilled.

Chapter 6 employs experimental and numerical methods to prove the research hypothesis, that large-strain phenomena commonly observed in elastomers have to be taken into account even in linear low-amplitude vibrations. The considered elastomer materials are subjected to a comprehensive

experimental characterisation in order to quantify the occurrence of the Mullins effect. Subsequently, this effect is further investigated on laminate level under vibration loading. In order to predict the occurrence and impact of the Mullins effect in CLD applications, two constitutive models are developed, parametrised and implemented. The model validation yields a discrepancy with experimental results and thus questions the suitability of the proposed material model in its current implementation. While Objective 2-1 and Objective 2-2 are fulfilled, Objective 2-3 is only partially fulfilled. Nevertheless, the research Hypothesis 1 is considered to be proven.

In Chapter 7, experimental methods are applied to characterise the damage occurring in FMELs due to low-velocity impact events. The results presented also give an insight into the impact resistance of different laminate configurations. Furthermore, numerical methods are proposed to predict the influence of these types of damage on the vibration behaviour of the laminates. A comprehensive parametric study is conducted in order to identify critical states of damage, which have a substantial impact on the vibrational behaviour. Further investigations include a more in-depth look into how the extent of different types of damages influence the vibration characteristics of FMELs. Consequently, Objectives 3-1 to 3-3 formulated in Chapter 3 are accomplished.

8.2 Conclusions

One major conclusion of this thesis is that the relation of laminate parameters, such as layup and material selection, and the resulting vibration behaviour of FMELs is a fairly complex one. This consolidates the need for models, which do not only predict modal damping ratios as most state-of-the-art models do, but also allow for predictions of the static behaviour. An increase of modal damping due to changes of laminate layup or material properties does not necessarily imply a reduced stiffness under static loading. Therefore, an efficient and optimized CLD design requires a thorough materials selection

and laminate layup, which is supported and accelerated by computationally efficient models such as the one presented in this work.

This work presents the first scientific investigation of the Mullins effect in CLD laminates. It is concluded based on experimental and numerical findings, that moderate quasi-static predeformations within the elastic regime of the laminate can trigger the Mullins effect and noticeably alter its vibration properties. This proves the Hypothesis 1, that an accurate investigation of CLD, even at low vibration amplitudes, in many cases has to take into account phenomena, which are usually restricted to a regime of large strains.

Additionally, the investigated FMELs have been shown to offer a high impact resistance with regard to damage due to the dissipative elastomer plies. Nevertheless, intra-ply damage of CFRP plies, delaminations and permanent deformation are identified as the resulting modes of damage. With regard to their influence on the damping capabilities of FMELs, intra-ply damage as well as delaminations are negligible compared to the permanent deformation of the laminates associated with the metal layers' plasticity. Consequently, laminates in which the plastic deformation of metal layers can be avoided, are considered to be highly damage tolerant with regard to their damping performance. Nevertheless, while not significantly influencing the modal damping capabilities, delaminations are shown to frequently cause mode shifts as well as the occurrence of additional opening modes.

8.3 Outlook

This thesis sheds light on numerous aspects of CLD in hybrid FMELs. The investigations and associated conclusions, however, are restricted to isothermal conditions at room temperature. Being highly temperature-dependent materials with regard to their mechanical properties, the elastomers are assumed to alter the obtained findings at elevated or reduced temperatures. This temperature dependence could for example be incorporated into the analytical model

proposed in Chapter 5. Furthermore, the observed damage resistance and tolerance of the hybrid FMELs with regard to impact loading, could be reassessed at different ambient temperatures. In addition, the full or partial recovery of the Mullins effect due to annealing at elevated temperatures could be investigated as a possible treatment to mitigate the initial softening of a CLD laminate.

From a material science point of view, the complex behaviour of elastomers also offers research opportunities. The anisotropy of the Mullins effect or the use of crystallising rubbers are a possible scope for further investigations. The corresponding characterisation techniques and constitutive models would have to be developed.

All of the above investigations have been conducted with laminates featuring a CLD treatment with continuous elastomer layers. As outlined in Section 2.3.2, however, partial CLD treatments for example in the form of patches are also possible. A transfer of the relations and findings uncovered in this work to such partial CLD treatments therefore offers further research potential.

A Appendix

A.1 Materials and manufacturing

A.1.1 Time-temperature superposition

Figure A.1 shows the horizontal shift factors a_T used to create the master curves introduced in Figure 4.4 as well as the parameters for the shift functions Equation (2.47)and Equation (2.46) for a reference temperature $T_{\mathrm{ref}} = T_{\mathrm{G}}$.

The associated parameters for the WLF (Equation (2.46)) and Arrhenius (Equation (2.47)) relations are listed in Table A.1.

Table A.2 shows the vertical shift factors b_T for a reference temperature of $T_{\mathrm{ref}} = T_{\mathrm{G}}$ for each sweep used in the construction of master curves in Figure 4.4.

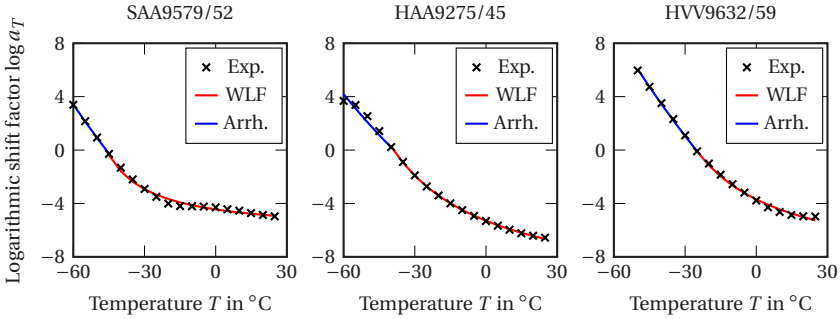

Figure A.1: Logarithmic horizontal shift factors for the three elastomer materials and predictions by WLF and Arrhenius relations.

Table A.1: Parameters of shift functions at the materials' glass transition temperature T_G.

Elastomer	T_G	$C_1(T_G)$	$C_2(T_G)$	E_a
SAA9579/52	−46.1 °C	6.2	17.7	525.7 kJ mol^{-1} K
HAA9275/45	−39.0 °C	11.1	42.8 K	437.9 kJ mol^{-1} K
HVV9632/59	−25.4 °C	9.2	38.1 K	600.6 kJ mol^{-1} K

Table A.2: Vertical shift factors b_T for a reference temperature of $T_{ref} = T_G$.

Temperature	SAA9579/52	HAA9275/45	HVV9632/59
−60 °C	−0.226	−0.098	-
−55 °C	−0.191	−0.081	-
−50 °C	−0.091	−0.059	−0.120
−45 °C	0.000	−0.030	−0.121
−40 °C	0.050	0.000	−0.117
−35 °C	0.069	0.025	−0.094
−30 °C	0.094	0.044	−0.040
−25 °C	0.126	0.060	0.000
−20 °C	0.151	0.076	0.040
−15 °C	0.180	0.089	0.049
−10 °C	0.211	0.103	0.057
−5 °C	0.241	0.117	0.065
0 °C	0.262	0.129	0.070
5 °C	0.276	0.143	0.079
10 °C	0.297	0.156	0.095
15 °C	0.314	0.169	0.116
20 °C	0.332	0.182	0.137
25 °C	0.349	0.194	0.165

A.2 Analytical modeling of constrained-layer damping laminates

A.2.1 Governing equations

The following variational equations with regard to displacements and out-of-plane stresses result from Equation (5.3):

$$
\begin{aligned}
\delta u_{x_{\alpha_x}}: \quad & - C_{11}^k \frac{\partial^2 \Phi_x}{\partial x^2} \int_{z_{\text{bot}}^k}^{z_{\text{top}}^k} F_{\alpha_x} F_{\beta_x} \mathrm{d}z \, U_{x_{\beta_x}}^k \\
& - C_{12}^k \frac{\partial^2 \Phi_y}{\partial x \partial y} \int_{z_{\text{bot}}^k}^{z_{\text{top}}^k} F_{\alpha_x} F_{\beta_y} \mathrm{d}z \, U_{y_{\beta_y}}^k \\
& - C_{13}^k \frac{\partial \Phi_z}{\partial x} \int_{z_{\text{bot}}^k}^{z_{\text{top}}^k} F_{\alpha_x} F_{\beta_{zz}} \mathrm{d}z \, S_{zz_{\beta_{zz}}}^k \\
& - C_{44}^k \frac{\partial^2 \Phi_x}{\partial y^2} \int_{z_{\text{bot}}^k}^{z_{\text{top}}^k} F_{\alpha_x} F_{\beta_x} \mathrm{d}z \, U_{x_{\beta_x}}^k \\
& - C_{44}^k \frac{\partial^2 \Phi_y}{\partial x \partial y} \int_{z_{\text{bot}}^k}^{z_{\text{top}}^k} F_{\alpha_x} F_{\beta_y} \mathrm{d}z \, U_{y_{\beta_y}}^k \\
& + \Phi_x \int_{z_{\text{bot}}^k}^{z_{\text{top}}^k} \frac{\mathrm{d}F_{\alpha_x}}{\mathrm{d}z} F_{\beta_{xz}} \mathrm{d}z \, S_{xz_{\beta_{xz}}}^k \\
& + \rho^k \, \Phi_x \int_{z_{\text{bot}}^k}^{z_{\text{top}}^k} F_{\alpha_x} F_{\beta_x} \mathrm{d}z \, \ddot{U}_{x_{\beta_x}}^k \\
& = \Phi_x \, F_{\alpha_x}|_{z=z_{\text{top}}^k} \, Q_x^{k,\text{top}} + \Phi_x \, F_{\alpha_x}|_{z=z_{\text{bot}}^k} \, Q_x^{k,\text{bot}}
\end{aligned}
\tag{A.1}
$$

$$
\begin{aligned}
\delta u_{y_{\alpha_y}}: \quad & - C_{12}^k \frac{\partial^2 \Phi_x}{\partial x \partial y} \int_{z_{\text{bot}}^k}^{z_{\text{top}}^k} F_{\alpha_y} F_{\beta_x} \mathrm{d}z \, U_{x_{\beta_x}}^k \\
& - C_{22}^k \frac{\partial^2 \Phi_y}{\partial y^2} \int_{z_{\text{bot}}^k}^{z_{\text{top}}^k} F_{\alpha_y} F_{\beta_y} \mathrm{d}z \, U_{y_{\beta_y}}^k \\
& - C_{23}^k \frac{\partial \Phi_z}{\partial y} \int_{z_{\text{bot}}^k}^{z_{\text{top}}^k} F_{\alpha_y} F_{\beta_{zz}} \mathrm{d}z \, S_{zz_{\beta_{zz}}}^k \\
& - C_{44}^k \frac{\partial^2 \Phi_x}{\partial x \partial y} \int_{z_{\text{bot}}^k}^{z_{\text{top}}^k} F_{\alpha_y} F_{\beta_x} \mathrm{d}z \, U_{x_{\beta_x}}^k \\
& - C_{44}^k \frac{\partial^2 \Phi_y}{\partial x^2} \int_{z_{\text{bot}}^k}^{z_{\text{top}}^k} F_{\alpha_y} F_{\beta_y} \mathrm{d}z \, U_{y_{\beta_y}}^k \\
& + \Phi_y \int_{z_{\text{bot}}^k}^{z_{\text{top}}^k} \frac{\mathrm{d}F_{\alpha_y}}{\mathrm{d}z} F_{\beta_{xz}} \mathrm{d}z \, S_{yz_{\beta_{yz}}}^k \\
& + \rho^k \, \Phi_y \int_{z_{\text{bot}}^k}^{z_{\text{top}}^k} F_{\alpha_y} F_{\beta_y} \mathrm{d}z \, \ddot{U}_{y_{\beta_y}}^k \\
& = \Phi_y \, F_{\alpha_y}|_{z=z_{\text{top}}^k} \, Q_y^{k,\text{top}} + \Phi_y \, F_{\alpha_y}|_{z=z_{\text{bot}}^k} \, Q_y^{k,\text{bot}}
\end{aligned}
\tag{A.2}
$$

$$
\begin{aligned}
\delta u_{z_{\alpha_z}}: \quad & - \frac{\partial \Phi_x}{\partial x} \int_{z_{\text{bot}}^k}^{z_{\text{top}}^k} F_{\alpha_z} F_{\beta_{xz}} \mathrm{d}z \, S_{xz_{\beta_{xz}}}^k \\
& - \frac{\partial \Phi_y}{\partial y} \int_{z_{\text{bot}}^k}^{z_{\text{top}}^k} F_{\alpha_z} F_{\beta_{yz}} \mathrm{d}z \, S_{yz_{\beta_{yz}}}^k \\
& + \Phi_z \int_{z_{\text{bot}}^k}^{z_{\text{top}}^k} \frac{\mathrm{d}F_{\alpha_z}}{\mathrm{d}z} F_{\beta_{zz}} \mathrm{d}z \, S_{zz_{\beta_{zz}}}^k \\
& + \rho^k \, \Phi_z \int_{z_{\text{bot}}^k}^{z_{\text{top}}^k} F_{\alpha_z} F_{\beta_z} \mathrm{d}z \, \ddot{U}_{z_{\beta_z}}^k \\
& = \Phi_z \, F_{\alpha_z}|_{z=z_{\text{top}}^k} \, Q_z^{k,\text{top}} + \Phi_z \, F_{\alpha_z}|_{z=z_{\text{bot}}^k} \, Q_z^{k,\text{bot}}
\end{aligned}
\tag{A.3}
$$

$$
\begin{aligned}
\delta\sigma_{xz_{\alpha_{xz}}}: \quad & \Phi_x \int_{z_{\text{bot}}^k}^{z_{\text{top}}^k} F_{\alpha_{xz}} \frac{\mathrm{d}F_{\beta_x}}{\mathrm{d}z}\, U_{x_{\beta_x}}^k \\
& + \frac{\partial \Phi_z}{\partial x} \int_{z_{\text{bot}}^k}^{z_{\text{top}}^k} F_{\alpha_{xz}} F_{\beta_z} \mathrm{d}z\, U_{z_{\beta_z}}^k \\
& - C_{55} \int_{z_{\text{bot}}^k}^{z_{\text{top}}^k} F_{\alpha_{xz}} F_{\beta_{xz}} \mathrm{d}z\, S_{xz_{\beta_{xz}}}^k \\
& = 0
\end{aligned}
\tag{A.4}
$$

$$
\begin{aligned}
\delta\sigma_{yz_{\alpha_{yz}}}: \quad & \Phi_y \int_{z_{\text{bot}}^k}^{z_{\text{top}}^k} F_{\alpha_{yz}} \frac{\mathrm{d}F_{\beta_y}}{\mathrm{d}z}\, U_{y_{\beta_y}}^k \\
& + \frac{\partial \Phi_z}{\partial y} \int_{z_{\text{bot}}^k}^{z_{\text{top}}^k} F_{\alpha_{yz}} F_{\beta_z} \mathrm{d}z\, U_{z_{\beta_z}}^k \\
& - C_{66} \int_{z_{\text{bot}}^k}^{z_{\text{top}}^k} F_{\alpha_{yz}} F_{\beta_{yz}} \mathrm{d}z\, S_{yz_{\beta_{yz}}}^k \\
& = 0
\end{aligned}
\tag{A.5}
$$

$$
\begin{aligned}
\delta\sigma_{zz_{\alpha_{zz}}}: \quad & \Phi_z \int_{z_{\text{bot}}^k}^{z_{\text{top}}^k} F_{\alpha_{zz}} \frac{\mathrm{d}F_{\beta_z}}{\mathrm{d}z}\, U_{z_{\beta_z}}^k \\
& + C_{13}^k \frac{\partial \Phi_x}{\partial x} \int_{z_{\text{bot}}^k}^{z_{\text{top}}^k} F_{\alpha_{zz}} F_{\beta_x} \mathrm{d}z\, U_{x_{\beta_x}}^k \\
& + C_{23}^k \frac{\partial \Phi_y}{\partial y} \int_{z_{\text{bot}}^k}^{z_{\text{top}}^k} F_{\alpha_{zz}} F_{\beta_y} \mathrm{d}z\, U_{y_{\beta_y}}^k \\
& - C_{33}^k \Phi_z \int_{z_{\text{bot}}^k}^{z_{\text{top}}^k} F_{\alpha_{zz}} F_{\beta_{zz}} \mathrm{d}z\, S_{zz_{\beta_{zz}}}^k \\
& = 0
\end{aligned}
\tag{A.6}
$$

A.2.2 Kernel matrices

The following kernel matrices are derived from A.2.1 and used in the formulation of the global system of equations in Equation (5.15).

Stiffness kernel matrices:

$$\mathbf{K}^k_{U_xU_x} \widehat{=} \frac{1}{\Phi_x}\left(-C^k_{11}\,\frac{\partial^2\Phi_x}{\partial x^2}\int_{z^k_{\text{bot}}}^{z^k_{\text{top}}} F_{\alpha_x}F_{\beta_x}\,\mathrm{d}z - C^k_{44}\,\frac{\partial^2\Phi_x}{\partial y^2}\int_{z^k_{\text{bot}}}^{z^k_{\text{top}}} F_{\alpha_x}F_{\beta_x}\,\mathrm{d}z\right) \tag{A.7}$$

$$\mathbf{K}^k_{U_xU_y} \widehat{=} \frac{1}{\Phi_x}\left(-C^k_{12}\,\frac{\partial^2\Phi_y}{\partial x\partial y}\int_{z^k_{\text{bot}}}^{z^k_{\text{top}}} F_{\alpha_x}F_{\beta_y}\,\mathrm{d}z - C^k_{44}\,\frac{\partial^2\Phi_y}{\partial x\partial y}\int_{z^k_{\text{bot}}}^{z^k_{\text{top}}} F_{\alpha_x}F_{\beta_y}\,\mathrm{d}z\right) \tag{A.8}$$

$$\mathbf{K}^k_{U_xS_x} \widehat{=} \int_{z^k_{\text{bot}}}^{z^k_{\text{top}}} \frac{\mathrm{d}F_{\alpha_x}}{\mathrm{d}z}F_{\beta_{xz}}\,\mathrm{d}z \tag{A.9}$$

$$\mathbf{K}^k_{U_xS_z} \widehat{=} \frac{1}{\Phi_x}\left(-C^k_{13}\,\frac{\partial\Phi_z}{\partial x}\int_{z^k_{\text{bot}}}^{z^k_{\text{top}}} F_{\alpha_x}F_{\beta_{zz}}\,\mathrm{d}z\right) \tag{A.10}$$

$$\mathbf{K}^k_{U_yU_y} \widehat{=} \frac{1}{\Phi_y}\left(-C^k_{22}\,\frac{\partial^2\Phi_y}{\partial y^2}\int_{z^k_{\text{bot}}}^{z^k_{\text{top}}} F_{\alpha_y}F_{\beta_y}\,\mathrm{d}z - C^k_{44}\,\frac{\partial^2\Phi_y}{\partial x^2}\int_{z^k_{\text{bot}}}^{z^k_{\text{top}}} F_{\alpha_y}F_{\beta_y}\,\mathrm{d}z\right) \tag{A.11}$$

$$\mathbf{K}^k_{U_yS_y} \widehat{=} \int_{z^k_{\text{bot}}}^{z^k_{\text{top}}} \frac{\mathrm{d}F_{\alpha_y}}{\mathrm{d}z}F_{\beta_{xz}}\,\mathrm{d}z \tag{A.12}$$

$$\mathbf{K}^k_{U_yS_z} \widehat{=} \frac{1}{\Phi_y}\left(-C^k_{23}\,\frac{\partial\Phi_z}{\partial y}\int_{z^k_{\text{bot}}}^{z^k_{\text{top}}} F_{\alpha_y}F_{\beta_{zz}}\,\mathrm{d}z\right) \tag{A.13}$$

$$\mathbf{K}^k_{U_zS_x} \widehat{=} \frac{1}{\Phi_z}\left(-\frac{\partial\Phi_x}{\partial x}\int_{z^k_{\text{bot}}}^{z^k_{\text{top}}} F_{\alpha_z}F_{\beta_{xz}}\,\mathrm{d}z\right) \tag{A.14}$$

$$\mathbf{K}^k_{U_zS_y} \widehat{=} \frac{1}{\Phi_z}\left(-\frac{\partial\Phi_y}{\partial y}\int_{z^k_{\text{bot}}}^{z^k_{\text{top}}} F_{\alpha_z}F_{\beta_{yz}}\,\mathrm{d}z\right) \tag{A.15}$$

$$\mathbf{K}^k_{U_zS_z} \widehat{=} \int_{z^k_{\text{bot}}}^{z^k_{\text{top}}} \frac{\mathrm{d}F_{\alpha_z}}{\mathrm{d}z}F_{\beta_{zz}}\,\mathrm{d}z \tag{A.16}$$

$$\mathbf{K}^k_{S_xS_x} \widehat{=} -C^k_{55}\int_{z^k_{\text{bot}}}^{z^k_{\text{top}}} F_{\alpha_{xz}}F_{\beta_{xz}}\,\mathrm{d}z \tag{A.17}$$

$$\mathbf{K}^k_{S_yS_y} \widehat{=} -C^k_{66}\int_{z^k_{\text{bot}}}^{z^k_{\text{top}}} F_{\alpha_{yz}}F_{\beta_{yz}}\,\mathrm{d}z \tag{A.18}$$

$$\mathbf{K}^k_{S_zS_z} \mathrel{\widehat{=}} -C^k_{33}\int_{z^k_{\text{bot}}}^{z^k_{\text{top}}} F_{\alpha_{zz}}F_{\beta_{zz}}\,\mathrm{d}z \tag{A.19}$$

Mass kernel matrices:

$$\mathbf{M}^k_{U_xU_x} \mathrel{\widehat{=}} \rho^k\int_{z^k_{\text{bot}}}^{z^k_{\text{top}}} F_{\alpha_x}F_{\beta_x}\,\mathrm{d}z \tag{A.20}$$

$$\mathbf{M}^k_{U_yU_y} \mathrel{\widehat{=}} \rho^k\int_{z^k_{\text{bot}}}^{z^k_{\text{top}}} F_{\alpha_y}F_{\beta_y}\,\mathrm{d}z \tag{A.21}$$

$$\mathbf{M}^k_{U_zU_z} \mathrel{\widehat{=}} \rho^k\int_{z^k_{\text{bot}}}^{z^k_{\text{top}}} F_{\alpha_z}F_{\beta_z}\,\mathrm{d}z \tag{A.22}$$

Load kernel vectors:

$$\mathbf{R}^k_x \mathrel{\widehat{=}} F_{\alpha_x}|_{z=z^k_{\text{top}}}\ Q^{k,\text{top}}_x + F_{\alpha_x}|_{z=z^k_{\text{bot}}}\ Q^{k,\text{bot}}_x \tag{A.23}$$

$$\mathbf{R}^k_y \mathrel{\widehat{=}} F_{\alpha_y}|_{z=z^k_{\text{top}}}\ Q^{k,\text{top}}_y + F_{\alpha_y}|_{z=z^k_{\text{bot}}}\ Q^{k,\text{bot}}_y \tag{A.24}$$

$$\mathbf{R}^k_z \mathrel{\widehat{=}} F_{\alpha_z}|_{z=z^k_{\text{top}}}\ Q^{k,\text{top}}_z + F_{\alpha_z}|_{z=z^k_{\text{bot}}}\ Q^{k,\text{bot}}_z \tag{A.25}$$

A.2.3 Free vibration of hybrid FMELs

Table A.3 lists the damped natural frequencies $f_{mn}.$ and damping ratios ξ_{mn} of six FMELs. The nine vibration modes (m,n) are considered, with indices m and n indicating the present mode's number of half-waves across the plate in x- and y-directions.

Table A.3: Natural frequencies and modal damping ratios of six different FMELs calculated analytically with theory Sub_{112}^{223} and an iterative algorithm. Values correspond to Figure 5.18.

Mode (m,n)	CE1A		CE2A		CE3A		AE1C		AE2C		AE3C	
	f_{mn} in Hz	ξ_{mn}	f_{mn} in Hz	ξ_{mn}	f_{mn} in Hz	ξ_{mn}	f_{mn} in Hz	ξ_{mn}	f_{mn} in Hz	ξ_{mn}	f_{mn} in Hz	ξ_{mn}
(1, 1)	618.11	0.0326	743.50	0.0023	714.21	0.0101	710.40	0.0333	855.60	0.0029	821.01	0.0104
(2, 1)	1068.81	0.0488	1400.27	0.0035	1329.19	0.0164	1215.15	0.0528	1624.16	0.0044	1536.35	0.0180
(1, 2)	1582.74	0.0775	2517.69	0.0065	2319.53	0.0322	1773.62	0.0669	2576.40	0.0058	2407.23	0.0255
(3, 1)	1759.98	0.0708	2688.70	0.0062	2487.15	0.0303	1924.84	0.0717	2876.92	0.0064	2675.29	0.0280
(2, 2)	1843.05	0.0774	2874.37	0.0065	2654.75	0.0313	2128.71	0.0770	3293.27	0.0070	3044.71	0.0313
(3, 2)	2346.49	0.0835	3784.71	0.0074	3475.97	0.0352	2682.71	0.0880	4472.45	0.0087	4079.95	0.0392
(1, 3)	2699.40	0.1049	5299.85	0.0119	4678.80	0.0559	3116.39	0.0881	5266.60	0.0095	4785.00	0.0424
(2, 3)	2883.85	0.1032	5544.04	0.0118	4911.27	0.0546	3376.47	0.0933	5925.36	0.0104	5346.65	0.0465
(3, 3)	3260.18	0.1034	6158.83	0.0116	5476.70	0.0535	3804.49	0.0997	7010.22	0.0118	6257.34	0.0524

List of figures

List of tables

Bibliography

[1] J. S. Bergström, *Mechanics of Solid Polymers: Theory and computational modeling*, ser. PDL Handbook Series. Norwich: Elsevier, 2015.

[2] P. J. Flory, "Thermodynamic relations for high elastic materials," *Transactions of the Faraday Society*, vol. 57, p. 829, 1961.

[3] G. A. Holzapfel, *Nonlinear solid mechanics: A continuum approach for engineering*. Chichester, England: John Wiley & Sons, 2000.

[4] P. Steinmann, M. Hossain, and G. Possart, "Hyperelastic models for rubber-like materials: consistent tangent operators and suitability for Treloar's data," *Archive of Applied Mechanics*, vol. 82, no. 9, pp. 1183–1217, 2012.

[5] S. K. Melly, L. Liu, Y. Liu, and J. Leng, "A review on material models for isotropic hyperelasticity," *International Journal of Mechanical System Dynamics*, vol. 1, no. 1, pp. 71–88, 2021.

[6] L. R. G. Treloar, "The elasticity of a network of long-chain molecules—II," *Transactions of the Faraday Society*, vol. 39, no. 0, pp. 241–246, 1943.

[7] M. Mooney, "A Theory of Large Elastic Deformation," *Journal of Applied Physics*, vol. 11, no. 9, pp. 582–592, 1940.

[8] R. S. Rivlin, "Large elastic deformations of isotropic materials IV. further developments of the general theory," *Philosophical Transactions of the Royal Society of London. Series A, Mathematical and Physical Sciences*, vol. 241, no. 835, pp. 379–397, 1948.

[9] O. H. Yeoh, "Some Forms of the Strain Energy Function for Rubber," *Rubber Chemistry and Technology*, vol. 66, no. 5, pp. 754–771, 1993.

[10] R. S. Rivlin and D. W. Saunders, "Large elastic deformations of isotropic materials VII. Experiments on the deformation of rubber," *Philosophical Transactions of the Royal Society of London. Series A, Mathematical and Physical Sciences*, vol. 243, no. 865, pp. 251–288, 1951.

[11] K. C. Valanis and R. F. Landel, "The Strain-Energy Function of a Hyperelastic Material in Terms of the Extension Ratios," *Journal of Applied Physics*, vol. 38, no. 7, pp. 2997–3002, 1967.

[12] R. W. Ogden, "Large deformation isotropic elasticity – on the correlation of theory and experiment for incompressible rubberlike solids," *Philosophical Transactions of the Royal Society of London. Series A, Mathematical and Physical Sciences*, vol. 326, no. 1567, pp. 565–584, 1972.

[13] R. W. Ogden, "Large deformation isotropic elasticity: on the correlation of theory and experiment for compressible rubberlike solids," *Philosophical Transactions of the Royal Society of London. Series A, Mathematical and Physical Sciences*, vol. 328, no. 1575, pp. 567–583, 1972.

[14] M. C. Wang and E. Guth, "Statistical Theory of Networks of Non-Gaussian Flexible Chains," *The Journal of Chemical Physics*, vol. 20, no. 7, pp. 1144–1157, 1952.

[15] E. M. Arruda and M. C. Boyce, "A three-dimensional constitutive model for the large stretch behavior of rubber elastic materials," *Journal of the Mechanics and Physics of Solids*, vol. 41, no. 2, pp. 389–412, 1993.

[16] R. S. Marlow, "A general first-invariant hyperelastic constitutive model," in *Constitutive models for rubber III*, J. Busfield and A. Muhr, Eds. Lisse: Balkema, 2003, pp. 157–160.

[17] T. Sussman and K.-J. Bathe, "A model of incompressible isotropic hyperelastic material behavior using spline interpolations of tension–compression test data," *Communications in Numerical Methods in Engineering*, vol. 25, no. 1, pp. 53–63, 2009.

[18] Dassault Systèmes Simulia Corp., "SIMULIA User Assistance 2023," 2023, Accessed: February 6th 2024. [Online]. Available: https://help.3ds.com/2023/english/DSSIMULIA_Established/SIMULIA_Established_FrontmatterMap/DSDocHome.htm?contextscope=all&id=9a16dc699ae149b59f4d8abdd9280118

[19] R. M. Christensen, *Theory of viscoelasticity*, 2nd ed. Mineola N.Y.: Dover Publications, 2003.

[20] N. W. Tschoegl, *The Phenomenological Theory of Linear Viscoelastic Behavior: An Introduction*. Berlin, Heidelberg: Springer Berlin Heidelberg, 1989.

[21] L. Cremer, M. Heckl, and B. A. T. Petersson, *Structure-borne sound: Structural vibrations and sound radiation at audio frequencies*, 3rd ed. Berlin and London: Springer, 2005.

[22] H. F. Brinson and L. C. Brinson, *Polymer engineering science and viscoelasticity: An introduction*. New York: Springer, 2008.

[23] K. P. Menard, *Dynamic mechanical analysis: A practical introduction*. Boca Raton, FL: CRC Press, 2008.

[24] A. V. Tobolsky and R. D. Andrews, "Systems Manifesting Superposed Elastic and Viscous Behavior," *The Journal of Chemical Physics*, vol. 13, no. 1, pp. 3–27, 1945.

[25] H. Markovitz, "Superposition in rheology," *Journal of Polymer Science: Polymer Symposia*, vol. 50, no. 1, pp. 431–456, 1975.

[26] M. L. Williams, R. F. Landel, and J. D. Ferry, "The Temperature Dependence of Relaxation Mechanisms in Amorphous Polymers and

Other Glass-forming Liquids," *Journal of the American Chemical Society*, vol. 77, no. 14, pp. 3701–3707, 1955.

[27] W. P. Hernández, D. A. Castello, N. Roitman, and C. Magluta, "Thermorheologically simple materials: A bayesian framework for model calibration and validation," *Journal of Sound and Vibration*, vol. 402, pp. 14–30, 2017.

[28] M. van Gurp and J. Palmen, "Time-Temperature Superposition for Polymer Blends," *Rheology Bulletin*, vol. 67, no. 1, pp. 5–8, 1998.

[29] K. S. Cole and R. H. Cole, "Dispersion and Absorption in Dielectrics II. Direct Current Characteristics," *The Journal of Chemical Physics*, vol. 10, no. 2, pp. 98–105, 1942.

[30] J. C. Duncan and D. M. Price, "Thermomechanical, Dynamic Mechanical and Dielectric Methods," in *Principles of Thermal Analysis and Calorimetry*, S. Gaisford, V. Kett, and P. Haines, Eds. The Royal Society of Chemistry, 2016, pp. 164–213.

[31] R. M. Guedes, "A viscoelastic model for a biomedical ultra-high molecular weight polyethylene using the time–temperature superposition principle," *Polymer Testing*, vol. 30, no. 3, pp. 294–302, 2011.

[32] L. Rouleau, J.-F. Deü, A. Legay, and F. Le Lay, "Application of Kramers–Kronig relations to time–temperature superposition for viscoelastic materials," *Mechanics of Materials*, vol. 65, no. 1, pp. 66–75, 2013.

[33] L. Kehrer, J. Keursten, V. Hirschberg, and T. Böhlke, "Dynamic mechanical analysis of PA 6 under hydrothermal influences and viscoelastic material modeling," *Journal of Thermoplastic Composite Materials*, p. 089270572311558, 2023.

[34] W. P. Fletcher and A. N. Gent, "Nonlinearity in the Dynamic Properties of Vulcanized Rubber Compounds," *Rubber Chemistry and Technology*, vol. 27, no. 1, pp. 209–222, 1954.

[35] A. R. Payne, "The dynamic properties of carbon black-loaded natural rubber vulcanizates. Part I," *Journal of Applied Polymer Science*, vol. 6, no. 19, pp. 57–63, 1962.

[36] A. R. Payne, "Strainwork dependence of filler–loaded vulcanizates," *Journal of Applied Polymer Science*, vol. 8, no. 6, pp. 2661–2686, 1964.

[37] A. R. Payne, "Hysteresis in rubber vulcanizates," *Journal of Polymer Science: Polymer Symposia*, vol. 48, no. 1, pp. 169–196, 1974.

[38] M.-J. Wang, "The Role of Filler Networking in Dynamic Properties of Filled Rubber," *Rubber Chemistry and Technology*, vol. 72, no. 2, pp. 430–448, 1999.

[39] M. Rendek and A. Lion, "Amplitude dependence of filler-reinforced rubber: Experiments, constitutive modelling and FEM – Implementation," *International Journal of Solids and Structures*, vol. 47, no. 21, pp. 2918–2936, 2010.

[40] L. Mullins, "Effect of Stretching on the Properties of Rubber," *Rubber Chemistry and Technology*, vol. 21, no. 2, pp. 281–300, 1948.

[41] L. Mullins and N. R. Tobin, "Stress softening in rubber vulcanizates. Part I. Use of a strain amplification factor to describe the elastic behavior of filler-reinforced vulcanized rubber," *Journal of Applied Polymer Science*, vol. 9, no. 9, pp. 2993–3009, 1965.

[42] J. A. C. Harwood and A. R. Payne, "Stress softening in natural rubber vulcanizates. Part III. Carbon black-filled vulcanizates," *Journal of Applied Polymer Science*, vol. 10, no. 2, pp. 315–324, 1966.

[43] J. A. C. Harwood, L. Mullins, and A. R. Payne, "Stress softening in natural rubber vulcanizates. Part II. Stress softening effects in pure gum and filler loaded rubbers," *Journal of Applied Polymer Science*, vol. 9, no. 9, pp. 3011–3021, 1965.

[44] J. A. C. Harwood and A. R. Payne, “Stress softening in natural rubber vulcanizates. Part IV. Unfilled vulcanizates,” *Journal of Applied Polymer Science*, vol. 10, no. 8, pp. 1203–1211, 1966.

[45] J. Plagge and M. Klüppel, “Mullins effect revisited: Relaxation, recovery and high-strain damage,” *Materials Today Communications*, vol. 20, p. 100588, 2019.

[46] J. Plagge and A. Lang, “Filler-polymer interaction investigated using graphitized carbon blacks: Another attempt to explain reinforcement,” *Polymer*, vol. 218, p. 123513, 2021.

[47] A.-M. M. R. Persson and E. Andreassen, “Cyclic Compression Testing of Three Elastomer Types-A Thermoplastic Vulcanizate Elastomer, a Liquid Silicone Rubber and Two Ethylene-Propylene-Diene Rubbers,” *Polymers*, vol. 14, no. 7, 2022.

[48] Y. Merckel, J. Diani, M. Brieu, and D. Berghezan, “Experimental characterization and modelling of the cyclic softening of carbon-black filled rubbers,” *Materials Science and Engineering: A*, vol. 528, no. 29-30, pp. 8651–8659, 2011.

[49] F. Carleo, E. Barbieri, R. Whear, and J. J. C. Busfield, “Limitations of Viscoelastic Constitutive Models for Carbon-Black Reinforced Rubber in Medium Dynamic Strains and Medium Strain Rates,” *Polymers*, vol. 10, no. 9, 2018.

[50] S. Trabelsi, P.-A. Albouy, and J. Rault, “Crystallization and Melting Processes in Vulcanized Stretched Natural Rubber,” *Macromolecules*, vol. 36, no. 20, pp. 7624–7639, 2003.

[51] S. Trabelsi, P.-A. Albouy, and J. Rault, “Effective Local Deformation in Stretched Filled Rubber,” *Macromolecules*, vol. 36, no. 24, pp. 9093–9099, 2003.

[52] J. Diani, B. Fayolle, and P. Gilormini, “A review on the Mullins effect,” *European Polymer Journal*, vol. 45, no. 3, pp. 601–612, 2009.

[53] F. Laraba-Abbes, P. Ienny, and R. Piques, "A new 'tailor-made' methodology for the mechanical behaviour analysis of rubber-like materials: I. Kinematics measurements using a digital speckle extensometry," *Polymer*, vol. 44, no. 3, pp. 807–820, 2003.

[54] Z. Rigbi, "Reinforcement of rubber by carbon black," in *Properties of Polymers*, ser. Advances in Polymer Science. Berlin, Heidelberg: Springer Berlin Heidelberg, 1980, vol. 36, pp. 21–68.

[55] L. Mullins, "Permanent Set in Vulcanized Rubber," *Rubber Chemistry and Technology*, vol. 22, no. 4, pp. 1036–1044, 1949.

[56] L. Mullins, "Softening of Rubber by Deformation," *Rubber Chemistry and Technology*, vol. 42, no. 1, pp. 339–362, 1969.

[57] A. Lion, "A constitutive model for carbon black filled rubber: Experimental investigations and mathematical representation," *Continuum Mechanics and Thermodynamics*, vol. 8, no. 3, pp. 153–169, 1996.

[58] A. Dorfmann and R. W. Ogden, "A constitutive model for the Mullins effect with permanent set in particle-reinforced rubber," *International Journal of Solids and Structures*, vol. 41, no. 7, pp. 1855–1878, 2004.

[59] J. Diani, M. Brieu, and J. M. Vacherand, "A damage directional constitutive model for Mullins effect with permanent set and induced anisotropy," *European Journal of Mechanics - A/Solids*, vol. 25, no. 3, pp. 483–496, 2006.

[60] J. Diani, M. Brieu, and P. Gilormini, "Observation and modeling of the anisotropic visco-hyperelastic behavior of a rubberlike material," *International Journal of Solids and Structures*, vol. 43, no. 10, pp. 3044–3056, 2006.

[61] W. V. Mars and A. Fatemi, "Observations of the Constitutive Response and Characterization of Filled Natural Rubber Under Monotonic and Cyclic Multiaxial Stress States," *Journal of Engineering Materials and Technology*, vol. 126, no. 1, pp. 19–28, 2004.

[62] C. O. Horgan, R. W. Ogden, and G. Saccomandi, "A theory of stress softening of elastomers based on finite chain extensibility," *Proceedings of the Royal Society of London. Series A: Mathematical, Physical and Engineering Sciences*, vol. 460, no. 2046, pp. 1737–1754, 2004.

[63] D. E. Hanson, M. Hawley, R. Houlton, K. Chitanvis, P. Rae, E. B. Orler, and D. A. Wrobleski, "Stress softening experiments in silica-filled polydimethylsiloxane provide insight into a mechanism for the Mullins effect," *Polymer*, vol. 46, no. 24, pp. 10 989–10 995, 2005.

[64] Y. Merckel, M. Brieu, J. Diani, and J. Caillard, "A Mullins softening criterion for general loading conditions," *Journal of the Mechanics and Physics of Solids*, vol. 60, no. 7, pp. 1257–1264, 2012.

[65] L. Ragni, E. Tubaldi, A. Dall'Asta, H. Ahmadi, and A. Muhr, "Biaxial shear behaviour of HDNR with Mullins effect and deformation-induced anisotropy," *Engineering Structures*, vol. 154, no. 1, pp. 78–92, 2018.

[66] A. F. Blanchard and D. Parkinson, "Breakage of Carbon-Rubber Networks by Applied Stress," *Rubber Chemistry and Technology*, vol. 25, no. 4, pp. 808–842, 1952.

[67] F. Bueche, "Molecular basis for the mullins effect," *Journal of Applied Polymer Science*, vol. 4, no. 10, pp. 107–114, 1960.

[68] A. P. Aleksandrov and J. S. Lazurkin, "Strength of Amorphous and of Crystallizing Rubberlike Polymers," *Rubber Chemistry and Technology*, vol. 19, no. 1, pp. 42–45, 1946.

[69] R. Houwink, "Slipping of Molecules during the Deformation of Reinforced Rubber," *Rubber Chemistry and Technology*, vol. 29, no. 3, pp. 888–893, 1956.

[70] G. Kraus, C. W. Childers, and K. W. Rollmann, "Stress softening in carbon black–reinforced vulcanizates. Strain rate and temperature effects," *Journal of Applied Polymer Science*, vol. 10, no. 2, pp. 229–244, 1966.

[71] M. E. Gurtin and E. C. Francis, "Simple Rate-Independent Model for Damage," *Journal of Spacecraft and Rockets*, vol. 18, no. 3, pp. 285–286, 1981.

[72] J. C. Simo, "On a fully three-dimensional finite-strain viscoelastic damage model: Formulation and computational aspects," *Computer Methods in Applied Mechanics and Engineering*, vol. 60, no. 2, pp. 153–173, 1987.

[73] C. Miehe and J. Keck, "Superimposed finite elastic–viscoelastic–plastoelastic stress response with damage in filled rubbery polymers. Experiments, modelling and algorithmic implementation," *Journal of the Mechanics and Physics of Solids*, vol. 48, no. 2, pp. 323–365, 2000.

[74] G. Chagnon, E. Verron, L. Gornet, G. Marckmann, and P. Charrier, "On the relevance of Continuum Damage Mechanics as applied to the Mullins effect in elastomers," *Journal of the Mechanics and Physics of Solids*, vol. 52, no. 7, pp. 1627–1650, 2004.

[75] C. Naumann and J. Ihlemann, "On the thermodynamics of pseudo-elastic material models which reproduce the Mullins effect," *International Journal of Solids and Structures*, vol. 69-70, pp. 360–369, 2015.

[76] M. Kaliske, L. Nasdala, and H. Rothert, "On damage modelling for elastic and viscoelastic materials at large strain," *Computers & Structures*, vol. 79, no. 22-25, pp. 2133–2141, 2001.

[77] Z. Guo and L. J. Sluys, "Computational modelling of the stress-softening phenomenon of rubber-like materials under cyclic loading," *European Journal of Mechanics - A/Solids*, vol. 25, no. 6, pp. 877–896, 2006.

[78] L. Mullins and N. R. Tobin, "Theoretical Model for the Elastic Behavior of Filler-Reinforced Vulcanized Rubbers," *Rubber Chemistry and Technology*, vol. 30, no. 2, pp. 555–571, 1957.

[79] M. F. Beatty and S. Krishnaswamy, "A theory of stress-softening in incompressible isotropic materials," *Journal of the Mechanics and Physics of Solids*, vol. 48, no. 9, pp. 1931–1965, 2000.

[80] H. J. Qi and M. C. Boyce, "Constitutive model for stretch-induced softening of the stress–stretch behavior of elastomeric materials," *Journal of the Mechanics and Physics of Solids*, vol. 52, no. 10, pp. 2187–2205, 2004. [Online]. Available: https://www.sciencedirect.com/science/article/pii/S0022509604000845

[81] R. W. Ogden and D. G. Roxburgh, "A pseudo–elastic model for the Mullins effect in filled rubber," *Proceedings of the Royal Society of London. Series A: Mathematical, Physical and Engineering Sciences*, vol. 455, no. 1988, pp. 2861–2877, 1999.

[82] A. Dorfmann and R. W. Ogden, "A pseudo-elastic model for loading, partial unloading and reloading of particle-reinforced rubber," *International Journal of Solids and Structures*, vol. 40, no. 11, pp. 2699–2714, 2003.

[83] W. V. Mars, "Evaluation of a Pseudo-Elastic Model for the Mullins Effect," *Tire Science and Technology*, vol. 32, no. 3, pp. 120–145, 2004.

[84] N. Diercks, M. Johlitz, and J. Calipel, "The dynamic Mullins effect: On the influence of the Mullins effect on dynamic moduli," *Proceedings of the Institution of Mechanical Engineers, Part L: Journal of Materials: Design and Applications*, vol. 230, no. 3, pp. 705–716, 2016.

[85] A. E. Zúñiga and M. F. Beatty, "A new phenomenological model for stress-softening in elastomers," *Zeitschrift für angewandte Mathematik und Physik*, vol. 53, no. 5, pp. 794–814, 2002.

[86] R. Kazakevičiūtė-Makovska, "Experimentally determined properties of softening functions in pseudo-elastic models of the Mullins effect," *International Journal of Solids and Structures*, vol. 44, no. 11-12, pp. 4145–4157, 2007.

[87] E. Peña, J. A. Peña, and M. Doblaré, "On the Mullins effect and hysteresis of fibered biological materials: A comparison between continuous and discontinuous damage models," *International Journal of Solids and Structures*, vol. 46, no. 7-8, pp. 1727–1735, 2009.

[88] X. F. Zhang, F. Andrieux, and D. Z. Sun, "Pseudo-elastic description of polymeric foams at finite deformation with stress softening and residual strain effects," *Materials & Design*, vol. 32, no. 2, pp. 877–884, 2011.

[89] B. Fazekas and T. J. Goda, "Constitutive modelling of rubbers: Mullins effect, residual strain, time-temperature dependence," *International Journal of Mechanical Sciences*, vol. 210, p. 106735, 2021.

[90] A. Dorfmann and F. Q. Pancheri, "A constitutive model for the Mullins effect with changes in material symmetry," *International Journal of Non-Linear Mechanics*, vol. 47, no. 8, pp. 874–887, 2012.

[91] A. Anssari-Benam, R. Akbari, and R. Dargazany, "Extending the theory of pseudo-elasticity to capture the permanent set and the induced anisotropy in the Mullins effect," *International Journal of Non-Linear Mechanics*, vol. 156, p. 104500, 2023.

[92] M. P. Wollner, M. Terzano, M. Rolf-Pissarczyk, and G. A. Holzapfel, "A general model for anisotropic pseudo-elasticity and viscoelasticity at finite strains," *Journal of the Mechanics and Physics of Solids*, vol. 180, p. 105403, 2023.

[93] S. Govindjee and J. Simo, "A micro-mechanically based continuum damage model for carbon black-filled rubbers incorporating Mullins' effect," *Journal of the Mechanics and Physics of Solids*, vol. 39, no. 1, pp. 87–112, 1991.

[94] S. Govindjee and J. Simo, "Transition from micro-mechanics to computationally efficient phenomenology: Carbon black filled rubbers incorporating mullins' effect," *Journal of the Mechanics and Physics of Solids*, vol. 40, no. 1, pp. 213–233, 1992.

[95] R. Dargazany and M. Itskov, "A network evolution model for the anisotropic Mullins effect in carbon black filled rubbers," *International Journal of Solids and Structures*, vol. 46, no. 16, pp. 2967–2977, 2009.

[96] R. Dargazany and M. Itskov, "Constitutive modeling of the Mullins effect and cyclic stress softening in filled elastomers," *Physical review. E, Statistical, nonlinear, and soft matter physics*, vol. 88, no. 1, p. 012602, 2013.

[97] M. Klüppel, J. Meier, and M. Dämgen, "Modeling of stress softening and filler induced hysteresis of elastomer materials," in *Constitutive Models for Rubber IV*, P.-E. Austrell and L. Kari, Eds. London: Routledge, 2005, pp. 171–178.

[98] M. Freund, H. Lorenz, D. Juhre, J. Ihlemann, and M. Klüppel, "Finite element implementation of a microstructure-based model for filled elastomers," *International Journal of Plasticity*, vol. 27, no. 6, pp. 902–919, 2011.

[99] H. Lorenz and M. Klüppel, "Microstructure-based modelling of arbitrary deformation histories of filler-reinforced elastomers," *Journal of the Mechanics and Physics of Solids*, vol. 60, no. 11, pp. 1842–1861, 2012.

[100] D. Juhre, R. Raghunath, and M. Klüppel, "The role of the rubber-filler interphase in linear viscoelasticity of SBRs filled with carbon-black nano-size particles," in *Constitutive models for rubber VIII*, N. Gil-Negrete and A. Alonso, Eds. Leiden: CRC Press/Balkema, 2013, pp. 299–304.

[101] G. Marckmann, E. Verron, L. Gornet, G. Chagnon, P. Charrier, and P. Fort, "A theory of network alteration for the Mullins effect," *Journal of the Mechanics and Physics of Solids*, vol. 50, no. 9, pp. 2011–2028, 2002.

[102] G. Chagnon, E. Verron, G. Marckmann, and L. Gornet, "Development of new constitutive equations for the Mullins effect in rubber using the network alteration theory," *International Journal of Solids and Structures*, vol. 43, no. 22-23, pp. 6817–6831, 2006.

[103] J. N. Reddy, *Mechanics of Laminated Composite Plates and Shells*. CRC Press, 2003.

[104] E. Carrera, "Theories and finite elements for multilayered, anisotropic, composite plates and shells," *Archives of Computational Methods in Engineering*, vol. 9, no. 2, pp. 87–140, 2002.

[105] E. Carrera, "Theories and Finite Elements for Multilayered Plates and Shells: A Unified compact formulation with numerical assessment and benchmarking," *Archives of Computational Methods in Engineering*, vol. 10, no. 3, pp. 215–296, 2003.

[106] H. Hu, S. Belouettar, M. Potier-Ferry, and E. M. Daya, "Review and assessment of various theories for modeling sandwich composites," *Composite Structures*, vol. 84, no. 3, pp. 282–292, 2008.

[107] M. F. Caliri, A. J. M. Ferreira, and V. Tita, "A review on plate and shell theories for laminated and sandwich structures highlighting the Finite Element Method," *Composite Structures*, vol. 156, no. 6, pp. 63–77, 2016.

[108] M. Filippi, E. Carrera, and S. Valvano, "Analysis of multilayered structures embedding viscoelastic layers by higher-order, and zig-zag plate elements," *Composites Part B: Engineering*, vol. 154, no. 23, pp. 77–89, 2018.

[109] E. Reissner, "The Effect of Transverse Shear Deformation on the Bending of Elastic Plates," *Journal of Applied Mechanics*, vol. 12, no. 2, pp. A69–A77, 1945.

[110] R. D. Mindlin, "Influence of Rotatory Inertia and Shear on Flexural Motions of Isotropic, Elastic Plates," *Journal of Applied Mechanics*, vol. 18, no. 1, pp. 31–38, 1951.

[111] J. N. Reddy, "A Simple Higher-Order Theory for Laminated Composite Plates," *Journal of Applied Mechanics*, vol. 51, no. 4, pp. 745–752, 1984.

[112] P. F. Pai and A. N. Palazotto, "A higher-order sandwich plate theory accounting for 3-D stresses," *International Journal of Solids and Structures*, vol. 38, no. 30-31, pp. 5045–5062, 2001.

[113] H. Matsunaga, "Assessment of a global higher-order deformation theory for laminated composite and sandwich plates," *Composite Structures*, vol. 56, no. 3, pp. 279–291, 2002.

[114] E. Carrera and L. Demasi, "Two Benchmarks to Assess Two-Dimensional Theories of Sandwich, Composite Plates," *AIAA Journal*, vol. 41, no. 7, pp. 1356–1362, 2003.

[115] A. Wetzel, L. Kärger, R. Rolfes, and K. Rohwer, "Evaluation of two finite element formulations for a rapid 3D stress analysis of sandwich structures," *Computers & Structures*, vol. 83, no. 19-20, pp. 1537–1545, 2005.

[116] L. Kärger, A. Wetzel, R. Rolfes, and K. Rohwer, "A three-layered sandwich element with improved transverse shear stiffness and stresses based on FSDT," *Computers & Structures*, vol. 84, no. 13-14, pp. 843–854, 2006.

[117] E. Carrera and S. Brischetto, "A Survey With Numerical Assessment of Classical and Refined Theories for the Analysis of Sandwich Plates," *Journal of Applied Mechanics*, vol. 62, no. 1, p. London, 2009.

[118] H. Murakami, "Laminated Composite Plate Theory With Improved In-Plane Responses," *Journal of Applied Mechanics*, vol. 53, no. 3, pp. 661–666, 1986.

[119] E. Reissner, "On a certain mixed variational theorem and a proposed application," *International Journal for Numerical Methods in Engineering*, vol. 20, no. 7, pp. 1366–1368, 1984.

[120] E. Carrera, "On the use of the Murakami's zig-zag function in the modeling of layered plates and shells," *Computers & Structures*, vol. 82, no. 7-8, pp. 541–554, 2004.

[121] E. Carrera, "Historical review of Zig-Zag theories for multilayered plates and shells," *Applied Mechanics Reviews*, vol. 56, no. 3, pp. 287–308, 2003.

[122] J.-S. Kao and R. J. Ross, "Bending of multilayer sandwich beams," *AIAA Journal*, vol. 6, no. 8, pp. 1583–1585, 1968.

[123] J. N. Reddy, "A generalization of two–dimensional theories of laminated composite plates," *Communications in Applied Numerical Methods*, vol. 3, no. 3, pp. 173–180, 1987.

[124] R. R. Valisetty and L. W. Rehfield, "Application of ply level analysis to flexural wave propagation," *Journal of Sound and Vibration*, vol. 126, no. 2, pp. 183–194, 1988.

[125] K. N. Cho, C. W. Bert, and A. G. Striz, "Free vibrations of laminated rectangular plates analyzed by higher order individual-layer theory," *Journal of Sound and Vibration*, vol. 145, no. 3, pp. 429–442, 1991.

[126] A. J. M. Ferreira, "Analysis of Composite Plates Using a Layerwise Theory and Multiquadrics Discretization," *Mechanics of Advanced Materials and Structures*, vol. 12, no. 2, pp. 99–112, 2005.

[127] L. Kärger, "Effiziente Simulation von Schlagschädigungen in Faserverbund-Sandwichstrukturen," Ph.D. dissertation, Technische Universität Carolo-Wilhelmina zu Braunschweig, Braunschweig, Germany, 2007.

[128] M. Petrolo, M. Cinefra, A. Lamberti, and E. Carrera, "Evaluation of mixed theories for laminated plates through the axiomatic/asymptotic method," *Composites Part B: Engineering*, vol. 76, no. 1, pp. 260–272, 2015.

[129] E. Carrera and A. Ciuffreda, "A unified formulation to assess theories of multilayered plates for various bending problems," *Composite Structures*, vol. 69, no. 3, pp. 271–293, 2005.

[130] N. Naderi Beni and M. Botshekanan Dehkordi, "An extension of Carrera unified formulation in polar coordinate for analysis of circular sandwich plate with FGM core using GDQ method," *Composite Structures*, vol. 185, pp. 421–434, 2018.

[131] E. Carrera, M. Cinefra, M. Petrolo, and E. Zappino, *Finite element analysis of structures through unified formulation*. Chichester, West Sussex: John Wiley & Sons, 2014.

[132] A. Robaldo, E. Carrera, and A. Benjeddou, "Unified Formulation for Finite Element Thermoelastic Analysis of Multilayered Anisotropic Composite Plates," *Journal of Thermal Stresses*, vol. 28, no. 10, pp. 1031–1065, 2005.

[133] D. Ballhause, M. D'Ottavio, B. Kröplin, and E. Carrera, "A unified formulation to assess multilayered theories for piezoelectric plates," *Computers & Structures*, vol. 83, no. 15-16, pp. 1217–1235, 2005.

[134] L. Demasi, "∞^3 Hierarchy plate theories for thick and thin composite plates: The generalized unified formulation," *Composite Structures*, vol. 84, no. 3, pp. 256–270, 2008.

[135] L. Demasi, "Three-Dimensional Closed Form Solutions and ∞ 3 Theories for Orthotropic Plates," *Mechanics of Advanced Materials and Structures*, vol. 17, no. 1, pp. 20–39, 2009.

[136] L. Demasi, "∞^6 Mixed plate theories based on the Generalized Unified Formulation. Part I: Governing equations," *Composite Structures*, vol. 87, no. 1, pp. 1–11, 2009.

[137] L. Demasi, "∞^6 Mixed plate theories based on the Generalized Unified Formulation.: Part II: Layerwise theories," *Composite Structures*, vol. 87, no. 1, pp. 12–22, 2009.

[138] L. Demasi, "∞^6 Mixed plate theories based on the Generalized Unified Formulation. Part III: Advanced mixed high order shear deformation theories," *Composite Structures*, vol. 87, no. 3, pp. 183–194, 2009.

[139] L. Demasi, "∞^6 Mixed plate theories based on the Generalized Unified Formulation. Part IV: Zig-zag theories," *Composite Structures*, vol. 87, no. 3, pp. 195–205, 2009.

[140] L. Demasi, "∞^6 Mixed plate theories based on the Generalized Unified Formulation. Part V: Results," *Composite Structures*, vol. 88, no. 1, pp. 1–16, 2009.

[141] M. D'Ottavio, "A Sublaminate Generalized Unified Formulation for the analysis of composite structures," *Composite Structures*, vol. 142, no. 923–934, pp. 187–199, 2016.

[142] M. D'Ottavio, L. Dozio, R. Vescovini, and O. Polit, "Bending analysis of composite laminated and sandwich structures using sublaminate variable-kinematic Ritz models," *Composite Structures*, vol. 155, pp. 45–62, 2016.

[143] F. Henning and E. Moeller, Eds., *Handbuch Leichtbau: Methoden, Werkstoffe, Fertigung*. München and Wien: Hanser, 2011.

[144] M. F. Ashby, *Materials selection in mechanical design*, 4th ed. Burlington MA: Butterworth-Heinemann, 2011.

[145] E. M. Kerwin and E. E. Ungar, "Requirements Imposed on Polymeric Materials by Structural Damping Applications," in *Sound and Vibration Damping with Polymers*, R. D. Corsaro and L. H. Sperling, Eds. Washington, DC: American Chemical Society, 1990, vol. 424, pp. 317–345.

[146] P. J. Torvik, "Analysis of Free-Layer Damping Coatings," *Key Engineering Materials*, vol. 333, pp. 195–214, 2007.

[147] H. Oberst, "Über die Dämpfung der Biegeschwingungen dünner Bleche durch fest haftende Beläge," *Acta Acustica united with Acustica*, vol. 2(4), pp. 181–194, 1952.

[148] M. D. Rao and S. He, "Dynamic analysis and design of laminated composite beams with multiple damping layers," *AIAA Journal*, vol. 31, no. 4, pp. 736–745, 1993.

[149] E. M. Kerwin, "Damping of Flexural Waves by a Constrained Viscoelastic Layer," *The Journal of the Acoustical Society of America*, vol. 31, no. 7, pp. 952–962, 1959.

[150] A. Jackstadt, W. V. Liebig, and L. Kärger, "Analytical modeling and investigation of constrained layer damping in hybrid laminates based on a unified plate formulation," *International Journal of Mechanical Sciences*, vol. 216, p. 106964, 2022.

[151] D. Ross, E. E. Ungar, and E. M. Kerwin Jr., "Damping of Plate Flexural Vibrations by Means of Viscoelastic Laminae," in *Structural Damping*, J. E. Ruzicka, Ed. New York: American Society of Mechanical Engineers, 1959, pp. 48–87.

[152] A. D. Nashif, D. I. G. Jones, and J. P. Henderson, *Vibration damping*. New York: Wiley, 1985.

[153] D. K. Rao, "Frequency and Loss Factors of Sandwich Beams under Various Boundary Conditions," *Journal of Mechanical Engineering Science*, vol. 20, no. 5, pp. 271–282, 1978.

[154] R. A. DiTaranto, "Theory of Vibratory Bending for Elastic and Viscoelastic Layered Finite-Length Beams," *Journal of Applied Mechanics*, vol. 32, no. 4, pp. 881–886, 1965.

[155] D. J. Mead and S. Markus, "The forced vibration of a three-layer, damped sandwich beam with arbitrary boundary conditions," *Journal of Sound and Vibration*, vol. 10, no. 2, pp. 163–175, 1969.

[156] J. B. Kosmatka and S. L. Liguore, "Review of Methods for Analyzing Constrained–Layer Damped Structures," *Journal of Aerospace Engineering*, vol. 6, no. 3, pp. 268–283, 1993.

[157] S.-C. Huang, C.-Y. Tsai, and C.-L. Liou, "A general vibration theory for constrained layer damping-treated thick sandwich structures," *Journal of Sandwich Structures & Materials*, vol. 18, no. 3, pp. 343–373, 2016.

[158] D. A. Saravanos and J. M. Pereira, "Effects of interply damping layers on the dynamic characteristics of composite plates," *AIAA Journal*, vol. 30, no. 12, pp. 2906–2913, 1992.

[159] J. Li and Y. Narita, "Analysis and optimal design for the damping property of laminated viscoelastic plates under general edge conditions," *Composites Part B: Engineering*, vol. 45, no. 1, pp. 972–980, 2013.

[160] A. Alaimo, C. Orlando, and S. Valvano, "Analytical frequency response solution for composite plates embedding viscoelastic layers," *Aerospace Science and Technology*, vol. 92, no. 8, pp. 429–445, 2019.

[161] S. Valvano, A. Alaimo, and C. Orlando, "Analytical analysis of sound transmission in passive damped multilayered shells," *Composite Structures*, vol. 253, no. 2, p. 112742, 2020.

[162] S. Wang, J. Zhang, Q. Li, J. Su, and S. Liang, "Free vibration of co-cured composite structures with different numbers of viscoelastic damping membranes," *Composite Structures*, vol. 247, no. 23, p. 112434, 2020.

[163] H. Li, Z. Wang, H. Lv, Z. Zhou, Q. Han, J. Liu, and Z. Qin, "Nonlinear vibration analysis of fiber reinforced composite cylindrical shells with partial constrained layer damping treatment," *Thin-Walled Structures*, vol. 157, no. 4, p. 107000, 2020.

[164] H. Li, W. Wang, X. Wang, Q. Han, J. Liu, Z. Qin, J. Xiong, and Z. Guan, "A nonlinear analytical model of composite plate structure with an MRE function layer considering internal magnetic and temperature fields," *Composites Science and Technology*, vol. 200, no. 9, p. 108445, 2020.

[165] M. D'Ottavio, A. Krasnobrizha, E. Valot, O. Polit, R. Vescovini, and L. Dozio, "Dynamic response of viscoelastic multiple-core sandwich structures," *Journal of Sound and Vibration*, vol. 491, no. 3, p. 115753, 2021.

[166] C. D. Johnson and D. A. Kienholz, "Finite Element Prediction of Damping in Structures with Constrained Viscoelastic Layers," *AIAA Journal*, vol. 20, no. 9, pp. 1284–1290, 1982.

[167] R. Rikards, A. Chate, and E. Barkanov, "Finite element analysis of damping the vibrations of laminated composites," *Computers & Structures*, vol. 47, no. 6, pp. 1005–1015, 1993.

[168] R. A. S. Moreira, J. D. Rodrigues, and A. J. M. Ferreira, "A generalized layerwise finite element for multi-layer damping treatments," *Computational Mechanics*, vol. 37, no. 5, p. 575, 2006.

[169] T. S. Plagianakos and D. A. Saravanos, "High-order layerwise finite element for the damped free-vibration response of thick composite and sandwich composite plates," *International Journal for Numerical Methods in Engineering*, vol. 77, no. 11, pp. 1593–1626, 2009.

[170] M. Bilasse, L. Azrar, and E. M. Daya, "Complex modes based numerical analysis of viscoelastic sandwich plates vibrations," *Computers & Structures*, vol. 89, no. 7-8, pp. 539–555, 2011.

[171] K. Akoussan, H. Boudaoud, E.-M. Daya, and E. Carrera, "Vibration Modeling of Multilayer Composite Structures with Viscoelastic Layers," *Mechanics of Advanced Materials and Structures*, vol. 22, no. 1-2, pp. 136–149, 2015.

[172] S. Ren, G. Zhao, and S. Zhang, "A layerwise finite element formulation for vibration and damping analysis of sandwich plate with moderately thick viscoelastic core," *Mechanics of Advanced Materials and Structures*, vol. 27, no. 14, pp. 1201–1212, 2020.

[173] O. Zarraga, I. Sarría, J. García-Barruetabeña, M. J. Elejabarrieta, and F. Cortés, "General Homogenised Formulation for Thick Viscoelastic Layered Structures for Finite Element Applications," *Mathematics*, vol. 8, no. 5, p. 714, 2020.

[174] A. J. M. Ferreira, A. L. Araújo, A. M. A. Neves, J. D. Rodrigues, E. Carrera, M. Cinefra, and C. M. Mota Soares, "A finite element model using a unified formulation for the analysis of viscoelastic sandwich laminates," *Composites Part B: Engineering*, vol. 45, no. 1, pp. 1258–1264, 2013.

[175] B. Liu, L. Zhao, A. J. M. Ferreira, Y. F. Xing, A. M. A. Neves, and J. Wang, "Analysis of viscoelastic sandwich laminates using a unified formulation and a differential quadrature hierarchical finite element method," *Composites Part B: Engineering*, vol. 110, no. 1, pp. 185–192, 2017.

[176] M. L. Ribeiro, G. F. O. Ferreira, R. D. Medeiros, A. J. M. Ferreira, and V. Tita, "Experimental and numerical dynamic analysis of laminate plates via Carrera Unified Formulation," *Composite Structures*, vol. 202, pp. 1176–1185, 2018.

[177] X. Q. Zhou, D. Y. Yu, X. Y. Shao, S. Q. Zhang, and S. Wang, "Research and applications of viscoelastic vibration damping materials: A review," *Composite Structures*, vol. 136, pp. 460–480, 2016.

[178] S. H. Zhang and H. L. Chen, "A study on the damping characteristics of laminated composites with integral viscoelastic layers," *Composite Structures*, vol. 74, no. 1, pp. 63–69, 2006.

[179] B. R. Sher and R. A. S. Moreira, "Dimensionless analysis of constrained damping treatments," *Composite Structures*, vol. 99, no. 1, pp. 241–254, 2013.

[180] T.-L. Teng and N.-K. Hu, "Analysis of damping characteristics for viscoelastic laminated beams," *Computer Methods in Applied Mechanics and Engineering*, vol. 190, no. 29-30, pp. 3881–3892, 2001.

[181] K. Akoussan, H. Boudaoud, E. M. Daya, Y. Koutsawa, and E. Carrera, "Sensitivity analysis of the damping properties of viscoelastic composite structures according to the layers thicknesses," *Composite Structures*, vol. 149, no. 7, pp. 11–25, 2016.

[182] H. Wang, H. P. Lee, and C. Du, "Analysis and Optimization of Damping Properties of Constrained Layer Damping Structures with Multilayers," *Shock and Vibration*, vol. 2021, no. 1, pp. 1–11, 2021.

[183] J. Öborn, H. Bertilsson, and M. Rigdahl, "Styrene–ethylene/butylene–styrene blends for improved constrained–layer damping," *Journal of Applied Polymer Science*, vol. 80, no. 14, pp. 2865–2876, 2001.

[184] P. P. Hujare and A. D. Sahasrabudhe, "Experimental Investigation of Damping Performance of Viscoelastic Material Using Constrained Layer

Damping Treatment," *Procedia Materials Science*, vol. 5, no. 18, pp. 726–733, 2014.

[185] R. Mateu Pastor, H. Le Sourne, E. Le Gal Salle, and P. Cartraud, "Experiments, numerical models and optimization of carbon-epoxy plates damped by a frequency-dependent interleaved viscoelastic layer," *Mechanics of Advanced Materials and Structures*, vol. 29, no. 21, pp. 3011–3029, 2022.

[186] M. Gröhlich, A. Lang, M. Böswald, and J. Meier, "Viscoelastic damping design – Thermal impact on a constrained layer damping treatment," *Materials & Design*, vol. 207, no. 7, p. 109885, 2021.

[187] H. Li, Z. Li, B. Safaei, W. Rong, W. Wang, Z. Qin, and J. Xiong, "Nonlinear vibration analysis of fiber metal laminated plates with multiple viscoelastic layers," *Thin-Walled Structures*, vol. 168, no. 7, p. 108297, 2021.

[188] A. L. Araújo, P. Martins, C. M. Mota Soares, C. A. Mota Soares, and J. Herskovits, "Damping optimization of viscoelastic laminated sandwich composite structures," *Structural and Multidisciplinary Optimization*, vol. 39, no. 6, pp. 569–579, 2009.

[189] J. F. A. Madeira, A. L. Araújo, C. M. Mota Soares, C. A. Mota Soares, and A. J. M. Ferreira, "Multiobjective design of viscoelastic laminated composite sandwich panels," *Composites Part B: Engineering*, vol. 77, pp. 391–401, 2015.

[190] S. Valvano, C. Orlando, and A. Alaimo, "Design of a noise reduction passive control system based on viscoelastic multilayered plate using PDSO," *Mechanical Systems and Signal Processing*, vol. 123, no. 2, pp. 153–173, 2019.

[191] M. Gröhlich, M. Böswald, and J. Wallaschek, "Viscoelastic damping design – A novel approach for shape optimization of Constrained Layer Damping treatments at different ambient temperatures," *Journal of Sound and Vibration*, vol. 555, p. 117703, 2023.

[192] M. D. Rao, "Recent applications of viscoelastic damping for noise control in automobiles and commercial airplanes," *Journal of Sound and Vibration*, vol. 262, no. 3, pp. 457–474, 2003.

[193] A. Fasana, A. Ferraris, A. G. Airale, D. Berti Polato, and M. Carello, "Experimental Characterization of Damped CFRP Materials with an Application to a Lightweight Car Door," *Shock and Vibration*, vol. 2017, no. 1, pp. 1–9, 2017.

[194] G. L. Ghiringhelli, M. Terraneo, and E. Vigoni, "Improvement of structures vibroacoustics by widespread embodiment of viscoelastic materials," *Aerospace Science and Technology*, vol. 28, no. 1, pp. 227–241, 2013.

[195] H. Zheng, C. Cai, and X. M. Tan, "Optimization of partial constrained layer damping treatment for vibrational energy minimization of vibrating beams," *Computers & Structures*, vol. 82, no. 29-30, pp. 2493–2507, 2004.

[196] B. Khalfi and A. Ross, "Transient response of a plate with partial constrained viscoelastic layer damping," *International Journal of Mechanical Sciences*, vol. 68, no. 3, pp. 304–312, 2013.

[197] R. Stanway, J. A. Rongong, and N. D. Sims, "Active constrained-layer damping: A state-of-the-art review," *Proceedings of the Institution of Mechanical Engineers, Part I: Journal of Systems and Control Engineering*, vol. 217, no. 6, pp. 437–456, 2003.

[198] S. C. Huang, D. J. Inman, and E. M. Austin, "Some design considerations for active and passive constrained layer damping treatments," *Smart Materials and Structures*, vol. 5, no. 3, pp. 301–313, 1996.

[199] Y. Liu, M. Zogg, and P. Ermanni, "An experimental comparative study on non-conventional surface and interface damping techniques for automotive panel structures," *Journal of Vibration and Control*, vol. 18, no. 14, pp. 2210–2233, 2012.

[200] T. Ehrig, K. Holeczek, and P. Kostka, "Experimental investigations of lightweight structures with fluidically actuated Compressible Constrained Layer Damping," *Materials Today Communications*, vol. 16, pp. 204–211, 2018.

[201] T. Ehrig, M. Dannemann, R. Luft, C. Adams, N. Modler, and P. Kostka, "Sound Transmission Loss of a Sandwich Plate with Adjustable Core Layer Thickness," *Materials (Basel, Switzerland)*, vol. 13, no. 18, 2020.

[202] R. C. Alderliesten, *Fatigue crack propagation and delamination growth in glare*. Netherlands: Delft University Press, 2005.

[203] R. C. Alderliesten, *Fatigue and fracture of fibre metal laminates*, ser. Solid mechanics and its applications. Cham, Switzerland: Springer, 2017, vol. 236.

[204] H. E. Etri, M. E. Korkmaz, M. K. Gupta, M. Gunay, and J. Xu, "A state-of-the-art review on mechanical characteristics of different fiber metal laminates for aerospace and structural applications," *The International Journal of Advanced Manufacturing Technology*, vol. 123, no. 9-10, pp. 2965–2991, 2022.

[205] T. Sinmazçelik, E. Avcu, M. Ö. Bora, and O. Çoban, "A review: Fibre metal laminates, background, bonding types and applied test methods," *Materials & Design*, vol. 32, no. 7, pp. 3671–3685, 2011.

[206] M. Sadighi, R. C. Alderliesten, and R. Benedictus, "Impact resistance of fiber-metal laminates: A review," *International Journal of Impact Engineering*, vol. 49, pp. 77–90, 2012.

[207] J. Bienias, P. Jakubczak, and K. Dadej, "Low-velocity impact resistance of aluminium glass laminates – Experimental and numerical investigation," *Composite Structures*, vol. 152, no. 15, pp. 339–348, 2016.

[208] C. T. Lin, P. W. Kao, and M.-H. R. Jen, "Thermal residual strains in carbon fibre-reinforced aluminium laminates," *Composites*, vol. 25, no. 4, pp. 303–307, 1994.

[209] C. T. Lin, P. W. Kao, and F. S. Yang, "Fatigue behaviour of carbon fibre-reinforced aluminium laminates," *Composites*, vol. 22, no. 2, pp. 135–141, 1991.

[210] G. Lawcock, L. Ye, Y.-W. Mai, and C.-T. Sun, "The effect of adhesive bonding between aluminum and composite prepreg on the mechanical properties of carbon-fiber-reinforced metal laminates," *Composites Science and Technology*, vol. 57, no. 1, pp. 35–45, 1997.

[211] W.-X. Wang, Y. Takao, and T. Matsubara, Eds., *Galvanic corrosion-resistant carbon fiber metal laminates*, 2007.

[212] L. Hamill, D. C. Hofmann, and S. Nutt, "Galvanic Corrosion and Mechanical Behavior of Fiber Metal Laminates of Metallic Glass and Carbon Fiber Composites," *Advanced Engineering Materials*, vol. 20, no. 2, 2018.

[213] E. Sarlin, "Characterisation of novel corrosion resistant stainless steel/rubber/composite hybrid structures," Ph.D. dissertation, Tampere University of Technology,, Tampere, Finland, 2014.

[214] E. Sarlin, Y. Liu, M. Vippola, M. Zogg, P. Ermanni, J. Vuorinen, and T. Lepistö, "Vibration damping properties of steel/rubber/composite hybrid structures," *Composite Structures*, vol. 94, no. 11, pp. 3327–3335, 2012.

[215] E. Sarlin, M. Apostol, M. Lindroos, V.-T. Kuokkala, J. Vuorinen, T. Lepistö, and M. Vippola, "Impact properties of novel corrosion resistant hybrid structures," *Composite Structures*, vol. 108, no. 1, pp. 886–893, 2014.

[216] E. Sarlin, M. Lindroos, M. Apostol, V.-T. Kuokkala, J. Vuorinen, T. Lepistö, and M. Vippola, "The effect of test parameters on the impact resistance of a stainless steel/rubber/composite hybrid structure," *Composite Structures*, vol. 113, pp. 469–475, 2014.

[217] E. Sarlin, E. Heinonen, J. Vuorinen, M. Vippola, and T. Lepistö, "Adhesion properties of novel corrosion resistant hybrid structures," *International Journal of Adhesion and Adhesives*, vol. 49, pp. 51–57, 2014.

[218] E. Sarlin, M. Hoikkanen, L. Frisk, J. Vuorinen, M. Vippola, and T. Lepistö, "Ageing of corrosion resistant steel/rubber/composite hybrid structures," *International Journal of Adhesion and Adhesives*, vol. 49, pp. 26–32, 2014.

[219] A. Taherzadeh-Fard, G. Liaghat, H. Ahmadi, O. Razmkhah, S. C. Charandabi, M. A. Zarezadeh-Mehrizi, and A. Khodadadi, "Experimental and numerical investigation of the impact response of elastomer layered fiber metal laminates (EFMLs)," *Composite Structures*, vol. 245, no. 11, p. 112264, 2020.

[220] M. Stoll, F. Stemmer, S. Ilinzeer, and K. A. Weidenmann, "Optimization of Corrosive Properties of Carbon Fiber Reinforced Aluminum Laminates due to Integration of an Elastomer Interlayer," *Key Engineering Materials*, vol. 742, pp. 287–293, 2017.

[221] V. Sessner, M. Stoll, A. Feuvrier, and K. A. Weidenmann, "Determination of the Damping Characteristics of Fiber-Metal-Elastomer Laminates Using Piezo-Indicated-Loss-Factor Experiments," *Key Engineering Materials*, vol. 742, pp. 325–332, 2017.

[222] V. Sessner, W. V. Liebig, L. Kärger, and K. A. Weidenmann, "Experimental and numerical characterisation of fibre–metal–elastomer laminates by using DMA regarding its damping behaviour," *PAMM*, vol. 18, no. 1, 2018.

[223] W. V. Liebig, V. Sessner, K. A. Weidenmann, and L. Kärger, "Numerical and experimental investigations of the damping behaviour of hybrid CFRP-elastomer-metal laminates," *Composite Structures*, vol. 202, no. 7, pp. 1109–1113, 2018.

[224] M. Stoll, V. Sessner, M. Kramar, J. Technau, and K. A. Weidenmann, "The effect of an elastomer interlayer thickness variation on the mechanical properties of Fiber-Metal-Laminates," *Composite Structures*, vol. 219, no. 103, pp. 90–96, 2019.

[225] S. Roth, M. Stoll, K. A. Weidenmann, S. Coutandin, and J. Fleischer, "A new process route for the manufacturing of highly formed fiber-metal-laminates with elastomer interlayers (FMEL)," *The International Journal of Advanced Manufacturing Technology*, vol. 104, no. 1-4, pp. 1293–1301, 2019.

[226] V. Sessner and K. A. Weidenmann, "Temperature Dependency of the Deformation Behavior of Hybrid CFRP/Elastomer/Metal Laminates under 3-Point Bending Loads," *Key Engineering Materials*, vol. 809, pp. 259–265, 2019.

[227] V. Sessner, A. Jackstadt, W. V. Liebig, L. Kärger, and K. A. Weidenmann, "Damping Characterization of Hybrid Carbon Fiber Elastomer Metal Laminates using Experimental and Numerical Dynamic Mechanical Analysis," *Journal of Composites Science*, vol. 3, no. 1, p. 3, 2019.

[228] V. Sessner, W. V. Liebig, and K. A. Weidenmann, "Modal damping behavior of plane and 3D curved constrained layer damping CFRP-elastomer-metal laminates," *Composites Part C: Open Access*, vol. 2, p. 100037, 2020.

[229] V. Sessner, W. V. Liebig, A. Jackstadt, D. Schmid, T. Ehrig, K. Holeczek, N. Gräbner, P. Kostka, U. von Wagner, K. A. Weidenmann, and L. Kärger, "Wide Scale Characterization and Modeling of the Vibration and Damping Behavior of CFRP-Elastomer-Metal Laminates—Comparison and Discussion of Different Test Setups," *Applied Composite Materials*, vol. 28, no. 5, pp. 1715–1746, 2021.

[230] V. Sessner, "Charakterisierung und Modellierung des Dämpfungsverhaltens von hybriden Faser-Metall-Elastomer-Laminaten," Dissertation, Karlsruhe Institute of Technology, Karlsruhe, Germany, 2021.

[231] M. Povolo, L. Raimondi, T. M. Brugo, A. Pagani, D. Comand, L. Pirazzini, and A. Zucchelli, "Design and manufacture of hybrid aluminum/composite co-cured tubes with viscoelastic interface layer," *Procedia Structural Integrity*, vol. 12, pp. 196–203, 2018.

[232] M. Povolo, T. M. Brugo, and A. Zucchelli, "Numerical and Experimental Investigation of Aluminum/CFRP Hybrid Tubes with Rubber-like Interlayer," *Applied Composite Materials*, vol. 27, no. 3, pp. 269–283, 2020.

[233] A. Jackstadt, W. V. Liebig, K. A. Weidenmann, and L. Kärger, "On the influence of low-velocity impact damage on constrained-layer damping in hybrid cfrp-elastomer-metal laminates," *Materials & Design*, vol. 241, p. 112882, 2024.

[234] W. He, L. Wang, Liu, H. Wang, C., L. Yao, Q. Li, and G. Sun, "On impact behavior of fiber metal laminate (FML) structures: A state-of-the-art review," *Thin-Walled Structures*, vol. 167, p. 108026, 2021.

[235] D. Düring, L. Weiß, D. Stefaniak, N. Jordan, and C. Hühne, "Low-velocity impact response of composite laminates with steel and elastomer protective layer," *Composite Structures*, vol. 134, no. 1110, pp. 18–26, 2015.

[236] D. Düring, E. Petersen, D. Stefaniak, and C. Hühne, "Damage resistance and low-velocity impact behaviour of hybrid composite laminates with multiple thin steel and elastomer layers," *Composite Structures*, vol. 238, no. 5, p. 111851, 2020.

[237] Z. Li, J. Zhang, A. Jackstadt, and L. Kärger, "Low-velocity impact behavior of hybrid CFRP-elastomer-metal laminates in comparison with conventional fiber-metal laminates," *Composite Structures*, vol. 287, no. 7, p. 115340, 2022.

[238] M. A. Zarezadeh-Mehrizi, G. Liaghat, H. Ahmadi, A. Taherzadeh-Fard, and A. Khodadadi, "Numerical and experimental investigation of fiber metal laminates with elastomeric layers under low–velocity impact," *Polymer Composites*, vol. 43, no. 4, pp. 1936–1947, 2022.

[239] V. Mahesh, "Comparative study on low velocity impact response of carbon-fiber-reinforced polymer/ thermoplastic elastomer based fiber metal laminates with and without interleaving of elastomeric layer," *Journal of Thermoplastic Composite Materials*, p. 089270572311804, 2023.

[240] R. L. Ramkumar, S. V. Kulkarni, and R. B. Pipes, "Free Vibration Frequencies of a Delaminated Beam," in *Proceedings of the 34th Annual Technical Conference*, vol. 22-E. Society of the Plastics Industry, 1979, pp. 1–5.

[241] J. T. S. Wang, Y. Y. Liu, and J. A. Gibby, "Vibrations of split beams," *Journal of Sound and Vibration*, vol. 84, no. 4, pp. 491–502, 1982.

[242] P. M. Mujumdar and S. Suryanarayan, "Flexural vibrations of beams with delaminations," *Journal of Sound and Vibration*, vol. 125, no. 3, pp. 441–461, 1988.

[243] J. E. Grady and E. H. Meyn, "Vibration testing of impact-damaged composite laminates," Cleveland, Ohio, 1989. [Online]. Available: https://ntrs.nasa.gov/api/citations/19890015919/downloads/19890015919.pdf

[244] M.-H. H. Shen and J. E. Grady, "Free vibrations of delaminated beams," *AIAA Journal*, vol. 30, no. 5, pp. 1361–1370, 1992.

[245] C. N. Della and D. Shu, "Vibration of delaminated multilayer beams," *Composites Part B: Engineering*, vol. 37, no. 2-3, pp. 227–236, 2005.

[246] G. S. Ramtekkar, "Free vibration analysis of delaminated beams using mixed finite element model," *Journal of Sound and Vibration*, vol. 328, no. 4-5, pp. 428–440, 2009.

[247] Z. Zhang, K. Shankar, M. Tahtali, and E. V. Morozov, "Vibration Modelling of Composite Laminates with Delamination Damage," in *20th International Congress on Acoustics 2010*, M. Burgess, Ed. Red Hook, N.Y.: Printed by Curran Associates, 2010, pp. 1–8.

[248] Y. Liu, J. Xiao, and D. Shu, "Free Vibration of Exponential Functionally Graded Beams with Single Delamination," *Procedia Engineering*, vol. 75, pp. 164–168, 2014.

[249] X. Li and D. Halim, "Free and forced vibration modelling of a delaminated beam structure using a Green's function method," *Acta Mechanica*, vol. 234, no. 7, pp. 2889–2906, 2023.

[250] H. Luo and S. Hanagud, "Dynamics of delaminated beams," *International Journal of Solids and Structures*, vol. 37, no. 10, pp. 1501–1519, 2000.

[251] R.-A. Jafari-Talookolaei, M. Abedi, and M. Hajianmaleki, "Vibration characteristics of generally laminated composite curved beams with single through-the-width delamination," *Composite Structures*, vol. 138, pp. 172–183, 2016.

[252] C. N. Della and D. Shu, "Vibration of Delaminated Composite Laminates: A Review," *Applied Mechanics Reviews*, vol. 60, no. 1, pp. 1–20, 2007.

[253] W.-L. Yin and K. C. Jane, "Vibration of a delaminated beam-plate relative to buckled states," *Journal of Sound and Vibration*, vol. 156, no. 1, pp. 125–140, 1992.

[254] H.-P. Chen, "Free vibration of prebuckled and postbuckled plates with delamination," *Composites Science and Technology*, vol. 51, no. 3, pp. 451–462, 1994.

[255] S. Dey and A. Karmakar, "Free vibration analyses of multiple delaminated angle-ply composite conical shells – A finite element approach," *Composite Structures*, vol. 94, no. 7, pp. 2188–2196, 2012.

[256] S. Ganesh, K. S. Kumar, and P. K. Mahato, "Free Vibration Analysis of Delaminated Composite Plates Using Finite Element Method," *Procedia Engineering*, vol. 144, pp. 1067–1075, 2016.

[257] Z.-X. Wang, P. Qiao, and J. Xu, "Vibration analysis of laminated composite plates with damage using the perturbation method," *Composites Part B: Engineering*, vol. 72, pp. 160–174, 2015.

[258] T. Nguyen-Thoi, T. Rabczuk, T. Lam-Phat, V. Ho-Huu, and P. Phung-Van, "Free vibration analysis of cracked Mindlin plate using an extended cell-based smoothed discrete shear gap method (XCS-DSG3)," *Theoretical and Applied Fracture Mechanics*, vol. 72, no. 1, pp. 150–163, 2014.

[259] A. Viglietti, E. Zappino, and E. Carrera, "Free vibration analysis of locally damaged aerospace tapered composite structures using component-wise models," *Composite Structures*, vol. 192, no. 2, pp. 38–51, 2018.

[260] H. Li, Z. Li, Z. Xiao, X. Wang, J. Xiong, J. Zhou, and Z. Guan, "Development of an integrated model for prediction of impact and vibration response of hybrid fiber metal laminates with a viscoelastic layer," *International Journal of Mechanical Sciences*, vol. 197, no. 3, p. 106298, 2021.

[261] J. Iriondo, L. Aretxabaleta, and A. Aizpuru, "Characterisation of the elastic and damping properties of traditional FML and FML based on a self-reinforced polypropylene," *Composite Structures*, vol. 131, no. 7, pp. 47–54, 2015.

[262] Hexcel Corporation, "Technical data sheet HexPly® M77 fast curing epoxy resin matrix for prepregs," 2017.

[263] Deutsches Institut für Normung e.V., "Plastics - Determination of tensile properties - Part 5: Test conditions for unidirectional fibre-reinforced plastic composites (ISO 527-5:2021); German version EN ISO 527-5:2021," Berlin, 2022.

[264] Deutsches Institut für Normung e.V., "Aerospace series - Fibre reinforced plastics - Test method - Determination of in-plane shear properties (± 45° tensile test); German and English version EN 6031:2015," Berlin, 2016.

[265] H. Schürmann, *Konstruieren mit Faser-Kunststoff-Verbunden*, 2nd ed., ser. VDI-Buch. Berlin, Heidelberg: Springer, 2007.

[266] W. V. Liebig, A. Jackstadt, V. Sessner, K. A. Weidenmann, and L. Kärger, "Frequency domain modelling of transversely isotropic viscoelastic fibre-reinforced plastics," *Composites Science and Technology*, vol. 180, no. 3, pp. 101–110, 2019.

[267] Gummiwerk KRAIBURG GmbH & Co. KG, “Technical Data Sheet KRAIBON® SAA9579/52,” 2014.

[268] Gummiwerk KRAIBURG GmbH & Co. KG, “Technical data sheet KRAIBON® HVV9632/59,” 2017.

[269] Gummiwerk KRAIBURG GmbH & Co. KG, “Technical data sheet KRAIBON® HAA9275/45,” 2022.

[270] American Society for Testing and Materials, “Standard Test Methods for Vulcanized Rubber and Thermoplastic Elastomers - Tension,” West Conshohocken, PA, 2021.

[271] P. Eyerer, G. Twardon, J. K. L. Schneider, F. Leibrandt, and V. Gettwert, “Eigenschaften von Kunststoffen in Bauteilen,” in *Polymer Engineering*, ser. VDI-Buch, P. Eyerer, T. Hirth, and P. Elsner, Eds. Berlin, Heidelberg: Springer Berlin Heidelberg, 2008, pp. 44–210.

[272] K. S. Cho, “Geometric interpretation of time-temperature superposition,” *Korea-Australia Rheology Journa*, vol. 21, no. 1, pp. 13–16, 2009.

[273] J.-E. Bae, K. S. Cho, K. H. Seo, and D.-G. Kang, “Application of geometric algorithm of time-temperature superposition to linear viscoelasticity of rubber compounds,” *Korea-Australia Rheology Journal*, vol. 23, no. 2, pp. 81–87, 2011.

[274] A. Jackstadt, W. V. Liebig, V. Sessner, K. A. Weidenmann, and L. Kärger, “Application of a mixed variational higher order plate theory towards understanding the deformation behavior of hybrid laminates,” *PAMM*, vol. 19, no. 1, 2019.

[275] A. Jackstadt and L. Kärger, “Extension of an analytical solution of a unified formulation to the frequency response of composite plates with viscoelastic layers,” *PAMM*, vol. 20, no. 1, 2021.

[276] E. Carrera, “A Reissner’s Mixed Variational Theorem Applied to Vibration Analysis of Multilayered Shell,” *Journal of Applied Mechanics*, vol. 66, no. 1, pp. 69–78, 1999.

[277] E. Carrera and L. Demasi, "Classical and advanced multilayered plate elements based upon PVD and RMVT. Part 1: Derivation of finite element matrices," *International Journal for Numerical Methods in Engineering*, vol. 55, no. 2, pp. 191–231, 2002.

[278] E. Carrera and L. Demasi, "Classical and advanced multilayered plate elements based upon PVD and RMVT. Part 2: Numerical implementations," *International Journal for Numerical Methods in Engineering*, vol. 55, no. 3, pp. 253–291, 2002.

[279] E. Carrera, "Evaluation of Layerwise Mixed Theories for Laminated Plates Analysis," *AIAA Journal*, vol. 36, no. 5, pp. 830–839, 1998.

[280] J. W. Park, K. C. Lee, and Y. H. Kim, "Comparative study of finite element based response evaluation methods for laminated plates," *Computational Mechanics*, vol. 32, no. 1-2, pp. 115–133, 2003.

[281] J.-B. Donnet and E. Custodero, "Reinforcement of Elastomers by Particulate Fillers," in *The Science and Technology of Rubber*, J. E. Mark, B. Erman, and C. M. Roland, Eds. Elsevier Academic Press, 2013, pp. 383–416.

[282] O. C. Zienkiewicz and R. L. Taylor, *The Finite Element Method: Volume 1: The Basis*, 5th ed. Oxford, United Kingdom: Butterworth-Heinemann, 2000.

[283] A. W. Leissa, "The historical bases of the Rayleigh and Ritz methods," *Journal of Sound and Vibration*, vol. 287, no. 4-5, pp. 961–978, 2005.

[284] L. Dozio and E. Carrera, "A variable kinematic Ritz formulation for vibration study of quadrilateral plates with arbitrary thickness," *Journal of Sound and Vibration*, vol. 330, no. 18-19, pp. 4611–4632, 2011.

[285] A. Jackstadt, F. Frölich, K. A. Weidenmann, and L. Kärger, "Modeling the Mullins effect of rubbers used in constrained–layer damping applications," *PAMM*, vol. 21, no. 1, 2021.

[286] A. Jackstadt, V. Sessner, W. Liebig, L. Kärger, and K. Weidenmann, "HyCEML – Hybrid CFRP Elastomer Metal Laminates Containing Elastomeric Interfaces for Deliberate Dissipation," in *Calm, Smooth and Smart*, ser. Lecture Notes in Applied and Computational Mechanics, P. Eberhard, Ed. Cham: Springer Nature Switzerland, 2024, vol. 102, pp. 105–125.

[287] F. Frölich, "Modellierung und numerische Untersuchung des Mullins-Effekts bezüglich des Dämpfungsverhaltens hybrider CFK-Elastomer-Metall Laminate," Master's thesis, Karlsruhe Institute of Technology, Karlsruhe, Germany, 2020.

[288] K. A. Lazopoulos and R. W. Ogden, "Nonlinear Elasticity Theory with Discontinuous Internal Variables," *Mathematics and Mechanics of Solids*, vol. 3, no. 1, pp. 29–51, 1998.

[289] M. Hossain and P. Steinmann, "More hyperelastic models for rubber-like materials: consistent tangent operators and comparative study," *Journal of the Mechanical Behavior of Materials*, vol. 22, no. 1-2, pp. 27–50, 2013.

[290] P. Chadwick and R. W. Ogden, "On the definition of elastic moduli," *Archive for Rational Mechanics and Analysis*, vol. 44, no. 1, pp. 41–53, 1971.

[291] P. Chadwick and R. W. Ogden, "A theorem of tensor calculus and its application to isotropic elasticity," *Archive for Rational Mechanics and Analysis*, vol. 44, no. 1, pp. 54–68, 1971.

[292] J. C. Simo and R. L. Taylor, "Quasi-incompressible finite elasticity in principal stretches. continuum basis and numerical algorithms," *Computer Methods in Applied Mechanics and Engineering*, vol. 85, no. 3, pp. 273–310, 1991.

[293] J. C. Simo, "Numerical analysis and simulation of plasticity," in *Handbook of numerical analysis*, P. G. Ciarlet and J.-L. Lions, Eds. Amsterdam and New York and New York: North-Holland and Distributors for the United States and Canada Elsevier Science Pub. Co, 1998, vol. 6, pp. 183–499.

[294] B. Jeremić and Z. Cheng, "Significance of equal principal stretches in computational hyperelasticity," *Communications in Numerical Methods in Engineering*, vol. 21, no. 9, pp. 477–486, 2005.

[295] S. J. Connolly, D. Mackenzie, and Y. Gorash, "Isotropic hyperelasticity in principal stretches: explicit elasticity tensors and numerical implementation," *Computational Mechanics*, vol. 64, no. 5, pp. 1273–1288, 2019.

[296] W. Ji, A. M. Waas, and Z. P. Bazant, "On the Importance of Work-Conjugacy and Objective Stress Rates in Finite Deformation Incremental Finite Element Analysis," *Journal of Applied Mechanics*, vol. 80, no. 4, p. 919, 2013.

[297] J. Kopp, "Efficient Numerical Diagonalization of Hermitian 3 × 3 Matrices," *International Journal of Modern Physics C*, vol. 19, no. 03, pp. 523–548, 2008.

[298] S. J. Connolly, "Numerical modelling of rubber hyperelasticity, parameter identification and finite element implementations," Ph.D. dissertation, University of Strathclyde, Glasgow, Scotland, United Kingdom, 2020.

[299] S. J. Connolly, "Data for: "Isotropic hyperelasticity in principal stretches: Fortran programs and subroutines"," 2019. [Online]. Available: https://pureportal.strath.ac.uk/en/datasets/data-for-isotropic-hyperelasticity-in-principal-stretches-fortran

[300] R. Storn and K. Price, "Differential Evolution – A Simple and Efficient Heuristic for global Optimization over Continuous Spaces," *Journal of Global Optimization*, vol. 11, no. 4, pp. 341–359, 1997.

[301] M. Brieu, J. Diani, C. Mignot, and C. Moriceau, "Response of a carbon-black filled SBR under large strain cyclic uniaxial tension," *International Journal of Fatigue*, vol. 32, no. 12, pp. 1921–1927, 2010.

[302] W. Yu, X. Chen, Y. Wang, L. Yan, and N. Bai, "Uniaxial ratchetting behavior of vulcanized natural rubber," *Polymer Engineering & Science*, vol. 48, no. 1, pp. 191–197, 2008.

[303] A. Zhong, "Discussions on "A constitutive model for the Mullins effect with permanent set in a particle-reinforced rubber" by A. Dorfmann and R.W. Ogden," *International Journal of Solids and Structures*, vol. 42, no. 13, pp. 3967–3969, 2005.

[304] A. Dorfmann, "Reply to A. Zhong "Discussions on 'A constitutive model for the Mullins effect with permanent set in a particle-reinforced rubber' by A. Dorfmann and R.W. Ogden"," *International Journal of Solids and Structures*, vol. 42, no. 16-17, pp. 4909–4910, 2005.

[305] M. Terzano, M. P. Wollner, M. P. Kainz, M. Rolf-Pissarczyk, N. Götzen, and G. A. Holzapfel, "Modelling the anisotropic inelastic response of polymeric scaffolds for in situ tissue engineering applications," *Journal of the Royal Society, Interface*, vol. 20, no. 206, p. 20230318, 2023.

[306] C. Miehe, "Numerical computation of algorithmic (consistent) tangent moduli in large-strain computational inelasticity," *Computer Methods in Applied Mechanics and Engineering*, vol. 134, no. 3-4, pp. 223–240, 1996.

[307] American Society for Testing and Materials, "Test Method for Measuring the Damage Resistance of a Fiber-Reinforced Polymer Matrix Composite to a Drop-Weight Impact Event," West Conshohocken, PA, 2015.

[308] I. Lapczyk and J. A. Hurtado, "Progressive damage modeling in fiber-reinforced materials," *Composites Part A: Applied Science and Manufacturing*, vol. 38, no. 11, pp. 2333–2341, 2007.

[309] S. F. M. Almeida and J. S. Hansen, "Natural frequencies of composite plates with tailored thermal residual-stresses," *International Journal of Solids and Structures*, vol. 36, no. 23, pp. 3517–3539, 1999.

[310] G. Capote Rodríguez, J. Carrillo, and M. L. Sánchez, "Influence of thermal residual stresses on the free vibration of reinforced laminates," *DYNA*, vol. 84, no. 203, pp. 298–305, 2017.

List of own publications

Book contributions

- A. Jackstadt, V. Sessner, W. Liebig, L. Kärger, and K. Weidenmann. HyCEML – Hybrid CFRP Elastomer Metal Laminates Containing Elastomeric Interfaces for Deliberate Dissipation. In P. Eberhard, editor, *Calm, Smooth and Smart*, volume 102 of *Lecture Notes in Applied and Computational Mechanics*, pages 105–125. Springer Nature, Cham, Switzerland, 2024.

Journal articles

- A. Jackstadt, W. V. Liebig, K. A. Weidenmann, and L. Kärger. On the influence of low-velocity impact damage on constrained-layer damping in hybrid cfrp-elastomer-metal laminates. *Materials & Design*, 241:112882, 2024.
- N. Meyer, E. L. Wagemann, A. Jackstadt, and R. Seifried. Material and particle size sensitivity analysis on coefficient of restitution in low-velocity normal impacts. *Computational Particle Mechanics*, 9(6):1293–1308, 2022.
- Z. Li, J. Zhang, A. Jackstadt, and L. Kärger. Low-velocity impact behavior of hybrid CFRP-elastomer-metal laminates in comparison with conventional fiber-metal laminates. *Composite Structures*, 287(7):115340, 2022.
- A. Jackstadt, W. V. Liebig, and L. Kärger. Analytical modeling and investigation of constrained layer damping in hybrid laminates based on

a unified plate formulation. *International Journal of Mechanical Sciences*, 216:106964, 2022.

- V. Sessner, W. V. Liebig, A. Jackstadt, D. Schmid, T. Ehrig, K. Holeczek, N. Gräbner, P. Kostka, U. von Wagner, K. A. Weidenmann, and L. Kärger. Wide Scale Characterization and Modeling of the Vibration and Damping Behavior of CFRP-Elastomer-Metal Laminates—Comparison and Discussion of Different Test Setups. *Applied Composite Materials*, 28(5):1715–1746, 2021.
- A. Jackstadt and L. Kärger. Extension of an analytical solution of a unified formulation to the frequency response of composite plates with viscoelastic layers. *PAMM*, 20(1), 2021.
- A. Jackstadt, F. Frölich, K. A. Weidenmann, and L. Kärger. Modeling the Mullins effect of rubbers used in constrained–layer damping applications. *PAMM*, 21(1), 2021.
- V. Sessner, A. Jackstadt, W. V. Liebig, L. Kärger, and K. A. Weidenmann. Damping Characterization of Hybrid Carbon Fiber Elastomer Metal Laminates using Experimental and Numerical Dynamic Mechanical Analysis. *Journal of Composites Science*, 3(1):3, 2019.
- A. Jackstadt, W. V. Liebig, V. Sessner, K. A. Weidenmann, and L. Kärger. Application of a mixed variational higher order plate theory towards understanding the deformation behavior of hybrid laminates. *PAMM*, 19(1), 2019.
- W. V. Liebig, A. Jackstadt, V. Sessner, K. A. Weidenmann, and L. Kärger. Frequency domain modelling of transversely isotropic viscoelastic fibre-reinforced plastics. *Composites Science and Technology*, 180(3):101–110, 2019.

Conference presentations

- A. Jackstadt, L. Kärger, and K. A. Weidenmann. The influence of impact damage on the damping behavior of constrained layer damping laminates. Presented at: 23rd International Conference on Composite Materials (ICCM 2023), Belfast, United Kingdom, July 31th – August 4th, 2023.

- A. Jackstadt, F. Frölich, W. V. Liebig, L. Kärger, and K. A. Weidenmann. Investigation into the influence of the Mullins effect on the dynamic behavior of hybrid laminates. Presented at: 11th European Solid Mechanics Conference (ESMC 2022), Galway, Ireland, July 4th – July 8th, 2022.

- A. Jackstadt, W. V. Liebig, and L. Kärger. A Multi-Layer Finite Shell Element based on the Generalized Unified Formulation for the Analysis of Hybrid Carbon Fiber Elastomer Metal Laminates. Presented at: 12th International Conference on Composite Science and Technology (ICCST12), Sorrento, Italy, May 8th – May 10th, 2019.

- A. Jackstadt, W. V. Liebig, V. Sessner, K. A. Weidenmann, and L. Kärger. Materialmodellierung zur Untersuchung des Schwingungs- und Dämpfungsverhaltens von hybriden CFK-Elastomer-Metall-Laminaten. Presented at: Sitzung des DGM Fachausschusses Polymerwerkstoffe Themenschwerpunkt Simulation, numerische Methoden und Kennwertermittlung, Kassel, Germany, November 15th – November 16th, 2018.

- A. Jackstadt, W. V. Liebig, S. Galkin, V. Sessner, K. A. Weidenmann, and L. Kärger. A Multi-Scale Approach for the Virtual Characterization of Transversely Isotropic Viscoelastic Materials in the Frequency Domain. Presented at: 8th KMM-VIN Industrial Workshop: Modelling of composite materials and composite coatings (IW8 2018), Freiburg im Breisgau, Germany, Octover 9th – October 10th, 2018.

- F. Frölich, D. Dörr, A. Jackstadt, and L. Kärger. Challenges in characterization of polylactic acid (PLA) for thermomechanical material modeling in material

extrusion. Presented at: 11th European Solid Mechanics Conference (ESMC 2022), Galway, Ireland, July 4th – July 8th, 2022.

Karlsruher Schriftenreihe Fahrzeugsystemtechnik
FAST Institut für Fahrzeugsystemtechnik
(ISSN 1869-6058)

Eine vollständige Übersicht der Bände finden Sie im Verlagsshop

Band 76 Kai-Lukas Bauer
Echtzeit-Strategieplanung für vorausschauendes automatisiertes Fahren
ISBN 978-3-7315-0949-3

Band 77 Thomas Schirle
Systementwurf eines elektromechanischen Fahrwerks für Megacitymobilität
ISBN 978-3-7315-0995-0

Band 78 Dominik Dörr
Simulation of the thermoforming process of UD fiber-reinforced thermoplastic tape laminates
ISBN 978-3-7315-0998-1

Band 79 Dominik Robert Naake
Simulation of damage mechanisms in weave reinforced materials based on multiscale modeling
ISBN 978-3-7315-1005-5

Band 80 Martin Hohberg
Experimental investigation and process simulation of the compression molding process of Sheet Molding Compound (SMC) with local reinforcements
ISBN 978-3-7315-1007-9

Band 81 Benedikt Fengler
Manufacturing-constrained multi-objective optimization of local patch reinforcements for discontinuous fiber reinforced composite parts
ISBN 978-3-7315-1006-2

Band 82 Johannes Masino
Road Condition Estimation with Data Mining Methods using Vehicle Based Sensors
ISBN 978-3-7315-1004-8

Band 83 **11. Kolloquium Mobilhydraulik**
10. September 2020, Karlsruhe
ISBN 978-3-7315-1036-9

Die Bände sind unter www.ksp.kit.edu als PDF frei verfügbar oder als Druckausgabe bestellbar.

Band 84 Felix Weber
Beitrag zur Entwicklung von Konstantflusspumpen für Frischbeton unter genauerer Betrachtung der Dickstoffventile
ISBN 978-3-7315-1037-6

Band 85 8. Fachtagung
Hybride und energieeffiziente Antriebe für mobile Arbeitsmaschinen. 23. Februar 2021, Karlsruhe
ISBN 978-3-7315-1071-0

Band 86 Sebastian Fünfgeld
Vorausschauende Regelung von Fahrzeugsystemen durch stochastische Vorhersage der Fahrzeugdynamik
ISBN 978-3-7315-1060-4

Band 87 Isabelle Charlotte Ays
Development of a CO2e quantification method and of solutions for reducing the greenhouse gas emissions of construction machines = Entwicklung einer CO2e Quantifizierungsmethode und von Lösungen zur Reduzierung von Treibhausgasemissionen in Baumaschinen
ISBN 978-3-7315-1033-8

Band 88 Alexander Bernath
Numerical prediction of curing and process-induced distortion of composite structures
ISBN 978-3-7315-1063-5

Band 89 Nils Bulthaupt
Objektivierung des Schwingungskomforts schwerer Nutzfahrzeuge
ISBN 978-3-7315-1075-8

Band 90 Lars Brinkschulte
Assistenzsysteme zur Reduktion des Schädigungsverhaltens von Komponenten einer mobilen Arbeitsmaschine
ISBN 978-3-7315-1089-5

Band 91 Dominik Dörr
Adaptive Fahrhinweise für ein längsdynamisches Fahrerassistenzsystem zur Steigerung der Energieeffizienz
ISBN 978-3-7315-1090-1

Band 92 Jürgen Römer
Steuerung und Regelung des Lenkradmoments durch Nutzung radselektiver Frontantriebe
ISBN 978-3-7315-1104-5

Band 93 Christian Riese
Werkzeuge und Konzepte für die Untersuchung und Entwicklung zukünftiger Kfz-Bremssysteme
ISBN 978-3-7315-1125-0

Band 94 Yaoqun Zhou
Dynamisches Bremsverhalten des Reifen-Fahrwerk-Systems
ISBN 978-3-7315-1156-4

Band 95 Stefan Haug
Ganzheitliche Optimierung einer Axialkolbenpumpe durch bedarfsangepasste Entlastung tribologischer Kontakte
ISBN 978-3-7315-1150-2

Band 96 Stefan Scheubner
Stochastic Range Estimation Algorithms for Electric Vehicles using Data-Driven Learning Models
ISBN 978-3-7315-1166-3

Band 97 Yusheng Xiang
AI and IoT Meet Mobile Machines: Towards a Smart Working Site
ISBN 978-3-7315-1165-6

Band 98 Nils Meyer
Mesoscale simulation of the mold filling process of Sheet Molding Compound
ISBN 978-3-7315-1173-1

Band 99 Christian Timo Poppe
Process simulation of wet compression moulding for continuous fibre-reinforced polymers
ISBN 978-3-7315-1190-8

Band 100 Torben Fischer
Modellprädiktive Regelung eines innovativen Thermomanagement-Systems für batterieelektrische Fahrzeuge
ISBN 978-3-7315-1199-1

Band 101 Florian Wittemann
Fiber-dependent injection molding simulation of discontinuous reinforced polymers
ISBN 978-3-7315-1217-2

Band 102 Sebastian Watzl
Experimentelle und numerische Analyse des Körperschallübertragungsverhaltens von Aggregatelagerelementen im akustisch relevanten Frequenzbereich
ISBN 978-3-7315-1226-4

Die Bände sind unter www.ksp.kit.edu als PDF frei verfügbar oder als Druckausgabe bestellbar.

Band 103 Dominik Stretz
Vibroakustische Analyse eines elektrischen Radnabenmotors und Optimierung durch geeignete Steuerungsansätze
ISBN 978-3-7315-1245-5

Band 104 Mohamed Elgharbawy
Measurable Safety of Automated Driving Functions in Commercial Motor Vehicles - Technological and Methodical Approaches
ISBN 978-3-7315-1254-7

Band 105 Bernhard Schmiedel
Indirekte Schätzung des Fahrbahnnässegrads zur Detektion von gefährlichen Fahrzuständen
ISBN 978-3-7315-1258-5

Band 106 9. Fachtagung
Hybride und energieeffiziente Antriebe für mobile Arbeitsmaschinen. 28. Februar 2023, Karlsruhe
ISBN 978-3-7315-1260-8

Band 107 Patrick Riehm
Zur Wechselwirkung zwischen Fahrbahntextur und Laufstreifenmischung von Pkw-Reifen
ISBN 978-3-7315-1268-4

Band 108 Markus Tesar
Deep Reinforcement Learning zur Steigerung von Energieeffizienz und Pünktlichkeit von Straßenbahnen
ISBN 978-3-7315-1277-6

Band 109 Michael Mürken
Methode zur Bewertung der Zuverlässigkeit der elektrischen Energieversorgung in der automobilen Vorentwicklung
ISBN 978-3-7315-1298-1

Band 110 Julien Pinay
Experimental investigation of relevant road surface descriptors for tire-road noise measurements on low-absorbing road surfaces
ISBN 978-3-7315-1328-5

Band 111 Adrian Strigel
Methode zur Ermittlung optimaler Rad- und Reifendimensionen in der frühen Entwicklungsphase von Personenkraftwagen
ISBN 978-3-7315-1321-6

Band 112 Jens Jauch
Trajectory optimization based on recursive B-spline approximation for automated longitudinal control of a battery electric vehicle
ISBN 978-3-7315-1332-2

Band 113 Nicolas Fraikin
Methodik zur effizienten Applikation automatisierter Fahrfunktionen
ISBN 978-3-7315-1339-1

Band 114 Jan Siebert
Effizienzoptimierung mobilhydraulischer Load-Sensing-Systeme durch Reduzierung systembedingter Druckverluste am Beispiel eines Hydraulikbaggers
ISBN 978-3-7315-1343-8

Band 115 Tobias Sebastian Straub
Flottendatenbasierte physikalische Routenenergiebedarfsprognose
ISBN 978-3-7315-1348-3

Band 116 Michael Herrmann
Eine Methodik zur Definition von Zielkriterien am Beispiel des tieffrequenten Geräuschkomforts eines Fahrzeugs
ISBN 978-3-7315-1370-4

Band 117 Adam Thor Thorgeirsson
Probabilistic Prediction of Energy Demand and Driving Range for Electric Vehicles with Federated Learning
ISBN 978-3-7315-1371-1

Band 118 Alexander Jackstadt
Constrained-layer damping in hybrid fibre metal elastomer laminates and its tolerance to damage
ISBN 978-3-7315-1376-6

Karlsruher Schriftenreihe
Fahrzeugsystemtechnik

FAST
Institut für
Fahrzeugsystemtechnik

Fibre-reinforced polymers are widely used in lightweight design due to their outstanding weight-specific mechanical properties such as stiffness and strength. The combination with sheets of metal, referred to as fibre metal laminates, additionally provides a high resistance and tolerance to damage. These advantages, however, come at a cost, particularly a proneness to vibrations. The addition of highly compliant layers consisting of viscoelastic materials can significantly increase the achievable material damping, following the principle of constrained-layer damping (CLD). Such a hybridisation then allows for highly damped lightweight laminates, which can be tailored to specific damping capabilities. This work considers hybrid fibre metal elastomer laminates (FMELs) consisting of carbon fibre-reinforced polymer, aluminium and different elastomer compounds in various laminate configurations. It presents experimental, analytical and numerical methods for predicting structural behaviour as well as damping capabilities of FMELs, with a focus on the assessment of the CLD mechanism's tolerance to damage.

ISSN 1869-6058
ISBN 978-3-7315-1376-6